

## Experiments on the physics of pulsed plasma jets

**Citation for published version (APA):**

van der Schans, M. (2018). *Experiments on the physics of pulsed plasma jets*. [Phd Thesis 1 (Research TU/e / Graduation TU/e), Applied Physics and Science Education]. Technische Universiteit Eindhoven.

**Document status and date:**

Published: 19/12/2018

**Document Version:**

Publisher's PDF, also known as Version of Record (includes final page, issue and volume numbers)

**Please check the document version of this publication:**

- A submitted manuscript is the version of the article upon submission and before peer-review. There can be important differences between the submitted version and the official published version of record. People interested in the research are advised to contact the author for the final version of the publication, or visit the DOI to the publisher's website.
- The final author version and the galley proof are versions of the publication after peer review.
- The final published version features the final layout of the paper including the volume, issue and page numbers.

[Link to publication](#)

**General rights**

Copyright and moral rights for the publications made accessible in the public portal are retained by the authors and/or other copyright owners and it is a condition of accessing publications that users recognise and abide by the legal requirements associated with these rights.

- Users may download and print one copy of any publication from the public portal for the purpose of private study or research.
- You may not further distribute the material or use it for any profit-making activity or commercial gain
- You may freely distribute the URL identifying the publication in the public portal.

If the publication is distributed under the terms of Article 25fa of the Dutch Copyright Act, indicated by the "Taverne" license above, please follow below link for the End User Agreement:

[www.tue.nl/taverne](http://www.tue.nl/taverne)

**Take down policy**

If you believe that this document breaches copyright please contact us at:

[openaccess@tue.nl](mailto:openaccess@tue.nl)

providing details and we will investigate your claim.

# Experiments on the physics of pulsed plasma jets

PROEFSCHRIFT

ter verkrijging van de graad van doctor aan de Technische Universiteit Eindhoven,  
op gezag van de rector magnificus, prof.dr.ir. F. P. T. Baaijens,  
voor een commissie aangewezen door het College voor Promoties,  
in het openbaar te verdedigen op woensdag 19 december 2018 om 16:00 uur

door

Marc van der Schans

geboren te Waalwijk

Dit proefschrift is goedgekeurd door de promotoren en de samenstelling van de promotiecommissie is als volgt:

voorzitter: prof.dr.ir. E. J. E. Cottaar  
1e promotor: prof.dr.ir. W. L. IJzerman  
2e promotor: prof.dr.ir. G. M. W. Kroesen  
copromotor: dr.ir. S. Nijdam  
leden: prof.dr. I. V. Adamovich (Ohio State University)  
prof.dr. R. Brandenburg (Universität Rostock)  
dr. R. A. H. Engeln  
prof.dr. U. Czarnetzki (Ruhr-Universität Bochum)

Het onderzoek dat in dit proefschrift wordt beschreven is uitgevoerd in overeenstemming met de TU/e Gedragscode Wetenschapsbeoefening.

# Experiments on the physics of pulsed plasma jets

Marc van der Schans

**Cover photos**

Bart van Overbeeke Fotografie

**Print**

Ipskamp Printing, Enschede

This research was performed within the framework of the strategic joint research program on Intelligent Lighting between TU/e and Signify N.V.



A catalogue record is available from the Eindhoven University of Technology Library.  
**ISBN:** 978-90-386-4660-2

© Marc van der Schans, 2018

---

# Summary

## Experiments on the physics of pulsed plasma jets

Pulsed plasma jets are discharges that are produced in an atmospheric pressure gas flow by repeatedly applying high voltage pulses. Under the right conditions, these discharges are highly reproducible guided streamer discharges, which are also popularly referred to as ‘plasma bullets’. The repeatable behaviour of guided streamer discharges is generally attributed to a memory effect, where the seed electrons for the next discharge are provided by remnants of the previous discharges. However, the exact details of the memory effect and the characteristics of the guided streamer discharges are not completely understood yet. The goal of this research is to attain a greater understanding of the properties and physical mechanisms of guided streamer discharges produced in pulsed plasma jets in nitrogen, helium and argon feed gas flowing into ambient air. To do so, various experimental techniques are used, including high-speed imaging, time-resolved emission measurements, microwave cavity resonance spectroscopy, and electric field four-wave mixing.

From imaging individual discharges with an intensified camera, it is found that guided streamers in nitrogen feed gas propagate along the centre of the jet with a lateral reproducibility of about  $13\ \mu\text{m}$ . Guided streamers in helium feed gas propagate along the gas mixing layer, and their spatial reproducibility is limited by the stability of the gas flow. In argon feed gas, the discharges consist of either guided streamer discharges that propagate on the centre of the jet until they branch to the gas mixing layer at lower applied voltages or streamer discharges that immediately branch to the gas mixing layer at higher applied voltages. They are not spatially reproducible but still guided in the sense that they are confined by the gas flow. The temporal reproducibility of the inception of the guided streamers is inferred from time-resolved emission measurements. For nitrogen and helium feed gas, temporal reproducibility down to 500 ps is observed. For argon feed gas, temporal reproducibility of down to 2 ns could be achieved.

To investigate the development of the memory effect in nitrogen and helium feed

gas, the first discharges are considered. For both nitrogen and helium, the inception of the first discharge occurs at a random moment in the voltage pulse. Starting from the second discharge, sub-nanosecond temporal reproducibility is achieved. This shows that the temporal memory requires only a single discharge to develop. For helium, the discharges are spatially guided by the gas mixing layer, and they all have similar trajectories, with the exception of the first one. The length of the first discharge in helium depends on the moment of inception. In contrast, for nitrogen feed gas, a development phase of about ten discharges is observed, in which the length of guided streamer increases. By numerical simulation of the gas flow, it is found that the development of the guided streamer length corresponds to the distance that discharge remnants have travelled in the flow starting from the first discharge. This shows that, unlike in the case of helium, for guided streamers in nitrogen there is an additional spatial memory effect that provides the guiding mechanism.

To study the role of charged species in the spatial memory effect of pulsed plasma jets in nitrogen feed gas, an external field perpendicular to the propagation direction of the discharge is applied between successive discharges. It is found that the trajectories of the discharges can be displaced by manipulating the memory effect this way. This result confirms that charged species play an important role in the memory effect. The magnitude and direction of the displacement correspond to the drift of positively charged ions. This is a surprising result because displacement in the direction of the electron drift was expected instead, as it is well known that a source of seed electrons is required for (positive) streamer propagation. The mechanism behind the observed displacement is still unclear.

The decay of the electron density between consecutive discharges in a pulsed plasma jet in nitrogen feed gas is investigated using microwave cavity resonance spectroscopy (MCRS) and a global model. The MCRS method is adapted for atmospheric pressure plasma jets and applied to a pulsed plasma jet in nitrogen. It is shown that the electron density, as well as the effective collision frequency, can be measured using this technique from about 1  $\mu\text{s}$  to approximately 60  $\mu\text{s}$  after the discharge, where the former is limited by the response time of the cavity and the latter by the detection limit of about  $10^{16} \text{ m}^{-3}$ . Although the data analysis requires an estimation of the plasma volume that limits the absolute accuracy of the electron density to its order of magnitude, the measured electron densities are in the same range as those predicted by the global model. There is a good qualitative agreement in the decay rate between the measurements and the model. Furthermore, it is inferred from the model that the minimum electron density required for repeatable guided streamer discharges is of the order of  $10^{15} \text{ m}^{-3}$ .

The electric field of pulsed plasma jets in nitrogen has been measured using electric field four-wave mixing. The method and its analysis have been extended to resolve radial profiles of non-uniform, but radially symmetric, electric field distributions. In addition, a calibration procedure using an electrode geometry different from the discharge geometry has been developed. A radial profile is obtained for the axial component of the electric field in front of the guided streamer with a peak value of about 12–18 kV/mm and a FWHM of 750–900  $\mu\text{m}$ . To verify the results, they are compared to a streamer model adapted to the conditions of the experiment. It is found

---

that there are some quantitative differences with the model, which predicts values approximately a factor 2 lower than those found in the experiment, as well as a faster radial decay. The temporal development shows similar features in both the experiment and the model. It is hypothesised that the factor 2 difference between the measured and modelled electric fields is partly due to the plane-wave approximation, which is used in the analysis of the four-wave mixing experiments. A theoretical description of the four-wave mixing process is developed using Gaussian beams instead of plane-waves to investigate this. It is demonstrated that the plane-wave approximation is indeed responsible for overestimating the measured electric field. Therefore, the validity of the plane-wave approximation should always be carefully considered in the calibration.





---

# Samenvatting

## Experimenten aan de fysica van gepulste plasma-jets

Gepulste plasma-*jets* zijn ontladingen die geproduceerd worden door herhaaldelijk hoogspanningspulsen aan te leggen in een gasstroming op atmosferische druk. Onder de juiste omstandigheden zijn deze ontladingen zeer reproduceerbare geleide *streamer*ontladingen, die ook wel ‘plasmakogels’ worden genoemd. Het herhaalbare gedrag van geleide streamerontladingen wordt in het algemeen toegeschreven aan een geheugeneffect, waarin de benodigde elektronen voor de volgende ontlading overblijfselen zijn van de voorgaande ontladingen. De exacte details van het geheugeneffect en de kenmerken van geleide streamerontladingen zijn echter onduidelijk. Het doel van dit onderzoek is het verkrijgen van een beter begrip van de eigenschappen en fysische mechanismen van geleide streamerontladingen geproduceerd in gepulste plasma-jets in stikstof-, helium- en argongas dat de omgevingslucht instroomt. Hiervoor worden verscheidene experimentele technieken gebruikt, waaronder hogesnelheidsopnames, tijdsopgeloste optische emissiemetingen, *microwave cavity resonance spectroscopy* en elektrisch veld-geïnduceerde *four-wave mixing*.

Uit afbeeldingen van individuele ontladingen gemaakt met een beeldversterkte camera blijkt dat geleide streamers in stikstof zich in het midden van de gasstroming voortbewegen met een reproduceerbaarheid van de laterale positie van ongeveer 13  $\mu\text{m}$ . Geleide streamers in helium bewegen zich voort langs de menglaag van het heliumgas en de omgevingslucht, en hun ruimtelijke reproduceerbaarheid wordt beperkt door de stabiliteit van de gasstroom. In argon bestaan de ontladingen ofwel uit geleide streamerontladingen die zich in het midden van de gasstroom voortbewegen totdat ze vertakken naar de menglaag bij lagere aangelegde spanningen, of uit streamerontladingen die zich onmiddellijk vertakken naar de menglaag bij hogere aangelegde spanningen. De ontladingen zijn niet ruimtelijk reproduceerbaar maar kunnen nog steeds als geleid beschouwd worden in de zin dat ze begrensd worden door de gasstroming. De tijdsreproduceerbaarheid van de aanvang van de geleide streamers is bepaald met tijdsopgeloste optische emissiemetingen. Voor zowel stikstof

als helium is een reproduceerbaarheid van 500 ps waargenomen. Voor argon wordt een reproduceerbaarheid van 2 ns bereikt.

Om de ontwikkeling van het geheugeneffect in stikstof en helium te onderzoeken worden de eerste ontladingen bestudeerd. Voor zowel stikstof als helium begint de eerste ontlading op een willekeurig moment tijdens de spanningspuls. Vanaf de tweede ontlading wordt een tijdsreproduceerbaarheid van minder dan een nanoseconde bereikt. Dit toont aan dat het geheugeneffect dat leidt tot tijdsreproduceerbaarheid slechts een enkele ontlading nodig heeft om zich te ontwikkelen. In het geval van helium worden de ontladingen ruimtelijk geleid door de menglaag en alle ontladingen volgen dezelfde baan, met uitzondering van de eerste. De lengte van de eerste ontlading in helium is afhankelijk van het precieze aanvangsmoment van de ontlading. Daarentegen vindt er voor stikstof een ontwikkelingsfase plaats van ongeveer tien ontladingen, waarin de lengte van de geleide streamer toeneemt. Door middel van numerieke simulatie van de gasstroming is gevonden dat de ontwikkeling van de lengte van de geleide streamerontlading overeenkomt met de afstand die overblijfselen van eerdere ontladingen kunnen hebben afgelegd sinds de eerste ontlading. Dit toont aan dat, in tegenstelling tot het geval van helium, voor geleide streamers in stikstof er een extra ruimtelijk geheugeneffect is dat voor het geleidingsmechanisme zorgt.

Om de rol van geladen deeltjes in het ruimtelijke geheugeneffect van gepulste plasma-jets in stikstofgas te bestuderen is een extern elektrisch veld loodrecht op de voortbewegingsrichting van de ontladingen aangelegd in de tijd tussen opeenvolgende hoogspanningspulsen. Het is gebleken dat de baan van de ontladingen inderdaad verplaatst kan worden door het geheugeneffect op deze manier te manipuleren. Dit resultaat bevestigt de belangrijke rol van geladen deeltjes in het geheugen effect. De grootte en richting van de verplaatsing komen overeen met de drift van positief geladen ionen in het elektrische veld. Dit is een verassend resultaat omdat verplaatsing in de richting van de elektronendrift verwacht werd, aangezien het bekend is dat een bron van elektronen vereist is voor (positieve) streamerpropagatie. Het achterliggende mechanisme van de waargenomen verplaatsing is nog onbegrepen.

Het verval van elektronendichtheid tussen opeenvolgende ontladingen in een gepulste plasma-jet in stikstof is onderzocht met behulp van microwave cavity resonance spectroscopy en een nuldimensionaal model. De bestaande meetmethode is aangepast voor plasma-jets op atmosferische druk en toegepast op een gepulste plasma-jet in stikstof. Er is gevonden dat de elektronendichtheid, evenals de effectieve botsingsfrequentie, gemeten kan worden met deze techniek vanaf ongeveer 1  $\mu\text{s}$  tot ongeveer 60  $\mu\text{s}$  na de ontlading, waarbij de eerstgenoemde wordt beperkt door de responstijd van de trillholte en de laatstgenoemde door de detectielimiet van ongeveer  $10^{16} \text{ m}^{-3}$ . Hoewel de analyse van de meetdata een schatting van het plasmavolume vereist, die de absolute nauwkeurigheid van de elektronendichtheid tot de orde van grootte beperkt, liggen de gemeten elektronendichtheden in hetzelfde bereik als die voorspeld door het model. Er is eveneens een goede kwalitatieve overeenkomst in het verval tussen de metingen en het model. Verder is uit het model afgeleid dat de minimale elektronendichtheid die benodigd is voor herhaalbare geleide streamerontladingen in de orde van  $10^{15} \text{ m}^{-3}$  is.

Het elektrische veld van gepulste plasma-jets in stikstof is gemeten met elektrisch veld-geïnduceerde four-wave mixing. De methode en analyse zijn uitgebreid om radiale

---

profielen van niet-uniforme, maar radiaal symmetrische, elektrische veldverdelingen op te kunnen lossen. Daarnaast is een kalibratieprocedure ontwikkeld met een elektrodegeometrie die verschilt van de ontladingsgeometrie. Een radiaal profiel van de axiale component van het elektrische veld van een geleide streamer in stikstof is verkregen. Deze heeft met een piekwaarde van ongeveer 12–18 kV/mm en een volle breedte bij halve maximale waarde van 750–900  $\mu\text{m}$ . Om de resultaten te verifiëren, zijn ze vergeleken met een streamermodel dat is aangepast aan de omstandigheden van het experiment. Het blijkt dat er enkele kwantitatieve verschillen zijn met het model, dat waarden van ongeveer een factor twee lager en een sneller radiaal verval voorspelt dan gemeten. Het gedrag als functie van tijd in het experiment is vergelijkbaar met het model. Er wordt verondersteld dat het verschil van een factor twee tussen de gemeten en gemodelleerde elektrische veldwaarden gedeeltelijk te wijten is aan de vlakkegolfbenadering, die gebruikt wordt bij de analyse van de four-wavemixingexperimenten. Een theoretische beschrijving van het four-wavemixingproces met Gaussische bundels in plaats van vlakke golven is ontwikkeld om dit te onderzoeken. Het is aangetoond dat de vlakkegolfbenadering inderdaad verantwoordelijk is voor de overschatting van de gemeten elektrische velden. Daarom moet in de kalibratie de geldigheid van de vlakkegolfbenadering altijd zorgvuldig worden overwogen.



---

# Contents

<b>Summary</b>	<b>v</b>
<b>Samenvatting</b>	<b>ix</b>
<b>1 Introduction</b>	<b>1</b>
1.1 Plasmas and pulsed plasma jets . . . . .	2
1.1.1 Pulsed plasma jets . . . . .	3
1.1.2 Applications of plasma jets . . . . .	3
1.2 Research goals . . . . .	4
1.3 Plasma source used in this research . . . . .	4
1.3.1 Basic propagation properties of the discharges . . . . .	7
1.3.2 Long-term reproducibility . . . . .	7
1.4 Thesis outline . . . . .	11
<b>2 Morphology and reproducibility of pulsed plasma jets</b>	<b>13</b>
2.1 Introduction . . . . .	14
2.2 Experimental setup and methods . . . . .	14
2.2.1 Setup . . . . .	14
2.2.2 Fluid dynamics model . . . . .	16
2.3 Results and discussion . . . . .	20
2.3.1 Morphology and spatial reproducibility . . . . .	20
2.3.2 Temporal reproducibility . . . . .	28
2.3.3 Length of guided streamers in N <sub>2</sub> and the role of O <sub>2</sub> . . . . .	28
2.4 Conclusions and outlook . . . . .	30
<b>3 Development of the memory effect</b>	<b>33</b>
3.1 Introduction . . . . .	34
3.2 Experimental setup and methods . . . . .	34
3.2.1 Setup . . . . .	34

3.2.2	Particle transport model . . . . .	37
3.3	Results and discussion . . . . .	37
3.3.1	Development of temporal reproducibility . . . . .	37
3.3.2	Development of spatial reproducibility . . . . .	41
3.4	Conclusions . . . . .	43
<b>4</b>	<b>Manipulation of the memory effect</b>	<b>45</b>
4.1	Introduction . . . . .	46
4.2	Experimental setup . . . . .	47
4.2.1	Plasma source and measurement system . . . . .	47
4.2.2	External electric field distribution . . . . .	49
4.3	Results and discussion . . . . .	51
4.3.1	Dependence on the external voltage . . . . .	51
4.3.2	Dependence on timing . . . . .	53
4.4	Conclusions and outlook . . . . .	55
<b>5</b>	<b>Electron densities between discharges</b>	<b>57</b>
5.1	Introduction . . . . .	58
5.2	Experimental setup and methods . . . . .	59
5.2.1	Setup and measurement system . . . . .	59
5.2.2	Microwave cavity resonance spectroscopy . . . . .	65
5.2.3	Global model . . . . .	71
5.3	Results and discussion . . . . .	74
5.4	Conclusions and outlook . . . . .	76
<b>6</b>	<b>Electric field measurements on plasma bullets in N<sub>2</sub> using four-wave mixing</b>	<b>79</b>
6.1	Introduction . . . . .	80
6.2	Experimental setup and methods . . . . .	81
6.2.1	Discharge setup . . . . .	81
6.2.2	Electric field four-wave mixing . . . . .	82
6.2.3	Laser setup and calibration . . . . .	87
6.2.4	Discharge simulation model . . . . .	90
6.3	Results and discussion . . . . .	94
6.3.1	Calibration measurement . . . . .	94
6.3.2	Plasma bullet measurements . . . . .	94
6.4	Conclusions and outlook . . . . .	100
<b>7</b>	<b>Four-wave mixing with focused laser beams</b>	<b>103</b>
7.1	Introduction . . . . .	104
7.2	Theory of four-wave mixing . . . . .	105
7.2.1	Non-linear optics and the driven wave-equation . . . . .	107
7.2.2	Plane-wave solution . . . . .	108
7.2.3	Gaussian beam solution . . . . .	109
7.3	Validity of the plane-wave approximation . . . . .	112
7.4	Revisiting the plasma bullet measurements . . . . .	116

---

7.5	Experimental test of the Gaussian beam solution . . . . .	118
7.6	Conclusions and outlook . . . . .	122
<b>8</b>	<b>General conclusions and recommendations</b>	<b>123</b>
	<b>Bibliography</b>	<b>140</b>
	<b>List of publications</b>	<b>141</b>
	<b>Contributions of the author</b>	<b>143</b>
	<b>Acknowledgements / Dankwoord</b>	<b>145</b>
	<b>Curriculum Vitae</b>	<b>147</b>





# Chapter 1

---

## Introduction

## 1.1 Plasmas and pulsed plasma jets

Plasma, often said to be the most abundant form of ordinary matter in the universe [1], is (partially) ionised gas. This means that the gas contains a significant amount of free charged particles—ions and electrons—besides the neutral particles. The presence of these charged particles profoundly changes the properties of the gas, and for this reason, plasma is commonly referred to as the fourth state of matter. Although it may go unnoticed, plasmas play an important role in everyday life, both directly and indirectly. For example, life would be impossible without the sun, which basically is a large ball of hot plasma, and our modern society would look vastly different without the computer chips that are manufactured using, among other things, plasma technology [2].

In the last decades, plasmas have been, and continue to be, researched and used for a wide variety of applications, including lighting, deposition and etching processes, gas treatment and purification, and medicine. Many of these applications benefit from the non-thermal state that often characterises the plasma. In this state, the electrons are hot, typically several 10 000 K, while the background gas remains near room temperature. This offers reaction mechanisms and chemistry that are inaccessible by any other means [3].

Laboratory and industrial plasmas are often produced by a gas discharge. When a sufficiently large electric field is applied to a gas, breakdown will occur, and a plasma is formed. This basically proceeds as follows. The electric field exerts a force on an electron, which, as a result, accelerates. If the accelerated electron acquires enough energy between collisions with the atoms or molecules of the background gas, the electron will be able to ionise an atom or molecule and produce an additional free electron. Now there are two electrons and the process repeats. The result is a cascade of ionisation events, called an electron avalanche, in which the ion and electron density grow exponentially and form a conductive channel. This process is called Townsend breakdown [4].

If the electron and ion densities become sufficiently large, space charge effects start to influence the electric field. A space charge layer is formed around the conductive channel which shields its interior from the electric field. At the same time, the electric field around the end of the channel is amplified. The amplified electric field subsequently promotes the generation of new electron avalanches in the vicinity of the end of the channel, provided there are free electrons available in this region. This process results in an extension of the conductive channel and is called a streamer discharge. The extension rate of the channel, which is the streamer's propagation velocity, is typically  $10^5$ – $10^6$  m/s [4].

Two types of streamer discharges can be distinguished: positive streamers and negative streamers. Positive streamers have a positive space charge layer and are associated with voltages of positive polarity, whereas negative streamers have a negative space charge layer and are associated with voltages of negative polarity. This means that electrons drift towards positive streamers, and away from negative streamers. As a consequence, negative streamers are able to supply the required electrons in front of the streamer channel themselves. Positive streamers, on the other hand, cannot do

this, and hence require another source of free electrons in front of the streamer channel. In air, photo-ionisation of oxygen molecules by ultraviolet (UV) photons emitted by excited nitrogen molecules can provide a source of free electrons. Alternatively, free electrons can be present already from background ionisation. Background ionisation can result from radioactive decay, cosmic radiation, or, when the time between successive discharges is sufficiently short, remnants of previous discharges. As will be discussed shortly, the latter is of critical importance in pulsed plasma jets.

### 1.1.1 Pulsed plasma jets

Plasma jets are gas discharges that are produced in a stream of gas, usually at atmospheric pressure. When the discharges of a plasma jet are generated by repeatedly applying high voltage pulses, it is called a pulsed plasma jet. As discovered by Teschke *et al* [5] and by Lu and Laroussi [6], the discharges in plasma jets driven by AC or pulsed voltage in the kHz range appear as ‘plasma bullets’ in nanosecond exposure images. It was found that these plasma bullets exhibit very repeatable behaviour in space and time. In fact, plasma bullets are not volumes of travelling plasma, but rather propagating ionisation waves.

It was later found that plasma bullets have properties that are similar to (positive) streamer discharges. For example, they have comparable propagation velocities of the order of  $10^5$ – $10^6$  m/s. However, the most notable difference is that plasma bullets are highly reproducible, whereas streamer discharges typically exhibit stochastic behaviour and often split into multiple branches. For this reason, plasma bullets are more accurately called guided streamer discharges. The reproducibility of guided streamer discharges in pulsed plasma jets is generally ascribed to a memory effect, where the seed electrons for the next discharge are provided by remnants of the previous discharges [7–9].

Since the first discovery of plasma bullets and guided streamer discharges, numerous experimental and numerical investigations have been performed on various aspects of guided streamer discharges in pulsed plasma jets. These include the effects of the operating parameters on the propagation dynamics of the guided streamers, the effects of photo-ionisation and seed electrons, the role of Penning ionisation, as well as the interaction of guided streamers with target surfaces and the mutual interaction between multiple jets (see for example [8–10] and the references therein). The large majority of these investigations have been carried out in He feed gas. While this has resulted in a better understanding of the properties of guided streamer discharges, many details of the exact physical mechanisms behind the memory effect and the resulting repeatable behaviour still remain unclear [9].

### 1.1.2 Applications of plasma jets

Atmospheric pressure plasma jets have a wide variety of applications, including surface activation, thin film deposition [11], surface cleaning and coating [12], and photoresist removal [13]. Due to their non-thermal character, plasma jets can also be applied to heat sensitive materials. One notable example of this is biological material, which over the last two decades has led to the rise of the research field of plasma medicine [14–16].

Medical applications of non-thermal plasmas that are being researched include bio-decontamination [17], stimulation of wound healing [18], and even the treatment of cancer [19]. According to the 2017 Plasma Roadmap [20], plasma medicine is among the fastest growing applications of non-thermal plasmas. However, it is also noted that the physics and chemistry of the used plasma sources, such as plasma jets, and their interaction with biological cells, tissue and organisms are far from completely understood.

A completely different application was considered in the context of this project: surface profiling of freeform optics. Freeform optics are optical elements that have a freeform surface. They are for example used as illumination optics for light-emitting diodes (LEDs) to create uniform or specifically prescribed illumination [21,22]. Profiling freeform surfaces is challenging: contact methods are relatively slow and may damage the surface, while interferometric methods are fast but do not work well for surfaces containing large steps or high curvature [23]. As an alternative to these two methods, it was wondered whether it would be possible to profile a surface by ‘shooting’ plasma bullets at it with a pulsed plasma jet and determining the (local) distance to the surface from properties of the discharge, such as when the discharge arrives at the surface (a ‘time-of-flight’ measurement). Ultimately, this application was not tested.

## 1.2 Research goals

The primary goal of this research is to attain a greater understanding of the properties and physical mechanisms of guided streamer discharges produced in pulsed plasma jets in nitrogen, helium and argon feed gas flowing into ambient air. Therefore, the following research questions are formulated:

- To what extent and under what conditions are guided streamer discharges in pulsed plasma jets temporally and spatially reproducible?
- Which physical mechanisms are involved in the memory effect and in guiding the streamer discharges?
- How does the electron density decay between successive discharges, and what is the minimum seed electron density required for the memory effect?
- What is the electric field of the guided streamer discharges?

To answer these questions, various experimental techniques are used, including high-speed imaging, time-resolved emission measurements, microwave cavity resonance spectroscopy, and electric field four-wave mixing. Each of these methods and the reasons for using them will be explained in detail in the individual chapters.

## 1.3 Plasma source used in this research

While various measurement techniques will be applied, the plasma source remains the same throughout the work described in this thesis. The plasma source and some of its basic properties will be described in this section. In figure 1.1, the discharge

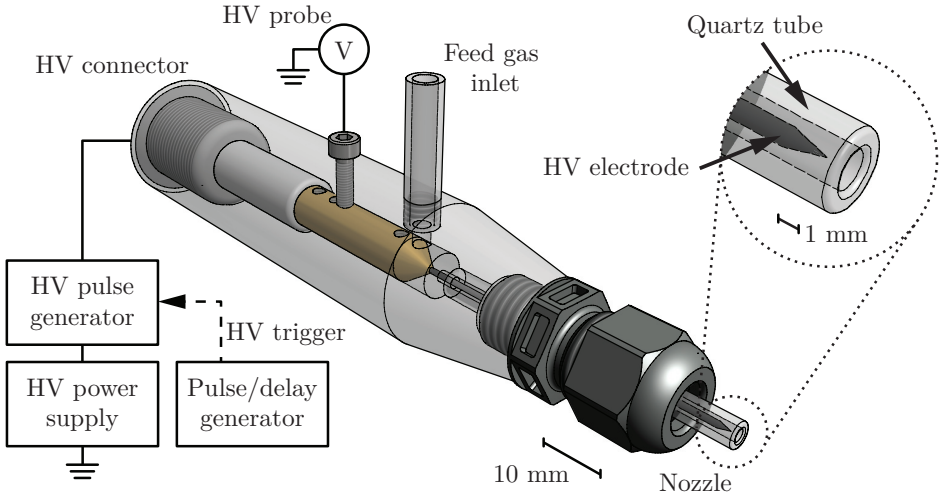


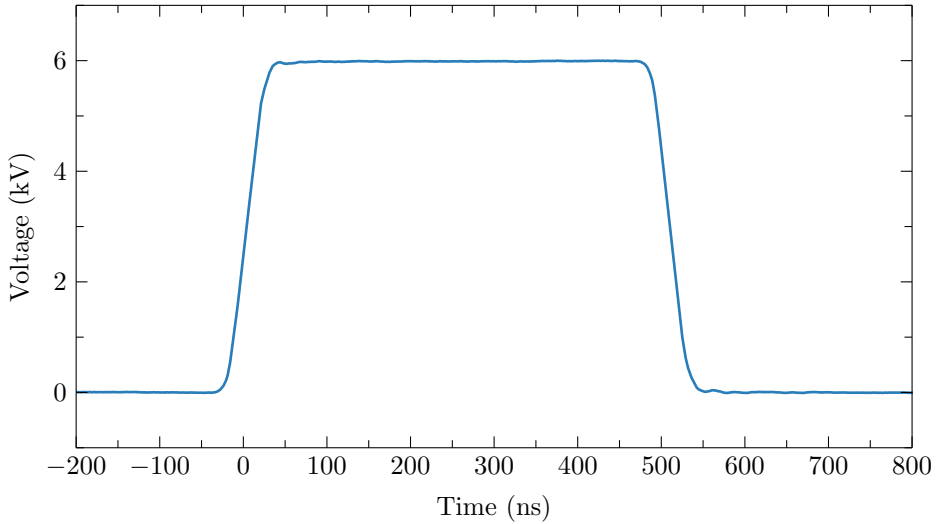
**Figure 1.1:** Schematic overview of the plasma source that is used throughout the research presented in this thesis.

setup is illustrated. A pulsed plasma jet is generated by repeatedly applying a high voltage pulse to a needle electrode. The casing of the device that houses the needle electrode is made of polycarbonate and has an inlet for the feed gas on top. In this work, three feed gases are used, namely  $N_2$ , He and Ar, each with a purity of 99.999%. The impurities, as specified by the supplier, in the used gases are listed in table 1.1. Typically, a volumetric flow rate  $\Phi$  around 1 slm (standard litre per minute) will be used. The feed gas subsequently flows into open air through the nozzle, which is a quartz tube of 1 mm inner radius and 2 mm outer radius. The needle electrode, which is placed concentrically inside the quartz tube, is made of tungsten, has a radius of 0.5 mm and its tip has an angle of approximately  $20^\circ$ . The tip of the needle is located 2 mm from the end of the quartz tube. The back of the casing has a high voltage (HV) connector that connects a pulsed power supply to the needle electrode through a brass screw terminal. An additional screw is placed in contact with the screw terminal and is connected to a HV probe (Tektronix P6015A) to monitor the applied voltage. As a grounded electrode is not specified in the setup, the discharge geometry is that of a single electrode plasma jet [10, 24]. A previous version of this plasma source was used in the research of Hofmann *et al* [7, 25].

To generate HV pulses, the output of a HV power supply (Spellman UHR10P60) is gated by a HV pulse generator (DEI PVX-4110). The gate signal for the HV pulse generator is provided by a pulse/delay generator (BNC model 575), which will also be used to synchronise the measurement setups to the discharges. Depending on the feed gas, voltage amplitudes  $V$  between 3 kV and 10 kV are used, and the repetition frequency  $f_{\text{rep}}$  is typically 3 kHz. The pulse width is kept at a fixed value of 500 ns throughout this work. The shape of the applied voltage pulses is shown in figure 1.2 for an amplitude of 6 kV. With this setup, rise and fall times of about 40 ns are achieved.

**Table 1.1:** Purity of the used feed gases, as specified by the supplier [26].

Gas	Purity (vol.-%)	Impurities (vol.-ppm)			
		N <sub>2</sub>	O <sub>2</sub>	H <sub>2</sub> O	C <sub>x</sub> H <sub>y</sub>
N <sub>2</sub>	≥ 99.999	≤ 5	≤ 5	≤ 5	≤ 0.2
He	≥ 99.999	≤ 5	≤ 2	≤ 3	≤ 1
Ar	≥ 99.999	≤ 5	≤ 5	≤ 5	≤ 0.2

**Figure 1.2:** Shape of the voltage pulses that are used to generate the pulsed plasma jet.

### 1.3.1 Basic propagation properties of the discharges

To illustrate the ‘plasma bullets’ generated by the pulsed plasma jet, a sequence of 1 ns exposures of the discharge, taken at 20 ns intervals with an intensified charge-coupled device (ICCD) camera (Stanford Computer Optics 4 Picos), are shown in figure 1.3 for N<sub>2</sub> feed gas and in figure 1.4 for He feed gas. In both cases, a discharge emerges from the needle electrode and propagates into the region outside the nozzle when a voltage pulse is applied. However, there are some readily observed differences. The discharge in N<sub>2</sub> feed gas closely resembles a traditional streamer discharge in N<sub>2</sub>, with the maximum emission intensity on the discharge axis. For the discharge in He feed gas, on the other hand, the emission appears more intense on the outer edges up to about 60 ns. This indicates an annular discharge structure that is typically observed in pulsed plasma jets in He feed gas [8, 27].

From a series of plasma bullet images, such as those shown in figure 1.3 and 1.4, the position and (axial) propagation velocity of the discharge can be determined as a function of time. This is done for a range of operating parameters for both N<sub>2</sub> and He feed gas. The results are shown in figure 1.5 for N<sub>2</sub> feed gas. In the position graphs, the zero position corresponds to the end of the quartz tube, and the hatched area indicates the region inside the quartz tube. The velocity graphs are discontinuous at the moment the discharge leaves the quartz tube because the curvature of the nozzle distorts the emission and this data is excluded. It can be seen that in the available range of operating parameters, the applied voltage has the most influence on the propagation dynamics of the discharges. For higher voltages, the guided streamer discharge propagates further and faster. However, in every case, a propagation velocity of the order of 10<sup>5</sup> m/s is achieved, which is typical for streamer discharges, as mentioned before. The positions and propagation velocities obtained from the discharges in He feed gas are shown in figure 1.6. Despite the difference in appearance, propagation behaviour very similar to that in N<sub>2</sub> feed gas is observed. The propagation dynamics are mainly dependant on the applied voltage, and the typical propagation velocity is of the order of 10<sup>5</sup> m/s.

### 1.3.2 Long-term reproducibility

The research presented in this thesis was performed over the course of approximately four years. During this time, the plasma source has been disassembled and reassembled several times. Additionally, the feed gas flows into the ambient air of the laboratory. There is no precise climate control in the laboratory where the experiments were performed. To see if this has had an impact on the results, the position and velocity measurements of the plasma bullets in N<sub>2</sub> feed gas measured at different moments during these four years are compared in figure 1.7. It can be seen that close to the nozzle, the propagation of the guided streamers in N<sub>2</sub> feed gas has not changed over time. Further downstream, the positions start to deviate slightly. Even so, the differences in position stay within 5% up to 100 ns.



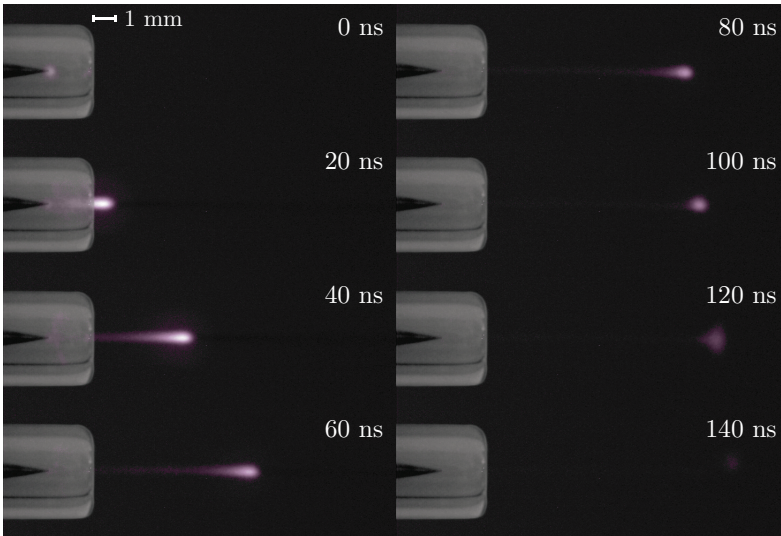


**Figure 1.3:** Plasma bullet propagation in  $N_2$  feed gas (8 kV, 3 kHz, 1 slm). For each of the images, 500 exposures are collected with a gate time of 1 ns. The nozzle, as well as the colours, were added in post-processing for illustrational purposes.

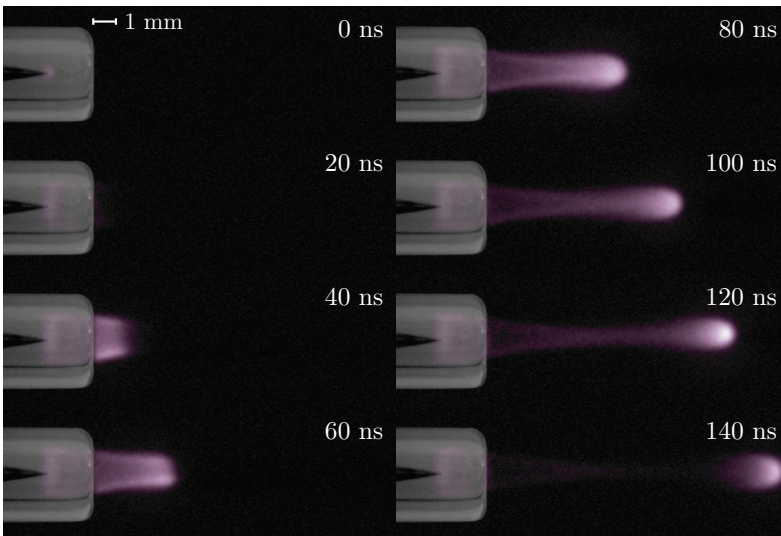


**Figure 1.4:** Plasma bullet propagation in He feed gas (5 kV, 3 kHz, 1 slm). For each of the images, 500 exposures are collected with a gate time of 1 ns. The nozzle, as well as the colours, were added in post-processing for illustrational purposes.

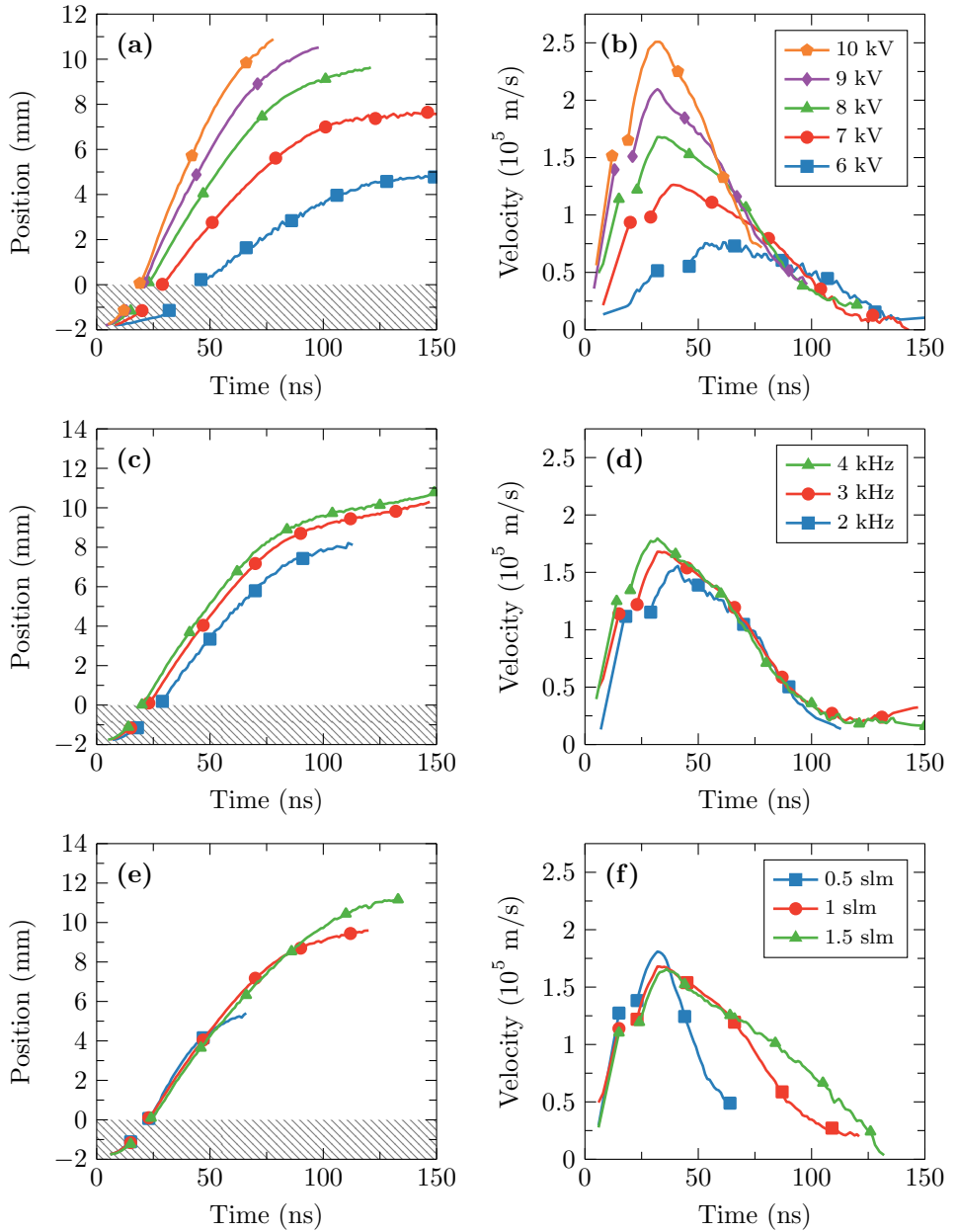


**Figure 1.5:** Position (left) and velocity (right) of plasma bullets in  $\text{N}_2$  for: (a and b) different voltages at  $f_{\text{rep}} = 3$  kHz and  $\Phi = 1$  slm, (c and d) different frequencies at  $V = 8$  kV and  $\Phi = 1$  slm, (e and f) different flow rates at  $V = 8$  kV and  $f_{\text{rep}} = 3$  kHz. A marker is placed every twenty data points.

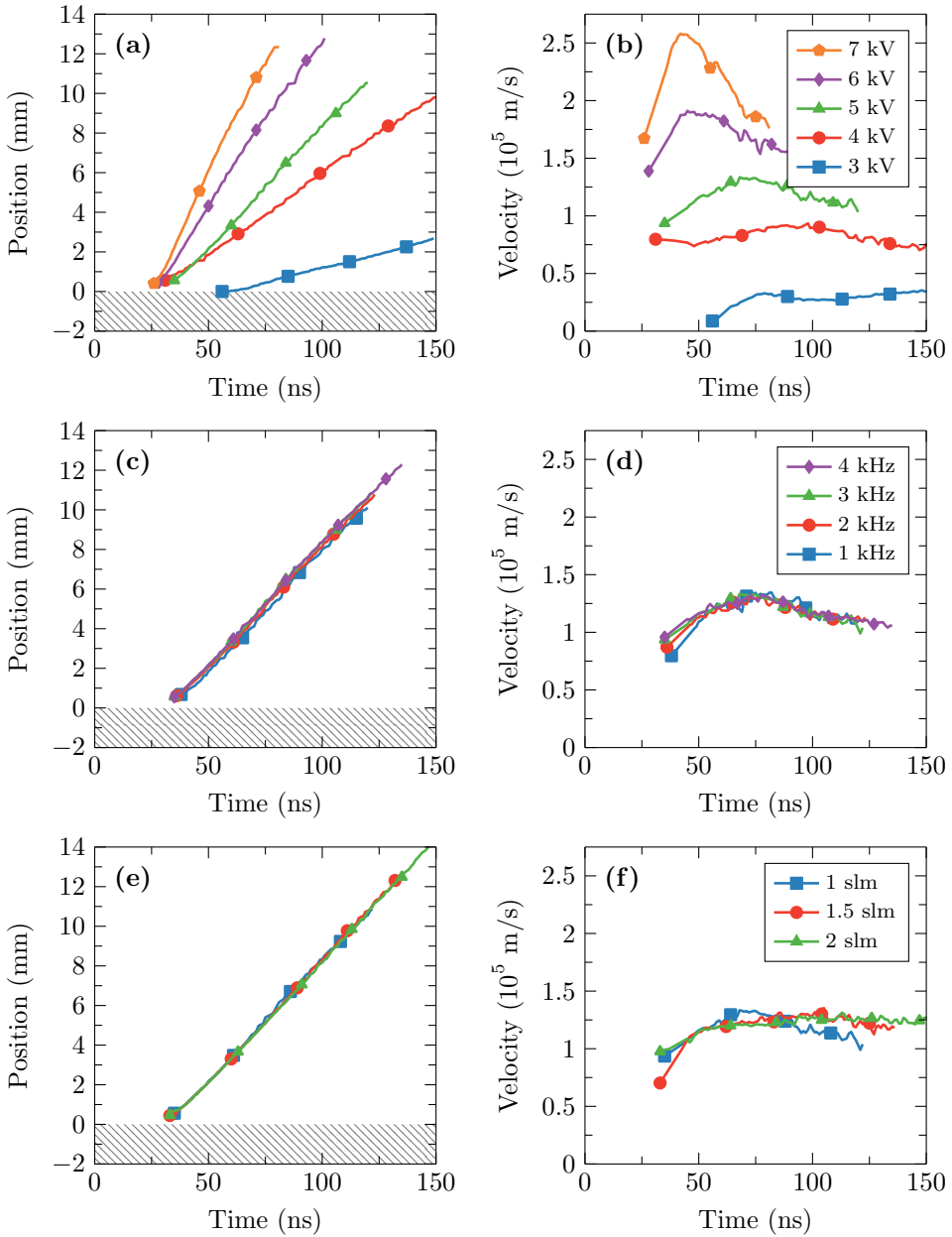


**Figure 1.6:** Position (left) and velocity (right) of plasma bullets in He for: (a and b) different voltages at  $f_{\text{rep}} = 3$  kHz and  $\Phi = 1$  slm, (c and d) different frequencies at  $V = 5$  kV and  $\Phi = 1$  slm, (e and f) different flow rates at  $V = 5$  kV and  $f_{\text{rep}} = 3$  kHz. A marker is placed every twenty data points.

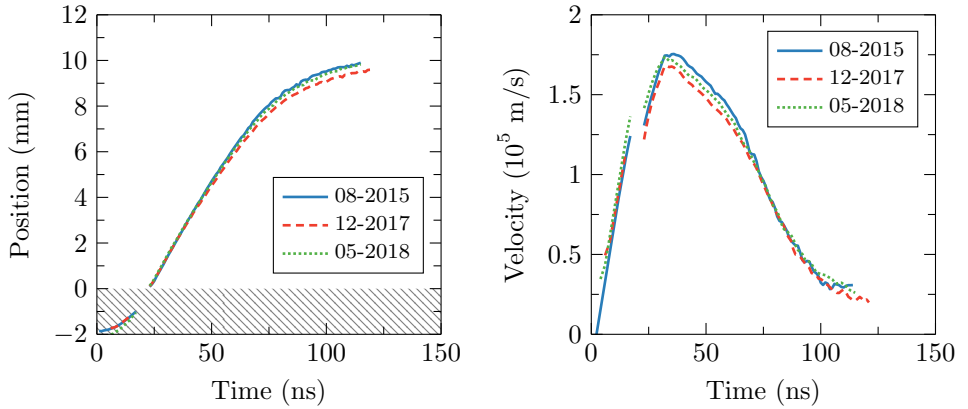


**Figure 1.7:** Position (left) and velocity (right) of plasma bullets in  $N_2$  at 8 kV, 3 kHz and 1 slm measured at several times during the research.

## 1.4 Thesis outline

In **chapters 2–7** the performed research and obtained results are described. Each of these chapters is organised as a self-contained part of the research, much like a journal article. Although the later chapters will sometimes refer back to earlier chapters for specific details, the chapters can in principle be read in any order. The following topics are discussed in the chapters:

- In **chapter 2**, high-speed imaging and time-resolved emission measurements are used to compare the morphology and to quantify the reproducibility of guided streamer discharges in pulsed plasma jets in  $N_2$ , He and Ar feed gas flowing into ambient air.
- In **chapter 3**, the development of the memory effect, which is responsible for the reproducibility of guided streamers, during the first discharges is discussed for pulsed plasma jets in  $N_2$  and He feed gas flowing into ambient air. This is done using high-speed imaging and time-resolved emission measurements.
- In **chapter 4**, the role of charged species in mediating the memory effect and in spatially guiding the guided streamer discharges is investigated for pulsed plasma jets in  $N_2$  feed gas flowing into ambient air by manipulating the charged species between successive discharges using an external electric field.
- In **chapter 5**, the decay of the electron density between successive discharges of a pulsed plasma jet in  $N_2$  feed gas flowing into ambient air is measured using microwave cavity resonance spectroscopy and compared to a global model.
- In **chapter 6**, the electric field of a guided streamer discharge produced in a pulsed plasma jet in  $N_2$  feed gas flowing into ambient is measured using four-wave mixing, a laser diagnostic based on non-linear optics, and the results

are compared to a two-dimensional streamer model. Differences between the measurements and the model are discussed.

- The differences between the measurements and the model in chapter 6 led to the hypothesis that the plane-wave approximation, which is used in the analysis of the electric field four-wave mixing measurements, is not valid. In **chapter 7**, a theoretical description of the four-wave mixing process using Gaussian beams instead of plane-waves is developed.

Finally, in **chapter 8**, the main conclusions of the presented research are reviewed, and several recommendations for future research are provided.

## Chapter 2

---

# Morphology and reproducibility of pulsed plasma jets

## 2.1 Introduction

Pulsed plasma jets are commonly imaged phase-resolved with nanosecond exposure times using an intensified charge-coupled device (ICCD) camera. Usually, hundreds or thousands of exposures are integrated or averaged. In such images, the emission of the discharges appears as a ‘plasma bullet’ [5,6]. However, plasma bullets only provide an accurate representation of the actual discharges if the individual discharges are spatially and temporally reproducible over many pulses. Under the right conditions, highly reproducible guided streamer discharges can, in fact, be generated in pulsed plasma jets [9].

While there exists some work on the repeatability of guided streamers (see for example [8–10] and the references therein), the large majority of the existing is focused on He feed gas. In this chapter, the similarities and differences between guided streamer discharges generated by a pulsed plasma jet in  $N_2$ , He and Ar feed gas flowing into ambient air are investigated. The morphology of the discharges in each of the feed gases is studied, and both the spatial and temporal reproducibility are quantified. These properties are assessed from spatially resolved and temporally resolved measurements of the plasma emission, using an ICCD camera and fast photomultiplier tube (PMT) respectively. To further understand the discharges, time-integrated emission spectra are measured. Additionally, a flow model is developed to investigate the role of the gas flow and mixing with the ambient air for the case of  $N_2$  feed gas.

## 2.2 Experimental setup and methods

### 2.2.1 Setup

The experimental setup is shown in figure 2.1. Discharges are generated in a stream of  $N_2$ , He or Ar (99.999% purity), flowing into open air. This is done by applying a repeatedly pulsed voltage to a needle electrode located concentrically inside the cylindrical nozzle of the plasma source. The nozzle is a quartz tube with inner radius  $r_i = 1$  mm and outer radius  $r_o = 2$  mm, and the electrode is a tungsten needle with radius  $r_n = 0.5$  mm and a tip of approximately  $20^\circ$  placed 2 mm before the end of the quartz tube. Since a grounded electrode is not explicitly specified in the setup, the discharge geometry is that of a single electrode plasma jet [10,24]. The high voltage (HV) pulses are produced by gating the output of a HV power supply (Spellman SL60) using a HV pulse generator (DEI PVX-4110). A pulse/delay generator (BNC model 575) is used to trigger and gate the HV pulse generator. Pulses with a width of 500 ns and rise and fall times of approximately 40 ns are used at a repetition frequency of 3 kHz in all experiments. A HV probe (Tektronix P6015A) is connected to the plasma source to monitor the applied voltage.

The spatial structure and reproducibility of the discharges are investigated by imaging the plasma emission using an ICCD camera (Stanford Computer Optics 4 Picos) with a UV camera lens (Nikon UV-Nikkor 105 mm f/4.5). A synchronised trigger signal for the ICCD camera is provided by the same pulse/delay generator that triggers the HV pulse generator. When pulsed plasma jets are imaged with an ICCD

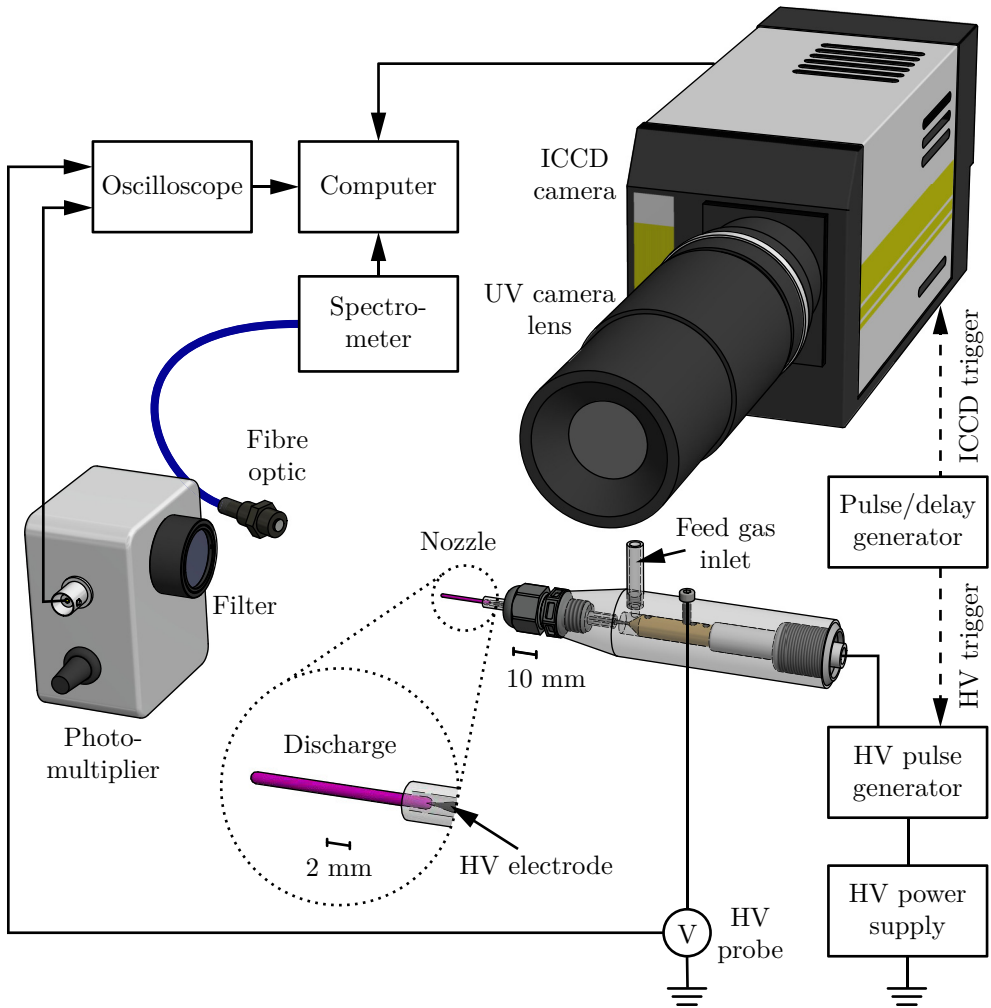


**Figure 2.1:** Schematic illustration of the experimental setup, including a magnified view of the nozzle with the discharge indicated in purple.



camera, short nanosecond exposures can be used to obtain images of ‘plasma bullets’, such as those shown in figures 1.3 and 1.4 in chapter 1. However, for the purpose of this experiment, single exposures with a longer exposure time of 500 ns are used to image the emission of an entire individual discharge on the rise of the HV pulse. This results in more typical streamer discharge images of individual discharges, in which the entire path of a discharge is visible. These paths of individual discharges are then compared to each other to assess the spatial reproducibility.

The temporal reproducibility of the inception of the discharge is investigated by measuring the emission temporally resolved with a PMT. By determining the jitter in the moment when the first emission is observed, a measure for the inception reproducibility can be obtained. The PMT (Hamamatsu H6779-04) is built into a metal enclosure to reduce electromagnetic interference from the HV pulses. The device is positioned with its line-of-sight along the discharge so that emission during the entire discharge can be measured. To obtain a sufficiently high signal-to-noise ratio, while also maintaining sufficiently low response times, the photocurrent produced by the PMT is measured through a  $560\ \Omega$  external terminator. The resulting voltage traces are recorded on an oscilloscope (LeCroy WaveSurfer 510, 1 GHz, 10 GS/s) and saved to a computer.

To further understand and characterise the discharges, emission spectra are also measured. For this purpose, a fibre optic is located directly next to the PMT. The optical fibre guides the light to a spectrometer (Avantes AvaSpec 2048TEC-USB2) that records time-integrated optical emission spectra. The spectrometer and fibre optic combination are calibrated for relative intensity using a deuterium lamp and a tungsten-ribbon lamp (Heraeus FiberLight DTM6/10). In addition, a band-pass filter can be placed in front of the PMT to measure specific spectral components of the emission temporally resolved. Three filters are used for this purpose: one for the  $(v', v'') = (0, 0)$  band of the second positive system (SPS) of  $N_2$  around 337.1 nm (Thorlabs FB-340-10), one for the Ar 696.5 nm line (Thorlabs FB-694.3-10), and one for the He 706.5 nm line (Thorlabs FB-710-10).

## 2.2.2 Fluid dynamics model

To gain more insight in the gas flow and how it might influence reproducibility, a computational fluid dynamics (CFD) model is developed using COMSOL. This is done for the case where  $N_2$  feed gas flows into ambient air. While typical flow velocities of several m/s are negligible on the typical time scale of the discharges, the flow dynamics determine the gas composition in which the discharge takes place. Several previous studies already showed that guided streamers in a He jet could propagate as long as there is a sufficiently high He fraction in the jet [28–30]. Additionally, other work has shown that admixing  $O_2$  in the jet influences the operating conditions under which reproducible guided streamers in a He jet can be formed [31]. Besides determining the gas composition, the gas flow also transports discharge remnants between consecutive discharges. The presented CFD model is used to calculate the flow velocity field and the local  $O_2$  distribution in the jet.

In our geometry, the feed gas flows through an annular duct, formed by the cylindrical part of the electrode and quartz tube, before the tapered part of the needle

is reached. In this duct, the Reynolds numbers for volumetric flow rates between 0.5 slm and 1.5 slm are between approximately 230 and 700 for  $N_2$ . Hence a laminar flow can be expected inside the tube. However, even without a discharge, in a free jet—a fluid flowing from a nozzle into an unconfined region—non-laminar behaviour can emerge from velocity shear between the jet and the quiescent ambient gas (Kelvin-Helmholtz instabilities) [32]. This effect has been reported to play a role in atmospheric pressure plasma jets [33–35].

Non-laminar effects are included in our model using Menter’s shear-stress transport (SST) turbulence model [36]. This is a so-called Reynolds-averaged Navier-Stokes (RANS) model. While the instantaneous flow might be fluctuating, models of this type only calculate the (time-)averaged quantities of the flow [32]. In general, Large-Eddy Simulation (LES) models, which do capture the larger scale fluctuating features of the flow, might be more appropriate when evaluating instantaneous flow structures in atmospheric pressure plasma jets [37]. However, the purpose of the current model is to compare average properties of the flow to average properties of the guided streamers.

The domain and computational mesh of the model are shown in figure 2.2. The last six millimetres of the quartz tube are included in the model. Solving the steady-state Navier-Stokes equations for an annular duct of inner radius  $r_1$  and outer radius  $r_2$  yields [38]:

$$v_z(r) = \frac{2\Phi}{\pi(r_2^2 - r_1^2)} \left[ r_2^2 + r_1^2 - \frac{r_2^2 - r_1^2}{\ln(r_2/r_1)} \right]^{-1} \left[ \frac{\ln(r/r_1)}{\ln(r_2/r_1)} (r_2^2 - r_1^2) - (r^2 - r_1^2) \right], \quad (2.1)$$

where  $\Phi$  is the volumetric flow rate. This equation is used with  $r_1 = r_n = 0.5$  mm and  $r_2 = r_i = 1$  mm as boundary condition on the feed gas inlet boundary. Furthermore, the no-slip condition ( $\mathbf{v} = 0$ ) is imposed on the boundaries of the needle and the quartz tube. At the open boundaries, the pressure is kept at 1 atm. The surrounding air is modelled as 0.79%  $N_2$  and 0.21%  $O_2$ . This is implemented by setting the  $O_2$  fraction to 0.21 at the open boundaries. The  $O_2$  impurity of the feed gas is specified as  $\leq 5$  ppm by the supplier. Therefore, the  $O_2$  fraction at the feed gas inlet boundary is set at this value. All COMSOL’s default values for the turbulence and turbulent mixing model parameters are used.

The resulting velocity magnitude fields and local  $O_2$  fractions are shown for volumetric flow rates of 0.5 slm, 1.0 slm and 1.5 slm in figure 2.3 and figure 2.4 respectively. Evidently, overall higher velocities are reached for higher flow rates. In the first part of the jet, just outside the nozzle, the maximum velocity does not occur on the symmetry axis. This is caused by the presence of the needle and results in relatively low velocities in the core of the jet, surrounded and shielded by faster moving gas. As the flow develops further downstream, the effect of the needle decreases and the maximum velocity is found at the symmetry axis. The point where this first occurs moves further downstream for higher volumetric flow rates. At the same time, the gas stays more pure, as visible from the 0.1% contour lines in figure 2.4. However, after the high purity region, the purity does decrease faster for higher flow rates as a result of turbulent mixing. This behaviour can be observed in the 10% and 20% contours, which are closer to the nozzle for increasing flow rates.

It should be noted that potential plasma-flow interactions are not accounted for.

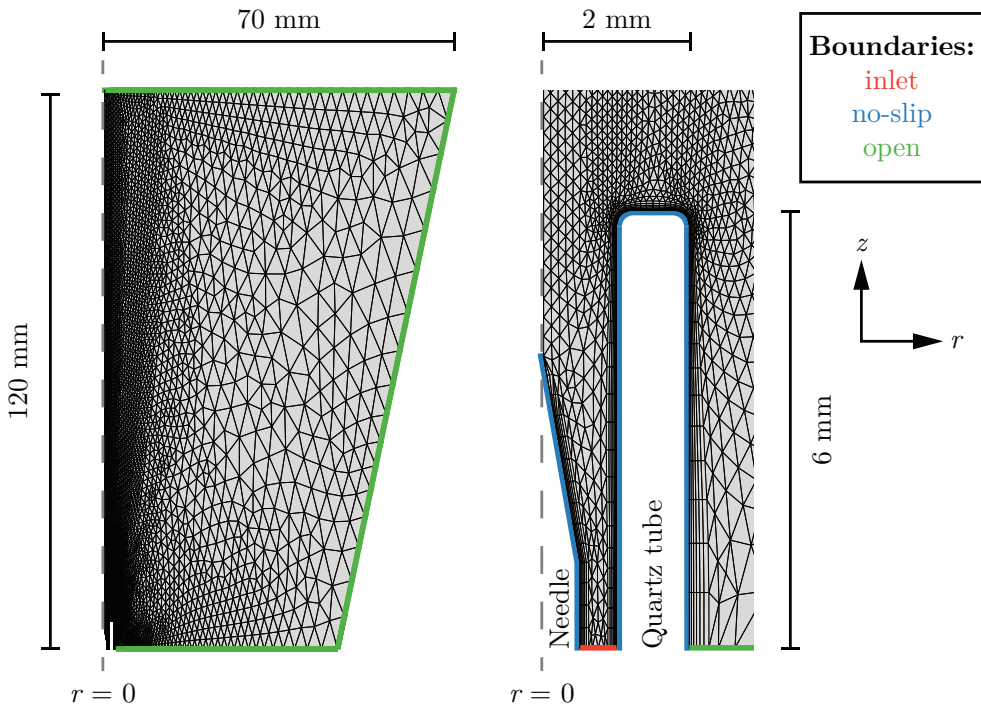


**Figure 2.2:** Computational mesh used in the CFD model. The full domain is shown on the left and a detailed view of the area around the nozzle, consisting of the needle electrode and the quartz tube, is shown on the right. Each of the boundaries is colour-coded according to the applied boundary conditions.

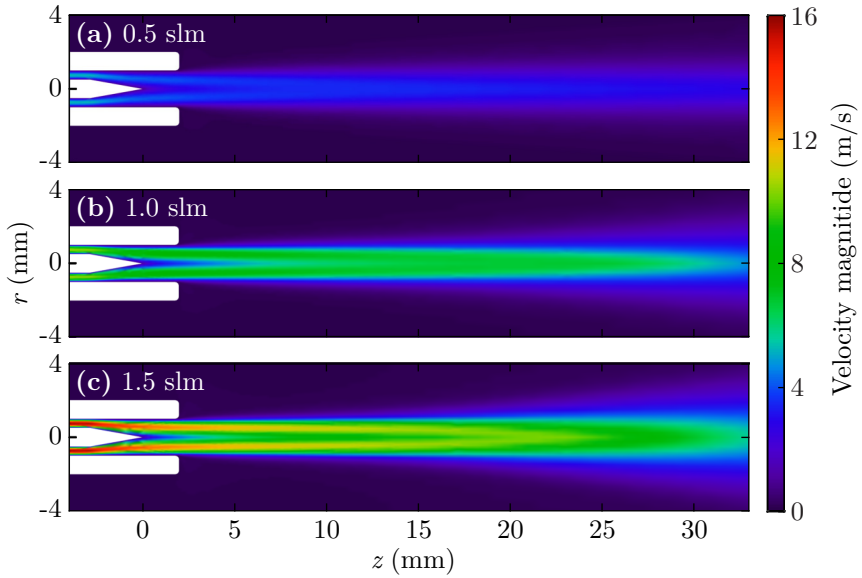


**Figure 2.3:** Magnitude of the velocity field for input volumetric flow rates of (a) 0.5 slm, (b) 1 slm, and (c) 1.5 slm. The needle and quartz tube are indicated by the white areas.

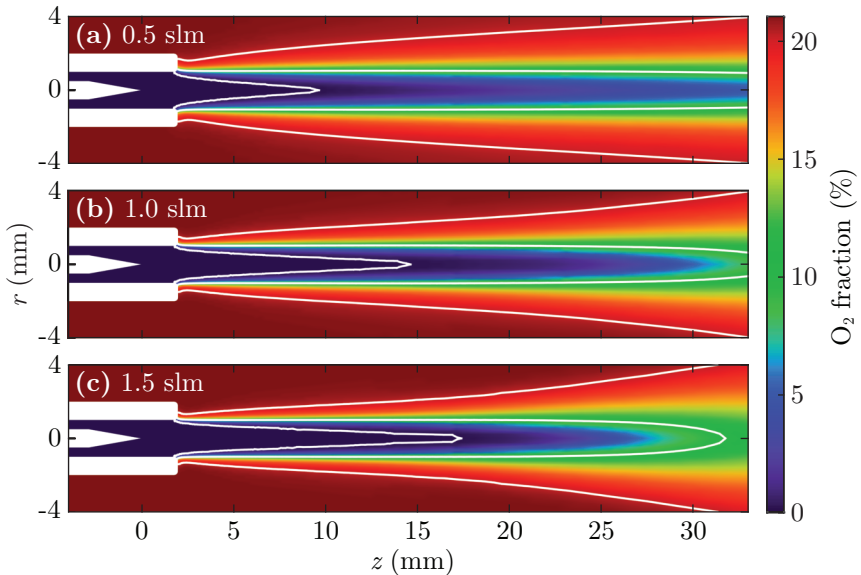


**Figure 2.4:** Fraction of  $O_2$  for input volumetric flow rates of (a) 0.5 slm, (b) 1 slm, and (c) 1.5 slm. The needle and quartz tube are indicated by the white areas. The three white lines are the 0.1% (inner), 10% (middle), and 20% (outer) contours respectively.

Previous research on pulsed plasma jets in He has shown that the gas flow can be influenced by both electrohydrodynamic and thermal effects of the discharges [39–46]. To our knowledge, there have been no detailed investigations on such effects in pulsed plasma jets specifically in N<sub>2</sub> yet.

## 2.3 Results and discussion

### 2.3.1 Morphology and spatial reproducibility

To demonstrate the structure and reproducibility of the discharges, two sets of images will be shown for each feed gas. The first set has images of the average discharge, integrated over 100 individual discharges, at several applied voltages. The second set has images composed of three individual discharges that are randomly chosen. Each of the three images is first assigned one of the RGB (red/green/blue) colours, and then they are superimposed. Where the individual discharges overlap, the colours mix. The places where all three discharges overlap is indicated in white (red + green + blue). At these places, the discharges follow the same path. All results presented in this section are obtained for a volumetric flow rate of 1 slm and a pulse repetition rate of 3 kHz.

#### Feed gas: N<sub>2</sub>

Average and individual discharges obtained in N<sub>2</sub> are shown in figure 2.5 for applied voltages of 6 kV, 8 kV and 10 kV. For this plasma source, 6 kV is the lowest voltage at which discharges in N<sub>2</sub> can be sustained. In the averaged images in figure 2.5a, the discharges appear as bright streamer channels on the symmetry axis of the jet. For higher voltages, this channel extends further downstream, and at the end a more diffuse cloud is observed. Inspecting the individual discharges in figure 2.5b, it is clear that only the part of the discharge on the symmetry axis of the jet is reproducible. This part is the guided streamer. At higher voltages branching occurs at the end of the guided streamer. The pattern of the branches is different for every discharge, and hence the discharges are not reproducible anymore from the branching point onward. This causes the more diffuse appearance of the averaged discharges at the end of the guided streamer channel. Additionally, as the voltage is increased, discharges inside the tube also start to appear. These discharges propagate from the tip of the needle to the dielectric and are not reproducible, as can most clearly be seen from the individual images in figure 2.5b at 10 kV.

To quantify the spatial reproducibility of the guided streamer, radial profiles of all the individually recorded discharges are fitted with a Gaussian function to determine their radius as well as their lateral position. The radius (HWHM) of the guided streamers is found at  $140 \pm 10 \mu\text{m}$ , although this value might be a slight overestimation and limited by the resolution of the camera. Within the uncertainty, this value stays constant along the guided streamer until its branching point. It is also independent of the applied voltage in the investigated range of 6 kV to 10 kV. The standard deviation of the lateral positions of the individual guided streamers is found

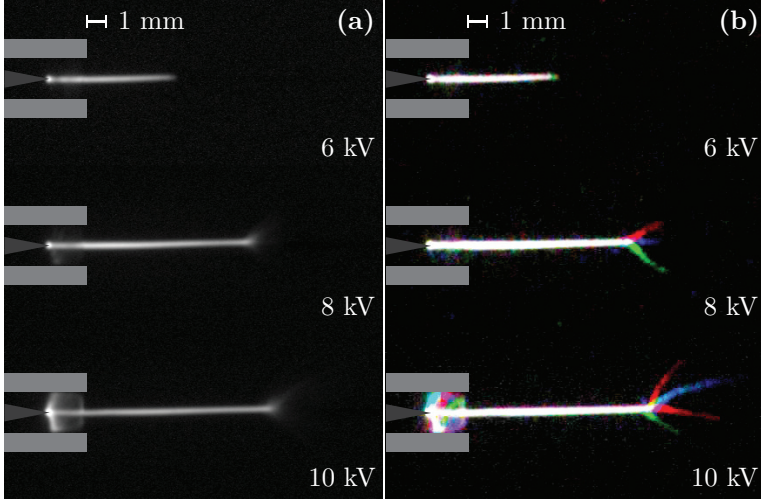


**Figure 2.5:** ICCD images of discharges in  $N_2$  for several applied voltages and a repetition frequency of 3 kHz and flow rate of 1 slm. In (a) the average of 100 discharges is shown. In (b) three randomly chosen individual discharges are shown: one in red, one in green and one in blue. Repeatable parts of the discharges are shown in white (red + green + blue). The needle (dark grey) and quartz tube (light grey) are drawn on top of the images for reference.

to be approximately  $13 \mu\text{m}$  at any point along the guided streamers, which is an order of magnitude lower than the radius itself. At this length scale vibrations in the setup and the imaging system might start to be significant, but they are not accounted for. Therefore, this value serves as an upper limit of the reproducibility of the guided streamer path in  $N_2$ . Variations in the direction perpendicular to the image plane cannot be detected this way, but they can be expected to be of similar value due to the symmetry of the discharge geometry. The fact that the guided streamer discharges propagate on the symmetry axis, where the flow is stable and mostly shielded from external effects (e.g. flow induced by other equipment and the ventilation in the laboratory) by the faster surrounding gas, likely plays an essential role in their spatial reproducibility.

In figure 2.8a, time-integrated emission spectra are given for applied voltages of 6 kV and 10 kV. The following emission bands are visible and indicated in the figure:

- $N_2(C^3\Pi_u \rightarrow B^3\Pi_g)$ : second positive system (SPS),
- $N_2(H^3\Phi_u \rightarrow G^3\Delta_g)$ : Gaydon-Herman green system (GHG),
- $N_2(C''^5\Pi_u \rightarrow A'^5\Sigma_g^+)$ : Herman infrared system (HIR),
- $N_2^+(B^2\Sigma_u^+ \rightarrow X^2\Sigma_g^+)$ : first negative system (FNS),
- $NO(A^2\Sigma^+ \rightarrow X^2\Pi)$ : gamma system (NO- $\gamma$ ).

The spectra for  $N_2$  feed gas are dominated by  $N_2$  SPS emission, and  $N_2^+$  FNS emission

is only weakly visible at the 391 nm. The NO- $\gamma$  emission that is visible indicates the presence of O<sub>2</sub>, which comes from impurities in the feed gas, as well as from the surrounding air. At higher wavelengths, several low-intensity bands of N<sub>2</sub> GHG and HIR emission are observed. Such spectra are commonly found for atmospheric pressure N<sub>2</sub> discharges, and the excitation mechanisms include: electron impact excitation and ionisation of N<sub>2</sub> (for SPS and FNS), metastable pooling of N<sub>2</sub>(A  $^3\Sigma_u^+$ ) (for HIR), and resonant energy transfer of N<sub>2</sub>(A  $^3\Sigma_u^+$ ) to NO (for NO- $\gamma$ ) [47–49].

From 6 kV to 10 kV the emission gets more intense, but the ratios of different bands in the spectra stay approximately the same. When inspecting the time-resolved N<sub>2</sub> SPS measurement with the PMT in figure 2.9a, a sharper peak in the emission is observed. This is due to higher propagation speeds of the discharges at higher voltages (see figure 1.5 in chapter 1), as well as the contribution of the discharges occurring inside the tube at higher voltages. When a large enough amount of charge accumulates on the dielectric tube during the discharge, a second discharge can occur on the fall of the HV pulse. However, only a weak signal is detected for both 6 kV and 10 kV, indicating that the interaction between the discharge and the dielectric is not strong in this case.

### Feed gas: He

Images of averaged and individual discharges for He feed gas are given in figure 2.6 for 3 kV, 5 kV and 7 kV. A voltage of 3 kV is the lowest value at which discharges in He can be generated. Compared to guided streamers in N<sub>2</sub>, the discharges in He are more spatially extended, both radially and axially. In addition, relatively intense discharges take place inside the nozzle already for 3 kV. From the exit of the nozzle to about 5 mm downstream, the emission is most intense on the edges of the discharge channel, as can be seen most clearly in the averaged images in figure 2.6a. It is well documented in literature that discharges in pulsed plasma jets in He jets propagate in the gas mixing layer, typically resulting in an annular discharge structure (often called ‘donut-shaped’) [8]. This annular structure causes the line-integrated emission detected by the ICCD camera to appear most intense on the edges. As more of the ambient air mixes into the jet further downstream, the discharge contracts and continues on the symmetry axis. Like for N<sub>2</sub>, the discharge channel becomes longer at higher voltages and starts to appear more diffuse further downstream in the averaged discharge images.

Looking at the individual discharges in figure 2.6b reveals that the individual discharges substantially overlap only up to about 7 mm downstream from the nozzle. At 5 kV and 7 kV branching occurs in the regions that look diffuse in the averaged images for 5 kV and 7 kV, although the branching point is not always at the same position, as was the case for N<sub>2</sub>. Nevertheless, it is clear that the individual guided streamers stop overlapping already before branching occurs. The variations in position increase further away from the nozzle. Since the discharges propagate in the gas mixing layer, this indicates that the gas flow is not stable. Possible causes are buoyancy (the jet is in a horizontal position) and external flows, which both become increasingly important further downstream where the flow velocity decreases. In fact, inspecting the plasma plume by eye, it is already visible that it indeed moves around. This

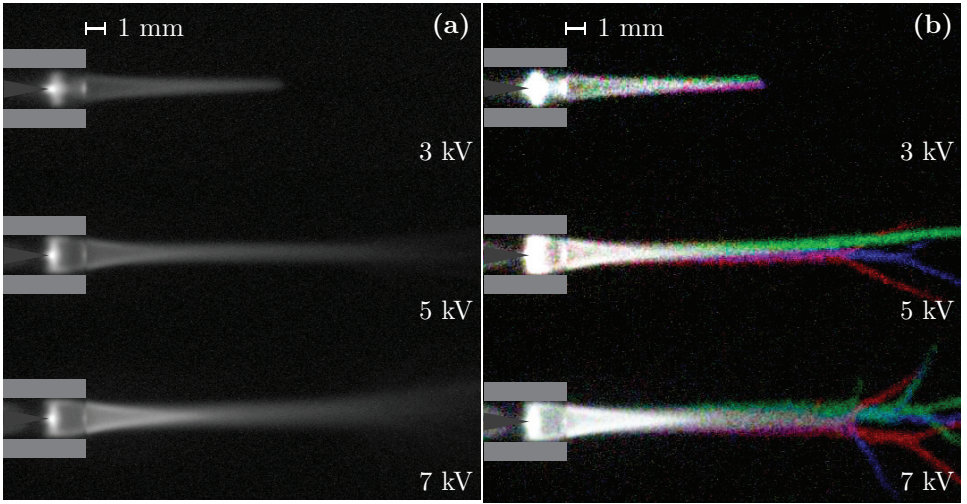


**Figure 2.6:** ICCD images of discharges in He for several applied voltages and a repetition frequency of 3 kHz and flow rate of 1 slm. In (a) the average of 100 discharges is shown. In (b) three randomly chosen individual discharges are shown: one in red, one in green and one in blue. Repeatable parts of the discharges are shown in white (red + green + blue). The needle (dark grey) and quartz tube (light grey) are drawn on top of the images for reference.

demonstrates that a stable flow is essential for achieving high spatial reproducibility over many discharges.

Time-integrated emission spectra for 3 kV and 7 kV are shown in figure 2.8b. Comparing the two spectra shows no significant qualitative differences. In both cases  $N_2$  SPS emission is dominant. Compared to the spectra for  $N_2$  feed gas in figure 2.8a, a relatively large peak of the  $N_2^+$  FNS at 391.4 nm appears. This is caused by Penning ionisation of  $N_2$  by metastable He, which produces  $N_2^+(B)$  [50]. Additionally, several atomic lines of He (He I) and O (O I) are visible, as well as the following OH band:

- $OH(A^2\Sigma_+ \rightarrow X^2\Pi)$ : Ångström system ( $OH\text{-}\text{Å}$ ).

OH is formed in He plasma jets as a dissociation product of  $H_2O$  [51, 52], which is present as an impurity in the feed gas, as well as in the surrounding air.

From the time-resolved measurements of the  $N_2$  SPS emission and He I line emission at 706.5 nm, it can be seen that the He emission originates from the start of the HV pulse. This is when the discharge inside the nozzle takes place, where the He feed gas is still pure. Afterwards, when the discharge leaves the nozzle and starts to propagate in the gas mixing layer, the  $N_2$  SPS emission becomes dominant. The difference in duration of the  $N_2$  SPS peaks is caused by an almost order of magnitude difference in propagation velocity for 3 kV and 7 kV (see figure 1.6 in chapter 1). A second, less intense, discharge occurs at the end of the voltage pulse, as a result of charge accumulation on the dielectric during the discharge on the rising edge of the pulse [6].



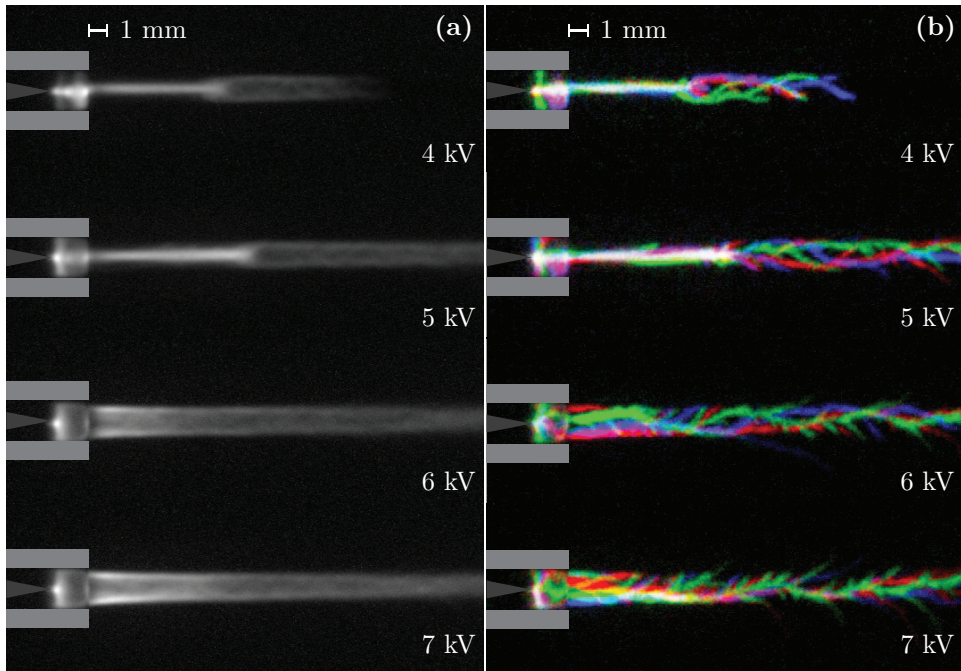


**Figure 2.7:** ICCD images of discharges in Ar for several applied voltages and a repetition frequency of 3 kHz and flow rate of 1 slm. In (a) the average of 100 discharges is shown. In (b) three randomly chosen individual discharges are shown: one in red, one in green and one in blue. Repeatable parts of the discharges are shown in white (red + green + blue). The needle (dark grey) and quartz tube (light grey) are drawn on top of the images for reference.

This second discharge appears similar in structure to the discharge at the rising edge of the pulse, although it extends only a few mm outside the nozzle.

### Feed gas: Ar

From the averaged images in figure 2.7a, it might seem as if at 4 kV and 5 kV the discharges start as guided streamers on the symmetry axis, like in  $N_2$  feed gas, and then continue to propagate in the gas mixing layer, like in He feed gas. At 6 kV and 7 kV, the discharges immediately start propagating in the gas mixing layer. However, for Ar feed gas the averaged images are not at all representative of the individual discharges, as shown by the images in figure 2.7b. Additionally, it should be mentioned that sometimes only a discharge inside the nozzle appears, without a streamer discharge propagating in the effluent. These discharges are excluded from the analysis in this section.

For 4 kV and 5 kV, the discharges outside the nozzle propagate on, or close to, the symmetry axis, where they overlap to some extent. The average radius (HWHM) of the

on-axis streamer channel, determined from the individual discharges, is  $210 \pm 30 \mu\text{m}$  and  $240 \pm 30 \mu\text{m}$  for 4 kV and 5 kV respectively. As can be already expected from the images, the standard deviation in the position of this part of the discharge is significantly larger than that for  $\text{N}_2$  feed gas:  $90 \mu\text{m}$  and  $140 \mu\text{m}$  for 4 kV and 5 kV respectively. After the on-axis part, the discharge branches to the gas mixing layer and continues to propagate there. At higher voltages, 6 kV and 7 kV, the on-axis part of the discharge is absent, and the entire discharge outside the nozzle consists of branching streamer discharges displaying a meandering pattern that is confined to the gas mixing layer. So, despite the fact that the discharges are not reproducible, they are still guided streamers in the sense that they follow the gas flow.

Behaviour similar to that seen at applied voltages of 4 kV and 5 kV has been observed before in an Ar pulsed plasma jet in [53]. Meandering streamer patterns were also reported for an Ar jet in [54], although in this case the discharges were produced in a fully turbulent flow. Possibly also related are the ‘snake-like’ patterns found in [55], however the discharge propagates in pure Ar inside a dielectric tube in this case. What exactly causes the transition from an on-axis discharge to discharges in the gas mixing layer and the meandering patterns is still unclear at the moment, but so far these phenomena seem exclusive to guided streamers in Ar. It has been suggested that non-laminar behaviour of the gas flow could be responsible for such effects [9].

Emission spectra for 4 kV and 6 kV are presented in figure 2.8c. In both cases, the spectrum consists of atomic lines of Ar (Ar I), and  $\text{N}_2$  SPS and OH- $\text{\AA}$  emission. Besides electron impact excitation, energy transfer from metastable Ar( $^3\text{P}_2$ ) is also an important excitation mechanism for  $\text{N}_2(\text{C}^3\Pi_u)$  in Ar/ $\text{N}_2$  mixtures [50]. Like for He, the presence of OH- $\text{\AA}$  emission indicates the presence of  $\text{H}_2\text{O}$  from impurities in the feed gas and the ambient air. In contrast to the cases of  $\text{N}_2$  and He, the spectrum does significantly change in the case of Ar. Whereas the Ar I emission is dominant at 4 kV, the spectrum is dominated by  $\text{N}_2$  SPS emission at 7 kV.

Inspecting the time-resolved Ar I and  $\text{N}_2$  SPS emission in figure 2.9c at 4 kV, first a peak in Ar I emission is seen around  $0.1 \mu\text{s}$ , which corresponds to the discharge in pure Ar inside the nozzle. Afterwards, the intensity first slightly drops and then slowly increases again until approximately  $0.3 \mu\text{s}$ . This is caused by the streamer propagating on, or close to, the symmetry axis where the Ar is pure. Then a rapid rise in  $\text{N}_2$  SPS emission occurs, which corresponds to the moment when the discharge transitions outwards to the gas mixing layer. As the falling edge of the HV pulse is reached, the branching streamers responsible for the  $\text{N}_2$  SPS emission terminate and the on-axis channel is reignited, resulting in the Ar I emission peak around  $0.6 \mu\text{s}$ . At 7 kV the discharge immediately starts to propagate in the gas mixing layer and there is barely any Ar I emission compared to  $\text{N}_2$  SPS emission. Like in the case of He, the discharge on the falling edge of the pulse has a similar structure as the one on the rising edge of the pulse, but the emission is less intense, and the discharge extends only several mm outside the nozzle.

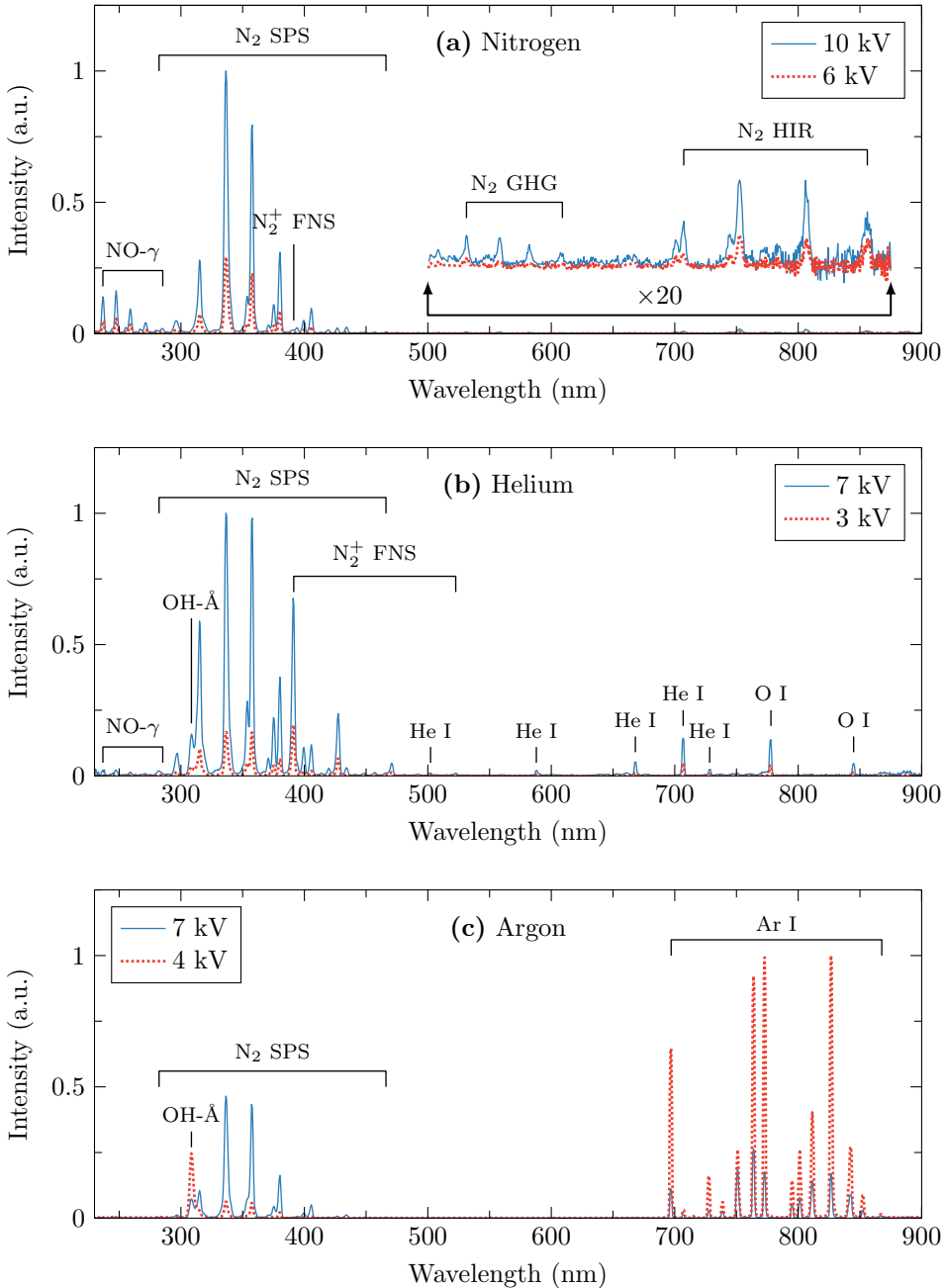


**Figure 2.8:** Time-integrated emission spectra of discharges with (a)  $N_2$ , (b) He, and (c) Ar as feed gas, at different applied voltages. Integration times of 2000 ms, 500 ms, and 400 ms were used for  $N_2$ , He and Ar, respectively. The  $N_2$ ,  $N_2^+$ , NO, and OH bands were identified using [56], and the He I, Ar I, and O I atomic lines were identified using [57].

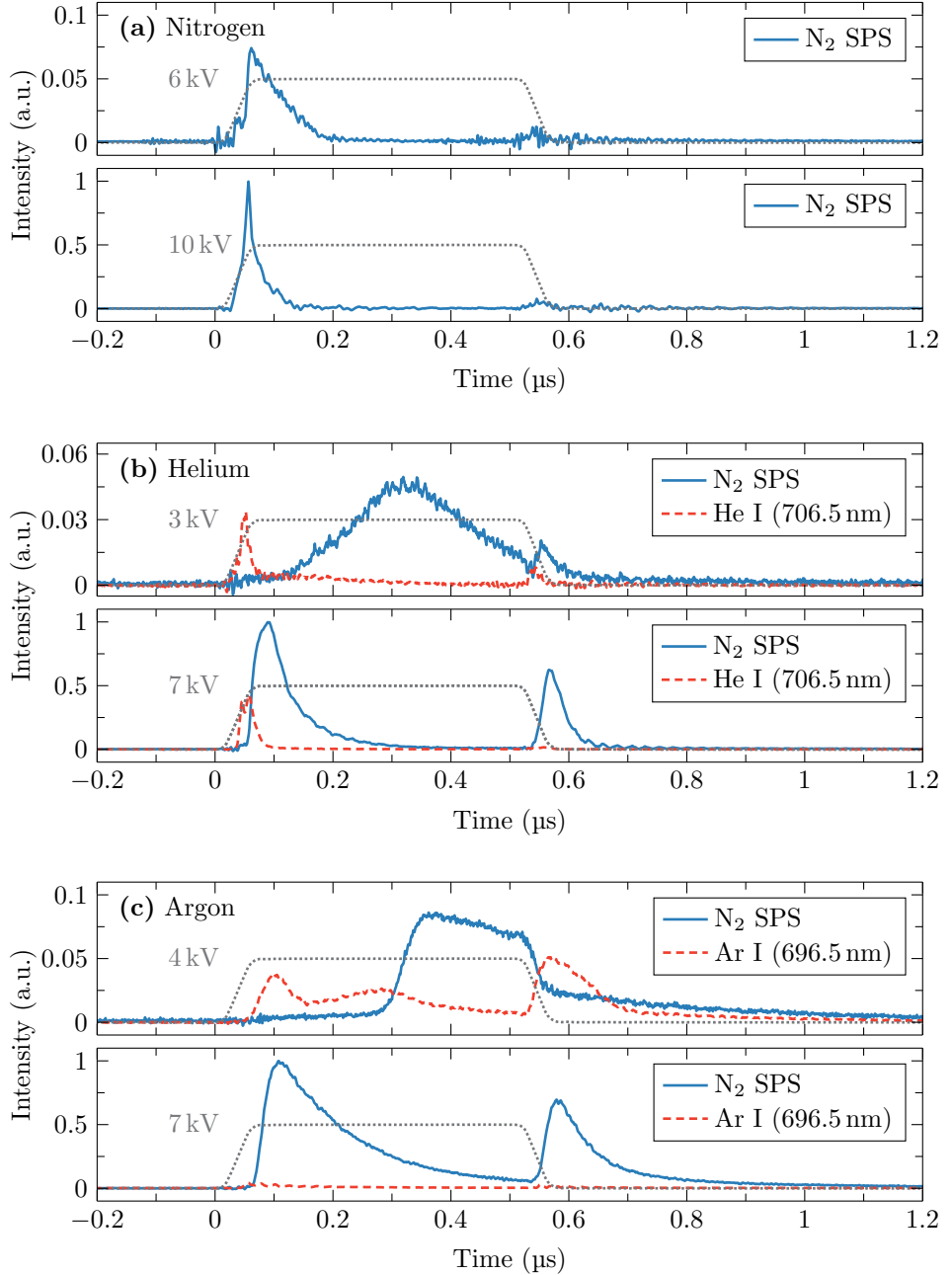


**Figure 2.9:** Time-resolved measurements of  $\text{N}_2$  SPS, He I and Ar I emission in discharges with (a)  $\text{N}_2$ , (b) He, and (c) Ar as feed gas, at different applied voltages. The shown data is corrected for the spectral sensitivity of the PMT and the transmission of the filters. The applied voltage pulse is illustrated by the grey dotted line.

### 2.3.2 Temporal reproducibility

To assess the temporal reproducibility of the discharges, the variation or jitter in the moment of inception is analysed. The moment of inception is determined from the PMT measurement as the moment when twice the maximum noise level is first reached. These measurements are performed without a filter in front of the PMT to increase the signal-to-noise ratio. While the actual inception might start shortly before the emission is visible on the PMT, the variation in the moment when the first emission is visible on the PMT signal should be representative for the jitter in inception time. To eliminate jitter caused by the HV pulse generator (specified as  $\leq 1$  ns shot-to-shot [58]), each PMT measurement is evaluated relative to its corresponding HV pulse measurement.

In figure 2.10 the temporal jitter in the inception of the discharges is shown for all three feed gases at different applied voltages. The inception jitter values are standard deviations of the inception moment, calculated over approximately 200 discharges. In all three cases, the jitter decreases for higher voltages. Applying higher voltages increases the background electric field, and electrons gain more energy between collisions as a result. At the same time, the region where the background field is high enough to start a discharge also increases. Therefore a new discharge is more easily started at higher voltages, and lower jitter can be expected. Both  $N_2$  and He have a jitter of about 3 ns at their lowest operation voltage, and this decreases to approximately 500 ps for higher applied voltages. These values are lower than the 7 ns reported in [59] for He once the discharges become stable. However, the authors of [59] show that this value is actually limited by the resolution of their setup. The jitter values in figure 2.10 for the discharges in Ar are substantially higher than those for  $N_2$  and He. At its lowest possible operation voltage of 4 kV, the jitter is about 11 ns. This decreases to 2 ns for 7 kV. Like for its spatial behaviour, non-laminar flow effects could be responsible for this. It is possible that turbulence increases the dispersion of discharge remnants, and hence seed electrons for the next discharge, and thereby increases the inception jitter.

### 2.3.3 Length of guided streamers in $N_2$ and the role of $O_2$

It was shown in figure 2.5 that the length of guided streamers in  $N_2$  increases for higher applied voltage. To see if the flow rate also plays a role in this, the lengths of guided streamers are determined for 0.5 slm, 1 slm and 1.5 slm as a function of applied voltage. The guided streamer length is defined from the tip of the needle electrode, located at  $z = 0$ , to either the point where the discharge stops or the point where branching occurs. The results are shown in figure 2.11a. It should be noted that at 1.5 slm the variation in guided streamer length is larger than for 0.5 slm and 1 slm. This is a result of instabilities arising in the flow at higher volumetric rates. In addition to the larger variation, sometimes there is only a discharge inside the nozzle without a guided streamer in the jet. These occurrences are neglected in determining the guided streamer length and its standard deviation.

For each of the three flow rates, the length of guided streamers increases with increasing voltage until a maximum value is reached. The maximum length the guided streamer can attain increases with the flow rate. This suggests that some property

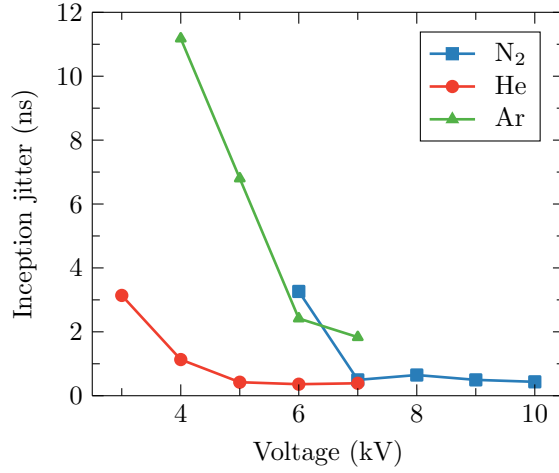


**Figure 2.10:** Inception jitter for discharges in N<sub>2</sub>, He and Ar for different applied voltages. The values are calculated as the standard deviation in the moment of inceptions obtained from approximately 200 individual discharges for each data point.

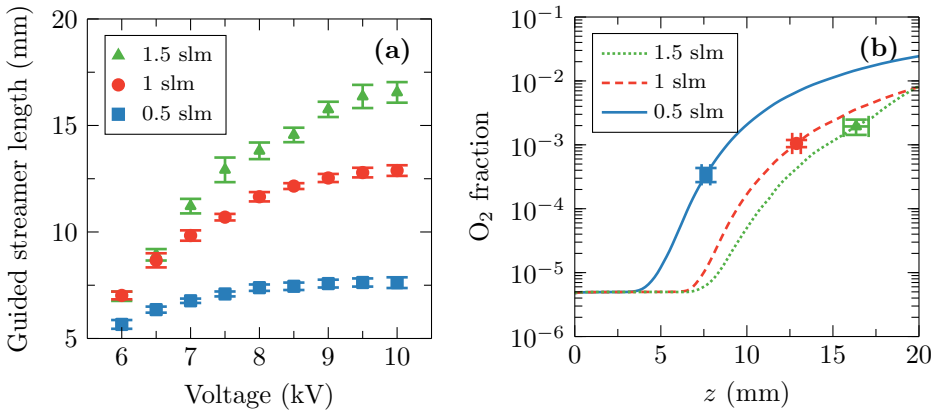


**Figure 2.11:** (a) Average length of the guided streamers in N<sub>2</sub> measured from the tip of the needle electrode as a function of the applied voltage for different volumetric flow rates. The error bars represent the standard deviation determined from 100 individual discharges. (b) O<sub>2</sub> fraction on the jet axis ( $r = 0$ ) obtained from the CFD model. The locations of the branching points for the longest guided streamers in each of the flow rates are indicated by a marker.

of the gas flow determines the maximum length of the guided streamers. A possible explanation could be that at this point the concentration  $O_2$  becomes too high and inhibits the memory effect as seed electrons are lost to attachment:



Although attached electrons can in principle be detached again in the high electric field of the streamer head and serve as seed electrons, in reality not all electrons will detach [9].

To test this explanation, the  $O_2$  fractions from the CFD model at the locations of the branching points of the longest guided streamer for each of the flow rates are analysed. The  $O_2$  fractions on the symmetry axis are plotted as a function of the axial position in figure 2.11b. The axial position corresponding to the branching point is indicated by a marker for each of the flow rates. The  $O_2$  fractions at these points are  $(3.4 \pm 0.9) \times 10^{-4}$ ,  $(1.1 \pm 0.2) \times 10^{-3}$  and  $(1.9 \pm 0.6) \times 10^{-3}$  for 0.5 slm, 1 slm and 1.5 slm respectively. The errors in these values are obtained from the uncertainty in the guided streamer length. While these values are not within each other's error bounds, they are within one order of magnitude. Calculating the rate coefficient for the attachment process (2.2) at room temperature, using the equations in [60, 61], results in  $k = 8.5 \times 10^{-44} \text{ m}^6/\text{s}$ . For  $O_2$  fractions of  $10^{-3}$  to  $10^{-4}$ , this corresponds to characteristic times of approximately 200  $\mu\text{s}$  to 20  $\mu\text{s}$  respectively. Compared to the period of about 333  $\mu\text{s}$  between discharges at 3 kHz, this shows that attachment processes become relevant in the time between discharges at the found  $O_2$  fractions and suggests that the  $O_2$  concentration could indeed play an important role in determining the guided streamer length.

## 2.4 Conclusions and outlook

Pulsed plasma jets in  $N_2$  consist of guided streamer discharges that travel in the centre of the jet. The streamer radius is approximately  $140 \pm 10 \mu\text{m}$  (HWHM), and a reproducibility of the discharge path of  $13 \mu\text{m}$  (standard deviation) is achieved at a volumetric flow rate of 1 slm. The temporal reproducibility of the inception improves from 3 ns for 6 kV, the lowest voltage where the discharges can be sustained, up to about 500 ps for higher applied voltages. It is proposed that the stable core of the flow plays a major role in achieving high spatial reproducibility. The length of the guided streamers increases with voltage until for sufficiently high voltages branching occurs at the end of the guided streamer. These branches are not reproducible. Besides the applied voltage, the volumetric flow rate also influences the length of the guided streamer and the point where branching happens. Comparison to a CFD model shows that the branching of guided streamers in  $N_2$  occurs where the  $O_2$  concentration is between  $(3.4 \pm 0.9) \times 10^{-4}$  and  $(1.9 \pm 0.6) \times 10^{-3}$ . From the attachment rate coefficient it is calculated that this coincides with the density where attachment on the time scale of the repetition period becomes important. This suggests that  $O_2$  indeed plays an important role in the branching of guided streamers in  $N_2$ . However, for a complete understanding of when and where this exactly happens, the role of  $O_2$  and the effects

of potential plasma-flow interactions that are not included in the model should be further investigated.

For He feed gas, the guided streamer discharges propagate in the gas mixing layer, resulting in the well-known annular structure close to the nozzle. Like in the case of  $N_2$  the discharge becomes longer for higher voltages and eventually branches. However, the spatial reproducibility of the guided streamers in He is limited by an unstable gas flow, most likely caused by buoyancy and external flows. Since the discharges follow the gas flow, a stable flow is essential for high spatial reproducibility. Nevertheless, temporal reproducibility of about 3 ns is achieved at the lowest possible applied voltage, and this improves to about 500 ps for higher applied voltages, similar to  $N_2$ .

At applied voltages of 4 kV and 5 kV, discharges in Ar feed gas start as a streamer on the symmetry axis in pure Ar, before they transition to branching streamer discharges in the gas mixing layer. For voltages of 6 kV and 7 kV, the discharges immediately start as branching streamers in the gas mixing layer, and no discharge on the symmetry axis occurs. The branching discharges in the gas mixing layer exhibit a meandering pattern and are not reproducible. The exact mechanism behind these discharges is not yet understood, but non-laminar behaviour of the gas flow might play a role. The jitter in inception time is 11 ns at the lowest operation voltage of 4 kV, and 2 ns at 7 kV, which is significantly larger than for  $N_2$  and He. Also here, non-laminar behaviour of the flow could be the cause. Despite that the branching streamer discharges in Ar are not reproducible, they are still guided in the sense that they are confined by the gas flow.





## **Chapter 3**

---

### **Development of the memory effect**

## 3.1 Introduction

Atmospheric pressure plasma jets driven by AC or pulsed voltage in the kHz-range typically consist of guided streamer discharges that are often referred to as plasma bullets [5,6]. Under the right conditions, the spatial and temporal behaviour of guided streamers generated in plasma jets is highly reproducible. For example, it was shown in chapter 2 that guided streamers in  $N_2$  and He feed gas can achieve sub-nanosecond variation in inception time. Furthermore, it was demonstrated that the trajectories of guided streamers in  $N_2$  were repeatable within  $13\ \mu\text{m}$ , and that the spatial reproducibility of guided streamers in He was limited by the stability of the outflowing gas. The reproducibility of guided streamer discharges in plasma jets is generally attributed to a memory effect in which the remnants of previous discharges provide the seed electrons for the next discharge [8–10]. However, many details of the exact physical mechanisms behind the memory effect and the resulting repeatable behaviour still remain unclear [9].

Insights into the memory effect and its role in achieving temporally and spatially reproducible guided streamers can be obtained from the first discharges. When the first discharge ignites, there is no memory effect related to previous discharges yet. If the reproducibility of the guided streamers requires a build-up of discharge remnants over multiple discharges, or if it relies on the transport of discharge remnants in the gas flow, there will be a start-up phase before the guided streamers become temporally and spatially reproducible. Therefore, the temporal and spatial behaviour of the first discharges show how the memory effect develops, and consequently what the role of build-up and transport of discharge remnants is. In fact, the development of temporal reproducibility in the first discharges was already investigated by Wu *et al* for a pulsed plasma jet in He feed gas [59]. It was found that the temporal jitter in inception decreases to 7 ns after approximately 100 discharges and to 3 ns after about 100 000 discharges.

In this chapter, the start-up phases of pulsed plasma jets generated in  $N_2$  and He feed gas are investigated. The development of temporal reproducibility is examined from the variation in inception moment of the first discharges, which is determined from the optical emission recorded with a fast photomultiplier tube (PMT). Furthermore, the first discharges are imaged using an intensified high frame-rate (HFR) camera to study the development of the spatial reproducibility and the spatial guiding mechanism. Additionally, to determine the role of transport of discharge remnants in the gas flow, the fluid dynamics model introduced in chapter 2 is extended with particle tracing. From the obtained results, the similarities and differences in memory effect and guiding mechanisms for guided streamers in  $N_2$  and He feed gas are discussed.

## 3.2 Experimental setup and methods

### 3.2.1 Setup

The experimental setup is shown in figure 3.1. The pulsed plasma jet that generates the guided streamer discharges is described in detail in chapter 1, and will only be

explained here briefly. The feed gas, which is either  $N_2$  or He in this work, flows at a volumetric rate of 1 slm into air ambient through a quartz tube of 1 mm inner radius and 2 mm outer radius. A tungsten needle of 0.5 mm radius, which serves as high voltage (HV) electrode, is positioned concentrically inside the quartz tube with its tip located 2 mm before the end of the quartz tube. The needle tip has an angle of approximately  $20^\circ$ . As a ground is not explicitly specified, this plasma jet has a single electrode geometry [10,24]. The discharges are generated by applying HV pulses to the needle electrode. A HV power supply (Spellman SL60) in combination with a HV pulse generator (DEI PVX-4110) is used to produce HV pulses that have a width of 500 ns and rise and fall times of approximately 40 ns. The applied voltage is measured using a HV probe (Tektronix P6015A) and recorded by an oscilloscope (LeCroy WaveSurfer 510, 1 GHz, 10 GS/s). A pulse/delay generator (BNC model 575) provides the gate signal for the HV pulse generator and is also used to synchronise the discharges and the optical measurement system. The discharges are produced at a repetition frequency of 3 kHz in this work.

Measurements of the first discharges require that the first discharge occurs spontaneously, in order to avoid external influence. However, this rarely occurs during the first HV pulse. Especially at lower applied voltages, it can take up to several tens of minutes before the first discharge ignites spontaneously. Therefore, it is highly advantageous to be able to record the emission of the first several discharges at once during a single start-up cycle. This requires an imaging system that can record successive individual discharges at the pulse repetition rate, which in this case is 3 kHz. For this reason, a high frame-rate (HFR) camera (Photron FASTCAM Mini UX100) coupled to a high-speed camera intensifier (Invisible Vision UVi 1850) is used. From images of the first discharges, the development of the spatial reproducibility is assessed. Additionally, a fast PMT (Hamamatsu H6779-04), placed with its line-of-sight parallel to the propagation direction of the discharge, is used to measure the optical emission of the discharges temporally resolved. From this data, the development of the temporal reproducibility is evaluated. The PMT is enclosed in an aluminium box to reduce interference from the HV pulses. The produced photocurrent is measured over a  $560 \Omega$  terminator, recorded by the oscilloscope, and saved to a computer together with the HV pulse measurement.

A measurement containing information of the first discharges is performed as follows. The intensifier and HFR camera are gated at every HV pulse, even when there is no discharge yet, and the HFR camera stores the recorded frames in its internal memory. When the PMT registers the emission of the first discharge, the oscilloscope is triggered, and it sends a trigger signal to the HFR camera. The HFR camera is programmed to save a number of frames after the trigger event, as well as the five frames recorded directly before the trigger event. Simultaneously, the oscilloscope saves segments of the HV probe and PMT traces that correspond to the first 10 periods after the trigger, as well as the 5 periods before. The recorded data from before the trigger is used to confirm that the measurement system was indeed triggered by the first discharge. Between each measurement, the HV pulses are switched off for about a minute. Afterwards, it can again take up to tens of minutes before the first discharge ignites, indicating there are no effects of previous discharges anymore.

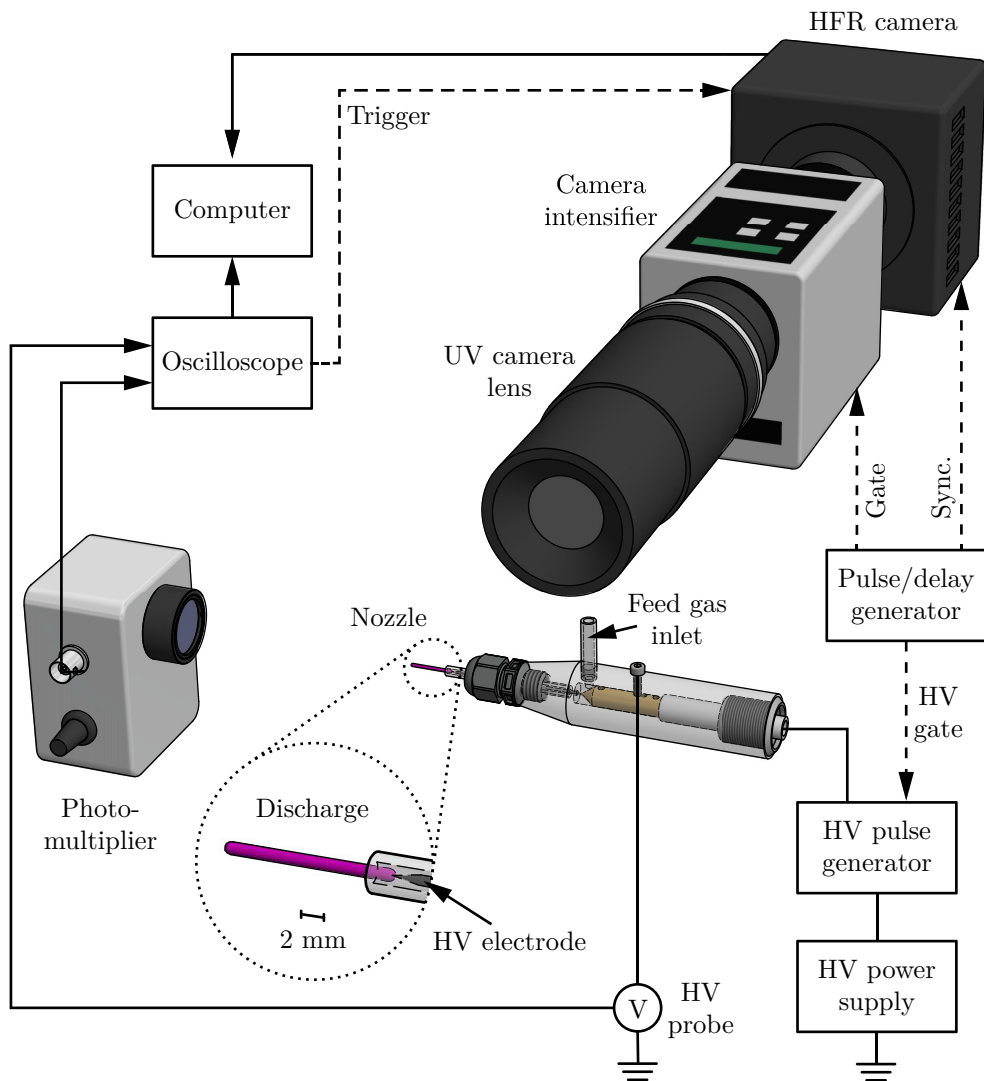


**Figure 3.1:** Schematic illustration of the experimental setup, including a magnified view of the nozzle with the discharge indicated in purple.

### 3.2.2 Particle transport model

As was shown in chapter 2, the gas flow plays an important role in pulsed plasma jets. It determines the gas composition and stability of the jet, which are both directly related to the reproducibility of the guided streamer discharges. In addition, discharge remnants that are responsible for the memory effect are transported between discharges by the gas flow. To investigate the role that transport plays in the development of the memory effect during the first discharges, particle tracing is implemented in the fluid dynamics model that was introduced in chapter 2. In summary, this model is a Reynolds-averaged Navier-Stokes (RANS) model that calculates the average quantities of the flow. In the model,  $N_2$  gas flows into artificial air.

Particles are released at  $t = 0$  at the axial position of the tip of the needle ( $z = 0$ ), between the tip of the needle and the inner surface of the quartz tube ( $0 \leq r \leq 1$  mm). The particles are massless and without charge. They are uniformly distributed over the radius with  $1 \mu\text{m}$  intervals. For each particle, the position is tracked in time. In figure 3.2, the positions of particles that are transported in a flow corresponding to a volumetric flow rate of 1 slm are illustrated. In figure 3.2a, the initial particle distribution at  $t = 0$  is indicated by the red line. Subsequent moments in times are given in figures 3.2b–g with  $0.33$  ms intervals, which corresponds to the moments when discharges occur at a repetition frequency of 3 kHz. Since the velocity field in the jet has an annular structure due to the presence of the needle (see section 2.2.2), the particles that start slightly off-axis travel faster than those near the axis. The guided streamer discharges in  $N_2$  feed gas have a half-width half-maximum (HWHM) radius of approximately  $150 \mu\text{m}$  and propagate on the axis, as shown in chapter 2. Therefore, the starting positions that are representative for the transport of the guided streamer discharge remnants in  $N_2$  are those within the streamer radius. The displacement in time of these particles will be compared to the spatial development of the guided streamer discharges in  $N_2$  in the next section.

## 3.3 Results and discussion

### 3.3.1 Development of temporal reproducibility

The temporal reproducibility is investigated from the repeatability of the inception time. This is defined as the time between the start of the HV pulse and the moment when the optical emission signal reaches the threshold of twice the noise level of the PMT. For each operating voltage, the inception times during the start-up phase are measured twenty times. This means that there are twenty measurements of the inception time for each of the first ten discharges. To illustrate, all measured inception times of the first ten discharges for  $N_2$  at 8 kV and He at 5 kV are shown in figure 3.3. It can be seen that in both cases the inception of discharge number 1 can occur at any time during the 500 ns HV pulse. While the data for the first discharge is not completely uniformly distributed over the width of the HV pulse, it is expected that this is a result of the limited sample size. It can take minutes, or equivalently hundreds of thousands to millions of HV pulses, for the first discharge to appear spontaneously.

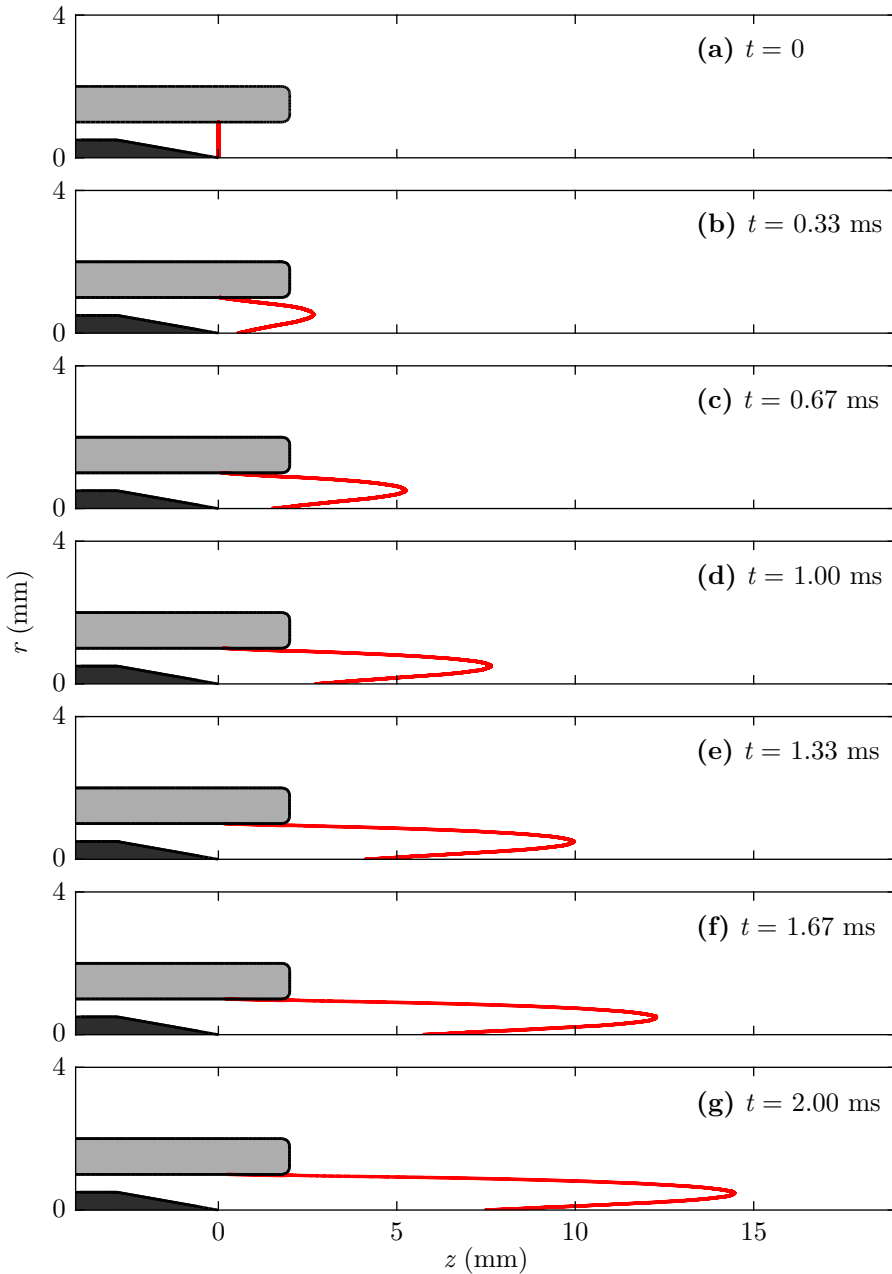


**Figure 3.2:** Positions of particles, indicated in red, at different times after being released at  $t = 0$  obtained from particle tracing in the gas flow at a volumetric flow rate of 1 slm. The needle and quartz tube are indicated by the dark grey and light grey areas respectively.

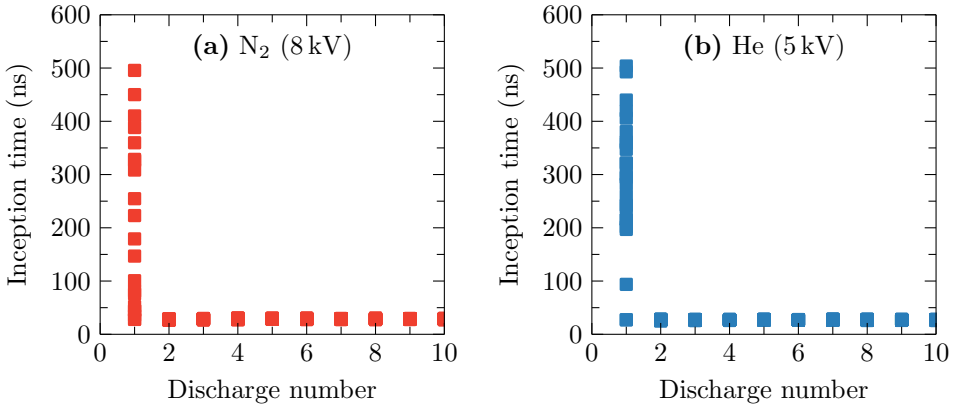


**Figure 3.3:** Inception times found for the first ten discharges in (a) N<sub>2</sub> at 8 kV, and (b) He at 5 kV. In both cases, the repetition frequency is 3 kHz, and the volumetric flow rate is 1 slm.

This likely happens because the first discharge requires a background electron at the right location that successfully develops into a streamer during the HV pulse. Subsequently, the remnants of this first discharge provide seed electrons for the next discharge.

These measurements are repeated at different applied voltages. While discharges in this pulsed plasma jet can be sustained at voltages down to 6 kV for N<sub>2</sub> and 3 kV for He once the jet is ignited, discharges were not observed to ignite spontaneously within an acceptable amount of time at these voltages. Therefore these measurements could only be performed at voltages higher than 8 kV for N<sub>2</sub> and 5 kV for He. The results are shown in figure 3.4. In these plots, the markers indicates the average inception time of twenty measurements and the bounds of the error bars are placed at the maximum and minimum value. With the exception of 10 kV for N<sub>2</sub>, the same behaviour is found for all the voltages in both feed gases. The first discharge can occur at any moment in the voltage pulse, and the discharges afterwards all take place on the rising edge of the pulse. At 10 kV in N<sub>2</sub>, the first discharge happens on the rise of the HV pulse or briefly after. However, it should be noted that this behaviour for 10 kV is not reproducible from day to day and therefore might also depend on the ambient conditions of the laboratory. Unfortunately, the power supply is limited to 10 kV, so we were unable to test if there is always a specific voltage at which the first discharge ignites at the first voltage pulse.

To quantify the temporal reproducibility of the first ten discharges, the jitter in the inception time for each discharge is considered. Like in chapter 2, these values are calculated as the standard deviation of the inception time. The results are shown in figure 3.5. Immediately after the first discharge, sub-nanosecond jitter is achieved in all investigated cases. So, temporal reproducibility is achieved at the second discharge, and hence the temporal memory effect only needs a single discharge to develop, for both N<sub>2</sub> and He feed gas.



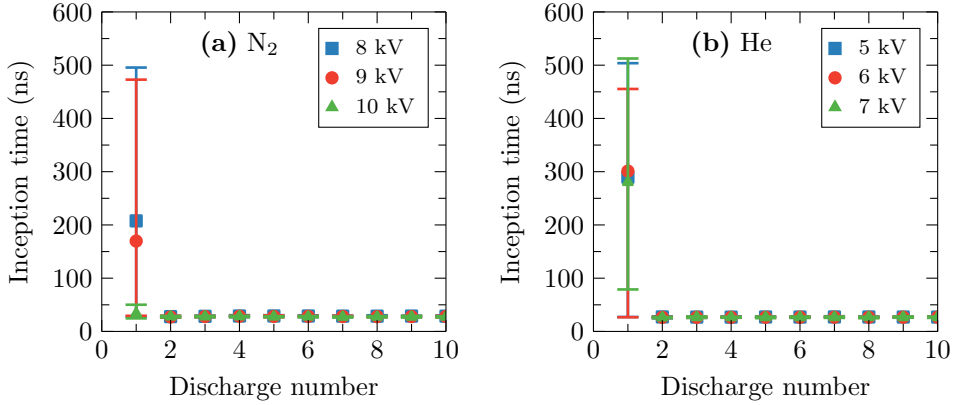


**Figure 3.4:** Moment of inception of the first ten discharges in (a) N<sub>2</sub> feed gas, and (b) He feed gas at different applied voltages. A repetition frequency of 3 kHz and a flow rate of 1 slm is used. The markers indicate the average value and the error bars indicate the maximum and minimum found value.

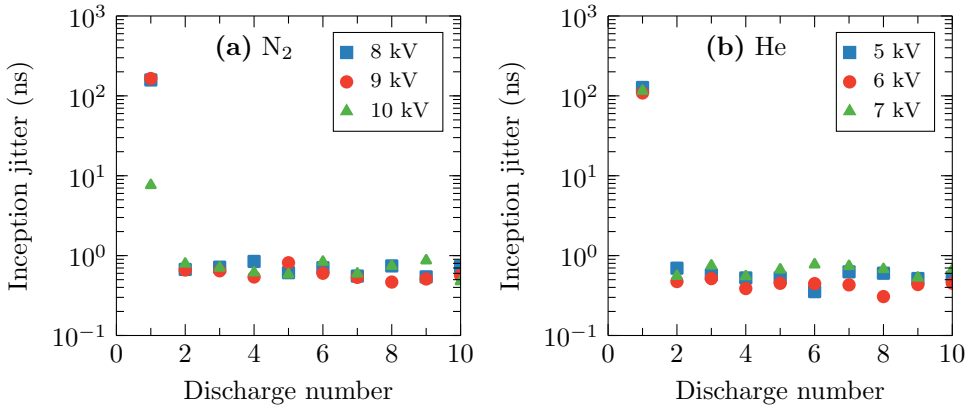


**Figure 3.5:** Jitter in the inception time of the first ten discharges in (a) N<sub>2</sub> feed gas, and (b) He feed gas at different applied voltages. These values are calculated as the standard deviation in the inception time.

This result is different from what was found for a pulsed plasma jet in He feed gas at similar operating parameters by Wu *et al* [59]. In their work, temporal jitter decreases to 7 ns after approximately 100 discharges and to 3 ns after about 100 000 discharges. A possible explanation could be the difference in the plasma source geometry. The plasma source used in [59] has a syringe-like tube with a radius of 0.6 mm at the nozzle [62], compared to 1 mm in our case, and their HV electrode is positioned 15 mm before the end of the tube, compared to 2 mm in our case. Therefore the interaction with the dielectric is likely stronger, and charging and discharging of the dielectric tube might play a more critical role in obtaining temporal reproducibility in their case. Similarly, Slikboer *et al* showed that repetitive discharges on a dielectric target, caused by an impinging 30 kHz AC plasma jet in He, become (spatially) reproducible only after 0.5 s to 1 s, or equivalently after 15 000 to 30 000 discharges, as a result of charge build-up [63].

### 3.3.2 Development of spatial reproducibility

Images of the first eight discharges in  $N_2$  at 8 kV and in He at 5 kV are given in figure 3.6. For  $N_2$ , the first discharge is a branching streamer discharge inside the quartz tube. During the following seven discharges a guided streamer develops on the symmetry axis that increases in length every discharge. So, although temporal reproducibility is reached after the first discharge, there is a start-up phase of around ten discharges before the discharges become spatially reproducible in the pulsed plasma jet in  $N_2$ .

In contrast, the discharges in He propagate along the gas mixing layer, and all appear the same, with the exception of the first one, which is shorter. The reason for this is the moment of inception of the first discharge. It was shown in the previous section that the inception of the first discharge could occur anywhere during the HV pulse. In this particular case, the first discharge started near the end of the voltage pulse. When the HV pulse ends, the guided streamer stops propagating, resulting in a shorter discharge. In fact, it is found that the first discharge appears the same as the succeeding discharges when its inception occurs early in the voltage pulse. This indicates that in the pulsed plasma jet in He there is only a temporal memory effect that is related to discharge remnants. The gas flow, and more specifically the resulting gas mixing layer, is responsible for the guiding mechanism and spatial reproducibility. This is in line with the findings of chapter 2, where it was discussed that guided streamers in He follow the gas flow.

The length of the guided streamers in  $N_2$  is plotted as a function of discharge number, as well as the corresponding time that has elapsed since the first discharge, in figure 3.7. The guided streamer length is defined from the tip of the needle electrode to either the point where the discharge stops or the point where branching occurs. It can be seen that the guided streamer length develops slightly faster for higher voltages. Before the final stable length is reached, the guided streamer length increases at a rate between approximately 3.5 m/s and 5.5 m/s, which is similar to the flow velocity in the vicinity of the symmetry axis where the discharge propagates. This implies that transport by the gas flow in the time between discharges plays an important role in the development of a spatial guiding mechanism and reproducibility.

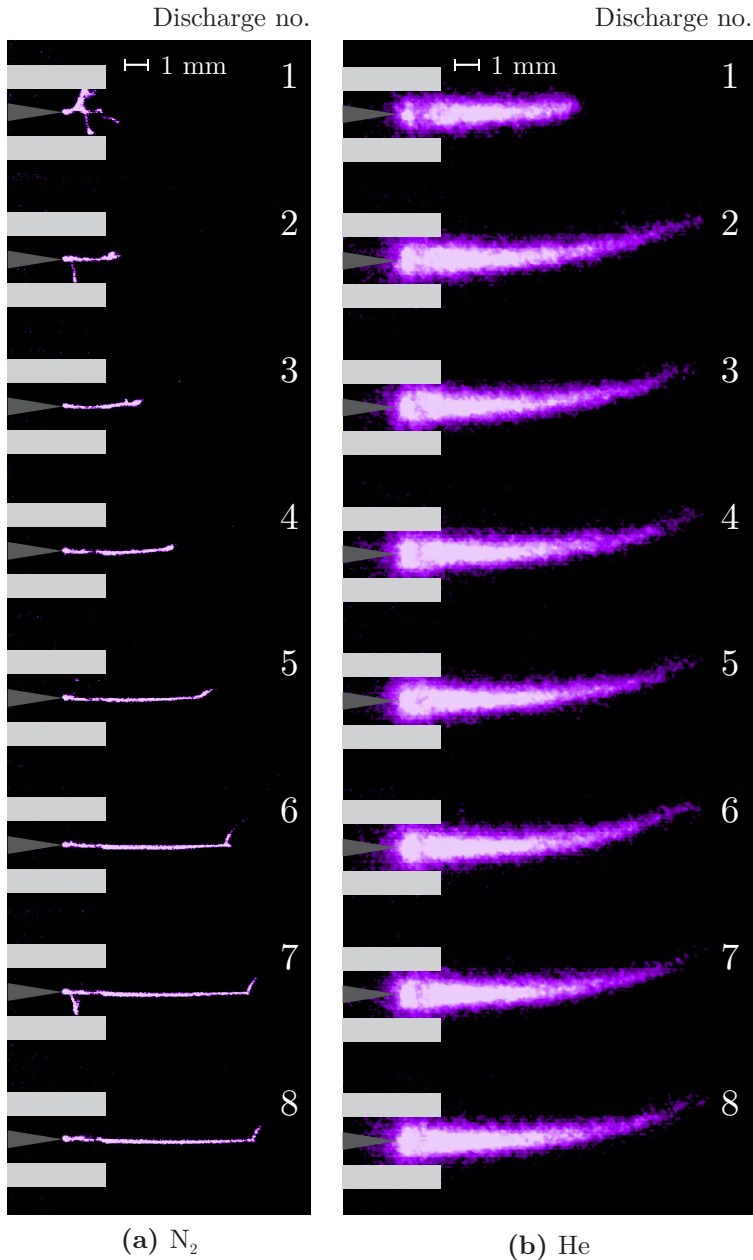


**Figure 3.6:** First eight discharges for (a)  $N_2$  at 8kV, and (b) He at 5kV. In both cases, the repetition frequency is 3kHz, and the flow rate is 1slm. The needle electrode and quartz tube are indicated by the light and dark grey areas respectively. The colour of the discharges was added in post-processing for illustrational purposes.

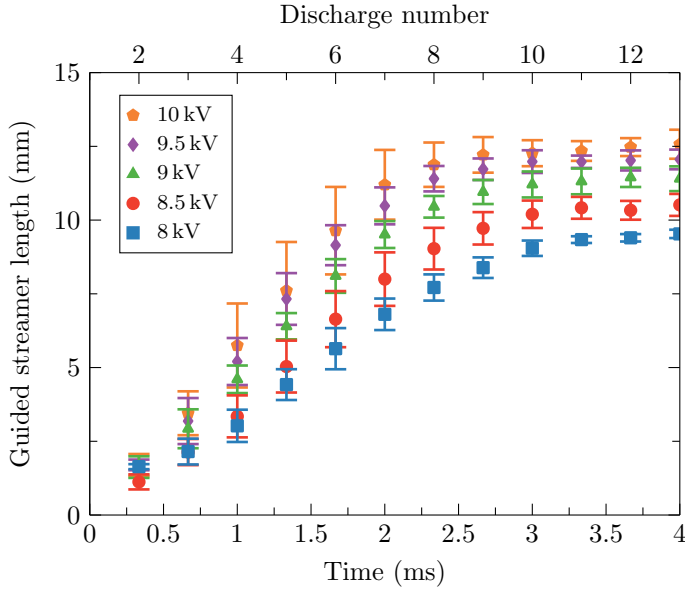


**Figure 3.7:** Development of the guided streamer length in  $N_2$  at different applied voltages.

To confirm the importance of transport in the development of the spatial memory effect, the measurements of guided streamer length at 9 kV are repeated for different volumetric flow rates. Additionally, the increase in length is compared to the average displacement of particles released in the flow, obtained from the model discussed in section 3.2.2. The average displacement is determined from the particles that have a starting position within the streamer radius of approximately  $150\ \mu\text{m}$ . The results are shown in figure 3.8. At higher volumetric flow rates and therefore higher flow velocities, the guided streamer length indeed increases at a larger rate between consecutive discharges. There is also a good agreement between the development of the guided streamer length in the first several discharges and the displacement of transported particles. This shows that for  $N_2$ , besides a temporal memory effect, there is also a spatial memory effect that provides the guiding mechanism and is responsible for spatial reproducibility. This spatial memory develops as the gas flow transports discharge remnants downstream in the time between the first discharges.

### 3.4 Conclusions

In this chapter, the development of the memory effect, which is responsible for the reproducibility of pulsed plasma jets in  $N_2$  and He feed gas is investigated. For both feed gases, it is found that the first discharge may occur at any time during the voltage pulse. After the first discharge, the jitter in the moment of inception immediately

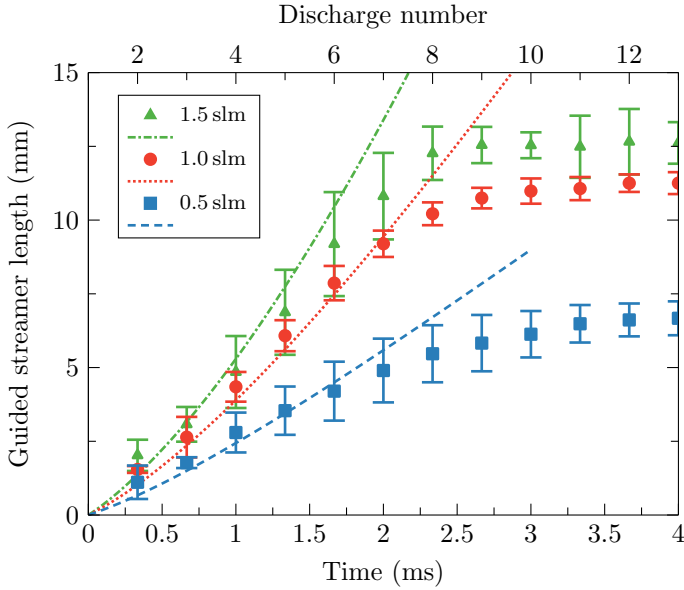


**Figure 3.8:** Development of the guided streamer length in  $N_2$  with an applied voltage of 9 kV at different volumetric flow rates (marks), and the corresponding displacement of transported particles obtained from the model (lines).

decreases to sub-nanosecond values. This shows that the first discharge provides sufficient remnants to mediate the temporal memory effect. However, this result is different from what is reported in previous research for a pulsed plasma jet in He, where a start-up phase of 100 discharges was observed before temporal reproducibility is reached [59]. This is potentially due to a different plasma source design, where interaction with the dielectric tube could be more significant.

The development of spatial reproducibility and the guiding mechanism is different for  $N_2$  and He feed gas. For He, only the length of the first discharge may differ. This depends on the moment in the voltage pulse at which the first discharge occurs. If the first discharge occurs early in the voltage pulse, it appears the same as for subsequent discharges, showing that there is no spatial memory effect related to discharge remnants in this case. In contrast, for  $N_2$ , there is a start-up phase in which a spatial memory effect develops before spatial reproducibility is attained. During this start-up phase of approximately ten discharges, the length of the guided streamer increases every discharge until its final length is reached. It is shown by numerical simulation of the flow that this growth corresponds to transport of discharge remnants in the flow. From this, it is concluded that in the case of  $N_2$  the guiding mechanism and spatial reproducibility are not only related to the presence of the outflowing feed gas, but to a spatial memory effect resulting from discharge remnants that are transported in the gas flow.

## Chapter 4

---

# Manipulation of the memory effect

## 4.1 Introduction

When atmospheric pressure pulsed plasma jets are driven by kHz-range repetition frequencies, guided streamer discharges are typically generated [5, 6, 10]. These discharges are sometimes referred to as plasma bullets. They can be highly reproducible, both spatially and temporally, under the right conditions, as discussed in chapter 2. The reproducibility of guided streamers in pulsed plasma jets is a result of the so-called memory effect [9]. For He feed gas flowing into open air, the memory effect provides a repeatable inception moment, and the streamer is spatially guided by the channel of He gas. In contrast, guided streamers in N<sub>2</sub> feed gas are guided by an additional spatial memory effect. Over the first several discharges, the guided streamer length increases as discharge remnants are transported downstream in the time between discharges by the gas flow, which was discussed in chapter 3. However, this result does not tell us what these remnants that are responsible for spatially guiding the discharges in N<sub>2</sub> are.

It is well known that positive streamer discharges require a source of seed electrons in front of their streamer head in order to propagate [4]. Additionally, Nijdam *et al* have shown that streamers in N<sub>2</sub>, with up to 0.5% O<sub>2</sub>, can be guided by weak pre-ionisation induced by a laser [64, 65]. The position of the laser-guided streamers was shown to be offset from the position of the laser by the distance that electrons drift in the background field before the streamer arrives, which demonstrates that the laser-guided streamers follow the electrons [65]. For these reasons, it would seem plausible that the spatial memory effect and the resulting guiding mechanism in pulsed plasma jets in N<sub>2</sub> are also mediated by electrons.

If charged species, such as electrons, indeed play an essential role in spatially guiding the discharges, it might be possible to influence the position of the discharge by manipulating the memory effect between successive discharges with an external electric field. The interaction between pulsed plasma jets and an external electric field has been investigated before for He feed gas [28, 66–70]. Usually, the purpose of the external electric field is to manipulate the properties of the discharge, so that they may be tailored for a specific application. So far, a substantial level of control over the propagation dynamics has been achieved [68]. It has been demonstrated that the generated guided streamer discharges can be (locally) displaced or bent [28, 66, 70], when the external field is applied perpendicular to the propagation direction. In these cases, the external field was applied *during* the discharge, which effectively changes the background electric field in which the discharge propagates. This is fundamentally different from our proposed approach, in which the external electric field will be applied in the time *between* consecutive discharges in order to manipulate the memory effect instead.

In order to successfully manipulate the location of charged discharge remnants, the external electric field must be able to separate the charged species to some extent. When subjected to an external electric field, charged species in a plasma will arrange themselves in a manner that effectively shields the field. The typical shielding distance

is given by the Debye length [2]

$$\lambda_D = \sqrt{\frac{\varepsilon_0 k_B T_e}{n_e e^2}}, \quad (4.1)$$

where  $\varepsilon_0$  is the vacuum permittivity,  $k_B$  is the Boltzmann constant,  $T_e$  is the electron temperature,  $n_e$  is electron density, and  $e$  is the elementary charge. As a result of the shielding, charge separation can only occur on length scales of the order of the Debye length. The electron density and temperature during and between discharges are discussed in more detail in chapter 5. During the discharge, typical values for the electron density and electron temperature are of the order of  $n_e \approx 10^{20} \text{ m}^{-3}$  and  $T_e \approx 1 \text{ eV}$ . This corresponds to a Debye length of  $\lambda_D \approx 1 \mu\text{m}$ . However, as the electron density decays to around the order of  $10^{15} \text{ m}^{-3}$  in the time between successive discharges (see chapter 5), the Debye length will increase significantly. This suggests that a deviation in the discharge trajectory, resulting from charge separation by an external electric field perpendicular to the propagation direction, should be observable if the discharge is guided by charged species.

In this work, it is shown that the spatial memory effect of pulsed plasma jets in  $\text{N}_2$  can indeed be manipulated by external electric fields applied in the time between discharges. This demonstrates that charged species play an essential role in the memory effect. It is found that in this case, the displacement of the guided streamer trajectories corresponds to the drift of positive ions instead of electrons. However, the mechanism that provides seed electrons, which are required for streamer propagation, at the location of the positive ions is not yet fully understood and still requires further investigation.

## 4.2 Experimental setup

### 4.2.1 Plasma source and measurement system

The experimental setup is schematically illustrated in figure 4.1. Guided streamers are generated in pure  $\text{N}_2$  (99.999%) flowing into ambient air at a volumetric flow rate of 1 slm. This is done by applying 500 ns high voltage (HV) pulses with a fixed amplitude of 6 kV and fixed repetition frequency of  $f_{\text{rep}} = 3 \text{ kHz}$  to a needle electrode that is placed concentrically inside a quartz tube, which functions as the nozzle of the pulsed plasma jet. The needle electrode has a radius of 0.5 mm, and its tip has an angle of about 20 degrees and is located 2 mm before the end of the quartz tube. The quartz tube has an inner radius of 1 mm and an outer radius of 2 mm. A HV power supply (Spellman SL10PN60) and HV pulse generator (DEI PVX-4110) are used to produce the HV pulses that generate the discharges. The HV pulse generator is triggered by a pulse/delay generator (BNC model 575). More details on the plasma source can be found in chapter 1.

To subject the discharge remnants to an external electric field, the nozzle of the plasma source is placed between two circular plate electrodes. The external electrodes have a diameter of 35.5 mm and the gap between the electrodes is 15 mm. The end of the quartz tube is located 8 mm from the centre of the gap (also see figure 4.3). A



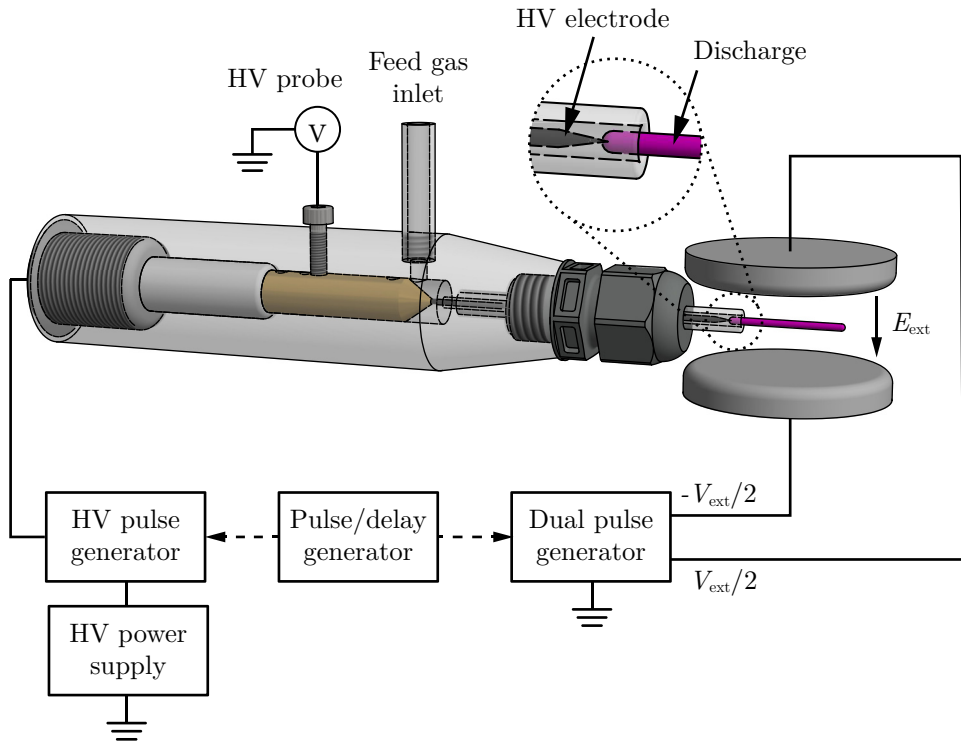


**Figure 4.1:** Schematic illustration of the setup. A magnified view of the nozzle is included, and a discharge is depicted in purple.

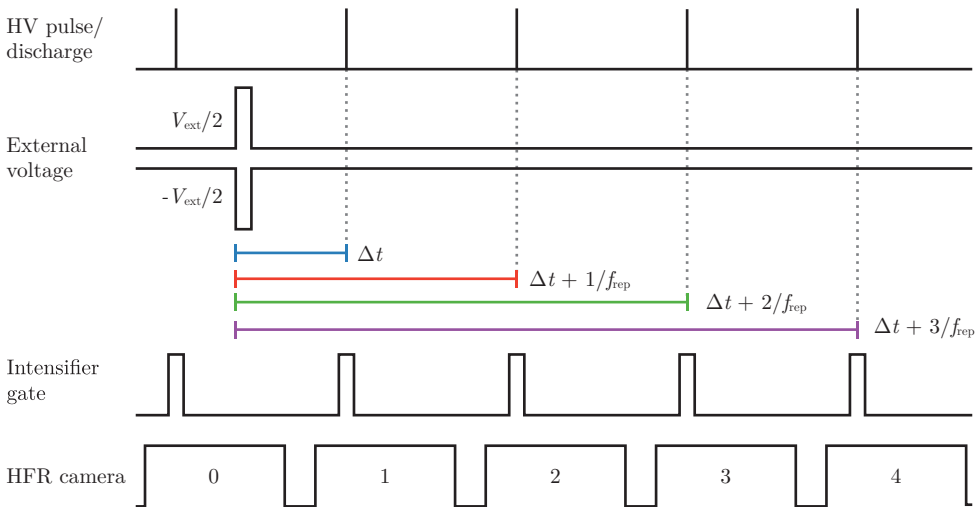


**Figure 4.2:** Overview of the timing in the setup. Durations are not to scale.

5  $\mu\text{s}$  external voltage pulse  $V_{\text{ext}}$  is applied across the external electrodes before one in every hundred discharges. It is found that this ensures that the discharge prior to the external voltage pulse is undisturbed, and no cumulative effects of multiple consecutive external voltage pulses build up. To minimise distortion of the external electric field  $E_{\text{ext}}$  by the needle electrode, the external voltage  $V_{\text{ext}}$  is applied symmetrically over the external electrodes:  $V_{\text{ext}}/2$  on the top electrode, and  $-V_{\text{ext}}/2$  on the bottom electrode. The two required synchronised voltage pulses of opposite polarity are produced using an in-house developed dual pulsed power supply. The generated external voltage pulses have a rise time of 5 ns and a fall time of 50 ns. The dual pulsed power supply is triggered once every hundred discharges by the same pulse/delay generator as the HV pulse generator. The timing of the 5  $\mu\text{s}$  external voltage pulse within the approximately 333  $\mu\text{s}$  interval between successive discharges can be controlled by varying the delay.

To image and record the discharge trajectories, a high frame-rate (HFR) camera (Photron FASTCAM Mini UX100) with a high-speed image intensifier (Invisible Vision UVi 1850) is used (not shown in figure 4.1). This imaging system is the same as the one used in chapter 3. The HFR camera and intensifier are synchronised to the discharges using the pulse/delay generator. The intensifier is gated for 1  $\mu\text{s}$  during every discharge in order to capture the entire trajectory of a discharge. With this system, the trajectories of consecutive individual discharges can be recorded.

A schematic timing diagram of the experiment is given in figure 4.2. The time between the external voltage pulse and the next discharge is  $\Delta t$ . Every time the external voltage pulse is applied, the HFR camera saves five frames, which are indicated by the numbers 0 through 4. Frame 0 contains the trajectory of the undisturbed discharge before the external voltage pulse, which is used as a reference in determining the displacement of the trajectories of the discharges after the external voltage pulse. Frames 1 through 4 contain the trajectories of the first four discharges following the external voltage pulse. From the trajectories of these discharges, it is assessed what the effects of the electric field on the memory effect are, and whether these effects persist for more than one discharge. This is done for different applied external voltages, as well as for different values of the delay  $\Delta t$ .

### 4.2.2 External electric field distribution

To compare the measured displacement of the discharge trajectories to drift displacement of charged species, knowledge on the external electric field is necessary. For this reason, a 3D electrostatic model is made using COMSOL. Besides the external electrodes, only the needle electrode and the quartz tube are included in the model. For the quartz tube, a relative permittivity of  $\epsilon_r = 4.2$  is used [71]. Since the situation between consecutive discharges is considered, the needle is kept at ground potential (0 V), and a total potential difference of 1 kV is applied symmetrically over the electrodes.

A cross section of the resulting potential distribution  $\phi$  is shown in figure 4.3. Although distortions to the external field are minimised by applying the external voltage symmetrically, the equipotential lines show that the needle and quartz tube still cause some distortion. The corresponding electric field strength on the axis of the jet is shown in figure 4.4.

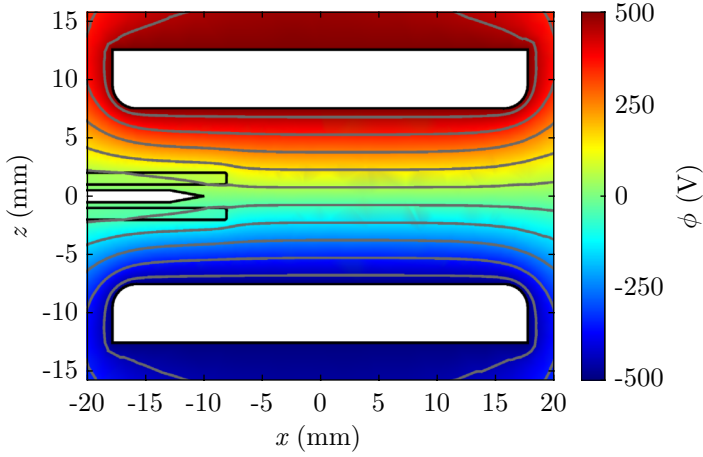


**Figure 4.3:** Potential distribution between the external electrodes in the plane of discharges for an applied external voltage  $V_{\text{ext}} = 1 \text{ kV}$ . The needle and external electrodes are indicated by the white areas, and the quartz tube is outlined in black. Several equipotential lines are drawn in grey. Only a part of the full computational domain ( $50 \text{ mm} \times 70 \text{ mm} \times 200 \text{ mm}$ ) is shown.

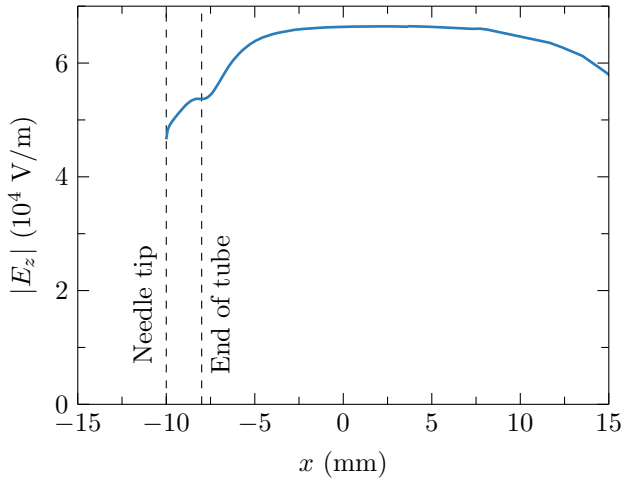


**Figure 4.4:** Electric field strength for an applied external voltage  $V_{\text{ext}} = 1 \text{ kV}$  on the axis of the jet ( $z = 0$  in figure 4.3). The positions of the needle tip ( $x = -10 \text{ mm}$ ) and the end of the quartz tube ( $x = -8 \text{ mm}$ ) are indicated by the dashed lines.

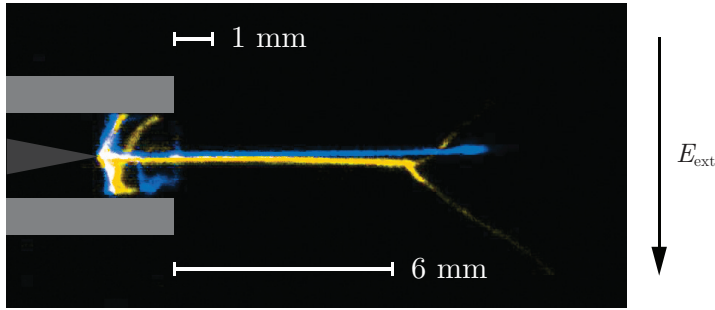


**Figure 4.5:** ICCD image of an undisturbed discharge (blue), and a displaced discharge (yellow). The displacement was achieved by applying a  $V_{\text{ext}} = 3 \text{ kV}$  pulse  $10 \mu\text{s}$  before the discharge. Overlapping parts of the discharges are white (blue + yellow). The direction of the external electric field is indicated by the arrow. The needle electrode (dark grey) and quartz tube (light grey) are drawn on top of the image for reference.

## 4.3 Results and discussion

In figure 4.5, a superimposed image of the undisturbed discharge and the first discharge after the external voltage pulse is shown. The amplitude of the external voltage pulse is  $3 \text{ kV}$ , and it is applied  $10 \mu\text{s}$  before the discharge. The most important thing that should be immediately noticed is that the trajectory of the discharge after the external voltage pulse is indeed displaced. This immediately demonstrates that the memory effect can be manipulated with an electric field, and hence that charged species play an important role in spatially guiding the streamers generated in a pulsed plasma jet in  $\text{N}_2$ . The displacement is somewhat larger further downstream. This can be explained by the fact that the electric field is higher at these positions, as shown in figure 4.4.

Another notable feature of the displaced discharge trajectory is the fact that the displacement is in the direction of the external electric field. This is the direction in which positively charged species drift. To further understand the observed displacement, its dependence on the external voltage pulse amplitude and timing is considered.

### 4.3.1 Dependence on the external voltage

To see how the displacement depends on the amplitude of the external voltage  $V_{\text{ext}}$ , the experiment is repeated at several voltages, while keeping the delay between the external voltage pulse and discharge at  $10 \mu\text{s}$ . In figure 4.6, the average displacement as a function of external voltage is given. The average displacement is calculated over the first  $6 \text{ mm}$  after the end of the quartz tube, as indicated in figure 4.5. This is done for each individual discharge, and then 60 measurements are averaged. The error bars indicate the standard deviation of the average displacement obtained from these 60 measurements. It is found that the displacement increases approximately linearly with

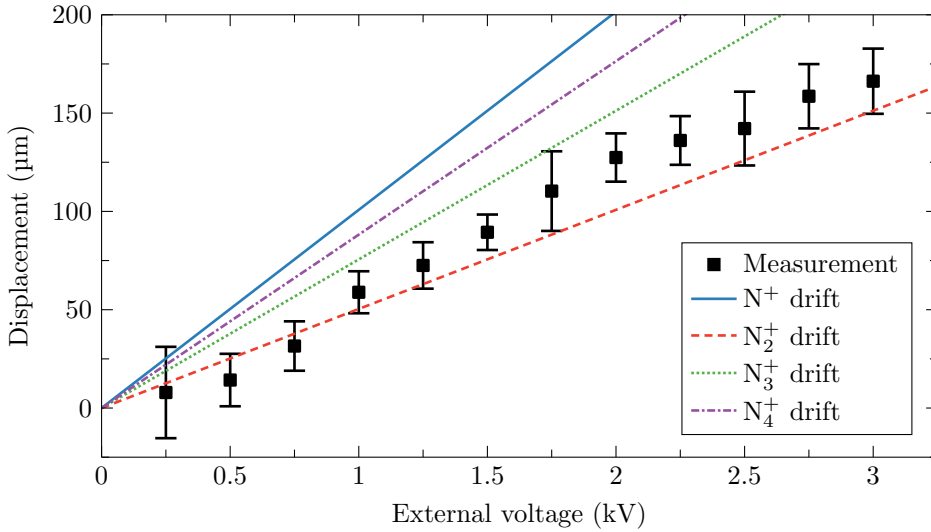


**Figure 4.6:** Average displacement of the discharge trajectory (marks), and the drift displacement calculated for the  $N^+$ ,  $N_2^+$ ,  $N_3^+$ , and  $N_4^+$  ions (lines) as a function of the external voltage. The external voltage pulse is applied  $10\ \mu\text{s}$  before the discharge.

the external voltage amplitude.

In order to compare the measured displacement to ion drift, the drift displacement is calculated. The motion of the charged species  $i$  in an electric field  $E$  is described by the drift velocity [2]

$$v_{d,i} = \mu_i E, \quad (4.2)$$

where  $\mu_i$  is the mobility of species  $i$ . Consequently, the ion drift displacement is

$$d_{d,i} = v_{d,i} \tau = \mu_i E \tau, \quad (4.3)$$

where  $\tau$  is the amount of time the electric field is applied, which in our case is  $5\ \mu\text{s}$ . Since the measured displacement is averaged over the first 6 mm after the end of the quartz tube, the electric field from the model is averaged over the same region, i.e.  $-8\ \text{mm} < x < -2\ \text{mm}$  in figure 4.4, for each applied external voltage. The mobilities for positive nitrogen ions are listed in table 4.1.

The curves representing the drift displacement of several ions were already included in figure 4.6. The measured data and the calculated ion drift displacements display very similar behaviour. This result seems to strongly imply that the streamer discharges follow the positive ions. However, this raises the question of how seed electrons, which are required for streamer propagation, are provided at the location of the positive ions. In figure 4.7a, the reduced electron mobility  $\mu_e N$  in pure  $N_2$  is given as a function of reduced electric field  $E/N$ , where  $N = 2.5 \times 10^{25}\ \text{m}^{-3}$  is the background density at atmospheric pressure. In our case, the external electric fields correspond to reduced

**Table 4.1:** Mobility of  $N^+$ ,  $N_2^+$ ,  $N_3^+$  and  $N_4^+$  ions in  $N_2$  background gas at atmospheric pressure. Calculated from reduced mobility values reported in [72].

Ion	Mobility ( $m^2/Vs$ )
$N^+$	$3.2 \times 10^{-4}$
$N_2^+$	$1.6 \times 10^{-4}$
$N_3^+$	$2.4 \times 10^{-4}$
$N_4^+$	$2.8 \times 10^{-4}$

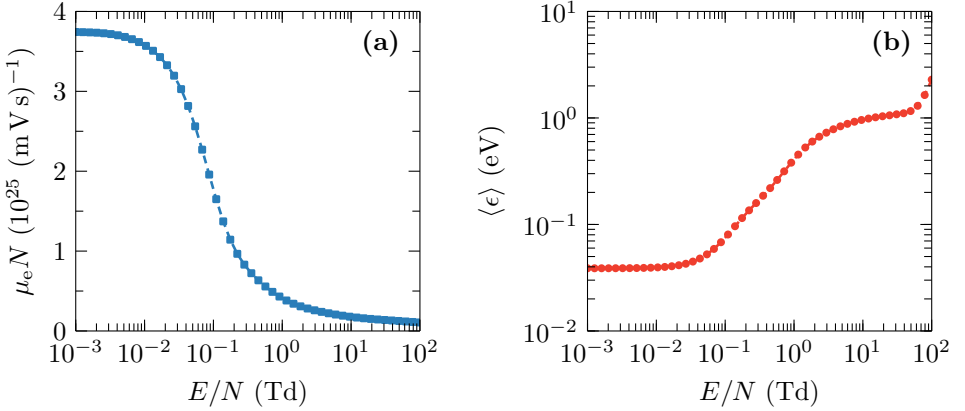


**Figure 4.7:** In (a) the reduced electron mobility is given as a function of reduced electric field, and in (b) the mean electron energy is given as a function of reduced electric field for pure  $N_2$ . Computed from the Phelps database [73] using BOLSIG+ [74].

electric fields between approximately 1 Td and 10 Td. Since the electron mobility is higher for fields lower than this value, it would, in theory, be possible that the electrons move to the position of the positive ions after the external voltage pulse. However, using the electron mobility to calculate electron drift displacement leads to values of several centimetres, which is larger than the external electrode gap. This implies that all free electrons that were present prior to the external voltage pulse are lost to the electrodes. Therefore, drift cannot by itself explain the observed behaviour.

### 4.3.2 Dependence on timing

To see how the displacement depends on the timing of the external voltage pulse, the experiment is repeated for several delays  $\Delta t$  between the external voltage pulse and the discharge, while keeping the external voltage amplitude fixed at 2 kV. In figure 4.8, the average displacement as a function of the delay is given. When the delay becomes longer than one (or multiple) periods of the discharge repetition frequency, one (or multiple) discharges have taken place in the time between the external voltage

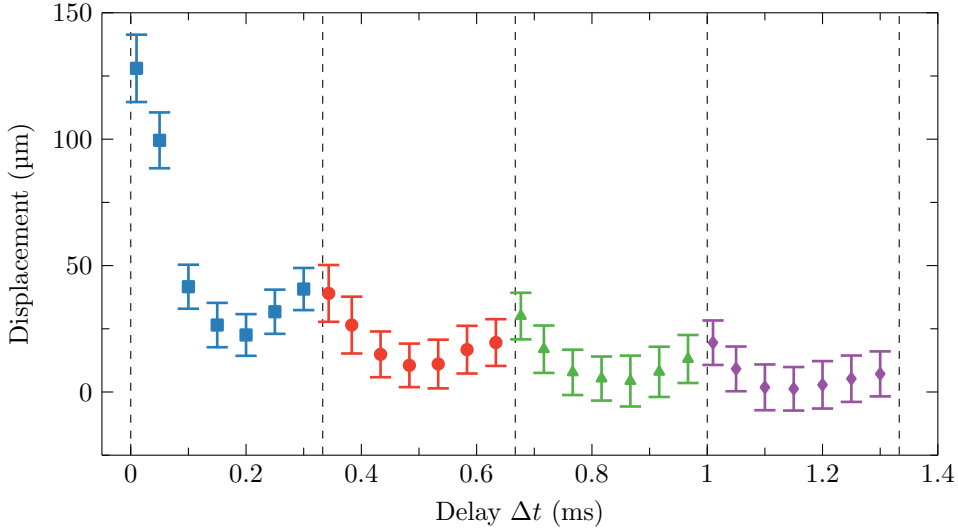


**Figure 4.8:** Average displacement of the discharge trajectory as a function of the delay between the external voltage pulse and the discharge. A dashed line is placed every period of the discharge repetition frequency. The amplitude of the external voltage pulse is  $V_{\text{ext}} = 2 \text{ kV}$ .

pulse and the discharge of which the displacement is measured. As explained in section 4.2, in practice these displacements are inferred from the second, third and fourth discharges after the external voltage pulse. For every period of the discharge repetition frequency, a vertical dashed line is placed in the figure.

First, the situation where the delay between the external voltage and the discharge is less than one period ( $0 < t < 0.33 \text{ ms}$ ) is considered. In this case, the displacement is determined from the discharge directly following the external voltage pulse. The displacement is largest when the external voltage is applied right before the discharge and decreases as the delay between the external voltage and the discharge is increased until about 0.2 ms. A possible explanation for this behaviour is that the electron density remaining from the previous discharges has decayed further, and hence the shielding effect becomes weaker closer to the next discharge. However, this does not explain why the displacement becomes larger again when the delay between the external voltage and the discharge is further increased to 0.3 ms. At this moment in time, the electron density is still higher than at 0.2 ms, and hence shielding should be stronger. Nevertheless, a larger displacement is found. This also implies that there must be an additional effect that plays a role.

A similar displacement pattern is visible for the second ( $0.33 \text{ ms} < t < 0.67 \text{ ms}$ ), third ( $0.67 \text{ ms} < t < 1 \text{ ms}$ ), and fourth ( $1 \text{ ms} < t < 1.33 \text{ ms}$ ) discharges following the external voltage pulse, although the amount of displacement steadily decreases. This shows that after a discharge trajectory is displaced by manipulation of the memory effect, it takes several discharges for the trajectory to return to its original position.

## 4.4 Conclusions and outlook

To conclude, we have shown that the trajectories of guided streamer discharges in  $N_2$  can indeed be displaced from their usual location on the jet axis by manipulating the memory effect between successive discharges. However, the direction of the displacement was unexpected. The displacement is achieved by applying a pulsed external electric field perpendicular to the propagation direction of the discharges and confirms that charged species play an important role in the memory effect. From the fact that seed electrons are required, as well as from laser-guided streamer experiments [64,65], it was expected that the displacement of discharge trajectories would be in the direction opposite to the external electric field, which corresponds to the direction of the electron drift. Instead, the resulting displacement is found in the direction of the external field, which is the direction in which positive ions drift.

When the external voltage pulse is applied  $10\ \mu\text{s}$  before the discharge, the magnitude of the displacement is linearly related to the applied external voltage, and it seemingly corresponds to the distance positive ions drift in the external electric field. However, how the required seed electrons would be provided at the location of the positive ions is not understood. Calculating the drift of free electrons in the external field results in distances much larger than the distance between the electrodes, meaning that all free electrons are effectively lost to the anode. Therefore, the observed behaviour cannot be explained solely by drift.

When the external voltage is applied earlier, up to about  $0.2\ \text{ms}$  before the discharge, the displacement decreases. This is likely a result of stronger shielding, as the electron density remaining from the previous discharge is still higher. On the other hand, the displacement increases again when the time between the external voltage pulse and the discharge is further increased to  $0.3\ \text{ms}$ . This suggests that also here an additional effect is at play.

Experimentally, some more insight into the dynamics of the charged species can potentially be obtained from measurements of the current through the external electrodes. Additionally, a numerical model of the discharge remnants and their interaction with the external electric field should be able to provide more knowledge on the involved processes leading to the observed displacement of the guided streamer trajectories.





## Chapter 5

---

# Electron densities between discharges

## 5.1 Introduction

Pulsed plasma jets at kHz repetition frequencies typically consist of highly reproducible guided streamers and are often named ‘plasma bullets’ [5, 6, 10]. Thanks to their reproducibility, guided streamer discharges are a useful tool to investigate streamer physics. The guided streamers in pulsed plasma jets are reproducible by virtue of the memory effect: remnants of previous discharges provide the seed electrons for the next discharge [9]. In chapter 3, it was shown that in the case of He feed gas, the memory effect ensures temporal reproducibility of the discharge inception, while in the case of N<sub>2</sub> feed gas it is also responsible for the spatial reproducibility of the discharges. Since seed electrons mediate the memory effect, knowledge on the electron density, as well as its evolution between successive discharges, is essential in understanding the physics of pulsed plasma jets and the memory effect. However, since the electron density decays exponentially between successive discharges, it is challenging to directly measure the electron density experimentally.

Various diagnostics exist to measure the electron density in atmospheric pressure plasma jets. For example, electron densities can be determined from Stark broadening of spectral lines measured using optical emission spectroscopy [75]. However, this technique is inherently limited to times when light is emitted by the plasma during a discharge. Thomson scattering, the scattering of laser light on free electrons, has also been used before to measure the electron densities in radio-frequency and microwave excited atmospheric pressure plasma jets [34, 76, 77], as well as in pulsed plasma jets in He and Ar during or briefly after the discharge [25, 78, 79]. With Thomson scattering both high temporal and spatial resolution can be achieved when tightly focused, short laser pulses are used. However, the detection limit of this technique at atmospheric pressure is usually of the order of  $10^{18} \text{ m}^{-3}$  for pure Thomson scattering and is higher when simultaneous rotational Raman scattering occurs [76], such as in N<sub>2</sub>. This is too high to measure the evolution of electron densities between consecutive discharges.

Several microwave techniques are also used for electron density measurements. For example, millimetre interferometry [80, 81] and microwave scattering [82] have recently been used to measure the evolution of electron density in pulsed discharges at atmospheric pressure. Another microwave technique, which will be used in this work, is microwave cavity resonance spectroscopy (MCRS). This diagnostic has been applied to a variety of low-pressure plasmas over the years [83–91]. Compared to Thomson scattering, MCRS is capable of measuring lower electron densities. The temporal resolution depends on the quality factor and the resulting response time of the used cavity. Typically cavities with a temporal resolution of the order of tens of ns to a  $\mu\text{s}$  are used. Furthermore, plasma properties obtained from MCRS are averaged over the cavity volume and are hence not spatially resolved. Nevertheless, with prior knowledge on the approximate electron density distribution, MCRS is potentially a suitable diagnostic for the electron densities in the time between successive discharges where  $\mu\text{s}$  resolution suffices. Additionally, it should also be noted that multi-mode MCRS, in which multiple cavity modes are used to reconstruct the spatial distribution of the electron density, was recently reported [92].

In MCRS, a microwave cavity is placed around the plasma. The resonances of

the cavity depend on the properties of the medium inside the cavity. Therefore, introducing a discharge in the cavity can change the resonance frequency as well as the quality factor of the cavity. Usually, cavity perturbation theory is used to relate changes in resonance behaviour to properties of the plasma. For low-pressure plasmas, where the electron-neutral collision frequency is negligible compared to the resonant microwave frequency, the electron density can be determined directly from the shift in resonance frequency [83]. However, the effects of electron-neutral collisions cannot be neglected at higher pressures. This makes the relation between the resonance properties of the cavity and the plasma properties more complex. In this case, a more intricate analysis is required, in which not only the shift in resonance frequency but also the change in quality factor has to be considered. The advantage, though, is that such an analysis also results in information on the collision frequency, in addition to the electron density.

In this work, MCRS is adapted for atmospheric pressure plasma jets and applied to a pulsed plasma jet in  $N_2$  feed gas flowing into ambient air. The required analysis is developed and used to determine the temporal behaviour of the electron density and collision frequency between successive discharges. In addition, the experimental results are compared to those predicted by a global model.

## 5.2 Experimental setup and methods

### 5.2.1 Setup and measurement system

The experimental setup is schematically illustrated in figure 5.1. The plasma source itself is described in more detail in chapter 1 and will only briefly be explained here. A pulsed plasma jet is generated in  $N_2$  feed gas (purity of 99.999%) flowing at a volumetric rate of 1 slm. A high voltage (HV) power supply (Spellman SL10PN60) provides a DC voltage to a HV pulse generator (DEI PVX-4110). The latter is gated by a pulse/delay generator (BNC model 575) in order to generate voltage pulses with a width of 500 ns and rise and fall times of about 40 ns. The HV pulses are applied to a needle electrode that has a radius of 0.5 mm and a tip angle of approximately  $20^\circ$ . The needle electrode is placed concentrically inside a quartz tube of inner radius 1 mm and outer radius 2 mm, with the tip of the needle located 2 mm before the end of the quartz tube. At the rising edge of every voltage pulse, a guided streamer is generated that propagates from the tip of the needle along the symmetry axis of the jet and has a radius of approximately  $150\ \mu\text{m}$ . The applied voltage is varied between 4 kV and 8 kV, and a repetition frequency between 2 kHz and 6 kHz is used. It should be noted that the lowest operating voltage is 2 kV lower than in the previous chapters. This is due to the presence of the cavity, which is grounded and increases the electric field.

A cylindrical microwave cavity of inner dimensions  $\varnothing 66 \times 16$  mm is placed concentrically to the jet. The two flat walls of the cavity have a thickness of 5 mm, and the curved wall has a thickness of 3 mm. The outer surface of the cavity is located at the same axial position as the end of the quartz tube (also see figure 5.5). The cavity has a hole of 13 mm diameter in the centre of each of its two flat walls to allow the gas flow and discharge to enter and exit the cavity. A microwave generator (Stanford Research

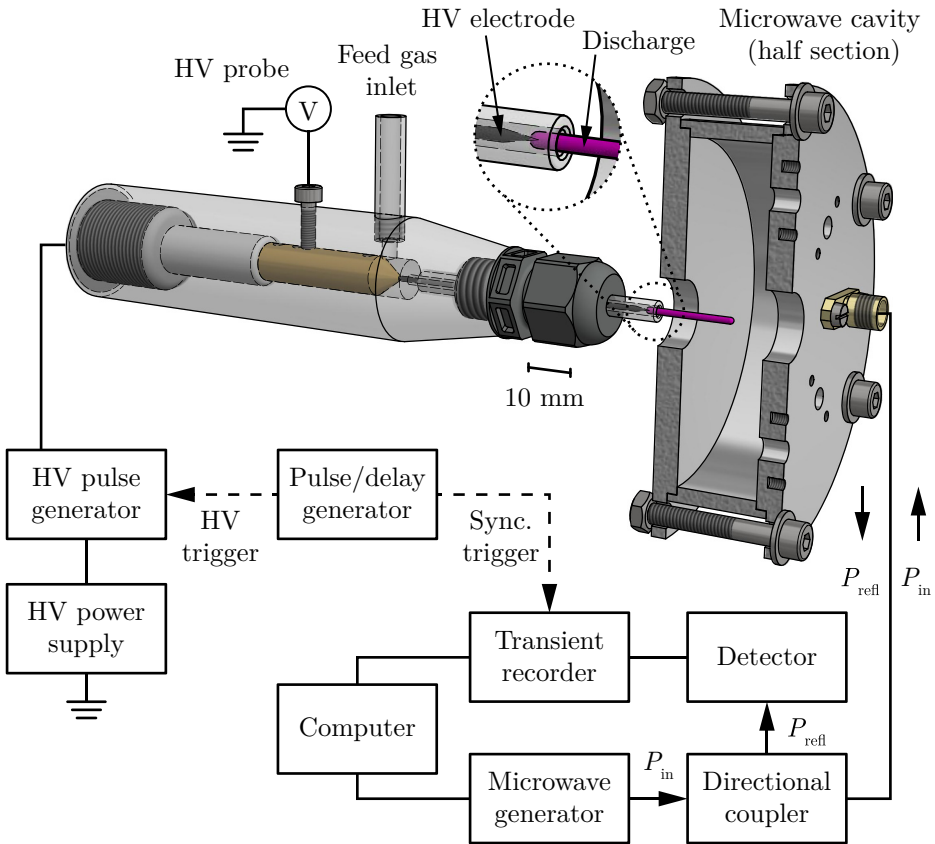


**Figure 5.1:** Schematic illustration of the setup. For clarity, only half of the microwave cavity is drawn, and a magnified view of the nozzle is included. The discharge is indicated in purple.

Systems SG386) generates a microwave signal with frequency  $f = \omega/2\pi$  and power  $P_{\text{in}}$ . The microwaves travel through a directional coupler (Mini-Circuits ZHDC-10-63-S+), a device that discriminates forward and reverse travelling waves, and are applied to an antenna that protrudes a few mm into the microwave cavity. Depending on the applied frequency, a certain part of the input power is reflected. When the applied frequency matches a resonance frequency of the cavity, the reflected power is minimal. The reflected microwave signal with power  $P_{\text{refl}}$  returns to the directional coupler and is measured by a logarithmic detector (Hittite 602LP4E). This measurement is sampled by a transient recorder (Spectrum M3i.4121-exp) with a sampling frequency of 100 MHz. The HV pulse generator of the plasma source and the transient recorder are triggered by the same pulse/delay generator. The transient recorder data of a time range covering slightly over one entire period of the pulsed voltage is saved to a computer. Since the discharges are reproducible, multiple measurements can be averaged, and the temporal evolution of the plasma properties between discharges can be measured this way. Scanning of the applied frequency and saving of the transient recorder data is automated using a computer program.

A scan of the full frequency range of the microwave generator for an ‘empty’ cavity, i.e. without a discharge, is shown in figure 5.2. This reveals two resonances in the available frequency range: the  $\text{TM}_{010}$  mode around 3.51 GHz and the  $\text{TM}_{110}$  mode around 5.45 GHz. The identification of these modes has been confirmed by a COMSOL model of the cavity. However, it is found that the  $\text{TM}_{110}$  peak is not prominent enough compared to the background to obtain accurate results from the fitting procedure, which will be explained shortly. Therefore, only the  $\text{TM}_{010}$  mode will be used in this work. For the actual measurements, a smaller frequency band of 10 MHz around 3.51 GHz is scanned at 50 kHz intervals. Such a measurement of the  $\text{TM}_{010}$  mode for the empty cavity is shown in figure 5.3. For each of the shown points, 128 measurements are averaged.

For an ideal lossless cavity, the resonance peak would be a delta peak. In reality, however, there is a band around the resonance frequency  $\omega_{\text{res}}$  that can lead to substantial excitation of the cavity mode. This is caused by the finite conductivity of the cavity material, as well as potential (ohmic) losses in the medium inside the cavity. The spectral power distribution  $P(\omega)$  of a resonance peak around  $\omega_0$  is Lorentzian and is given by [93]

$$P(\omega) \propto \left[ (\omega - \omega_0)^2 + \left( \frac{\omega_0}{2Q} \right)^2 \right]^{-1}, \quad (5.1)$$

where  $Q$  is the so-called quality factor of the cavity mode. The quality factor is related to power losses and determines the width of the resonance peak. It is also directly related to the characteristic decay time  $\tau = 2Q/\omega_0 = Q/\pi f_0$  of fields in the cavity. The cavity mode can adjust to any changes on the time scale of several  $\tau$ . Therefore, the characteristic time  $\tau$  is also a measure for the temporal resolution of the measurements.

When a plasma is introduced in the cavity, the resonance frequency shifts and the quality factor changes. How these changes relate to the properties of the plasma is explained in the next section. To obtain the frequency shift and the quality factor from

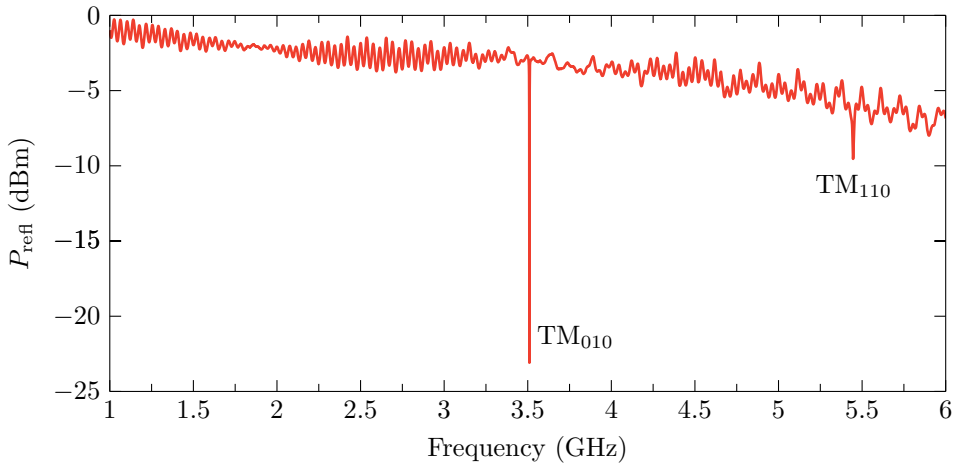


**Figure 5.2:** Full frequency range scan of the reflected power with an empty cavity. Two minima and their corresponding cavity modes are indicated.

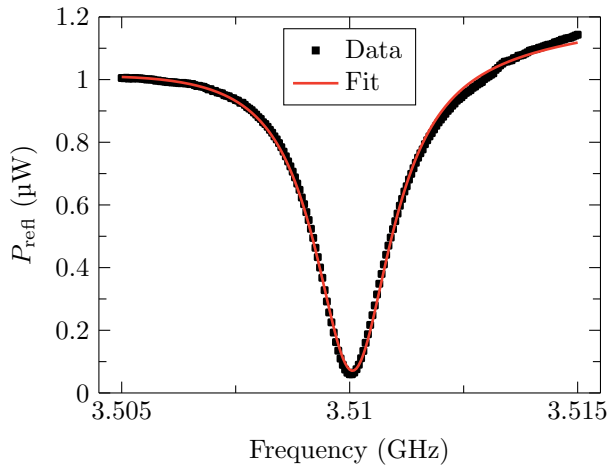


**Figure 5.3:** Resonance peak of the  $\text{TM}_{010}$  mode in the empty cavity (black marks) and a fit (red line).

the measurements, the resonance peak is fitted using the spectral power distribution. This is done in two steps: Firstly, the undisturbed resonance frequency  $f_1$  and quality factor  $Q_1$  are determined for an empty cavity using the fit function

$$L_{\text{fit}}^{\text{empty}}(f; \underbrace{f_1, Q_1, A, a_0, a_1}_{\text{fit variables}}) = A \frac{\left(\frac{f_1}{2Q_1}\right)^2}{(f - f_1)^2 + \left(\frac{f_1}{2Q_1}\right)^2} + a_0 + a_1(f - f_1), \quad (5.2)$$

where the last two terms are added to account for a linear baseline, and  $A$ ,  $a_0$  and  $a_1$  are scaling factors. A fit for the empty cavity using (5.2) was already included in figure 5.3. The resonance frequency and quality factor of the empty cavity are  $f_1 = 3.51$  GHz and  $Q_1 = 1900$  respectively. This means that the characteristic decay time of the system is  $\tau \approx 0.2$   $\mu\text{s}$  and that the temporal resolution is about 1  $\mu\text{s}$ . Secondly, the frequency shift  $\Delta f$  and quality factor  $Q_2$  in the measurements with a discharge are determined using the fit function

$$L_{\text{fit}}(f; \underbrace{\Delta f, Q_2}_{\text{fit variables}}) = A \frac{\left(\frac{f_1}{2Q_2}\right)^2}{(f - f_1 - \Delta f)^2 + \left(\frac{f_1}{2Q_2}\right)^2} + a_0 + a_1(f - f_1), \quad (5.3)$$

where the values for  $f_1$ ,  $A$ ,  $a_0$  and  $a_1$  obtained from the first fit are used as constants.

As mentioned before, the transient recorder data is saved for a time range covering slightly over one entire period of the pulsed voltage. Examples of the resonance frequency shift  $\Delta f$ , relative frequency shift  $\Delta f/f_1$ , quality factor  $Q_2$ , and change in reciprocal quality factor  $\Delta(1/Q) = 1/Q_2 - 1/Q_1$  as functions of time are given in figure 5.4 for an applied voltage of 6 kV and a pulse repetition frequency of 3 kHz. In the first 500 ns after the start of the HV pulses at  $t = 0$  and at about  $t = 333$   $\mu\text{s}$ , some large oscillations are present in the signals. This is most clearly visible in figures 5.4a and 5.4c. This time range corresponds to the duration of the HV pulse, and these artefacts are caused by interference. For this reason, these data points will be removed from the measurements. After this, the resonance frequency and quality factor increase and decrease respectively, and then decay to their initial empty cavity values. The rise time of these signals is approximately 1  $\mu\text{s}$ , which corresponds to the temporal resolution time of the cavity. As can be seen in figures 5.4b and 5.4d, both the resonance frequency and quality factor have returned to their empty cavity values within the detection limit of the measurements well before the next voltage pulse at approximately 333  $\mu\text{s}$ . Therefore, the resonance frequency and quality factor measured at  $t < 0$ , so in the recorded time before the first voltage pulse, can be averaged and subsequently used as empty cavity values. Doing so has the advantage that a separate measurement of the empty cavity values is not required. This minimises potential drift of the resonance frequency that might occur between the empty cavity measurement and the discharge measurement due to, for example, temperature fluctuations in the laboratory. Typically, a complete measurement for one set of operating parameters takes several minutes.



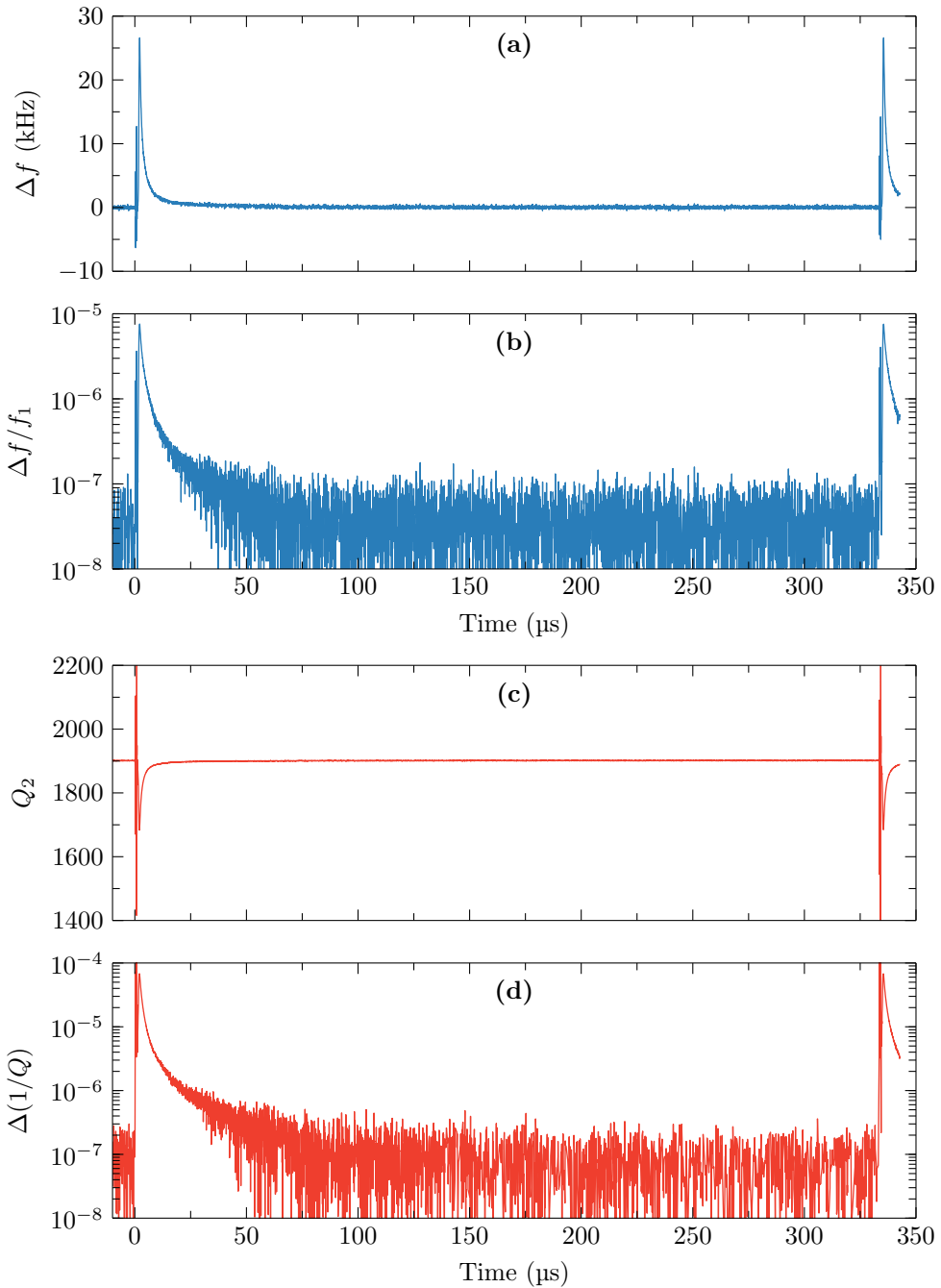


**Figure 5.4:** Measurements of (a) the resonance frequency shift, (b) the relative frequency shift, (c) the quality factor, and (d) the change in reciprocal quality factor, as a function of time for discharges at 6 kV and a repetition rate of 3 kHz.

## 5.2.2 Microwave cavity resonance spectroscopy

### Cavity perturbation theory

To relate the measured relative shift in resonance frequency  $\Delta f/f_1$  and the changes in quality factor  $\Delta(1/Q)$  to properties of the discharge, cavity perturbation theory is used [94–96]. The plasma itself will be approximated by a cylindrical volume  $V_p = \pi r_p^2 l_p$  with uniform properties, which will be further specified shortly. The change in the medium caused by the presence of plasma is treated as a perturbation to the empty cavity. First, the unperturbed cavity is considered. The electromagnetic fields in the cavity are described by Maxwell's equations. For time-harmonic fields, they are given by:

$$-\nabla \times \mathbf{E}_1 = i\tilde{\omega}_1 \mu_1 \mathbf{H}_1, \quad (5.4)$$

$$\nabla \times \mathbf{H}_1 = i\tilde{\omega}_1 \varepsilon_1 \mathbf{E}_1, \quad (5.5)$$

where  $\tilde{\omega}_1$  is the unperturbed (complex) resonance frequency,  $\varepsilon_1$  is the permittivity and  $\mu_1$  is the permeability of the medium inside the cavity, and  $\mathbf{E}_1$  and  $\mathbf{H}_1$  are the unperturbed electric and magnetic microwave fields respectively. For the empty cavity,  $\varepsilon_1 = \varepsilon_0$  and  $\mu_1 = \mu_0$ , where  $\varepsilon_0$  and  $\mu_0$  are the vacuum permittivity and permeability respectively. In the case of an ideal lossless cavity,  $\tilde{\omega}_1$  is purely real. In reality, however, it is a complex quantity given by  $\tilde{\omega}_1 = \omega_1 + i\omega_1/2Q_1$ .

Now a perturbation, in the form of a plasma, is introduced in the medium of the cavity. In the perturbed situation, Maxwell's equations become

$$-\nabla \times \mathbf{E}_2 = i\tilde{\omega}_2 \tilde{\mu}_2 \mathbf{H}_2, \quad (5.6)$$

$$\nabla \times \mathbf{H}_2 = i\tilde{\omega}_2 \tilde{\varepsilon}_2 \mathbf{E}_2, \quad (5.7)$$

where  $\tilde{\omega}_2 = \omega_2 + i\omega_2/2Q_2$  is the new complex resonance frequency, and  $\tilde{\varepsilon}_2$  and  $\tilde{\mu}_2$  are the permittivity and permeability of the plasma. The plasma permittivity and permeability are in general complex and can also be space dependent.

Multiplying (5.4) by  $\mathbf{H}_2$  and (5.7) by  $\mathbf{E}_1$  results in

$$(-\nabla \times \mathbf{E}_1) \cdot \mathbf{H}_2 = i\tilde{\omega}_1 \mu_0 \mathbf{H}_1 \cdot \mathbf{H}_2, \quad (5.8)$$

$$(\nabla \times \mathbf{H}_2) \cdot \mathbf{E}_1 = i\tilde{\omega}_2 \tilde{\varepsilon}_2 \mathbf{E}_2 \cdot \mathbf{E}_1. \quad (5.9)$$

Adding (5.8) and (5.9), and using the identity  $\nabla \cdot (\mathbf{A} \times \mathbf{B}) = \mathbf{B} \cdot (\nabla \times \mathbf{A}) - \mathbf{A} \cdot (\nabla \times \mathbf{B})$ , this can be written as

$$\nabla \cdot (\mathbf{H}_2 \times \mathbf{E}_1) = i\tilde{\omega}_2 \tilde{\varepsilon}_2 \mathbf{E}_1 \cdot \mathbf{E}_2 + i\tilde{\omega}_1 \mu_0 \mathbf{H}_1 \cdot \mathbf{H}_2. \quad (5.10)$$

Similar operations can be applied to (5.5) and (5.6) to obtain

$$\nabla \cdot (\mathbf{H}_1 \times \mathbf{E}_2) = i\tilde{\omega}_2 \tilde{\mu}_2 \mathbf{H}_1 \cdot \mathbf{H}_2 + i\tilde{\omega}_1 \varepsilon_0 \mathbf{E}_1 \cdot \mathbf{E}_2. \quad (5.11)$$

The difference of (5.10) and (5.11) is

$$\begin{aligned} \nabla \cdot (\mathbf{H}_2 \times \mathbf{E}_1 - \mathbf{H}_1 \times \mathbf{E}_2) = \\ i(\tilde{\omega}_2 \Delta \tilde{\varepsilon} + \varepsilon_0 \Delta \tilde{\omega}) \mathbf{E}_1 \cdot \mathbf{E}_2 - i(\tilde{\omega}_2 \Delta \tilde{\mu} + \mu_0 \Delta \tilde{\omega}) \mathbf{H}_1 \cdot \mathbf{H}_2, \end{aligned} \quad (5.12)$$

where  $\Delta\tilde{\omega} = \tilde{\omega}_2 - \tilde{\omega}_1$ ,  $\Delta\tilde{\varepsilon} = \tilde{\varepsilon}_2 - \varepsilon_0$  and  $\Delta\tilde{\mu} = \tilde{\mu}_2 - \mu_0$ . Next, the left-hand side of (5.12) is integrated over the cavity volume  $V_{\text{cav}}$ , and the divergence theorem is used to show that this integral is equal to zero, as both  $\mathbf{n} \times \mathbf{E} = 0$  and  $\mathbf{n} \times \mathbf{H} = 0$  on the cavity surface  $S_{\text{cav}}$ :

$$\iiint_{V_{\text{cav}}} \nabla \cdot (\mathbf{H}_2 \times \mathbf{E}_1 - \mathbf{H}_1 \times \mathbf{E}_2) d^3\mathbf{r} = \oint_{S_{\text{cav}}} (\mathbf{H}_2 \times \mathbf{E}_1 - \mathbf{H}_1 \times \mathbf{E}_2) \cdot \mathbf{n} d^2\mathbf{r} = 0. \quad (5.13)$$

Equivalently, integrating the right-hand side of (5.12) over the cavity volume yields

$$\iiint_{V_{\text{cav}}} [(\tilde{\omega}_2 \Delta\tilde{\varepsilon} + \varepsilon_0 \Delta\tilde{\omega}) \mathbf{E}_1 \cdot \mathbf{E}_2 - (\tilde{\omega}_2 \Delta\tilde{\mu} + \mu_0 \Delta\tilde{\omega}) \mathbf{H}_1 \cdot \mathbf{H}_2] d^3\mathbf{r} = 0. \quad (5.14)$$

Finally, with some manipulation, this can be written as

$$\frac{\Delta\tilde{\omega}}{\tilde{\omega}_2} = - \frac{\iiint_{V_{\text{cav}}} (\Delta\tilde{\varepsilon} \mathbf{E}_1 \cdot \mathbf{E}_2 - \Delta\tilde{\mu} \mathbf{H}_1 \cdot \mathbf{H}_2) d^3\mathbf{r}}{\iiint_{V_{\text{cav}}} (\varepsilon_0 \mathbf{E}_1 \cdot \mathbf{E}_2 - \mu_0 \mathbf{H}_1 \cdot \mathbf{H}_2) d^3\mathbf{r}}. \quad (5.15)$$

Now some approximation will be made, where it is assumed that the perturbations by the plasma are small. Usually, small perturbations would require that the plasma-electron frequency  $\omega_{\text{pe}}$  is smaller than the microwave frequency  $\omega$ , such that the plasma does not shield the microwave fields. The plasma-electron frequency is defined as

$$\omega_{\text{pe}} = \sqrt{\frac{n_e e^2}{\varepsilon_0 m_e}}, \quad (5.16)$$

where  $n_e$  is the electron density,  $e$  is the elementary charge, and  $m_e$  is the electron mass. For the  $\text{TM}_{010}$  mode at 3.51 GHz, this condition would only be met for electron densities lower than about  $10^{17} \text{ m}^{-3}$ . However, when the typical plasma dimension is smaller than the (collisional) skin depth, this constraint is circumvented, and higher densities can be measured [97]. This is the case for our guided streamer discharges in  $\text{N}_2$  with a typical radius of  $150 \mu\text{m}$ . The fact that the perturbations indeed remain small in the present case is demonstrated by the small relative changes in resonance frequency and quality factor in figure 5.4.

Firstly, using  $\omega_2 \approx \omega_1$  and  $Q_1, Q_2 \gg 1$ , the left-hand side of (5.15) can be approximated as

$$\frac{\Delta\tilde{\omega}}{\tilde{\omega}_2} \approx \frac{\Delta\omega}{\omega_1} + i \frac{1}{2} \Delta \left( \frac{1}{Q} \right). \quad (5.17)$$

Secondly, the perturbed microwave fields are approximated by the unperturbed fields,  $\mathbf{E}_2 \approx \mathbf{E}_1 = |\mathbf{E}_1|$  and  $\mathbf{H}_2 \approx \mathbf{H}_1 = i|\mathbf{H}_1|$ . Furthermore, the discharges discussed in this work are assumed to be unmagnetised,  $\Delta\tilde{\mu} = 0$ , resulting in

$$\frac{\Delta\omega}{\omega_1} + i \frac{1}{2} \Delta \left( \frac{1}{Q} \right) = - \frac{\iiint_{V_{\text{cav}}} \Delta\tilde{\varepsilon} |\mathbf{E}_1|^2 d^3\mathbf{r}}{\iiint_{V_{\text{cav}}} (\varepsilon_0 |\mathbf{E}_1|^2 + \mu_0 |\mathbf{H}_1|^2) d^3\mathbf{r}} = - \frac{\iiint_{V_{\text{cav}}} \Delta\tilde{\varepsilon} |\mathbf{E}_1|^2 d^3\mathbf{r}}{2\varepsilon_0 \iiint_{V_{\text{cav}}} |\mathbf{E}_1|^2 d^3\mathbf{r}}, \quad (5.18)$$

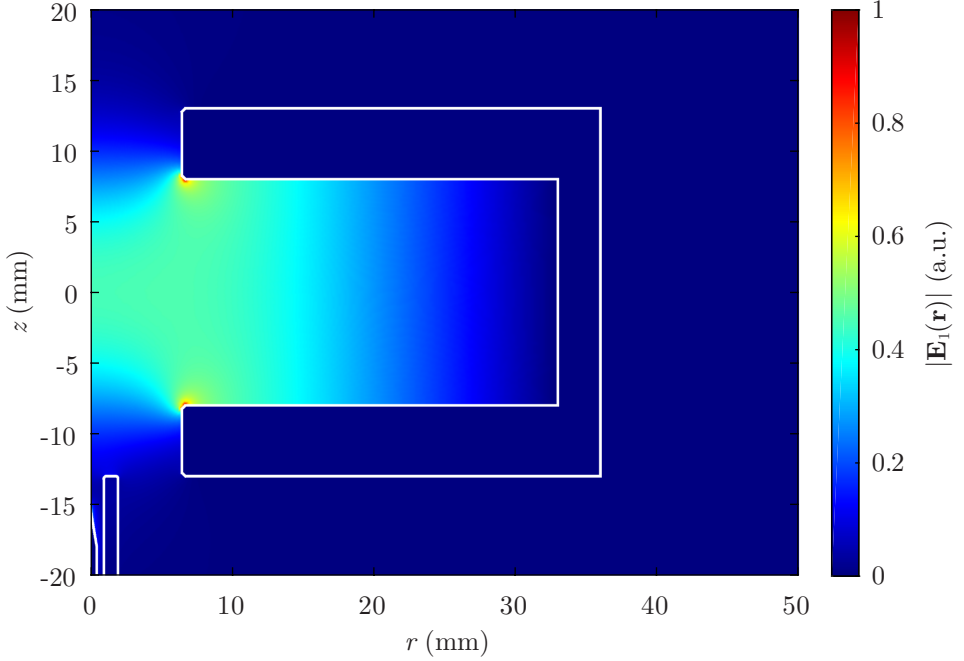


**Figure 5.5:** Electric field magnitude of the  $\text{TM}_{010}$  mode obtained from the model. Outlines of the cavity, the quartz tube and the needle are given by the white lines.

where in the last step  $\iiint \varepsilon |\mathbf{E}|^2 d^3\mathbf{r} = \iiint \mu |\mathbf{H}|^2 d^3\mathbf{r}$  for a cavity at resonance was used [96].

In order to use (5.18) to translate the measured relative frequency shift and reciprocal quality factor to properties of the plasma, two more things are required: the plasma permittivity, and the electric field of the  $\text{TM}_{010}$  mode of the cavity.

### Electric field distribution of the $\text{TM}_{010}$ mode

Since our cavity has two concentric holes on its symmetry axis, as well as a dielectric (the quartz tube) and a conductor (the needle electrode) in its vicinity, the field distribution will inevitably be different from the ideal case. Therefore, a model is used to numerically determine the electric field distribution  $\mathbf{E}_1(\mathbf{r})$  of the empty cavity. This is done using the frequency domain electromagnetic wave modelling tools in COMSOL. As the  $\text{TM}_{010}$  mode is cylindrically symmetric, a 2D axisymmetric model can be used. A resonance frequency of 3.51 GHz is obtained from the model, confirming the experimentally measured value in the setup. The corresponding electric field magnitude distribution is shown in figure 5.5. It can be seen that the electric field ‘leaks’ through the two holes and that amplification occurs at the inner corners of the two holes.

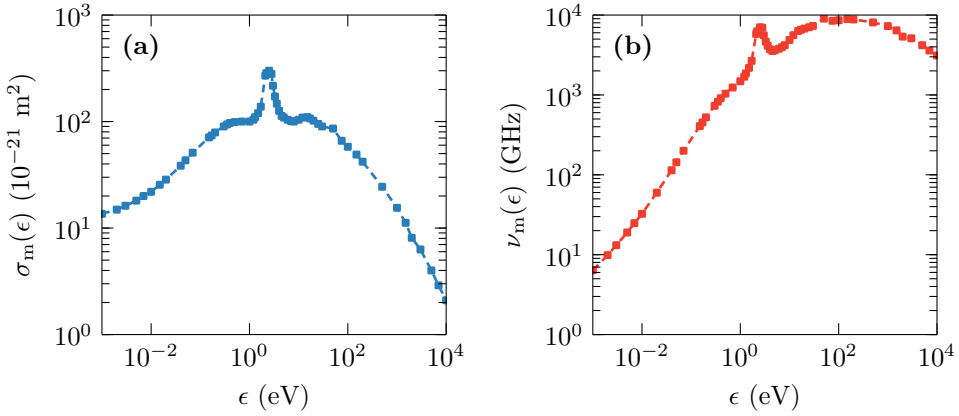


**Figure 5.6:** In (a) the momentum transfer cross section as a function of electron energy for N<sub>2</sub> [98] is given, and in (b) the corresponding collision frequencies are given for atmospheric pressure ( $N = 2.5 \times 10^{25} \text{ m}^{-3}$ ).

### Permittivity of a collisional plasma

The permittivity of a plasma subjected to a time-harmonic electric field at angular frequency  $\omega$  is given by [2]

$$\tilde{\epsilon}_2 = \epsilon_0 - i \frac{\tilde{\sigma}}{\omega}, \quad (5.19)$$

with  $\tilde{\sigma}$  the complex plasma conductivity. The plasma conductivity is commonly expressed as [2]

$$\tilde{\sigma} = \epsilon_0 \frac{\omega_{pe}^2}{\nu_m + i\omega}, \quad (5.20)$$

where  $\nu_m$  is the momentum transfer collision frequency of the electrons. However, (5.20) is only valid for a so-called Lorentz gas, in which the electron-neutral momentum transfer cross section  $\sigma_m$  is inversely proportional to the electron velocity  $v$ , i.e.  $\sigma_m \propto 1/v$  [83]. In that case, the collision frequency  $\nu_m = Nv\sigma_m$ , where  $N$  is the background gas number density, is independent of the electron velocity, and thereby independent of the electron energy  $\epsilon$ . The cross sections and collision frequencies for N<sub>2</sub> at atmospheric pressure are given in figure 5.6. Clearly, for N<sub>2</sub> the collision frequency is not independent of the electron energy.

A general equation for the complex conductivity of a plasma can be obtained from kinetic theory [99]:

$$\tilde{\sigma} = -\frac{2}{3} \epsilon_0 \omega_{pe}^2 \int_0^\infty \frac{\epsilon^{3/2}}{\nu_m(\epsilon) + i\omega} \frac{df}{d\epsilon} d\epsilon, \quad (5.21)$$

where  $f(\epsilon)$  is the electron energy distribution function (EEDF) with normalisation  $\int_0^\infty \sqrt{\epsilon} f(\epsilon) d\epsilon = 1$ . Comparing (5.20) and (5.21), it can be derived that an equation

of the form of (5.20) can still be used if the collision frequency  $\nu_m$  is replaced by an effective collision frequency  $\nu_{\text{eff}}$  defined as [100]

$$\nu_{\text{eff}} = \frac{\int_0^\infty \epsilon^{3/2} \frac{\nu_m(\epsilon)}{\nu_m^2(\epsilon) + \omega^2} \frac{df}{d\epsilon} d\epsilon}{\int_0^\infty \epsilon^{3/2} \frac{1}{\nu_m^2(\epsilon) + \omega^2} \frac{df}{d\epsilon} d\epsilon}. \quad (5.22)$$

Using this, the conductivity can be written as

$$\tilde{\sigma} = \epsilon_0 \frac{\omega_{\text{pe}}^2}{\nu_{\text{eff}} + i\omega} = \epsilon_0 \frac{\omega_{\text{pe}}^2}{\nu_{\text{eff}}^2 + \omega^2} (\nu_{\text{eff}} - i\omega). \quad (5.23)$$

Finally, substituting (5.23) in (5.19) gives the plasma permittivity

$$\tilde{\epsilon}_2 = \epsilon_0 \left[ 1 - \frac{\omega_{\text{pe}}^2}{(\nu_{\text{eff}}^2 + \omega^2)} - i \frac{\nu_{\text{eff}}}{\omega} \frac{\omega_{\text{pe}}^2}{(\nu_{\text{eff}}^2 + \omega^2)} \right]. \quad (5.24)$$

Using the plasma permittivity of (5.24) in (5.18), and separating the real and imaginary parts, leads to the following equations for the relative frequency shift and change in reciprocal quality factor [101]:

$$\frac{\Delta f}{f_1} = \frac{\Delta\omega}{\omega_1} = \frac{\iiint_{V_{\text{cav}}} \frac{\omega_{\text{pe}}^2}{(\omega_1^2 + \nu_{\text{eff}}^2)} |\mathbf{E}_1|^2 d^3\mathbf{r}}{2 \iiint_{V_{\text{cav}}} |\mathbf{E}_1|^2 d^3\mathbf{r}}, \quad (5.25)$$

and

$$\Delta \left( \frac{1}{Q} \right) = \frac{\iiint_{V_{\text{cav}}} \frac{\nu_{\text{eff}}}{\omega_1} \frac{\omega_{\text{pe}}^2}{(\omega_1^2 + \nu_{\text{eff}}^2)} |\mathbf{E}_1|^2 d^3\mathbf{r}}{\iiint_{V_{\text{cav}}} |\mathbf{E}_1|^2 d^3\mathbf{r}}. \quad (5.26)$$

### Obtaining $n_e$ and $\nu_{\text{eff}}$ from $\Delta f/f_1$ and $\Delta(1/Q)$

As mentioned, the plasma is approximated by a uniform cylindrical volume  $V_p = \pi r_p^2 l_p$  with electron density  $n_e$  and effective collision frequency  $\nu_{\text{eff}}$ . In this case, (5.25) and (5.26) can be simplified to

$$\frac{\Delta f}{f_1} = \frac{1}{2} \frac{\omega_{\text{pe}}^2}{(\omega_1^2 + \nu_{\text{eff}}^2)} \mathcal{V}, \quad (5.27)$$

and

$$\Delta \left( \frac{1}{Q} \right) = \frac{\nu_{\text{eff}}}{\omega_1} \frac{\omega_{\text{pe}}^2}{(\omega_1^2 + \nu_{\text{eff}}^2)} \mathcal{V}, \quad (5.28)$$

where  $\mathcal{V}$  is the ratio of the effective (field squared weighted) plasma volume and the effective (field squared weighted) cavity volume given by

$$\mathcal{V} = \frac{\iiint_{V_p} |\mathbf{E}_1|^2 d^3\mathbf{r}}{\iiint_{V_{\text{cav}}} |\mathbf{E}_1|^2 d^3\mathbf{r}}, \quad (5.29)$$

which is calculated using the field distribution from the numerical model. The volume integral in the numerator of (5.29) is taken only over the space that the plasma occupies. Furthermore, it should be noted that volume integral over  $V_{\text{cav}}$  in the denominator of (5.29) is not just the ‘inner volume’ enclosed by the cavity, but rather the entire space that the microwave fields permeate. For this reason, the volume integral over  $V_{\text{cav}}$  is taken over the entire domain of the model.

From (5.27) and (5.28), first the effective collision frequency is determined as

$$\nu_{\text{eff}} = \omega_1 \frac{1}{2} \frac{\Delta(1/Q)}{\Delta f/f_1} = \pi f_1 \frac{\Delta(1/Q)}{\Delta f/f_1}. \quad (5.30)$$

Interestingly,  $\nu_{\text{eff}}$  does not depend on  $\mathcal{V}$  and is therefore also independent of our estimation of  $V_p$ . With the effective collision frequency known, the electron density can be determined using (5.27) as

$$n_e = 2 \frac{\varepsilon_0 m_e}{e^2} \frac{\nu_{\text{eff}}^2 + \omega_1^2}{\mathcal{V}} \frac{\Delta f}{f_1} = 2 \frac{\varepsilon_0 m_e}{e^2} \frac{\nu_{\text{eff}}^2 + 4\pi^2 f_1^2}{\mathcal{V}} \frac{\Delta f}{f_1}, \quad (5.31)$$

where the definition of the plasma-electron frequency (5.16) was used. Equivalently, (5.28) could be used to determine the electron density, but the result would be the same. In contrast to the effective collision frequency, the electron density does depend on  $\mathcal{V}$  and the estimated plasma volume  $V_p$ . In the results section, a constant plasma radius  $r_p = 150 \mu\text{m}$  and length  $l_p = 10 \text{mm}$  are used, resulting in  $\mathcal{V} = 7.9 \times 10^{-6}$ . These dimensions are based on images of the optical emission recorded for discharges in the absence of the cavity (see chapter 2). However, errors in this estimation will directly translate to errors in the calculated electron density. The presence of the cavity, which acts as a ground for the plasma source, could potentially alter the discharge. Additionally, in reality convective and diffusive transport will change the electron density distribution in the time between discharges. To evaluate the sensitivity of the electron density to the estimated plasma volume,  $\mathcal{V}$  is also calculated for  $r_p = 100 \mu\text{m}$  and  $l_p = 7.5 \text{mm}$ , and for  $r_p = 200 \mu\text{m}$  and  $l_p = 12.5 \text{mm}$ . This results in  $\mathcal{V} = 1.7 \times 10^{-6}$  and  $\mathcal{V} = 2.1 \times 10^{-5}$ , respectively. This shows that the absolute values of the obtained electron densities will only be accurate up to their order of magnitude. Nevertheless, since the error introduced by the plasma volume is systematic, the temporal behaviour of the electron density is still captured by these measurements.

### 5.2.3 Global model

To compare results from the MCRS measurements to simulations, the discharges are modelled using a global model in PLASIMO [102]. In this model, the densities  $n_i$  of species  $i$  are calculated from

$$\frac{dn_i}{dt} = S_i, \quad (5.32)$$

where  $S_i$  is the net rate at which the species are produced (or destroyed) in their respective reactions. Since the discharges mostly take place in a stream of pure  $N_2$ , a pure  $N_2$  chemistry is used. The model includes 11 species and 34 reactions, which are listed in table 5.1. The rates of the electron impact reactions (R1-R6) are computed from the SIGLO database [103] using BOLSIG+ [104]. Additionally, the electron energy density is calculated from

$$\frac{d}{dt} \left( \frac{3}{2} n_e k_B T_e \right) = P_{\text{in}} + P_{\text{elastic}} + P_{\text{inelastic}}, \quad (5.33)$$

where  $k_B$  is the Boltzmann constant,  $T_e$  is the electron temperature (i.e. the temperature associated with the average electron energy),  $P_{\text{in}}$  is the input power density, and  $P_{\text{elastic}}$  and  $P_{\text{inelastic}}$  are the contributions to the electron energy density from elastic and inelastic collisions respectively. To avoid effects of the initial values for the species, the model is run until a periodic steady state is obtained.

The input power density of the experiment is not exactly known for our plasma source. For this reason, a power density resembling the applied voltage pulses is used, i.e. 500 ns wide pulses with linearly rising and falling edges of 40 ns. The peak power density of the pulses is varied between  $P_{\text{in}} = 10^{19} \text{ W/m}^3$  and  $P_{\text{in}} = 10^{11} \text{ W/m}^3$  to investigate the effects on the resulting electron density and temperature. These values correspond to an energy dissipation per discharge between approximately 1  $\mu\text{J}$  and 100  $\mu\text{J}$  for an estimated plasma volume of  $V_p \approx 10^{-9} \text{ m}^3$ . In figure 5.7,  $n_e$  and  $T_e$  are shown for each of the input power densities for an entire period at a repetition rate of 3 kHz.

For each of the tested input power densities, the electron temperature rapidly increases to about 3 eV at the start of the pulse. After the pulse it decays to less than 0.1 eV in several 100 ns for  $P_{\text{in}} = 10^9 \text{ W/m}^3$  and in about 3  $\mu\text{s}$  for  $P_{\text{in}} = 10^{11} \text{ W/m}^3$ . The peak electron density increases considerably for higher input power densities. Nevertheless, at larger time scales after the discharge, it is only weakly dependent on the input power density and the peak electron density. For these three input power densities, the electron densities differ by more than an order of magnitude only in the first several  $\mu\text{s}$  following the pulse and are within a factor of two from each other from about 10  $\mu\text{s}$  after the pulse. Nevertheless, the temporal resolution of the measurement is limited to about 1  $\mu\text{s}$ , and these differences cannot be resolved in the measurements. Therefore detailed knowledge on the exact input power density is also not essential in comparing electron densities obtained from the measurements and the model in this case.



**Table 5.1:** Reactions included in the global model. Units of the electron temperature  $T_e$  and effective ion temperatures  $T_{\text{eff},i}$  are K. The rates of the electron impact reactions (R1–R6) are computed from the SIGLO database [103] using BOLSIG+ [104].

No.	Reaction	Rate coefficient	Ref.
R1	$\text{N}_2 + e \rightarrow \text{N}_2 + e$	BOLSIG+	
R2	$\text{N}_2 + e \rightarrow \text{N}_2(\text{A}) + e$	BOLSIG+	
R3	$\text{N}_2 + e \rightarrow \text{N}_2(\text{B}) + e$	BOLSIG+	
R4	$\text{N}_2 + e \rightarrow \text{N}_2(\text{a}') + e$	BOLSIG+	
R5	$\text{N}_2 + e \rightarrow \text{N}_2(\text{C}) + e$	BOLSIG+	
R6	$\text{N}_2 + e \rightarrow \text{N}_2^+ + e + e$	BOLSIG+	
R7	$\text{N}_2(\text{A}) + \text{N}_2(\text{a}') \rightarrow \text{N}_4^+ + e$	$4 \times 10^{-18} \text{ m}^3 \text{ s}^{-1}$	[105]
R8	$\text{N}_2(\text{a}') + \text{N}_2(\text{a}') \rightarrow \text{N}_4^+ + e$	$1 \times 10^{-17} \text{ m}^3 \text{ s}^{-1}$	[105]
R9	$\text{N}^+ + e + \text{N}_2 \rightarrow \text{N} + \text{N}_2$	$6.0 \times 10^{-39} (300/T_e)^{1.5} \text{ m}^6 \text{ s}^{-1}$	[105]
R10	$\text{N}_2^+ + e \rightarrow \text{N} + \text{N}$	$1.8 \times 10^{-13} (300/T_e)^{0.39} \text{ m}^3 \text{ s}^{-1}$	[105]
R11	$\text{N}_3^+ + e \rightarrow \text{N} + \text{N}_2$	$2 \times 10^{-13} (300/T_e)^{0.5} \text{ m}^3 \text{ s}^{-1}$	[105]
R12	$\text{N}_4^+ + e \rightarrow \text{N}_2 + \text{N}_2$	$2.3 \times 10^{-12} (300/T_e)^{0.53} \text{ m}^3 \text{ s}^{-1}$	[105]
R13	$\text{N}^+ + \text{N} + \text{N}_2 \rightarrow \text{N}_2^+ + \text{N}_2$	$1 \times 10^{-41} \text{ m}^6 \text{ s}^{-1}$	[105]
R14	$\text{N}^+ + \text{N}_2 + \text{N}_2 \rightarrow \text{N}_3^+ + \text{N}_2$	$1.7 \times 10^{-41} (300/T_{\text{eff},\text{N}^+})^{2.1} \text{ m}^6 \text{ s}^{-1}$	[105]
R15	$\text{N}_2^+ + \text{N} \rightarrow \text{N}^+ + \text{N}_2$	$7.2 \times 10^{-19} (T_{\text{eff},\text{N}_2^+}/300) \text{ m}^3 \text{ s}^{-1}$	[105]
R16	$\text{N}_2^+ + \text{N}_2 + \text{N} \rightarrow \text{N}_3^+ + \text{N}$	$9 \times 10^{-42} \exp(400/T_{\text{eff},\text{N}_2^+}) \text{ m}^6 \text{ s}^{-1}$	[105]
R17	$\text{N}_2^+ + \text{N}_2 + \text{N}_2 \rightarrow \text{N}_4^+ + \text{N}_2$	$5.2 \times 10^{-41} (300/T_{\text{eff},\text{N}_2^+})^{2.2} \text{ m}^6 \text{ s}^{-1}$	[105]
R18	$\text{N}_3^+ + \text{N} \rightarrow \text{N}_2^+ + \text{N}_2$	$6.6 \times 10^{-17} \text{ m}^3 \text{ s}^{-1}$	[105]
R19	$\text{N}_4^+ + \text{N} \rightarrow \text{N}^+ + \text{N}_2 + \text{N}_2$	$1 \times 10^{-17} \text{ m}^3 \text{ s}^{-1}$	[105]
R20	$\text{N}_4^+ + \text{N}_2 \rightarrow \text{N}_2^+ + \text{N}_2 + \text{N}_2$	$2.1 \times 10^{-22} \exp(T_{\text{eff},\text{N}_4^+}/121) \text{ m}^6 \text{ s}^{-1}$	[105]
R21	$\text{N}_2(\text{A}) \rightarrow \text{N}_2 + h\nu$	$5.0 \times 10^{-1} \text{ s}^{-1}$	[105]
R22	$\text{N}_2(\text{B}) \rightarrow \text{N}_2(\text{A}) + h\nu$	$1.34 \times 10^5 \text{ s}^{-1}$	[105]
R23	$\text{N}_2(\text{a}') \rightarrow \text{N}_2 + h\nu$	$1 \times 10^2 \text{ s}^{-1}$	[105]
R24	$\text{N}_2(\text{C}) \rightarrow \text{N}_2(\text{B}) + h\nu$	$2.45 \times 10^7 \text{ s}^{-1}$	[105]
R25	$\text{N}_2(\text{A}) + \text{N} \rightarrow \text{N}_2 + \text{N}$	$2 \times 10^{-18} \text{ m}^3 \text{ s}^{-1}$	[105]
R26	$\text{N}_2(\text{A}) + \text{N}_2 \rightarrow \text{N}_2 + \text{N}_2$	$3 \times 10^{-22} \text{ m}^3 \text{ s}^{-1}$	[105]
R27	$\text{N}_2(\text{A}) + \text{N}_2(\text{A}) \rightarrow \text{N}_2(\text{B}) + \text{N}_2$	$3 \times 10^{-16} \text{ m}^3 \text{ s}^{-1}$	[105]
R28	$\text{N}_2(\text{A}) + \text{N}_2(\text{A}) \rightarrow \text{N}_2(\text{C}) + \text{N}_2$	$1.5 \times 10^{-16} \text{ m}^3 \text{ s}^{-1}$	[105]
R29	$\text{N}_2(\text{B}) + \text{N}_2 \rightarrow \text{N}_2 + \text{N}_2$	$2 \times 10^{-18} \text{ m}^3 \text{ s}^{-1}$	[105]
R30	$\text{N}_2(\text{B}) + \text{N}_2 \rightarrow \text{N}_2(\text{A}) + \text{N}_2$	$3 \times 10^{-17} \text{ m}^3 \text{ s}^{-1}$	[105]
R31	$\text{N}_2(\text{a}') + \text{N}_2 \rightarrow \text{N}_2(\text{B}) + \text{N}_2$	$1.9 \times 10^{-19} \text{ m}^3 \text{ s}^{-1}$	[105]
R32	$\text{N}_2(\text{C}) + \text{N}_2 \rightarrow \text{N}_2(\text{a}') + \text{N}_2$	$1 \times 10^{-17} \text{ m}^3 \text{ s}^{-1}$	[105]
R33	$\text{N} + \text{N} + \text{N}_2 \rightarrow \text{N}_2(\text{A}) + \text{N}_2$	$1.7 \times 10^{-45} \text{ m}^6 \text{ s}^{-1}$	[105]
R34	$\text{N} + \text{N} + \text{N}_2 \rightarrow \text{N}_2(\text{B}) + \text{N}_2$	$2.4 \times 10^{-45} \text{ m}^6 \text{ s}^{-1}$	[105]

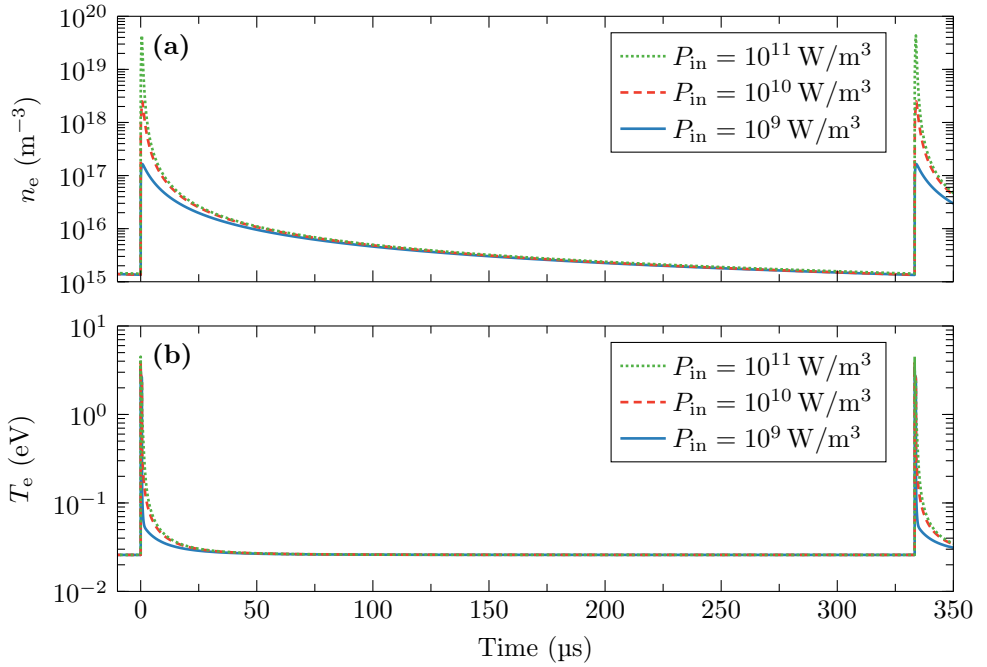


**Figure 5.7:** Temporal evolution in the global model of (a) the electron density, and (b) the electron temperature between successive discharges at 3 kHz for different input power densities.

### 5.3 Results and discussion

Electron densities and effective collision frequencies are measured for various applied voltages and repetition frequencies. Figure 5.8 shows the results for different voltages at a fixed repetition frequency of 3 kHz, and figure 5.9 shows the results for different repetition frequencies at a fixed voltage of 6 kV. As mentioned before, when the HV pulse switches on and off there is interference in the measurement signal. The affected parts of the signals were removed from the graphs.

For each of the applied voltages in figure 5.8a, a similar decay rate of the electron density can be observed. However, the absolute values increase for higher voltages. The maximum value that is measured, at about 1  $\mu\text{s}$  after the discharge, increases from about  $4 \times 10^{17} \text{ m}^{-3}$  for 4 kV to  $1 \times 10^{19} \text{ m}^{-3}$  for 8 kV. These values are in the same range as those found in the global model, as shown in figure 5.7a. Briefly after the discharge, the difference in electron density for the different applied voltages could be the result of the input power density, as shown by the model. Nevertheless, the global model also shows that the decay curves should converge to each other, within a factor of two after approximately 10  $\mu\text{s}$ . Despite its lower signal-to-noise ratio, it can be seen that the curve measured for 4 kV remains significantly below the others. This strongly indicates that the low electron densities found for 4 kV are for a large part the result of an overestimation of the plasma volume, and hence  $\mathcal{V}$ , for this voltage. In chapter 2, it was in fact already found that the streamer length increases for higher voltages until a plateau is reached (see figure 2.11a). Looking at the electric field distribution in figure 5.5, it can be seen that shorter guided streamers will also not reach the regions where the electric field in the cavity is high. As the calculations for  $\mathcal{V}$  in the previous section already indicated, this could easily result in an order of magnitude error in absolute values. These two things likely explain the large (apparent) increase in electron density from 4 kV to 5 kV.

The temporal evolution of the effective collision frequency is shown in figure 5.8b for each of the voltages. In each case, the effective collision frequency decays to a constant value of about 80 GHz. This value corresponds to the room temperature value  $\nu_{\text{eff}}(300 \text{ K}) = 76 \text{ GHz}$ , which can be calculated from (5.22) using the data from figure 5.6b and assuming a Maxwell-Boltzmann EEDF. The decay of the effective collision frequency occurs on a time scale of several  $\mu\text{s}$ , which is significantly shorter than the time scale of the electron density decay. The decay of the effective collision frequency is related to the decrease in electron temperature, although a direct comparison between the two would require knowledge on the EEDF. Nevertheless, the global model also predicts that the electron temperature decays much faster than the electron density. A similar result to this was reported for a pulsed plasma jet in He [80].

In figure 5.8b, it can be seen that the electron density and effective collision frequency do not depend on the repetition frequency. Although, there could still be differences in peak values that occur on a time scale shorter than 1  $\mu\text{s}$ . To test this, the global model is run again, but this time for different repetition frequencies. The results are shown in figure 5.10, where it can be seen that the behaviour of the electron density is indeed similar at different repetition frequencies. Nevertheless, 2 kHz is the lowest repetition frequency at which guided streamers can be maintained, and hence

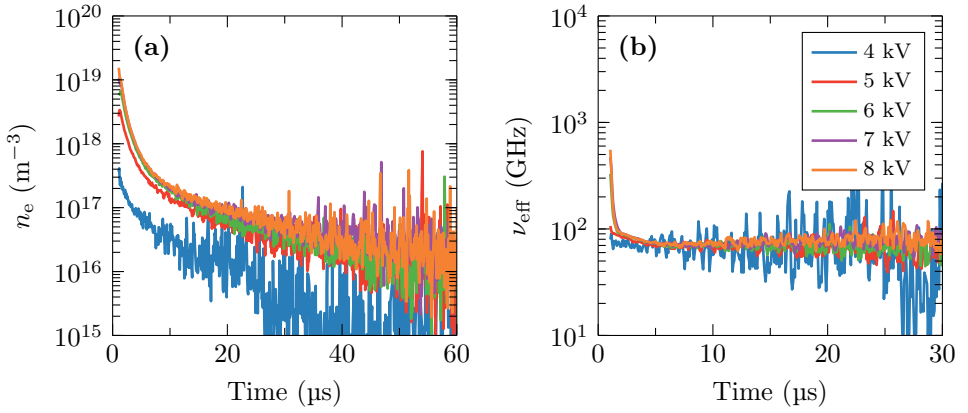


**Figure 5.8:** Measured (a) electron density, and (b) effective collision frequency, for different applied voltages at the fixed repetition frequency of 3 kHz.

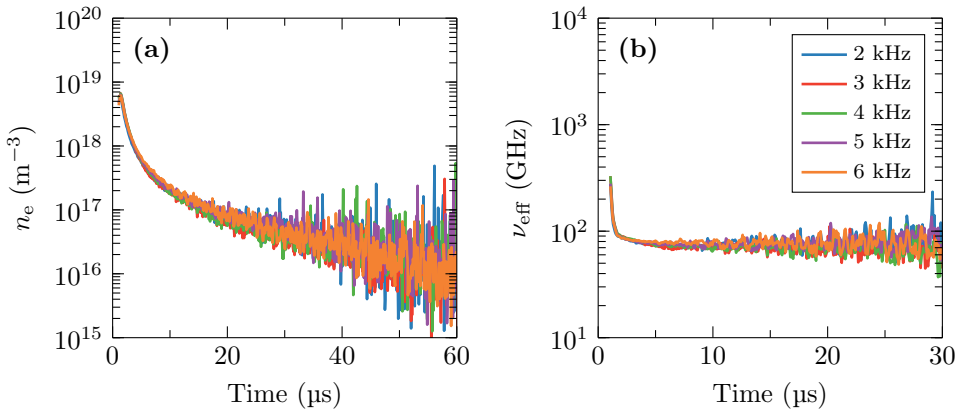


**Figure 5.9:** Measured (a) electron density, and (b) effective collision frequency, for different repetition frequencies at the fixed applied voltage of 6 kV.

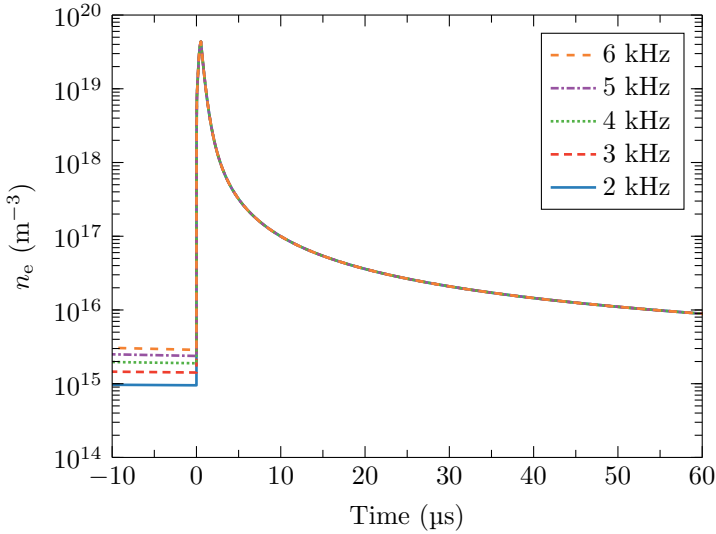


**Figure 5.10:** Electron densities for different repetition frequencies obtained from the global model. A pulsed input power density of  $10^{11} \text{ W/m}^3$  is used.

the lowest frequency where there is a memory effect that is responsible for reproducible discharges. For lower frequencies, the electron density becomes too low in the time between successive discharges. So, the electron density right before the discharges at 2 kHz constitutes the minimum required seed electron density for guided streamers in  $\text{N}_2$ . From figure 5.10 it can be seen that this is about  $10^{15} \text{ m}^{-3}$ . The same order of magnitude for the minimum required seed electron density is reported for a pulsed plasma jet in pure He [9, 31].

Finally, to directly compare the decay rate of the electron density between the measurements and the model, the measured electron densities for an applied voltage of 6 kV and repetition frequency of 3 kHz are shown together with two electron density curves from the model corresponding to the two highest input power densities in figure 5.11. In fact, the measurements and the model show a good qualitative agreement. After about 10  $\mu\text{s}$ , when the effects of the initial peak electron density are gone, the three curves are approximately parallel, indicating the same decay rate. It should be noted however that in both the analysis of measurements and in the global model transport of electrons is neglected. As a result, the decay might be somewhat faster in reality.

## 5.4 Conclusions and outlook

In this work, MCRCs is applied to guided streamers generated in a pulsed plasma jet in  $\text{N}_2$ . It is shown that electron densities, as well as effective collision frequencies, can be measured using this technique from about 1  $\mu\text{s}$  up to approximately 60  $\mu\text{s}$  after

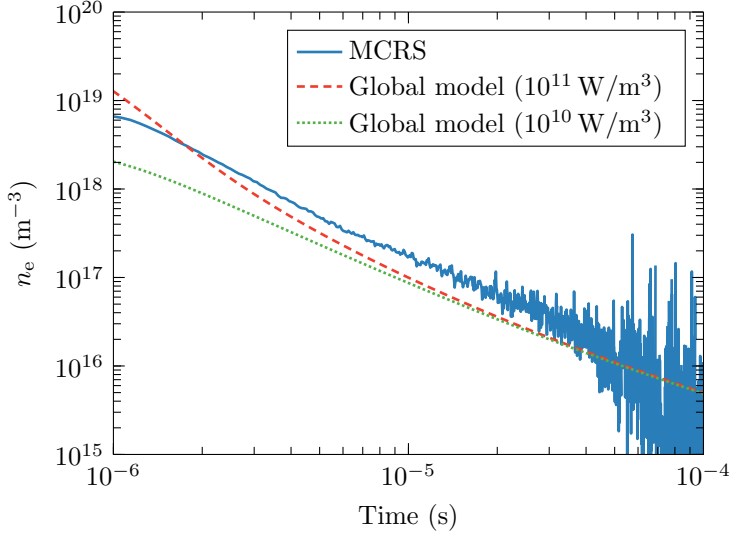


**Figure 5.11:** Comparison between electron density from the MCRS experiment at 6 kV and 3 kHz, and the global model with input power densities of  $10^{10} \text{ W/m}^3$  and  $10^{11} \text{ W/m}^3$ .

the discharge, where the former is limited by the response time of the cavity and the latter by the detection limit of about  $10^{16} \text{ m}^{-3}$ . However, the assumptions on the spatial distribution of the electron density, which are required in the analysis of the measurements, limit the absolute accuracy of the electron density to about an order of magnitude. Despite the large uncertainty in the absolute values, the measured electron densities are in the same range as those predicted by a global model. There is also a good qualitative agreement in the decay rate between the measurements and the model. Although it should be noted that transport remains unaccounted for in both. Furthermore, from the model it is evaluated that the minimum seed electron density required for reproducible guided streamers in  $\text{N}_2$  is of the order of  $10^{15} \text{ m}^{-3}$ , which is similar to what is reported for pulsed plasma jets in He [9]. In addition to the electron density, the MCRS analysis provides information on the effective collision frequency of the electrons. It is found that the effective collision frequency drops to its room temperature value several  $\mu\text{s}$  after the discharge, which corresponds to the rapid decrease in electron temperature that is observed in the model.

While these results demonstrate that MCRS provides a useful electron density diagnostic for pulsed plasma jets in  $\text{N}_2$ , the following improvements have to be made to obtain more accurate quantitative electron densities. Firstly, the detection limit of around  $10^{16} \text{ m}^{-3}$  is still an order of magnitude too high to completely measure the evolution of the electron density between consecutive discharges. Potentially, using a higher quality factor cavity, and hence narrower resonance peaks, could improve the detection limit. However, this would be at the cost of temporal resolution. Another option is to increase the number of samples that are averaged. This would increase the

measurement time, and it might be necessary to monitor and account for fluctuations in the lab environments in this case. Secondly, and more importantly, the accuracy in absolute electron densities has to be increased. Currently, the major source of uncertainty in the measurements originates from the estimation of the plasma volume. To start, it would be useful to use a cavity with optical access to observe the discharge, which could, for example, be achieved by making a slit in the curved part of the cavity wall or by replacing it with a metal mesh. This way the emission of the discharge can be observed from a side-view using an ICCD camera and the effects of the presence of the cavity on the discharge can be assessed. This would help in estimating the initial plasma volume during the discharge. Furthermore, the plasma volume was assumed to be constant in this work. However, transport of the electrons in the time between discharges will change the electron density distribution. To obtain accurate electron density values, this should also be accounted for, both in the analysis and in the model. One way to do this would be to develop a spatial model of the complete system, including the microwave cavity and the pulsed discharges. Alternatively, the recently introduced multi-mode MCRS method could be used [92]. With this technique, the spatial electron density distribution can actually be reconstructed from measurements of multiple cavity modes. Therefore, applying multi-mode MCRS would avoid the need for assumptions of the electron density distribution.

## Chapter 6

---

# Electric field measurements on plasma bullets in N<sub>2</sub> using four-wave mixing

---

This chapter is based on:

M van der Schans, P Böhm, J Teunissen, S Nijdam, W IJzerman and U Czarnetzki “Electric field measurements on plasma bullets in N<sub>2</sub> using four-wave mixing” (2017) *Plasma Sources Science and Technology* **26** 115006



## 6.1 Introduction

Atmospheric pressure plasma jets have been a topic of high interest in the past few decades for their numerous potential applications in materials processing and biomedicine [10, 24, 106]. By now, a wide variety of designs for plasma jet devices utilising different electrode geometries, feed gas (mixtures) and driving voltages and frequencies exists. As first noted by Teschke *et al* [5] and Lu and Laroussi [6], when AC or pulsed DC voltages in the kHz-range are used, so-called plasma bullets are typically observed in short exposure images of the discharge. These plasma bullets are highly periodic and repeatable guided streamer discharges that all propagate along the same trajectory. The repeatable behaviour of plasma bullets is the result of a memory effect due to remnants of previous discharges [7–9]. More on the reproducibility of these discharges and the memory effect can be found in chapter 2 and chapter 3.

Numerous experimental and numerical investigations have been performed on plasma jets and plasma bullets [8]. In the large majority of these studies a noble gas (He, Ar, Ne or Kr) or a noble gas mixture is used as feed gas, sometimes with small admixtures of molecular species (N<sub>2</sub>, O<sub>2</sub> or H<sub>2</sub>O). Pure molecular gases or mixtures can also be used, but there are only a few studies on plasma jets with N<sub>2</sub> or air as feed gas [10]. Nevertheless, plasma bullets have been observed even with air as feed gas [107].

Knowledge of the spatial and temporal distribution of the electric field is essential for both theory and applications, as the electric field drives the discharge and is related to rate coefficients of plasma processes. Still, direct electric field measurements on transient atmospheric pressure discharges have remained challenging. Several recent electric field strength measurements based on the Stark effect in H<sub>2</sub> and/or He containing discharges [108–114] and line intensity ratios in He [115] or N<sub>2</sub> [116, 117] containing discharges have led to new insights. However, these emission-based methods are limited to the place where and the moment when photons are emitted, and they cannot probe the electric field in regions outside the discharge. Another approach is to use the Pockels effect: remote electric field measurements on a plasma jet have been demonstrated using an electro-optic probe [118–120]. In addition, the deposited surface charge and the electric field of plasma bullets impinging on a birefringent target have been investigated [63, 121–123]. While such measurements are highly relevant for applications where a target surface is present and the delivered electric field could play an important role, such as in plasma medicine [15], having a target surface present is invasive to the discharge itself.

In this work, the electric field of plasma bullets in N<sub>2</sub> at atmospheric pressure is investigated by electric field four-wave mixing. This nonlinear laser technique based on coherent Raman scattering (CRS) can be used to determine the strength of an electric field as well as its direction. The principle of this technique was first mentioned by Gavrilenko *et al* [124]. Basically, two collinear laser beams are used to produce coherent anti-Stokes Raman scattering (CARS) radiation, while simultaneously generating coherent infrared (IR) radiation on a dipole-forbidden molecular Raman transition in the presence of an external electric field. Both processes are examples of four-wave mixing, and the intensity ratio of the resulting CARS and IR radiation

is directly related to the electric field. Up to now, this method has primarily been used for electric field measurement in discharges containing  $\text{H}_2$  [125–134], because of its large Raman cross section. However, it has been shown that  $\text{N}_2$  can also be used as probe molecule instead [135–140]. It should be noted that recently another four-wave mixing method, based on field-induced second harmonic generation (SHG) instead of CRS, was introduced [141, 142]. Since this variation of four-wave mixing is non-resonant and does not depend on any specific Raman transition, it opens the way to electric field measurements in a wider variety of gases, including atomic ones [141].

When applying electric field four-wave mixing to plasma bullets, a few things need to be considered. Like streamer discharges, plasma bullets are expected to have highly non-uniform electric fields. Because the two laser beams in the experiment are collinear, the IR radiation is produced along some length of the laser path where the electric field of the plasma bullet is not constant. This means that the result of the measurement is actually the line-integrated electric field. To obtain spatially resolved electric field values, the four-wave mixing technique has to be extended with an inversion method. In this work, it is shown for the first time that this is feasible. Furthermore, a calibration measurement in a known electric field is required to obtain absolute values from the measurements. The calibration is normally performed by applying a voltage that is below the breakdown value to the discharge electrodes and subsequently measuring the generated CARS and IR beams. However, this is impossible in the present case. The reason is that the plasma bullets propagate into an open atmosphere rather than between two electrodes and as a result the background electric field is too low to calibrate when the applied voltage remains below the breakdown voltage. Therefore, a new calibration procedure using an electrode geometry different from the discharge geometry is also demonstrated. The obtained results are compared to the electric field profiles acquired from a streamer simulation adapted to the conditions of the plasma bullets.

## 6.2 Experimental setup and methods

### 6.2.1 Discharge setup

In figure 6.1 the discharge setup is illustrated. Plasma bullets are generated by applying pulsed DC voltages to a needle electrode. The casing of the device that houses the needle electrode is made of polycarbonate and has an inlet for the feed gas on top. In this work  $\text{N}_2$  (99.999% purity) at a volumetric flow rate of 1 slm (standard litre per minute) is used as feed gas. The feed gas subsequently flows into open air through the nozzle, which is a quartz tube of 1 mm inner radius and 2 mm outer radius. The needle electrode, which is placed concentrically inside the quartz tube, is made of tungsten, has a radius of 0.5 mm and its tip has an angle of approximately  $20^\circ$ . The tip of the needle is located 2 mm from the end of the quartz tube. The back of the casing has a high voltage (HV) connector that connects a pulsed power supply to the needle electrode through a brass screw terminal. An additional screw is placed in contact with the screw terminal and is connected to a HV probe (Tektronix P6015A) to monitor the applied voltage. As a grounded electrode is not specified in the setup,

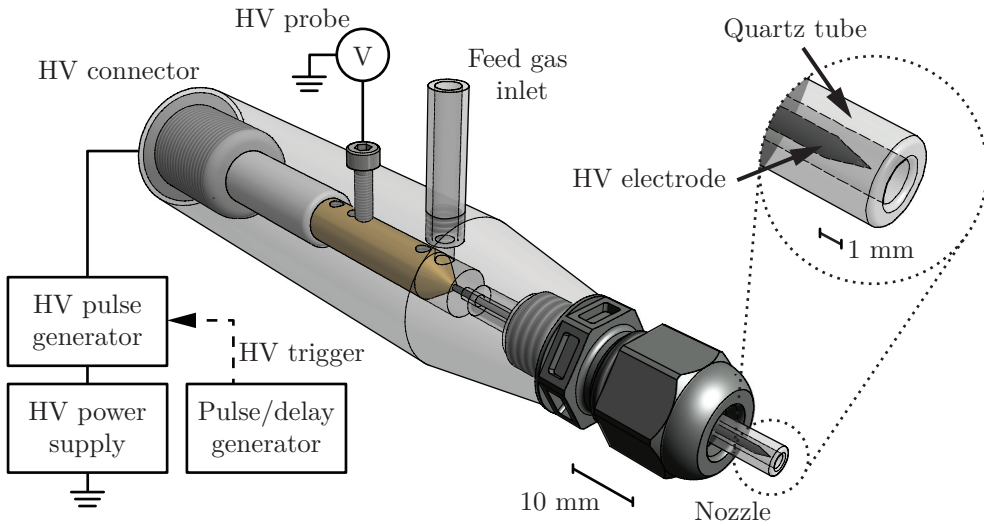


**Figure 6.1:** Illustration of the discharge setup including a magnified view of the nozzle and electrode geometry.

the discharge geometry is that of a single electrode plasma jet [10, 24]. A previous version of this plasma source was also used in the research of Hofmann *et al* [7, 25] where plasma bullets in helium and argon were investigated.

To generate HV pulses, the output of a DC HV power supply (Spellman UHR10P60) is gated by a HV pulse generator (DEI PVX-4110). The trigger/gate signal for the HV pulse generator is provided by a pulse/delay generator (Stanford Research Systems DG535), which will also be used to synchronise the discharge to the laser system used for the electric field measurement. For experiments presented in this work a voltage amplitude of 8 kV, a repetition frequency of 3 kHz, and a pulse width of 500 ns are chosen. With this setup, voltage rise and fall times of about 40 ns are achieved.

Figure 6.2 shows a series of images illustrating the propagation of the resulting plasma bullets. Images of the optical emission are recorded using an ICCD camera (Stanford Computer Optics 4 Picos) at several intervals after the inception of the discharge. The discharge closely resembles a traditional streamer discharge in N<sub>2</sub>, with the maximum emission intensity on the discharge axis. It should be remarked that this is different from the more commonly studied plasma bullets in pure He, where interaction between the discharge and the dielectric tube is often important and typically ring-shaped discharge structures are observed in the emission [8, 27]. From the images, the average propagation speed of the bullets is determined to be around  $10^5$  m/s.

### 6.2.2 Electric field four-wave mixing

In the electric field four-wave mixing technique [143, 144] two laser beams are used, a pump laser beam and a Stokes laser beam. The wavelengths of the lasers are

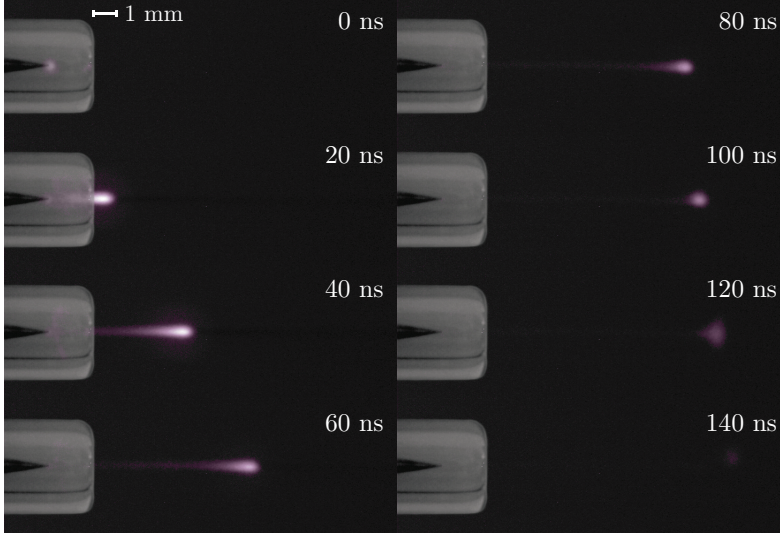


**Figure 6.2:** Composed images illustrating the propagation of the plasma bullets. For each of the images, 500 exposures are collected with a gate time of 1 ns. The background of the image showing the nozzle as well as the colours were added in post-processing for illustrational purposes.

chosen such that the difference between the pump beam frequency  $\omega_1$  and the Stokes beam frequency  $\omega_2$  matches a dipole-forbidden vibrational Raman transition of the probe molecule. In this case, the transition is the Q-branch of  $N_2$  in the electronic ground state, which corresponds to a wavenumber of  $2331 \text{ cm}^{-1}$  or a wavelength of  $4.3 \mu\text{m}$  [135]. At sufficiently high laser intensities this will lead to two third-order nonlinear optical interactions between the lasers and the present  $N_2$  molecules. Firstly, coherent anti-Stokes Raman scattering (CARS) will occur. In this interaction, photons with a frequency  $\omega_{\text{CARS}} = 2\omega_1 - \omega_2$  that is anti-Stokes shifted from the pump frequency  $\omega_1$  are generated coherently in a laser-like beam. When an external electric field  $\mathbf{E}$  is present a second four-wave mixing process, similar to CARS, will occur simultaneously. In this process, IR photons with frequency  $\omega_{\text{IR}} = \omega_1 - \omega_2$  are coherently generated on the Raman transition in a laser-like beam. Energy diagrams for both CARS and coherent IR generation are shown in figure 6.3, where  $|g\rangle$  and  $|e\rangle$  indicate the ground state and vibrationally excited state respectively. It should be noted that both processes are single parametric events and hence do not result in population of the excited state.

From non-linear optics, the following equations can be derived for the amplitudes  $A_{\text{CARS}}$  and  $A_{\text{IR}}$  of the CARS and IR signals in the plane-wave approximation [145]:

$$\frac{d}{dx} A_{\text{CARS}} \propto \chi^{(3)}(\omega_{\text{CARS}}) A_1^2 A_2^* \exp(-i\Delta kx), \quad (6.1)$$

$$\frac{d}{dx} A_{\text{IR}} \propto \chi^{(3)}(\omega_{\text{IR}}) A_1 A_2^* E \exp(-i\Delta k'x), \quad (6.2)$$

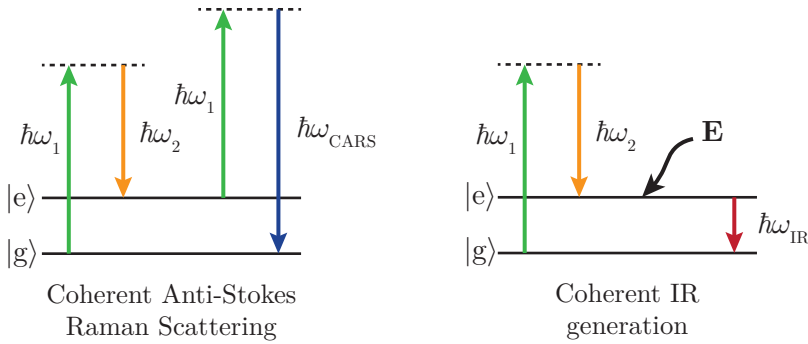


**Figure 6.3:** Energy diagrams for the two four-wave mixing processes. The dashed lines indicate virtual levels.

where  $\chi^{(3)}(\omega)$  is the third-order nonlinear susceptibility corresponding to the interaction,  $A_1$  and  $A_2$  are the amplitudes of the incident pump and Stokes beams, and  $\Delta k = k_{\text{CARS}} - 2k_1 + k_2$  and  $\Delta k' = k_{\text{IR}} - k_1 + k_2$  are wavevector mismatches. The fields are generated most efficiently under perfect phase matching conditions,  $\Delta k = \Delta k' = 0$ . In a conventional CARS experiment, phase matching can be achieved with crossed laser beams, which is called the BOXCARS configuration [144]. Local measurements with high spatial resolution can be achieved this way because the CARS beam is only generated in the small region where the laser beams cross. However, for the coherent IR generation process, phase matching is only achieved when the pump and Stokes beams are collinear, and therefore a collinear laser beam configuration has to be used.

The wavevector mismatch in this configuration can be estimated as

$$\Delta k' = (n_{\text{IR}}\omega_{\text{IR}} - n_1\omega_1 + n_2\omega_2)/c \approx -0.2 \text{ cm}^{-1}, \quad (6.3)$$

where  $n$  is the refractive index at each of the frequencies and  $c$  is the vacuum speed of light. This corresponds to a coherence length of the process,  $L_{\text{IR}}^{\text{coh}} = \pi/|\Delta k'|$ , of the order of 10 cm. The spatial extent of the studied electric fields in the direction of the laser beams will typically only be around a centimetre and shorter. Hence the maximum phase mismatch is only about  $|\Delta k'x| = 0.2$ . Since  $0.2 < \pi$ , this indicates that each part of the electric field distribution will contribute constructively to  $A_{\text{IR}}$ . (Note that this is equivalent to stating that the spatial extent of the electric field is shorter than  $L_{\text{IR}}^{\text{coh}}$ ). Furthermore, the factor by which the final IR amplitude is multiplied due to the mismatch, compared to the perfectly phase-matched case, can be estimated by  $\text{sinc}(\Delta k'x/2)$  [145], which results in 0.998. So the impact of the mismatch can be expected to be less than 1% in this case, and it is therefore neglected.

With both incident laser beams propagating along the  $x$ -axis and neglecting the phase matching exponents, (6.1) and (6.2) are now integrated, which results in

$$A_{\text{CARS}} \propto \chi^{(3)}(\omega_{\text{CARS}})A_1^2 A_2^* L_{\text{CARS}}, \quad (6.4)$$

$$A_{\text{IR}} \propto \chi^{(3)}(\omega_{\text{IR}})A_1 A_2^* \int_{-\frac{1}{2}L_{\text{IR}}}^{\frac{1}{2}L_{\text{IR}}} E \, dx, \quad (6.5)$$

where  $L_{\text{CARS}}$  and  $L_{\text{IR}}$  are the ‘interaction lengths’, the regions along the laser beams that can contribute to the generated signals. In practice focused laser beams are used, and the interaction length is typically multiple Rayleigh lengths around the focus spot (which is here chosen at  $x = 0$ ) [146]. In fact, in a recent study by Simeni *et al.*, the response of the IR beam was measured as a function of distance from the focus spot. It showed that regions more than 10 cm from the focus spot can still generate an IR signal [138]. However, in the present case, the electric field to be measured should ideally be contained in a region well within the Rayleigh range from each side of the focus point. In this way, the only contribution to the IR beam comes from the part of the interaction length where the plane-wave approximation holds, and hence 6.5 is valid. This fact is actually also reflected in the measured IR response in [138]: while the IR beam can still be generated at locations more than 10 cm away from the focus spot, the response is flat in a range of only several centimetres around the focus spot. Additionally, in more extended electric field distributions the phase matching that was neglected in (6.5) should also be considered.

Now the intensities,  $I \propto AA^*$ , of the CARS and IR beams are given by

$$I_{\text{CARS}} \propto |\chi^{(3)}(\omega_{\text{CARS}})|^2 I_1^2 I_2 L_{\text{CARS}}^2, \quad (6.6)$$

$$I_{\text{IR}} \propto |\chi^{(3)}(\omega_{\text{IR}})|^2 I_1 I_2 \left( \int_{-\frac{1}{2}L_{\text{IR}}}^{\frac{1}{2}L_{\text{IR}}} E \, dx \right)^2, \quad (6.7)$$

where  $I_1$  and  $I_2$  are the intensities of the incident pump and Stokes laser beams respectively. Finally, (6.6) and (6.7) can be combined to obtain

$$\left| \int_{-\frac{1}{2}L_{\text{IR}}}^{\frac{1}{2}L_{\text{IR}}} E \, dx \right| = C_{\text{cal}} \sqrt{I_1 \frac{I_{\text{IR}}}{I_{\text{CARS}}}}, \quad (6.8)$$

where  $C_{\text{cal}}$  is a constant that can be determined from a calibration measurement in a known electric field. In the case of a constant electric field, (6.8) can be reduced to  $|E| = C_{\text{cal}} \sqrt{I_1 I_{\text{IR}} I_{\text{CARS}}^{-1}}$  (here  $L_{\text{IR}}$  is absorbed into  $C_{\text{cal}}$ ). This is the form that is used in [125–138]. It should be realised however that the result is an average value of the field strength when this equation is used in a non-uniform electric field.

Up to now, it has been implicitly assumed, through the scalar nature of (6.2), that the polarisation direction of the lasers and the direction of the electric field are all parallel to each other. This is however not necessary and actually the direction of the electric field, apart from its sign, can be determined by considering the polarisation of the IR beam. When the lasers are polarised parallel to each other, say in the  $z$ -direction, it can be shown that [143]

$$I_{\text{IR}}^{(z)} \propto |\chi_{zzzz}^{(3)}(\omega_{\text{IR}})|^2 I_1 I_2 \left( \int_{-\frac{1}{2}L_{\text{IR}}}^{\frac{1}{2}L_{\text{IR}}} E_z \, dx \right)^2, \quad (6.9)$$

$$I_{\text{IR}}^{(y)} \propto |\chi_{yyzz}^{(3)}(\omega_{\text{IR}})|^2 I_1 I_2 \left( \int_{-\frac{1}{2}L_{\text{IR}}}^{\frac{1}{2}L_{\text{IR}}} E_y \, dx \right)^2, \quad (6.10)$$

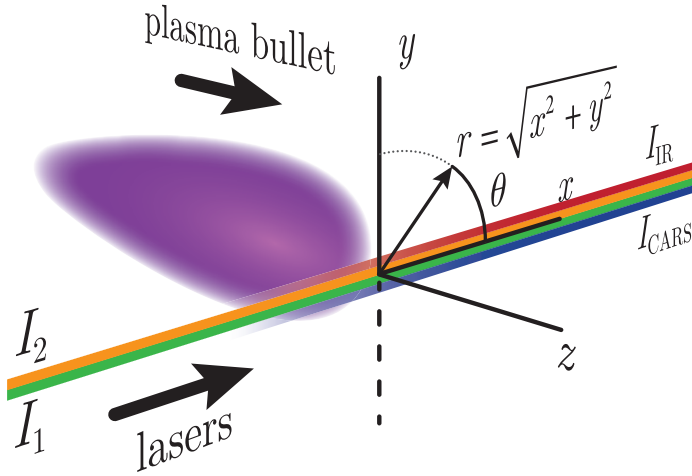


**Figure 6.4:** Illustration of the generated CARS and coherent IR beams in the electric field in front of the plasma bullet.

where the superscript on  $I_{\text{IR}}$  indicates which polarisation component of the IR beam is measured. The subscripts on the corresponding elements of the susceptibility tensor indicate from left to right the polarisation (component) of the IR beam, the electric field, the pump beam and the Stokes beam. Thus, by measuring the IR intensity polarisation-resolved, parallel and perpendicular to the laser polarisation, two orthogonal components of the electric field can be determined separately. Combining (6.9) and (6.10) with (6.6) gives

$$\left| \int_{-\frac{1}{2}L_{\text{IR}}}^{\frac{1}{2}L_{\text{IR}}} E_z \, dx \right| = C_{\text{cal}}^{(z)} \sqrt{I_1 \frac{I_{\text{IR}}^{(z)}}{I_{\text{CARS}}}}, \quad (6.11)$$

$$\left| \int_{-\frac{1}{2}L_{\text{IR}}}^{\frac{1}{2}L_{\text{IR}}} E_y \, dx \right| = C_{\text{cal}}^{(y)} \sqrt{I_1 \frac{I_{\text{IR}}^{(y)}}{I_{\text{CARS}}}}, \quad (6.12)$$

where  $C_{\text{cal}}^{(z)}$  and  $C_{\text{cal}}^{(y)}$  are again calibration constants, which can be determined by measuring the intensities in a known electric field distribution. These are the equations in the form that will be used in this work to measure the electric field distribution of plasma bullets.

As a side note, it can be seen from (6.9) and (6.10) that the IR polarisation is parallel to the electric field if the electric field is either parallel or perpendicular to the laser polarisation. However, since  $\chi_{zzzz}^{(3)} = \chi_{yyyy}^{(3)} + \chi_{yyzz}^{(3)} + \chi_{yzzz}^{(3)}$  [145], there can be an angle of up to 6° for the case of N<sub>2</sub> between the IR polarisation and the electric field when the electric field is neither parallel nor perpendicular to the laser polarisation [146].

The plasma bullet, incident laser beams and the generation of the CARS and IR beams are illustrated in figure 6.4. A coordinate system is chosen such that the bullet

propagates along the  $z$ -axis in the positive direction and the laser beams travel parallel to the  $x$ -axis in the positive direction and are linearly polarised in the  $z$ -direction. It is assumed that the electric field  $\mathbf{E}$  of the plasma bullet is radially symmetric:

$$\mathbf{E}(r, z, t) = E_r(r, z, t)\hat{\mathbf{e}}_r + E_z(r, z, t)\hat{\mathbf{e}}_z. \quad (6.13)$$

The electric field component perpendicular to the laser propagation direction,  $\mathbf{E}_\perp$ , consists of the  $y$ -component and the  $z$ -component and is given by

$$\mathbf{E}_\perp(r, \theta, z, t) = E_y(r, \theta, z, t)\hat{\mathbf{e}}_y + E_z(r, z, t)\hat{\mathbf{e}}_z \quad (6.14)$$

$$= E_r(r, z, t) \sin \theta \hat{\mathbf{e}}_y + E_z(r, z, t)\hat{\mathbf{e}}_z. \quad (6.15)$$

When the incident laser beams are at a position  $(y, z)$ , the equations for each of the polarisation components can be written as

$$\left| \int_{-\frac{1}{2}L_{\text{IR}}}^{\frac{1}{2}L_{\text{IR}}} E_z(r, z, t) dx \right| = C_{\text{cal}}^{(z)} \sqrt{I_1 \frac{I_{\text{IR}}^{(z)}(y, z, t)}{I_{\text{CARS}}}}, \quad (6.16)$$

$$\left| \int_{-\frac{1}{2}L_{\text{IR}}}^{\frac{1}{2}L_{\text{IR}}} E_r(r, z, t) \sin \theta dx \right| = C_{\text{cal}}^{(y)} \sqrt{I_1 \frac{I_{\text{IR}}^{(y)}(y, z, t)}{I_{\text{CARS}}}}. \quad (6.17)$$

To obtain  $E_z$  and  $E_r$ , except for their signs, an inversion has to be applied. Since  $E_z(r, z, t)$  is radially symmetric, (6.16) has the form of an Abel transform [147]. Therefore,  $|E_z(r, z_0, t_0)|$  can be obtained for an axial position  $z = z_0$  and time  $t = t_0$  by determining the right-hand side of (6.16) as a function of  $y$  and subsequently performing an Abel inversion. The integrand of (6.17),  $E_r(r, z, t) \sin \theta$ , is however not radially symmetric because of the  $\sin \theta$  factor, and an Abel inversion cannot be applied. Although not attempted in this work, it should in principle be possible to adjust a (Fourier) series expansion algorithm for Abel inversion, such as those described in [148, 149], to include this factor in the calculation and perform the inversion. Finally, it must be noted that these inversions result in radially resolved profiles, but the resulting spatial and temporal resolution still depends on the measurement system.

### 6.2.3 Laser setup and calibration

The laser system used for the experiments is mostly the same as the one described in [133], with only the wavelengths adapted for the vibrational Raman transition of  $\text{N}_2$  instead of  $\text{H}_2$ . Furthermore, an additional polariser was placed in front of the IR detector to measure  $I_{\text{IR}}^{(z)}$  and  $I_{\text{IR}}^{(y)}$  separately. A schematic representation of the setup is shown in figure 6.5.

Two 20 Hz ns-pulsed lasers are used to generate the pump ( $I_1$ ) and Stokes ( $I_2$ ) beams for the four-wave mixing experiment. The primary laser is a frequency doubled Nd:YAG laser (Continuum Powerlite Precision II 9020) that produces 6.0 ns FWHM pulses with a pulse energy of 650 mJ and  $\lambda_1 = 532$  nm. Part of its output (approximately 10%) is used as the pump beam in the experiment, and the other part (approximately 90%) is used to pump a dye laser (Radiant Dyes Jaguar D90MA). A



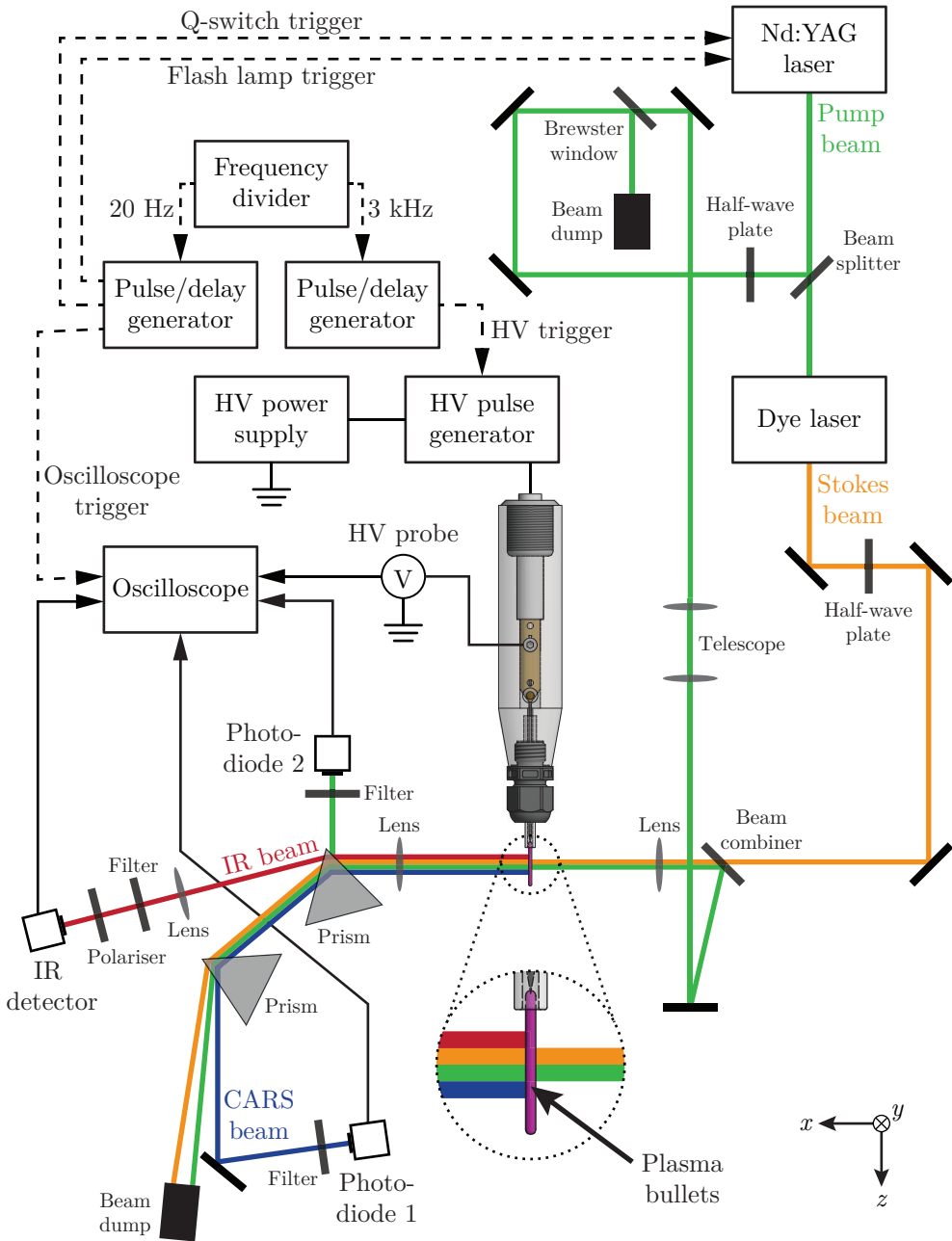


**Figure 6.5:** Schematic drawing of the experimental setup used for the electric field measurements.

**Table 6.1:** Properties of the focused laser beams.

Laser	Waist ( $\mu\text{m}$ )	Rayleigh length (mm)	Pulse duration (ns)
Nd:YAG	98	14	6.0
dye	135	24	4.3

mix of Rhodamine B and Rhodamine 101 dyes dissolved in ethanol is used to produce the Stokes beam, which consists of 4.3 ns FWHM pulses with a pulse energy of 47 mJ and  $\lambda_2 = 607$  nm.

Both laser beams are focused collinearly in front of the nozzle of the discharge setup by an  $f = 300$  mm lens. The generated CARS and IR beams are collected by a second lens and dispersed by a set of prisms. The first prism separates the IR beam, which is subsequently focused onto a HgCdTe IR detector (Vigo System PVI-3 TE-4). A polariser is placed in front of the IR detector to measure each of the polarisation components of the IR beam, and hence each of the components of the electric field, individually. The laser beams and the CARS beam pass through another prism, after which the laser beams are directed into a beam dump, and the CARS beam intensity is measured by photodiode 1. To monitor the intensity of the pump laser, a higher order reflection of the pump beam from the first prism is measured by photodiode 2.

A frequency divider paired with two pulse/delay generators (Stanford Research Systems DG535) is used to generate synchronised 20 Hz and 3 kHz signals to trigger the laser system and HV pulser respectively. By adjusting the delay between the laser trigger and HV trigger the electric field can be measured at different times during the propagation of the plasma bullet. Furthermore, the plasma source itself is mounted on a three-axis motorised stage (Zaber Technologies T-XYZ-LSM050A) to probe the electric field at different positions. Therefore this setup allows for the determination of the spatial and temporal development of the electric field and its polarisation direction.

The achievable resolution of the system is largely determined by the properties of the focused laser beams, which are summarised in table 6.1. Since both laser beams need to be present, the spatial and temporal resolution is approximated by the smallest waist diameter and shortest pulse duration respectively. This means that the spatial resolution is about  $100 \mu\text{m}$ . However, the temporal resolution of about 4.3 ns limits the axial resolution, because, at an average propagation speed of about  $10^5 \text{ ms}^{-1}$ , the plasma bullet advances about  $500 \mu\text{m}$  during the duration of the laser pulse. So the spatial resolution for the electric field measurements on plasma bullets is estimated at  $100 \mu\text{m}$  laterally and  $500 \mu\text{m}$  axially.

When a discharge takes place between two electrodes, the setup can normally be calibrated in-situ or at least using the discharge electrodes themselves because the background fields produced by voltages below the breakdown value are sufficiently large. For the currently used single electrode plasma jet this is, however, not the case and therefore an alternative ex-situ absolute calibration procedure is implemented. Equations (6.9) and (6.10) show that  $C_{\text{cal}}^{(z)}$  and  $C_{\text{cal}}^{(y)}$  can actually be obtained from any electrode geometry as long as the electric field distribution is known and the integral on the left-hand side can be calculated. To this end, two square  $19 \text{ mm} \times 19 \text{ mm}$  parallel

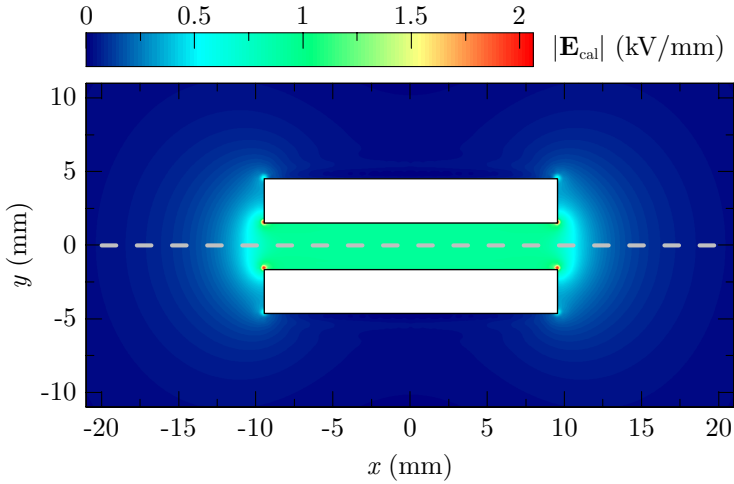


**Figure 6.6:** Centre part of the electric field distribution of the calibration geometry when 3 kV is applied. The white rectangles indicate the position of the electrodes and the dashed grey line shows a part of the path along which the electric field is integrated. The full domain of the model is 260 mm wide and 40 mm high.

plate electrodes with a gap of 3.1 mm are used. The centre of the gap is placed at the same point along the beam path where the actual measurements take place. The size of 19 mm was chosen such that the calibration electric field is situated well within the shortest Rayleigh range from each side of the focus spot ( $2 \times 14 \text{ mm} = 28 \text{ mm}$ ). In addition, the electrodes can be rotated around the laser beam path such that the calibration field is oriented in either the  $z$ - or  $y$ -direction. The resulting electric field distribution is obtained from an electrostatic model in COMSOL, and subsequently the integral along the laser path is calculated. An example is shown in figure 6.6. The full domain of the electrostatic model is 260 mm by 40 mm to make sure the entire calibration field is accounted for in the integral.

## 6.2.4 Discharge simulation model

To compare results from the four-wave mixing experiment to simulations, an axisymmetric fluid model was adjusted to the experimental conditions. The model is of the drift-diffusion type in combination with the local field approximation [150], so that the electron density  $n_e$  and ion density  $n_i$  evolve in time as:

$$\frac{\partial}{\partial t} n_e = \nabla \cdot (\mu_e \mathbf{E} n_e + D_e \nabla n_e) + \alpha \mu_e E n_e, \quad (6.18)$$

$$\frac{\partial}{\partial t} n_i = \alpha \mu_e E n_e, \quad (6.19)$$

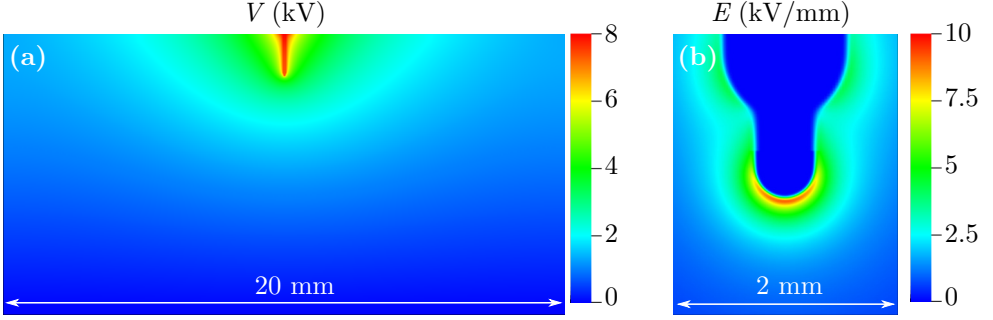


**Figure 6.7:** Cross section of the electric potential in the domain, illustrating (a) the artificial electrode represented by an ionised channel, and (b) a magnified view of the tip of the channel and the resulting electric field.

where  $\mu_e$ ,  $D_e$  and  $\alpha$  are the electric field dependent electron mobility, diffusion and ionisation coefficients respectively. The electric potential  $\phi$  is calculated using Poisson's equation

$$\nabla^2 \phi = -\frac{e(n_i - n_e)}{\epsilon_0}, \quad (6.20)$$

where  $e$  is the elementary charge and  $\epsilon_0$  is the vacuum permittivity, and the electric field is given by  $\mathbf{E} = -\nabla\phi$ . The transport coefficients for  $\text{N}_2$  (at 1 bar and 293 K) were computed from the Phelps database [151] using BOLSIG+ [104]. Note that the model assumes that ions are immobile, and that the discharges propagate in  $\text{N}_2$  and therefore photoionisation is not included. The above equations are solved on an adaptively refined mesh using the Afivo framework [152], which was used before in [65].

A computational domain with a radius and height of 10 cm was used, mimicking the typical dimensions of the experiment. However, precisely reproducing the experiment's electrode geometry was not possible: the electrode and the surrounding dielectrics cannot easily be included in our numerical model, and the experiments are performed in open space without a clear reference point for the boundary conditions for the potential. Therefore, to simulate the electrode as well as possible in this situation, it is approximated by an ionised channel protruding 1.5 cm into the domain. The resulting potential of this artificial electrode is illustrated in figure 6.7a. The channel representing the electrode has a charged particle density of  $n_e = n_i = 10^{20} \text{ m}^{-3}$  and a radius of 0.5 mm, which is reduced to 0.25 mm at its tip. The decrease in radius and electric field at the tip of the channel is shown in figure 6.7b. As the electrons electrically screen the channel, it acts approximately as a conducting electrode. On the top boundary of the domain, a potential of 8 kV is applied, which radially decays as  $\log(1 + d_0/r)$ , with  $d_0 = 10$  cm. The bottom boundary is electrically grounded, and a Neumann zero boundary condition is used at the radial boundary.

The background pre-ionisation due to previous pulses (the memory effect) is included as a Gaussian profile of electrons and ions. The profile has a characteristic width of 0.25 mm, assuming the previous discharges had a radius approximately equal to the emission HWHM of about 0.15 mm, and that the typical diffusion length  $\sqrt{4Dt}$

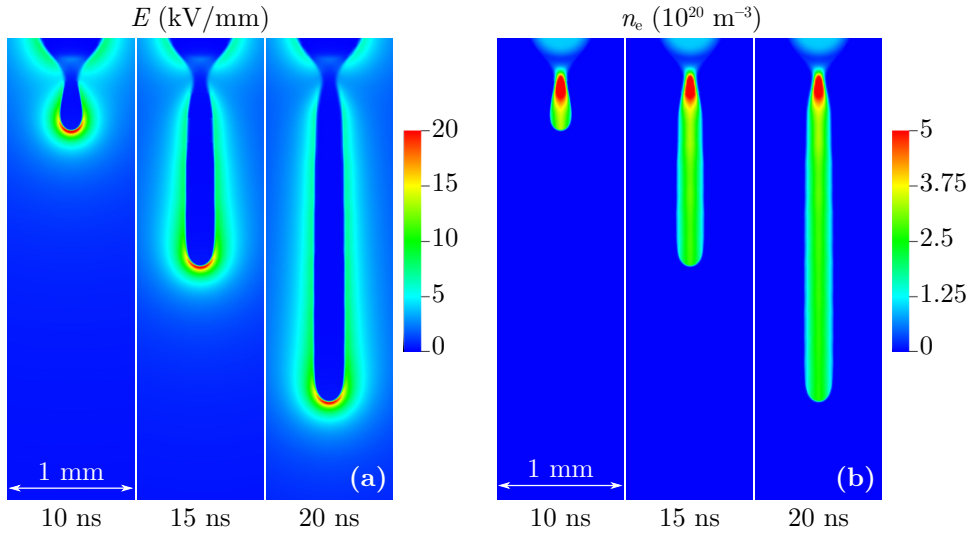
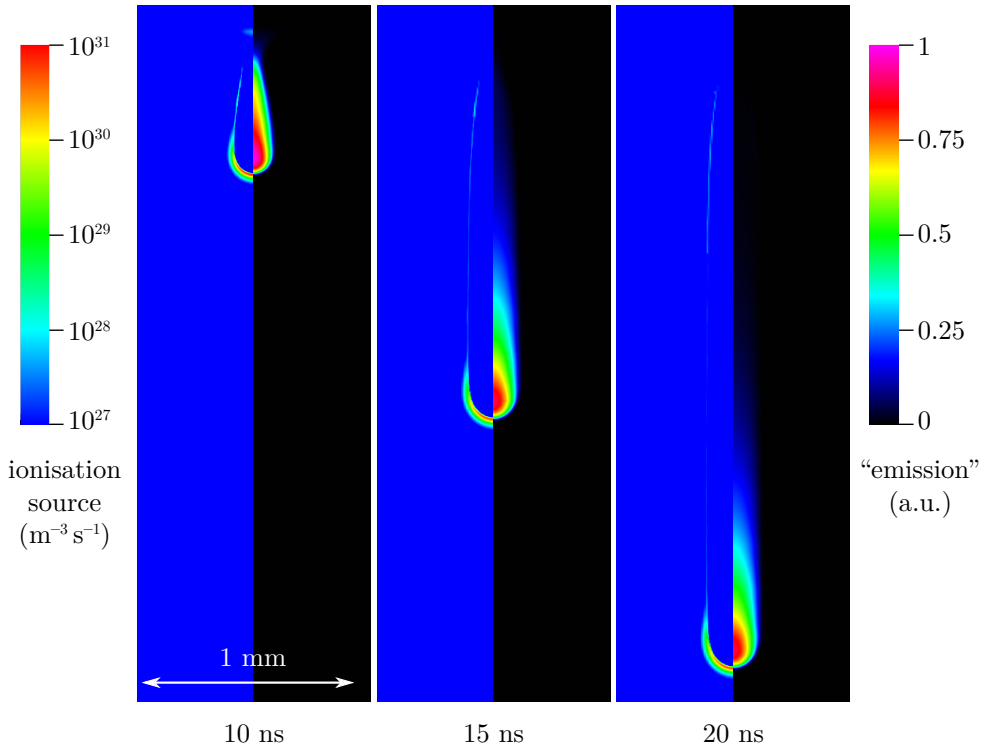


**Figure 6.8:** Cross sections showing (a) the simulated electric field, and (b) the electron density at 10, 15 and 20 ns. The streamer’s velocity is about  $2 \times 10^5$  m/s during the shown interval.

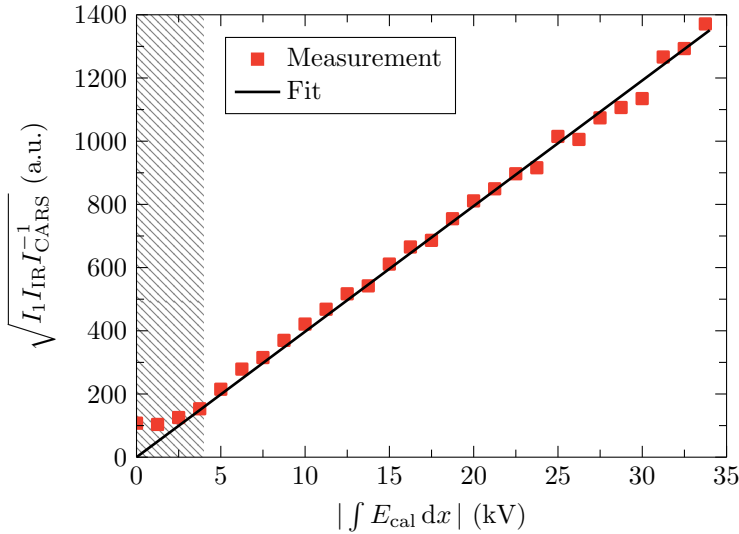
between pulses at 3 kHz is about 0.1 mm. The maximum density of the pre-ionisation at the start of a new discharge was estimated to be  $10^{15} \text{ m}^{-3}$  from a zero-dimensional model presented in [153], which is consistent with the value that was found in chapter 5.

Figure 6.8 shows the time evolution of the simulated discharge. Between 10 and 20 ns, the streamer has a velocity of approximately  $2 \times 10^5$  m/s, in good agreement with the experimental measurement of  $1.8 \times 10^5$  m/s in the same time interval. In the simulations, the streamer’s diameter (0.2 mm), maximum electric field (20 kV/mm) and its degree of ionisation ( $3 \times 10^{20} \text{ m}^{-3}$ ) show little variation between 10 and 20 ns.

Although our numerical model does not calculate the excited species and their emission, it is interesting to consider the ionisation source term,  $\alpha\mu_e En_e$ , and use this to qualitatively approximate the emission profile. To do so, it is assumed that the number of excited states produced is proportional to the ionisation source term and that the decay of emitting states is dominated by collisional quenching. Furthermore, assuming that most of the emission is from the second positive system (SPS) of N<sub>2</sub> results in an effective radiative lifetime that is equal to the quenching time  $\tau_q = 2$  ns [154, 155]. The “emission” is computed from the equation  $\partial_t I = -I/\tau_q + \alpha\mu_e En_e$ , and subsequently an Abel transform is applied to obtain a line-of-sight integrated profile. Figure 6.9 shows both the ionisation source term and the approximated emission profile. While the emission profiles indeed resemble the bullet-like shapes observed in the emission shown in figure 6.2, it should be realised that the ionisation is concentrated in a thin region in front of the streamer.



**Figure 6.9:** Cross sections showing the ionisation source term on the left, and a qualitative approximation of the line-of-sight integrated emission profile (see text) on the right, at 10, 15 and 20 ns.



**Figure 6.10:** Example of a calibration measurement. The hatched area indicates the region that is below the measurement threshold.

## 6.3 Results and discussion

### 6.3.1 Calibration measurement

First, the calibration electrodes are placed in the setup, such that the calibration field in the gap is parallel to the electric field component to be measured, and a calibration measurement is performed as described earlier. The intensities measured for a range of applied voltages and their corresponding calculated electric field integrals are plotted in figure 6.10. As expected from (6.11) and (6.12), a linear relationship between the electric field integrals and the square root of the intensities is found. Now  $C_{\text{cal}}^{(z)}$  and  $C_{\text{cal}}^{(y)}$  are given by the reciprocal of the slope of a linear fit from a measurement with the calibration field in the  $z$ - and  $y$ -direction respectively. Since the laser system has a certain pointing stability, this procedure is repeated before every measurement series to account for changes in the spatial overlap of the two laser beams between measurement series. Furthermore, the threshold value of the electric field integral for which the IR intensity surpasses the noise level of the IR detector also depends on how well the laser beams are aligned. It is found that this usually leads to a threshold value around  $|\int E dx| \approx 4$  kV.

### 6.3.2 Plasma bullet measurements

The results of two types of experiments are presented in this subsection. The first is a spatial scan made in the  $y$ -direction by moving the plasma source using the motorised stages, at a fixed distance from the nozzle, at a fixed time after the bullet's inception,

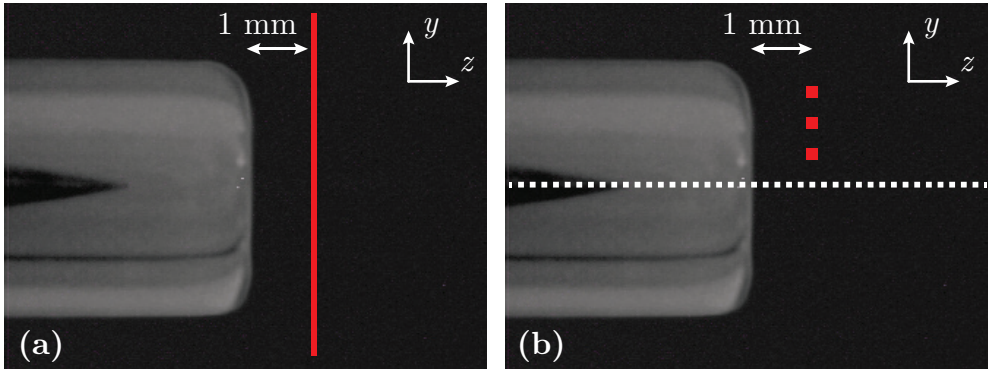


**Figure 6.11:** Illustration of the measurement positions. The spatial scan is performed along the red line shown in (a). The temporal scans are performed at the fixed  $y$ -positions indicated by the red points in (b). The white dotted line indicates the axis of the jet.

to determine the radial distribution of the electric field. The second is a temporal scan, made by changing the delay between the HV trigger and the laser trigger, performed at three fixed  $y$ -positions to determine the evolution of the electric field integrals as the plasma bullet propagates. In each case, both the  $y$ - and  $z$ -components of the electric field are measured separately by rotating the transmission axis of the polariser in front of the IR detector accordingly.

### Spatial scan and radial distribution

The spatial scan in the  $y$ -direction is performed at a fixed distance from the nozzle  $z_0 = 1$  mm (and hence 3 mm from the needle tip) at a fixed time after the bullet's inception  $t_0$ . The red line in figure 6.11a shows the measurement positions of this experiment. The fixed timing  $t_0$ , which is controlled by the delay between the HV trigger and laser trigger, for this measurement set was chosen such that the highest signal from the IR detector was obtained. This timing corresponds to the situation where the plasma bullet reaches the laser beam path during the measurement, as confirmed by ICCD camera images. Figure 6.12 shows the integrated electric field values for each of the components. The measurements were performed with  $0.5 \mu\text{m}$  intervals in the  $y$ -direction and then collected in  $200 \mu\text{m}$  wide bins, so each of the points in figure 6.12 contains the data of 400 individual laser shots. The  $z$ -component of the electric field, which is in the propagation direction of the plasma bullet, shows a clear peak at the jet axis. Several millimetres from the jet axis the measured  $z$ -component integrals are still significantly above the measurement threshold value. As expected, the  $y$ -component is significantly lower than the  $z$ -component. In fact, all the measurements of the  $y$ -component are around the threshold value, and only the  $z$ -component is further analysed.

In order to obtain  $|E_z(r, z_0, t_0)|$ , the  $z$ -component data has to be Abel inverted. However, it is necessary to know how the distribution decreases to zero for the inversion.



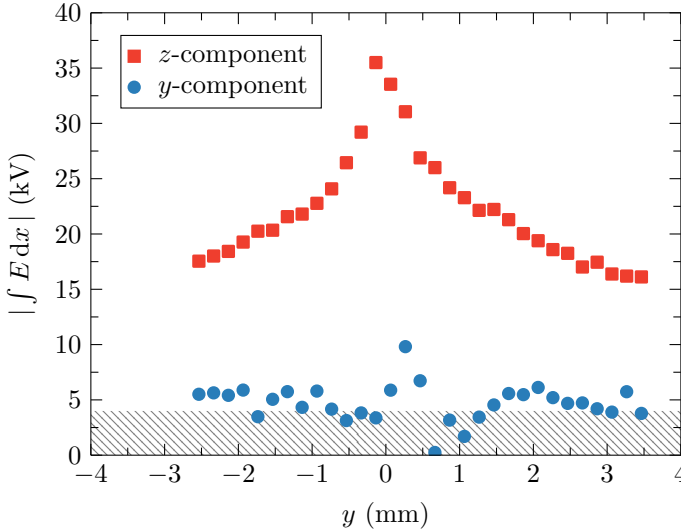


**Figure 6.12:** Measured radial profiles of the line-integrated electric field components. The hatched area indicates the region that is below the measurement threshold.

Since the measurements do not reach zero in the probed range, a function is first fitted to the data. Because the shape of the chosen function will influence the peak value and the radial decay of the inverted profiles, two fit functions that fit the data reasonably well are used: one that decreases rapidly and one that decreases slowly to zero. The actual shape is expected to be somewhere in between. Fit 1 is the sum of a Gaussian function and a Lorentzian function and fit 2 is the convolution of a generalised normal function, i.e.  $f(y; a, b, c) = a \exp(-|y|^c/b)$ , and a Gaussian function. The data and these fits are shown together in figure 6.13. The fits are subsequently Abel inverted, and the obtained electric field profiles are shown in figure 6.14.

The obtained electric field profile has a peak value of about 12–18 kV/mm and a full width at half maximum (FWHM) of about 750–900  $\mu\text{m}$ . The found peak value is in the same range of about 10 kV/mm to 35 kV/mm as the values reported for other streamer discharges in N<sub>2</sub> and N<sub>2</sub>-O<sub>2</sub> mixtures [156–158]. However, it should be noted that the experimental value found in this work underestimates the peak value, due to the limited spatial resolution in the axial direction resulting from the propagation of the bullet during the laser pulse.

These experimental results will now be compared with the results from the streamer model discussed in section 2.4. In order to do so, the axial ( $z$ ) component of the electric field is calculated from the simulation data. Subsequently, the electric field is spatially and temporally convolved with the profiles of the laser beams. Finally, the resulting radial profile at the timing and position equivalent to the measurement, i.e. 3 mm from the artificial electrode, is convolved with a 200  $\mu\text{m}$  wide rectangular function to mimic the effect of the binning. The obtained peak value after convolution

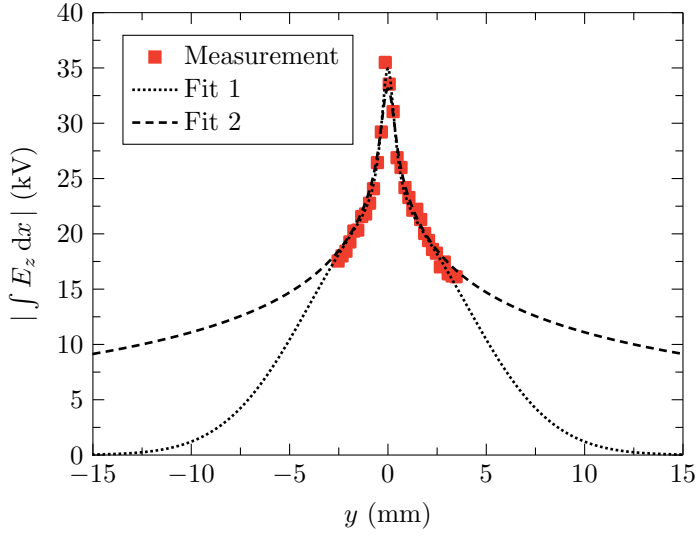


**Figure 6.13:** Radial profile of the line integrated  $z$ -component values together with the two fits.

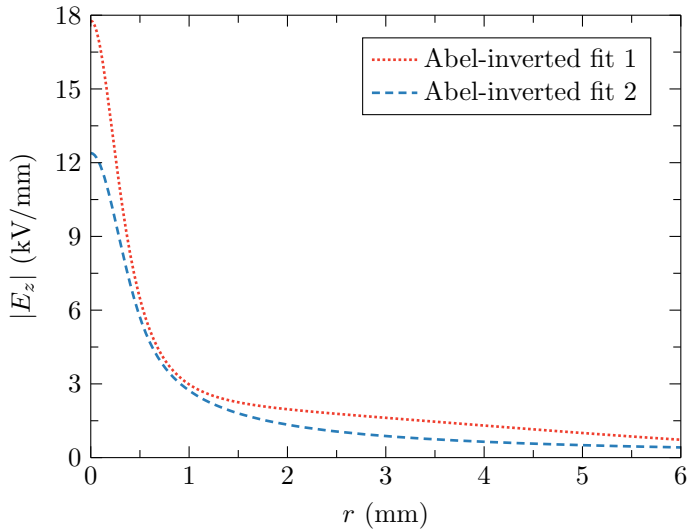


**Figure 6.14:** Radial profile of the  $z$ -component of the electric field.

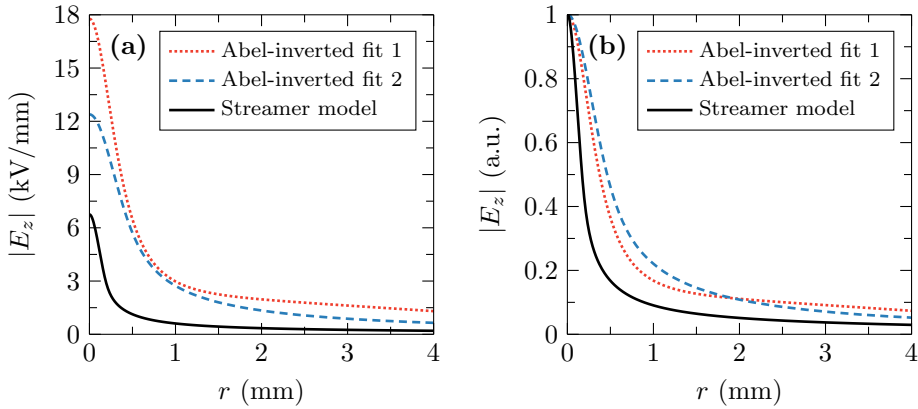


**Figure 6.15:** Comparison between the results obtained from the experiment and the model convolved with the laser beam profiles in (a) absolute values, and (b) normalised values.

is about 7 kV/mm, which is approximately a factor 2.5 lower than the peak value of about 20 kV/mm before convolution, as visible in figure 6.8. This is mostly due to the convolution with the temporal beam profile.

A comparison between the experiments and the model (after convolution) in absolute values is shown in figure 6.15a. It can be seen that the model predicts lower electric field values. The peak value is about a factor 2 lower than the value from the experiment. From the comparison of the normalised profiles in figure 6.15b, it is also apparent that the model predicts a faster radial decay with a FWHM of approximately 350  $\mu\text{m}$ .

From the modelling point of view, several factors could contribute to these differences. In general, the approximations used for the plasma fluid model could cause differences of perhaps 10–30% in quantities such as the maximum electric field. The model could also only approximate the experimental electrode geometry: it uses a pre-ionised channel instead of an electrode, it does not contain dielectric material around it, and there is also uncertainty in the boundary conditions for the electric potential. The amount of background ionisation from previous pulses mimicking the memory effect was estimated from a zero-dimensional model and could be an order of magnitude higher or lower. The radial decay of the background ionisation could be inaccurate as well. Lastly, the background ionisation was included as electrons and positive ions in the model, whereas realistically there are many species.

In previous numerical studies on plasma bullets in He, Boeuf *et al* found that the on-axis electric field at the streamer front increased by only a factor 1.3 when the pre-ionisation density was decreased by four orders of magnitude [159], and Breden *et al* found that the electrode geometry mostly affects the breakdown and propagation inside the nozzle, while the streamer structure outside the nozzle remains relatively unaffected [160]. As mentioned before in section 2.1, it should be remarked that plasma bullets in He typically exhibit ring-shaped discharge structures that are different from

those observed in  $N_2$  [8,27], and that in both former studies a ring electrode geometry was used instead of a single needle electrode. For streamer discharges in artificial air, Wormeester *et al* showed that, although the evolution times are different, the streamer radius and maximum electrical field remain practically the same while the pre-ionisation density was changed by two orders of magnitude in the absence of photoionisation [157].

The effect of the characteristic width of the background ionisation channel in our model was investigated by changing it to 0.125 mm and 0.375 mm. For the 0.125 mm case, the on-axis maximum field and the velocity were about 25% higher. In the 0.375 mm case, instabilities related to branching occurred, which resulted in fluctuating properties that are hard to evaluate. Since this behaviour is not observed in the experiment, it could indicate that the channel is at least narrower than 0.375 mm. On average, the on-axis field was about 15% lower in this case than in the 0.25 mm case, and the velocity was about 25% lower.

Considering all this, the before mentioned factors together could perhaps explain a difference of 50% between the experimental and modelled field amplitudes presented in this work. On the other hand, with the same applied voltage, a very similar propagation velocity is observed in the simulations and the experiments. While this agreement could indicate that the simulations represent the experimental discharge quite well, it must be remarked that the velocity not only depends strongly on the electric field around the streamer but also on its radius [156,161].

From the experimental point of view, an error in the calibration could be a cause of error in the amplitudes. While care was taken to choose calibration electrodes shorter than twice the shortest Rayleigh length, deviations from the plane-wave approximation could result in an overestimation of the electric field integrals in the calibration. This would subsequently lead to an overestimation of the calibration constants and hence of the final electric field values. Moreover, potential calibration errors are also introduced by the spatial drift of the laser beams between the calibration and the actual measurements. In addition, spatial drift of the laser beams during a series of measurements, as well as the sampling of 400 shots, could contribute to broadening of the measured distribution. Lastly, the choice of fit function also has some influence on the final electric field profile, particularly on the centre values. Taking these things into account, the error in the experimentally found values is also estimated up to several tens of percent. Given these uncertainties, the differences between the electric field profiles from the measurements and the model are reasonable.

### Temporal scans

The temporal scans are also made at a fixed distance from the nozzle  $z_0 = 1$  mm at three fixed  $y$ -positions to see the evolution of the electric field at these points as the bullet propagates. The three  $y$ -positions are 465, 965 and 1465  $\mu\text{m}$  from the jet axis and are illustrated by the red points in figure 6.11b. Comparing with figure 6.2, it can be seen that the outer two  $y$ -positions are situated well outside the region of optical emission. The results of the temporal scans are shown in figure 6.16. Since these measurements are conducted at only three fixed  $y$ -positions, an inversion cannot be performed. Instead, the square root of the ratio of measured intensities, which is

proportional to the electric field integral, is qualitatively compared to the model at these positions. To get the equivalent data from the model, the electric field is this time projected onto a cartesian grid, spatially and temporally convolved with the laser beam profiles, and integrated along the  $x$ -axis. Since the measured temporal profiles are obtained by changing the timing between the discharge and the lasers, it should be realised that the interval between data points does not indicate the actual temporal resolution of the measurement system, which is limited by the laser pulse duration as discussed before.

In figure 6.16a the measured evolution of the  $z$ -component of the field is shown. The axial fields increase until the bullet reaches the position of the laser at about 20 ns, and then decrease again as the bullet propagates past the lasers. As expected, the axial component is largest at the position closest to the jet axis and decreases further away. The evolution of the electric fields in the model shows comparable behaviour in figure 6.16b. The  $y$ -component measurements in figure 6.16c are all around the threshold value before 20 ns. This is in line with the spatial scan in the previous subsection, which was performed right before the bullet reaches the laser position and where no significant  $y$ -component could be detected. Looking at the results from the model in figure 6.16d indeed shows that the radial fields before 20 ns are lower than after 20 ns at all three positions. For the profiles at 465  $\mu\text{m}$  from the jet axis, a similar shape can be recognised after 20 ns. This increase of the  $y$ -component of the electric field when the bullet propagates past the laser beam position around 20 ns results from the net space charge layer that surrounds and screens the inner streamer channel and produces a radial electric field outside the streamer channel. For the two profiles further from the axis, this is less obvious in the measurements because they remain close to the threshold. However, the values of the points measured after 20 ns at 965  $\mu\text{m}$  are on average larger than the points measured at 1465  $\mu\text{m}$ , which is in agreement with the model. Similar behaviour of the radial field component was also observed with an electro-optic probe placed outside the dielectric tube for plasma bullets in He [120]. Finally, both the experiments and the model show that the maximum value of the  $y$ -component is lower than the maximum value of the  $z$ -component.

## 6.4 Conclusions and outlook

In this work, the electric field four-wave mixing technique is applied to plasma bullets in N<sub>2</sub>. It is demonstrated that it is feasible to obtain local values of a non-uniform electric field distribution by extending this technique with an inversion method. Furthermore, a calibration procedure using electrodes different from the discharge geometry is demonstrated. A radial profile is obtained for the axial component of the electric field in front of the plasma bullet with a peak value of about 12–18 kV/mm and a FWHM of 750–900  $\mu\text{m}$ . While the limited temporal resolution of the system leads to an underestimation of the true peak value, the found value is in the expected range for streamer discharges from literature. The streamer model predicts electric field values about a factor two lower than the experiment as well as a faster radial decay. Nevertheless, these differences are reasonable considering the used approximations

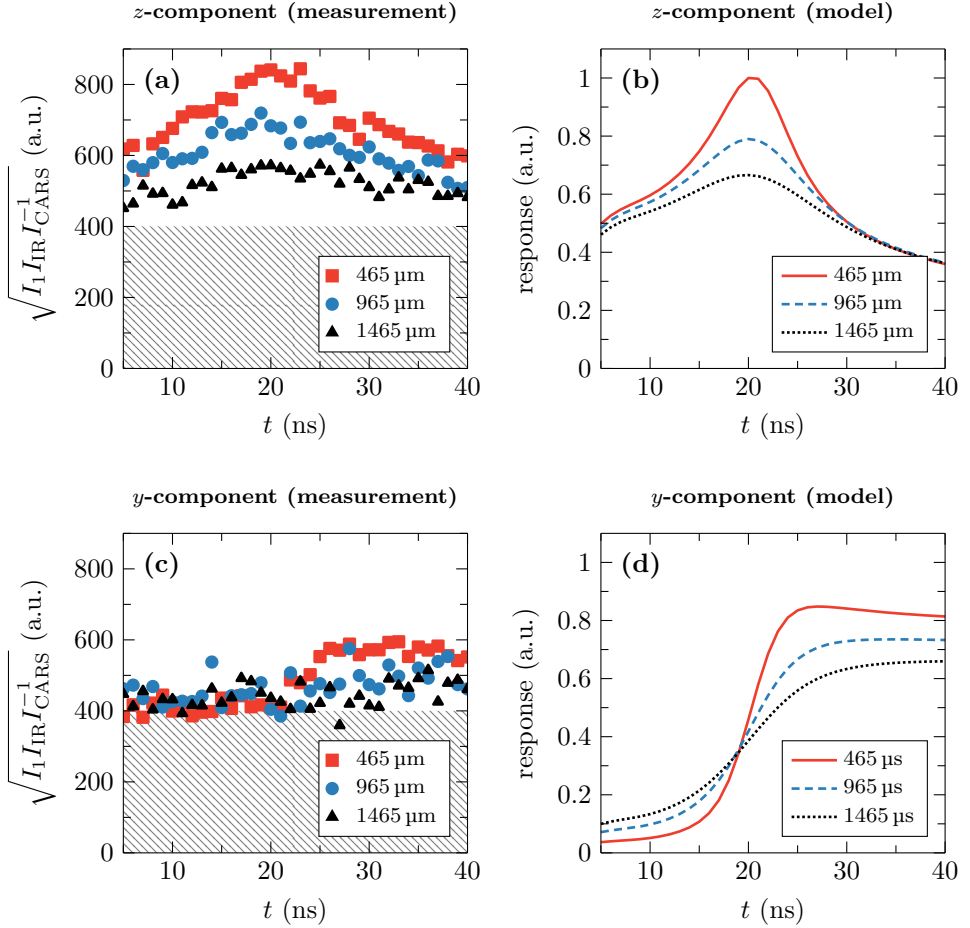


**Figure 6.16:** Temporal profiles of the integrated  $z$ -component of the electric field obtained from the experiment (a) and the model (after convolution and integration) (b), and of the integrated  $y$ -component of the electric field obtained from the experiment (c) and the model (after convolution and integration) (d). The hatched areas in (a) and (c) indicate the region that is below the measurement threshold.

and the experimental uncertainties. In addition, three temporal profiles were obtained for fixed points in space as the bullet propagates. Here it is found that the axial component increases as the bullet travels towards the measurement position and then decreases again. The radial component of the electric field only reaches values above the measurement threshold after the front of the bullet has passed the measurement position. Qualitatively similar features are observed in the model.

To further improve the measurements in the future, most importantly the temporal resolution of the setup needs to be increased. One way to achieve this is by using a picosecond laser system, such as used by Goldberg *et al* [131, 132], instead of a nanosecond laser system. Furthermore, it would be preferable to move from the currently used CRS-based four-wave mixing method to the recently introduced field-induced SHG-based four-wave mixing method [141, 142]. This method has some significant practical advantages over the CRS-based method. Firstly, only one laser is required, and therefore any misalignment between beams, both spatially and temporally, is automatically avoided. Secondly, when a (near) infrared laser is used as the pump beam, the second harmonic signal, from which the electric field is determined in this case, is generated at an optical wavelength. Fast and sensitive detectors are widely available for optical wavelengths, whereas the IR signal generated in the CRS-based method requires a special IR detector.

For either of the methods, the effect of the size of the calibration electrodes, and the resulting calibration electric field, relative to the Rayleigh length of the focused laser beams should be investigated to establish the accuracy of the calibration constant and hence of the electric field amplitudes. To do this, a theoretical description of the four-wave mixing processes using Gaussian beams instead of the plane-wave approximation is needed. This is the subject of the next chapter.

For a better comparison to the model, most importantly a reference potential should be defined in the experiment to provide a proper boundary condition. This can, for example, be achieved by placing a grounded cylindrical vessel around the plasma source. The uncertainty in the current implementation of the memory effect as a Gaussian channel of background ionisation could be avoided by extending the model to multiple consecutive discharges and including the gas flow. Furthermore, calculating radiative decay of excited species in the model would allow a direct comparison of the model to the ICCD camera images and the corresponding radii.

Together, these improvements will make it possible to obtain fully spatially and temporally resolved electric field profiles of plasma bullets in  $N_2$ .

## Chapter 7

---

# Four-wave mixing with focused laser beams



## 7.1 Introduction

One of the key parameters of a discharge is its electric field: it drives the discharge and is directly related to rate coefficients of plasma processes [4]. Therefore, detailed knowledge of the electric field is essential, both for theory and applications. Over the past years, field-induced four-wave mixing methods have been investigated and used as electric field diagnostics for (near-)atmospheric pressure discharges. Discharges at atmospheric pressure are generally highly transient and small in size: electrical breakdown typically occurs at (sub)nanosecond time scales, and the typical dimensions are of the order of 100  $\mu\text{m}$  [162]. This demands diagnostics with high temporal and spatial resolution. Field-induced four-wave mixing methods are laser diagnostics, based on non-linear optics, that can accommodate these needs [163]. At the moment, two electric field four-wave mixing methods are used: one based on field-induced coherent Raman scattering (CRS) [124], and another based on field-induced second harmonic generation (SHG) [141].

The idea for CRS-based four-wave mixing as an electric field diagnostic was first mentioned by Gavrilenko *et al* [124]. Basically, two collinear laser beams are used to produce coherent anti-Stokes Raman scattering (CARS) radiation, while simultaneously generating coherent infrared (IR) radiation on a dipole-forbidden molecular Raman transition in the presence of an external electric field. Each of these two processes is itself a four-wave mixing process. The intensity ratio of the resulting CARS and IR radiation is directly related to the external electric field. This method has since been used to measure electric fields in  $\text{H}_2$  containing gases [125–134], and  $\text{N}_2$  containing gases [135–140, 164]. In most of these cases, nanosecond pulsed laser systems have been used [125–130, 133, 135, 136, 164], but picosecond pulsed laser system have also been applied to achieve higher temporal resolution [131, 132, 134, 138–140].

Recently, Dogariu *et al* demonstrated the SHG-based four-wave mixing method [141]. In this case, one laser beam is used to induce second harmonic generation in the presence of an external electric field. The intensity of the produced second harmonic (SH) is directly related to the external electric field. Whereas the CRS-based method requires a Raman transition, the SHG-based variation is non-resonant and works in a wider variety of gases, including atomic ones [141, 142]. Furthermore, the SHG-based method also has some practical advantages over the CRS-based method. Firstly, only one incident laser beam is required instead of two, which avoids the need for careful alignment of two laser beams. Secondly, when a (near-)infrared laser is used, the second harmonic is generated at a visible wavelength. Fast and sensitive detectors are widely available for visible wavelengths, whereas the IR wavelength generated in the CRS-based method requires a special IR detector. Up to now, SHG-based four-wave mixing has been used with a femtosecond laser system [141], and it was recently demonstrated also to work using a picosecond laser system [142].

High spatial resolution in the transverse direction of the laser beam can be achieved by focused laser beams. However, one of the drawbacks of the electric field four-wave mixing techniques is that the electric field is line-integrated along the laser beam in the longitudinal direction. Therefore, the obtained electric field value is averaged along some length of the laser beam. It is proposed in [141] that sub-millimetre spatial

resolution in the direction along the laser beam might be obtained by very tightly focusing the laser beams. Another approach, which can be used for radially symmetric electric fields, to obtain spatially resolved fields is by applying an Abel inversion to a set of lateral measurements, as was demonstrated in chapter 6.

Even though focused laser beams are used in the four-wave mixing experiments, the equations used in the analysis are based on the plane-wave approximation. However, this approximation is only accurate close to the focus, where the wavefront is approximately flat, and can potentially lead to large errors if it is not valid. In fact, in chapter 6 it was hypothesised that the difference between the measured and modelled electric field of a guided streamer in  $N_2$  is (partly) due to the plane-wave approximation. This chapter provides a theoretical description of electric field four-wave mixing with fundamental Gaussian laser beams. Using the developed theory, it is possible to assess the validity of the plane-wave approximation and to quantify the potential errors that arise in the analysis of four-wave mixing measurements. While the emphasis will mostly be on the CRS-based scheme, the theory in this chapter can also be applied directly to the SHG-based scheme with some minor changes.

## 7.2 Theory of four-wave mixing

In general, four-wave processes are third-order non-linear optical interactions that couple four electromagnetic waves together. In four-wave mixing, three incident electromagnetic waves interact non-linearly with a material medium to produce a fourth wave at a new frequency. All waves may have a different frequency (non-degenerate four-wave mixing), or two of the frequencies can coincide (degenerate four-wave mixing). In the latter case, two of the incident waves can, for example, originate from a single laser source.

In the CRS-based four-wave mixing method for electric field measurement, two incident laser beams are used: a pump laser beam with frequency  $\omega_1$  and a Stokes laser beam with frequency  $\omega_2$ . The frequencies of the lasers are tuned such that their difference matches a dipole-forbidden vibrational Raman transition of the medium, which in practice is a gas containing either  $H_2$  or  $N_2$ , due to their relatively high Raman cross-sections. At sufficiently high laser intensities, and in the presence of an external electric field  $\mathbf{E}$ , this will induce two simultaneous four-wave mixing processes. The first one is coherent anti-Stokes Raman scattering (CARS). In this interaction, a wave with frequency  $\omega_{\text{CARS}} = 2\omega_1 - \omega_2$ , which is anti-Stokes shifted from the pump frequency  $\omega_1$ , is produced. The second four-wave mixing is coherent infrared (IR) generation<sup>1</sup>, in which waves with frequency  $\omega_{\text{IR}} = \omega_1 - \omega_2$  are generated on the vibrational Raman transition. Both the CARS and IR waves are generated in coherent laser-like beams. Energy diagrams for both CARS and coherent IR generation are shown in figure 7.1, where  $|g\rangle$  and  $|e\rangle$  indicate the ground state and vibrationally excited state respectively. It should be noted that both processes are parametric and hence do not populate the excited state  $|e\rangle$ .

In the SHG-based four-wave mixing method, only a single incident laser beam

<sup>1</sup>Technically, this process could be called field-induced resonant difference frequency generation.

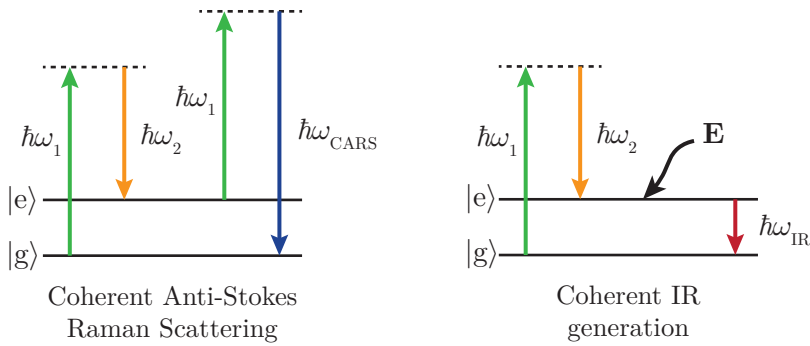


**Figure 7.1:** Energy diagrams for the two processes in CRS-based four-wave mixing processes. The dashed lines indicate virtual levels.

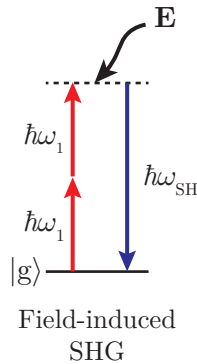


**Figure 7.2:** Energy diagram for the process in SHG-based four-wave mixing processes. The dashed line indicates a virtual level.

is used at frequency  $\omega_1$ . At sufficiently high laser intensity, and in the presence of an external electric field  $\mathbf{E}$ , this will induce a four-wave mixing process called field-induced second harmonic generation (SHG). In this interaction, a wave with frequency  $\omega_{\text{SH}} = 2\omega_1$ , i.e. the second harmonic (SH), is generated. An energy diagram for field-induced SHG is given in figure 7.2. Since this process is non-resonant, it can be applied to a wider variety of gases [141]. It should be realised that this process is different from ‘regular’ SHG, which is a second-order non-linear effect and does not occur in centrosymmetric media like gases.

As mentioned, the coherent IR generation process and the field-induced SHG process require the presence of an external electric field. How these processes depend on the electric field can be derived from the theory of non-linear optics.

### 7.2.1 Non-linear optics and the driven wave-equation

In general, electromagnetic fields corresponding to a wave at frequency  $\omega_n$  obey the inhomogeneous wave-equation

$$\left(\nabla^2 - \frac{n_n^2}{c^2} \frac{\partial^2}{\partial t^2}\right) E_n(\mathbf{r}, t) = \frac{1}{\varepsilon_0 c^2} \frac{\partial^2}{\partial t^2} P_n(\mathbf{r}, t), \quad (7.1)$$

where  $\varepsilon_0$  is the vacuum permittivity and  $c$  is the vacuum speed of light, and  $E_n$ ,  $P_n$  and  $n_n$  are the electric field, the polarisation and the refractive index at frequency  $\omega_n$  respectively. If incident waves induce a polarisation  $P_n$  in the medium at frequency  $\omega_n$ , this equation shows that an electromagnetic wave  $E_n$  at the same frequency will be generated. For this reason, the equation is also referred to as the driven wave-equation. This mechanism is what causes the IR or SH waves to arise in the four-wave mixing experiments. Therefore, to understand the properties of the waves generated by four-wave mixing, the polarisation of the medium and the propagation of the subsequently generated waves need to be considered.

When the dominant direction of propagation of the incident waves is along the  $z$ -axis, the electric field and polarisation can be represented as

$$E_n(\mathbf{r}, t) = \frac{1}{2} A_n(\mathbf{r}) \exp(i[k_n z - \omega_n t]) + \text{c.c.}, \quad (7.2)$$

$$P_n(\mathbf{r}, t) = \frac{1}{2} p_n(\mathbf{r}) \exp(i[k'_n z - \omega_n t]) + \text{c.c.}, \quad (7.3)$$

where  $A_n$  and  $p_n$  are the amplitudes of the electric field and polarisation waves respectively, which may themselves be spatially varying quantities,  $k_n$  and  $k'_n$  are the corresponding wavevectors, and c.c. indicates the complex conjugate. By allowing the wavevectors of the electric field and polarisation to be different, potential phase mismatches can be accounted for.

Substituting (7.2) and (7.3) in (7.1) results in the following equation for the electric field amplitude:

$$\left(2ik_n \frac{\partial}{\partial z} + \frac{\partial^2}{\partial z^2} + \nabla_{\text{T}}^2\right) A_n(\mathbf{r}) + \left(\frac{n_n^2 \omega_n^2}{c^2} - k_n^2\right) A_n(\mathbf{r}) = -\frac{\omega_n^2}{\varepsilon_0 c^2} p_n(\mathbf{r}) \exp(-i\Delta k z), \quad (7.4)$$

where  $\nabla_{\text{T}}^2$  is the transverse Laplacian operator and  $\Delta k = k_n - k'_n$  is the wavevector mismatch. Using the slowly varying amplitude approximation, which assumes that the longitudinal variation of  $A_n$  is only significant on length scales much larger than the wavelength,

$$\left|\frac{\partial^2 A_n}{\partial z^2}\right| \ll \left|k_n \frac{\partial A_n}{\partial z}\right|, \quad (7.5)$$

the second partial derivative to  $z$  in the first term of (7.4) can be neglected [145, 165]. Furthermore, using the definition  $k_n \equiv n_n \omega_n / c$ , equation (7.4) is simplified to

$$\left(2ik_n \frac{\partial}{\partial z} + \nabla_{\text{T}}^2\right) A_n(\mathbf{r}) = -\frac{\omega_n^2}{\varepsilon_0 c^2} p_n(\mathbf{r}) \exp(-i\Delta k z), \quad (7.6)$$

The amplitude of the induced polarisation that produces the coherent IR wave in CRS-based four-wave mixing is given by [145, 165]

$$p_{\text{IR}} = 3\varepsilon_0\chi_{\text{IR}}^{(3)} A_1(\mathbf{r})A_2^*(\mathbf{r})E(\mathbf{r}), \quad (7.7)$$

where  $\chi_{\text{IR}}^{(3)}$  is the third-order non-linear susceptibility corresponding to the interaction,  $A_1$  is the amplitude of the incident pump beam,  $A_2^*$  is the complex conjugate of the amplitude of the Stokes beam, and  $E$  is the amplitude of the external electric field. It should be noted that the value of the pre-factor in (7.7) depends on the definition of the fields in (7.2) and (7.3) [165]. For the case in which  $\text{N}_2$  gas is used as a medium, and a frequency doubled Nd:YAG laser as pump laser beam, the wavevector mismatch for CRS-based four-wave mixing was calculated in chapter 6 as

$$\Delta k_{\text{IR}} = k_{\text{IR}} - k_1 + k_2 \approx -0.2 \text{ cm}^{-1}, \quad (7.8)$$

which corresponds to a coherence length of the process of  $L_{\text{IR}}^{\text{coh}} = \pi/|\Delta k_{\text{IR}}| \approx 16 \text{ cm}$ .

For the amplitude of the induced polarisation that generates the SH wave in SHG-based four-wave mixing, an expression similar to (7.7) can be given [145, 165]:

$$p_{\text{SH}} = \frac{3}{2}\varepsilon_0\chi_{\text{SH}}^{(3)} A_1^2(\mathbf{r})E(\mathbf{r}). \quad (7.9)$$

The factor 2 difference in pre-factor between the IR and SHG polarisation is related to the number of possible permutations of the involved incident wave frequencies. When  $\text{N}_2$  gas is used as a medium, and the fundamental beam of a Nd:YAG laser as pump beam, the wavevector mismatch is

$$\Delta k_{\text{SH}} = k_{\text{SH}} - 2k_1 = 2\omega_1(n_{\text{SH}} - n_1)/c \approx 0.5 \text{ cm}^{-1}. \quad (7.10)$$

This value is calculated using refractive indices from [166] and corresponds to a coherence length of  $L_{\text{SH}}^{\text{coh}} = \pi/|\Delta k_{\text{SH}}| \approx 6 \text{ cm}$ .

With knowledge of the amplitudes of the incident beams and the electric field distribution, (7.6) and (7.9) provide the means to determine the generated IR and SH waves. This is done in the next section for the IR waves generated in CRS-based four-wave mixing using plane waves, as well as Gaussian beams. For simplicity, it will be assumed that the electric field only depends on the longitudinal coordinate along the laser beams:  $E(\mathbf{r}) = E(z)$ .

## 7.2.2 Plane-wave solution

In the plane-wave approximation, the incident beams are infinitely large and have a flat wave-front. This means that the amplitudes  $A_1$  and  $A_2$  are independent of spatial coordinates. The amplitude of the IR polarisation of (7.7) can then be written as

$$p_{\text{IR}}(z) = 3\varepsilon_0\chi_{\text{IR}}^{(3)} A_1 A_2^* E(z). \quad (7.11)$$

Since the polarisation only depends on  $z$ , the IR amplitude  $A_{\text{IR}} = A_{\text{IR}}(z)$  will also only depend on  $z$ . In this case, the transverse Laplacian in (7.6) is zero and the differential

equation for  $A_{\text{IR}}$  reduces to

$$\frac{d}{dz} A_{\text{IR}}(z) = i \frac{3}{2} \frac{\omega_{\text{IR}}}{n_{\text{IR}} c} \chi_{\text{IR}}^{(3)} A_1 A_2^* E(z) \exp(-i \Delta k_{\text{IR}} z). \quad (7.12)$$

This is the same equation as (6.2) that was used in chapter 6. The amplitude of the IR wave is now obtained by direct integration,

$$A_{\text{IR}}(z) = i \frac{3}{2} \frac{\omega_{\text{IR}}}{n_{\text{IR}} c} \chi_{\text{IR}}^{(3)} A_1 A_2^* \int_{-\infty}^z E(z') \exp(-i \Delta k_{\text{IR}} z') dz'. \quad (7.13)$$

Finally, the intensity of the IR wave can be calculated using  $I = c \varepsilon_0 n_{\text{IR}} |A|^2 / 2$  as

$$I_{\text{IR}}(z) = \frac{9}{2} \frac{\omega_{\text{IR}}^2}{\varepsilon_0 c^3 n_1 n_2 n_{\text{IR}}} |\chi_{\text{IR}}^{(3)}|^2 I_1 I_2 \left( \int_{-\infty}^z E(z') \exp(-i \Delta k_{\text{IR}} z') dz' \right)^2, \quad (7.14)$$

where  $I_1$  and  $I_2$  are the intensities of the incident pump and Stokes beams respectively.

In section 7.3, a simple uniform electric field of width  $L$ ,

$$E(z) = \begin{cases} E_0, & \text{for } |z| \leq L/2 \\ 0, & \text{otherwise} \end{cases}, \quad (7.15)$$

will be used to compare this plane-wave solution to a Gaussian beam solution, which will be discussed shortly. For such an electric field, the integral in (7.14) can be evaluated analytically [145, 165]. The final intensity that is achieved in this case,  $I_{\text{IR}}(L/2)$ , is given by

$$I_{\text{IR}}(L/2) = \frac{9}{2} \frac{\omega_{\text{IR}}^2}{\varepsilon_0 c^3 n_1 n_2 n_{\text{IR}}} |\chi_{\text{IR}}^{(3)}|^2 I_1 I_2 E_0^2 \left( \int_{-L/2}^{L/2} \exp(-i \Delta k_{\text{IR}} z') dz' \right)^2 \quad (7.16)$$

$$= \frac{9}{2} \frac{\omega_{\text{IR}}^2}{\varepsilon_0 c^3 n_1 n_2 n_{\text{IR}}} |\chi_{\text{IR}}^{(3)}|^2 I_1 I_2 E_0^2 L^2 \text{sinc}^2 \left( \frac{\Delta k_{\text{IR}} L}{2} \right). \quad (7.17)$$

### 7.2.3 Gaussian beam solution

Instead of using plane-waves to describe the incident waves, they are now treated as focused Gaussian beams. Gaussian beams are characterised by a transverse Gaussian amplitude distribution that is given by [145, 165]

$$A(r, z) = A_0 \frac{w_0}{w(z)} \exp\left(\frac{-r^2}{w^2(z)}\right) \exp\left(\frac{ikr^2}{2R(z)}\right) \exp(-i\Phi(z)), \quad (7.18)$$

where

$$w(z) = w_0 \left[ 1 + \left( \frac{z}{z_{\text{R}}} \right)^2 \right]^{1/2} \quad (7.19)$$

is the waist function, which describes the  $1/e$  amplitude radius of the field distribution,

$$R(z) = z \left[ 1 + \left( \frac{z_{\text{R}}}{z} \right)^2 \right] \quad (7.20)$$

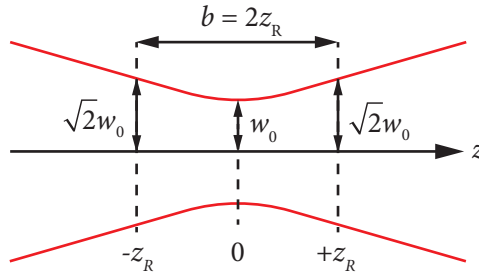


**Figure 7.3:** Illustration of a focused Gaussian beam. The red lines represent the waist function  $w(z)$  of the beam. The waist size at the focus  $w_0$ , and the waist size at one Rayleigh length  $z_R$  from the focus are indicated.

is the curvature of the wavefront, and

$$\Phi(z) = \arctan\left(\frac{z}{z_R}\right) \quad (7.21)$$

is the so-called Gouy phase. In these equations, the parameter  $z_R$  is the Rayleigh length, which is given by

$$z_R = \frac{\pi w_0^2}{\lambda} = \frac{1}{2} k w_0^2, \quad (7.22)$$

where  $w_0$  is the  $1/e$  radius at the focus and  $\lambda$  the wavelength of the beam. The Rayleigh length indicates the distance from the focal spot where the  $1/e$  radius has increased by a factor of  $\sqrt{2}$ . A quantity related to the Rayleigh length is the confocal parameter  $b = 2z_R$ , which represents the region within the Rayleigh length on both sides of the focus. A schematic drawing of a Gaussian beam illustrating these quantities is shown in figure 7.3.

For theoretical work, the Gaussian amplitude distribution of (7.18) is usually written in a less intuitive but more compact form as [145, 165]

$$A_n(r, z) = \frac{\mathcal{A}_n}{(1 + i\zeta_n)} \exp\left[\frac{-k_n r^2}{b_n(1 + i\zeta_n)}\right], \quad (7.23)$$

where  $\mathcal{A}_n$  is the amplitude at the centre of the focal plane (at  $r = z = 0$ ),  $b_n$  is the earlier mentioned confocal parameter, and  $\zeta_n = 2z/b_n$  is a dimensionless longitudinal coordinate.

With incident Gaussian wave amplitudes  $A_1(r, z)$  and  $A_2(r, z)$ , the amplitude of the IR polarisation of (7.7) becomes

$$p_{\text{IR}}(r, z) = 3\epsilon_0 \chi_{\text{IR}}^{(3)} A_1(r, z) A_2^*(r, z) E(z) \quad (7.24)$$

$$= 3\epsilon_0 \chi_{\text{IR}}^{(3)} \frac{\mathcal{A}_1 \mathcal{A}_2^*}{(1 + i\zeta_1)(1 - i\zeta_2)} \exp\left[\frac{-k_1 r^2}{b_1(1 + i\zeta_1)}\right] \exp\left[\frac{-k_2 r^2}{b_2(1 - i\zeta_2)}\right]. \quad (7.25)$$

Since the IR polarisation now depends on the radial coordinate, the IR amplitude will also depend on the radial coordinate. Therefore, the transverse Laplacian in (7.6)

cannot be disregarded in this case, and the wave-equation that needs to be solved remains

$$\left(2ik_{\text{IR}}\frac{\partial}{\partial z} + \nabla_{\text{T}}^2\right) A_{\text{IR}}(r, z) = -\frac{\omega_{\text{IR}}^2}{\epsilon_0 c^2} p_{\text{IR}}(r, z) \exp(-i\Delta k_{\text{IR}}z). \quad (7.26)$$

Solving for  $A_{\text{IR}}(r, z)$  is now more difficult than it was in the case of the plane-wave approximation. An approach similar to that applied by Bjorklund [167] and Moosmüller *et al* [168] is followed.

First, the Hankel transform of order zero,  $\mathcal{H}_0$ , will be applied to the wave-equation. This transform is defined as [169]

$$\tilde{f}(K) = \mathcal{H}_0[f(r)] = \int_0^\infty f(r) J_0(Kr) r dr, \quad (7.27)$$

where  $J_0$  is the zeroth-order Bessel function of the first kind. The Hankel transform takes functions from radial space  $r$  into radial wavevector space  $K$ . The transformed wave-equation is given by [168]

$$\left(2ik_{\text{IR}}\frac{\partial}{\partial z} - K^2\right) \tilde{A}_{\text{IR}}(K, z) = -\frac{\omega_{\text{IR}}^2}{\epsilon_0 c^2} \tilde{p}_{\text{IR}}(K, z) \exp(-i\Delta k_{\text{IR}}z). \quad (7.28)$$

In fact, the Hankel transform of  $p_{\text{IR}}$  can be performed analytically in this case and results in

$$\begin{aligned} \tilde{p}_{\text{IR}}(K, z) = & \frac{3}{2} \epsilon_0 \chi_{\text{IR}}^{(3)} \frac{\mathcal{A}_1 \mathcal{A}_2^*}{(1 + i\zeta_1)(1 - i\zeta_2)} \frac{b_1 b_2 (1 + i\zeta_1)(1 - i\zeta_2)}{k_1 b_2 (1 - i\zeta_2) + k_2 b_1 (1 + i\zeta_1)} \\ & \times \exp\left[-\frac{b_1 b_2 (1 + i\zeta_1)(1 - i\zeta_2)}{4k_1 b_2 (1 - i\zeta_2) + 4k_2 b_1 (1 + i\zeta_1)} K^2\right] E(z). \end{aligned} \quad (7.29)$$

Next, by multiplying both sides of (7.28) by  $(2ik_{\text{IR}})^{-1} \exp(iK^2z/2k_{\text{IR}})$ , the left-hand side can be written as a single derivative term, and the equation becomes

$$\begin{aligned} \frac{\partial}{\partial z} \left( \tilde{A}_{\text{IR}}(K, z) \exp\left[\frac{iK^2z}{2k_{\text{IR}}}\right] \right) = \\ i \frac{\omega_{\text{IR}}^2}{2k_{\text{IR}} \epsilon_0 c^2} \exp\left[\frac{iK^2z}{2k_{\text{IR}}}\right] \tilde{p}_{\text{IR}}(K, z) \exp(-i\Delta k_{\text{IR}}z). \end{aligned} \quad (7.30)$$

This expression can be integrated with respect to  $z$  and rearranged to result in

$$\begin{aligned} \tilde{A}_{\text{IR}}(K, z) = \\ i \frac{\omega_{\text{IR}}^2}{2k_{\text{IR}} \epsilon_0 c^2} \exp\left[-\frac{iK^2z}{2k_{\text{IR}}}\right] \int_{-\infty}^z \exp\left[\frac{iK^2z'}{2k_{\text{IR}}}\right] \tilde{p}_{\text{IR}}(K, z') \exp(-i\Delta k_{\text{IR}}z') dz'. \end{aligned} \quad (7.31)$$

Together, (7.29) and (7.31) provide everything required to (numerically) calculate the Hankel transformed amplitude of the IR wave for a given electric field  $E(z)$ . If we would like to know the spatial properties of the IR wave, an inverse Hankel transform



could be applied to (7.31). However, as will be shown, an inverse Hankel transform is not necessary to obtain the power contained in the IR beam.

Similar to the plane-wave case, the intensity in the IR wave is given by

$$I_{\text{IR}}(r, z) = \frac{1}{2} c \varepsilon_0 n_{\text{IR}} |A_{\text{IR}}(r, z)|^2. \quad (7.32)$$

This time the intensity also depends on the radial coordinate, and it is more convenient to consider the generated power  $\mathcal{P}_{\text{IR}}(z)$  instead. This is obtained by integrating the intensity over its transverse cross-sectional area

$$\mathcal{P}_{\text{IR}}(z) = 2\pi \int_0^\infty I_{\text{IR}}(r, z) r \, dr = \pi c \varepsilon_0 n_{\text{IR}} \int_0^\infty |A_{\text{IR}}(r, z)|^2 r \, dr. \quad (7.33)$$

Finally, Parseval's theorem [169],

$$\int_0^\infty |A_{\text{IR}}(r, z)|^2 r \, dr = \int_0^\infty |\tilde{A}_{\text{IR}}(K, z)|^2 K \, dK, \quad (7.34)$$

is invoked to change the integral over the IR amplitude in (7.33) to an integral over the Hankel transformed IR amplitude:

$$\mathcal{P}_{\text{IR}}(z) = \pi c \varepsilon_0 n_{\text{IR}} \int_0^\infty |\tilde{A}_{\text{IR}}(K, z)|^2 K \, dK. \quad (7.35)$$

In the case of the simple electric field distribution of (7.36), which will be used in the next section to compare the plane-wave solution and the Gaussian beam solution, the final power that is achieved in the IR wave is  $\mathcal{P}_{\text{IR}}(L/2)$ . When calculating this power value for this field distribution, the lower limit of  $-\infty$  in the integral in (7.31) can be replaced by  $-L/2$ .

Before moving on, it should be noted that while Gaussian beams certainly describe focused laser beams more accurately than the plane-wave approximation, it is still an approximation itself nonetheless. In reality, laser beams generally do usually not consist of just the fundamental Gaussian beam. Other possible modes that may be present are for example Hermite-Gaussian or Laguerre-Gaussian beams [170]. In principle, these modes could be introduced in the derived equations to investigate the effects of deviations caused by higher order modes. The only change that has to be made is that the Hankel transform introduced in (7.28) needs to be replaced by a 2D Fourier transform in the case that one of the modes is not cylindrically symmetric.

### 7.3 Validity of the plane-wave approximation

To assess when the plane-wave approximation is valid and how large the errors are compared to the Gaussian beam approximation, the generated IR waves from the plane-wave solution and from the Gaussian beam solution are compared. As mentioned before, this is done for a simple field described by

$$E(z) = \begin{cases} E_0, & \text{for } |z| \leq L/2 \\ 0, & \text{otherwise} \end{cases}. \quad (7.36)$$

However, the plane-wave solution is given in terms of intensity, while the Gaussian beam solution is given in terms of power. To obtain a power value from the plane-wave solution that corresponds to the situation of a specific Gaussian solution, the plane-wave IR intensity  $I_{\text{IR}}^{\text{PW}}$  obtained from (7.14) has to be multiplied by an effective area  $a_{\text{eff}}$  defined as

$$a_{\text{eff}} = 2\pi \int_0^\infty \exp\left(-\frac{2r^2}{w_{01}^2}\right) \exp\left(-\frac{2r^2}{w_{02}^2}\right) r \, dr = \frac{\pi}{2} \frac{w_{01}^2 w_{02}^2}{w_{01}^2 + w_{02}^2}, \quad (7.37)$$

where the exponents in the integral represent the intensity distribution of the incident Gaussian beams at their waists ( $z = 0$ ). For the purpose of comparison, it is more convenient to divide the IR power of the Gaussian solution  $\mathcal{P}_{\text{IR}}^{\text{GB}}$  by  $a_{\text{eff}}$ , because this keeps the solution for the plane-waves independent of the parameters of the Gaussian beams. Doing so results in an ‘effective intensity’ for the Gaussian solution,

$$I_{\text{IR}}^{\text{GB}} = \mathcal{P}_{\text{IR}}^{\text{GB}} / a_{\text{eff}}. \quad (7.38)$$

The power of the Gaussian solution,  $\mathcal{P}_{\text{IR}}^{\text{GB}}$ , is numerically calculated from (7.35). MATLAB’s `integral` function is utilised to perform the numerical integration using global adaptive quadrature.

In the limit  $z_{\text{R}} \rightarrow \infty$ , Gaussian beams become plane-waves. Therefore, the IR intensity calculated using the Gaussian beam solution should converge to the plane-wave solution for large Rayleigh lengths. To test the numerical implementation of the Gaussian solution, the calculated IR intensity for large Rayleigh lengths is compared to that obtained from the plane-wave solution. This is done for electric fields distributions with  $L = 0$  to  $L > 2L_{\text{IR}}^{\text{coh}} \approx 32$  cm. This way, the phase matching behaviour of Gaussian beams can be inspected simultaneously. The Rayleigh length of the pump beam and of the Stokes beam are kept equal for now:  $z_{\text{R}1} = z_{\text{R}2} = z_{\text{R}}$ .

The results of this test case are shown in figure 7.4. Most importantly, it can be seen that the IR intensity calculated from the Gaussian beam solution indeed converges to the plane-wave solution for large Rayleigh lengths. Also, the correct phase matching behaviour is displayed: first the IR intensity increases for larger  $L$  until the coherence length is reached, and then it decreases when  $L$  is further increased. The reason for this is that the wavevector mismatch causes a progressively larger phase mismatch between the IR polarisation wave and the IR wave itself. At the coherence length, the IR polarisation starts to contribute destructively to the existing IR wave and hence its intensity decreases. In fact, at twice the coherence length, the entire IR wave has been completely cancelled out. For shorter Rayleigh lengths the maximum occurs at a length shorter than the coherence length. This is caused by additional phase shifts in the Gaussian beam amplitudes. Furthermore, when the Rayleigh length becomes shorter, contributions to the IR wave, either constructively or destructively, further from the focus also become less significant. For this reason, the IR wave does not entirely cancel out anymore in the case of  $z_{\text{R}} = 1$  m for example.

In practice, Rayleigh lengths of the order of 1 mm to 10 mm are typically used in electric field four-wave mixing experiments. The spatial extent of the electric fields is generally also much shorter than the coherence length, in which case phase-matching effects can be ignored. Therefore, these more typical values are used for further analysis.

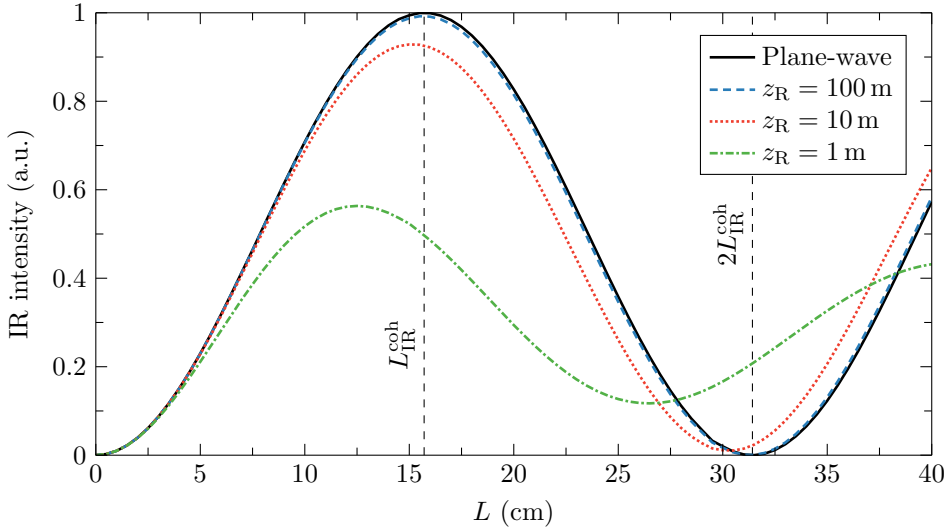


**Figure 7.4:** Comparison of the IR intensity calculated using the plane-wave approximation and using Gaussian beams for large Rayleigh lengths. The vertical dashed lines indicate the coherence length and twice the coherence length.

In figure 7.5, the IR intensity as a function of  $L$  obtained from the plane-wave solution is compared to the Gaussian solution for several Rayleigh lengths. The plane-wave solution exhibits the quadratic dependence on  $L$  that is expected from (7.17) when phase matching can be ignored. In contrast, the Gaussian solutions show a more linear behaviour. The values of the IR intensity are also significantly smaller when Gaussian beams are used. For example, it can be seen that for  $z_R = 20$  mm there is already a factor of approximately 4 difference between the plane-wave solution and the Gaussian beam solution at  $L = z_R$ . The relative error in the plane-wave solution compared to the Gaussian beam solution,  $|I_{\text{IR}}^{\text{GB}} - I_{\text{IR}}^{\text{PW}}|/I_{\text{IR}}^{\text{GB}}$ , is plotted in figure 7.6 as a function of the electric field dimension scaled to the Rayleigh length,  $L/z_R$ . It can now be clearly seen that errors smaller than 10% are obtained using the plane-wave approximation only when the dimension of the electric field is smaller than 10% of the Rayleigh length ( $L/z_R < 0.1$ ). An electric field with the size of the confocal parameter ( $L/z_R = 2$ ) results in nearly an order of magnitude error in the IR intensity.

To explain the implications this might have on measured electric field values, the situation of chapter 6 is considered. In this case, electric field integrals were determined from measured intensities of the pump beam, the CARS beam and the IR beam according to (6.8):

$$\left| \int E \, dz \right| = C_{\text{cal}} \sqrt{I_1 \frac{I_{\text{IR}}}{I_{\text{CARS}}}}. \quad (7.39)$$

In this equation,  $C_{\text{cal}}$  is a calibration constant that was determined by performing the measurements in a known, in this case from numerical simulation, calibration electric

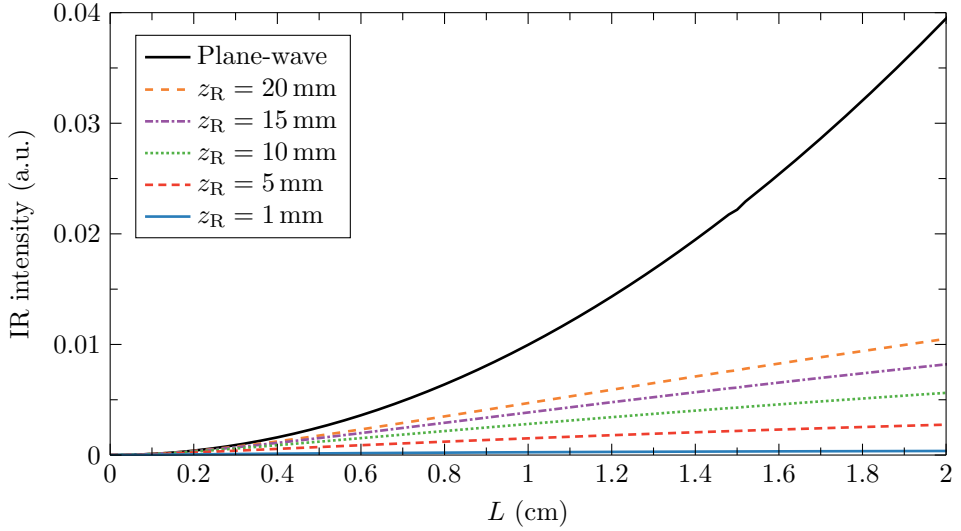


**Figure 7.5:** Comparison of the IR intensity calculated using the plane-wave approximation and using Gaussian beams of several different Rayleigh lengths.

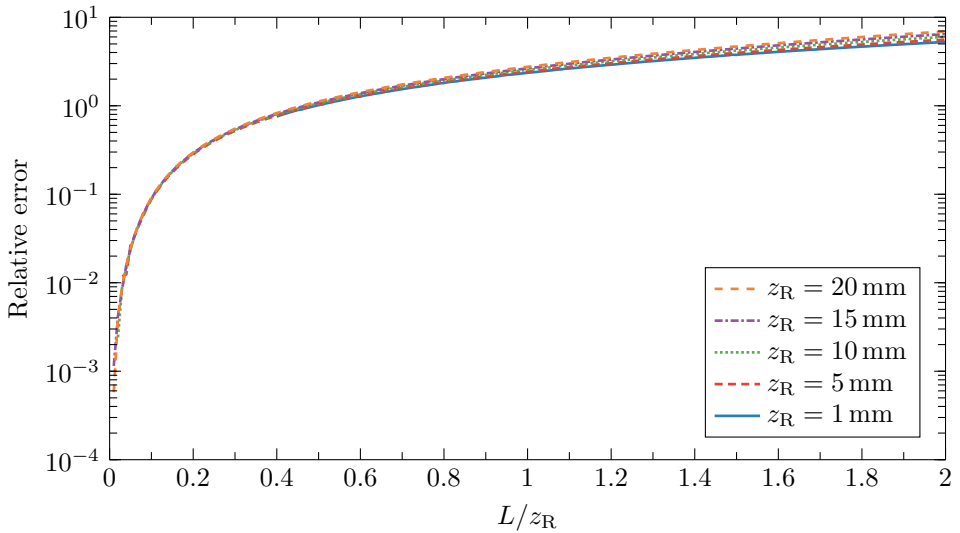


**Figure 7.6:** Relative error in the calculated IR intensity between the plane-wave solution and the Gaussian beam solution for several different Rayleigh lengths.

field distribution  $E_{\text{cal}}$ :

$$C_{\text{cal}} = \frac{|\int E_{\text{cal}} dz|}{\sqrt{I_1 I_{\text{IR}}/I_{\text{CARS}}}}. \quad (7.40)$$

Both equations are derived using the plane-wave approximation (see chapter 6 for more details). Basically, the integral over the calibration field in the numerator of (7.40) is a measure for how much IR light the calibration field would produce according to the plane-wave approximation. As was demonstrated in figure 7.5 and figure 7.6, unless the spatial dimension of the calibration field is much smaller than the Rayleigh length of the lasers, the generated IR intensity is overestimated by the plane-wave approximation. This also means that the calibration field integral in (7.40) is overestimated, which leads to an overestimation of the calibration constant. Subsequently, if the dimension of the electric field to be measured is significantly smaller than the dimension of the calibration field, this will result in too high measured electric field values. However, it should be noted that the overestimation in the calibration field integral, and hence in the calibration constant, is less severe than the overestimation in the IR intensity itself. This is because the field integral depends on the square root of the IR intensity, as shown in (7.39).

## 7.4 Revisiting the plasma bullet measurements

In chapter 6, the electric fields of plasma bullets in  $\text{N}_2$  were measured and compared to those obtained from a numerical model. It was found that the measured peak value was approximately a factor 2 higher than that predicted by the model. In the discussion of chapter 6, it was already hypothesised that this might be, at least partly, due to deviations from the plane-wave approximation in the calibration measurement. With the knowledge acquired in the present work, we now have the means to verify whether this is the case.

As mentioned in table 6.1 in chapter 6, the Rayleigh lengths of the used pump and Stokes lasers are  $z_{\text{R1}} = 14$  mm and  $z_{\text{R2}} = 24$  mm respectively. The calibration was performed in the electric field between two  $19 \text{ mm} \times 19 \text{ mm}$  parallel plate electrodes with a gap of 3.1 mm. The resulting distribution of the calibration field was shown in figure 6.6. In figure 7.7, the electric field along the laser beam is illustrated. Calculating the IR intensity using both the plane-wave solution and the Gaussian beam solution for these Rayleigh lengths and this electric field distribution results in  $I_{\text{IR}}^{\text{PW}}/I_{\text{IR}}^{\text{GB}} \approx 3.9$ . This means that the calculated IR intensity is overestimated by a factor 3.9, and hence that the calibration field and the calibration constant are overestimated by a factor  $\sqrt{3.9} \approx 2$ . When this is corrected for in the calibration constant, the peak value obtained from the model falls between the peak values determined from the four-wave mixing experiment, as shown in figure 7.8. Scaling does however not change the profile of the measured electric field, and the possible causes for this difference that were discussed in chapter 6 still stand. Nevertheless, this result does verify that the plane-wave approximation indeed introduced an error in the calibration constant.

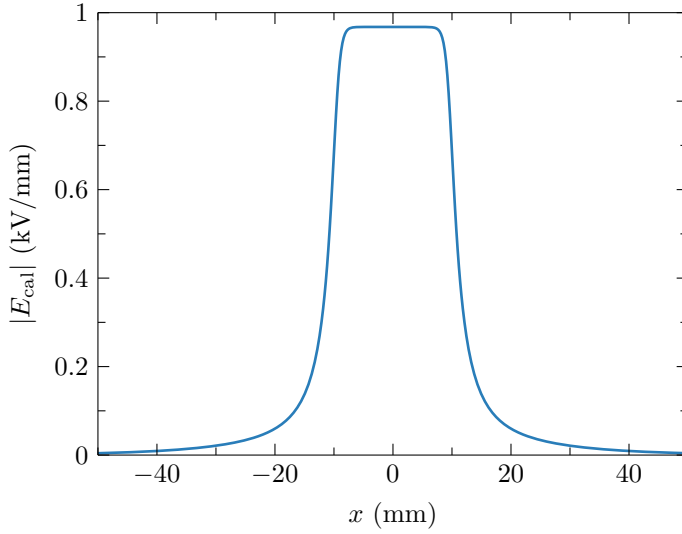


**Figure 7.7:** Calibration field distribution used in the measurements of chapter 6.

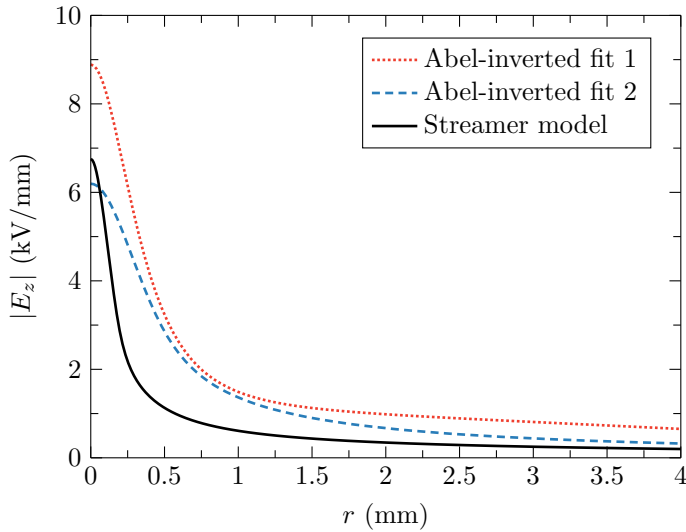


**Figure 7.8:** Comparison between the results obtained from the experiment in chapter 6, with a corrected calibration constant, and the model convolved with the laser beam profiles.

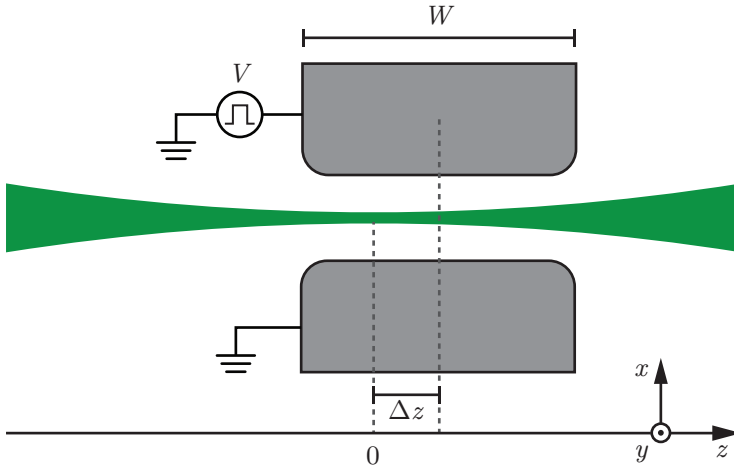


**Figure 7.9:** Schematic illustration of the experiment. The electrodes are indicated in grey. The incident focused laser beams are depicted in green, and their focal points are located at  $z = 0$ . The centre of the electrodes is displaced by  $\Delta z$  from the focal point of the lasers.

## 7.5 Experimental test of the Gaussian beam solution

As mentioned before, the Gaussian beam solution itself is also an approximation, and real laser beams generally have some higher-order components. To test how well the Gaussian solution represents the beams in a real setup, the experiment illustrated in figure 7.9 is performed. Two parallel plate electrodes of width  $W$  are placed around the focused laser beams, centred at the focal spot at  $z = 0$ , such that their electric field is directed along the  $x$ -axis. The electrodes are then translated along the laser beam's propagation axis, i.e. the  $z$ -axis. The measured response  $I_1 I_{\text{IR}} / I_{\text{CARS}}$  is compared to the calculated IR intensity, using (7.35) and (7.38), as a function of the electrode displacement  $\Delta z$ .

The laser setup used for this test is nearly identical to the one described in chapter 6. The main differences are the used lasers and their beam properties, and the focusing lens. The primary laser is an unseeded frequency doubled Nd:YAG laser (Quantel Q-smart 450), which provides the pump beam for the experiment at  $\lambda_1 = 532$  nm. This laser also pumps a dye laser (Sirah CBR-LG-2400), which produces the Stokes beam at  $\lambda_2 = 607$  nm for the experiment. The pump and Stokes beams are focussed collinearly by an  $f = 200$  mm air-spaced achromatic doublet (Thorlabs ACA254-200-A). The spatial properties of the focused beams are determined from multiple horizontal ( $x$ -direction) and vertical ( $y$ -direction) knife-edge measurements along the laser beams. The waist radii, effective Rayleigh lengths, and beam propagation factors  $M^2$ , which is sometimes called the beam quality factor [171], of the beams are listed in table 7.1. It should be noted that the effective Rayleigh lengths  $z_{\text{R,eff}} = z_{\text{R}} / M^2$  are substantially shorter than the Rayleigh lengths in the setup that was used in chapter 6

**Table 7.1:** Waist radii, effective Rayleigh lengths and  $M^2$ -factors of the focused laser beams obtained from multiple knife-edge measurements.

Laser	Direction	$w_0$ ( $\mu\text{m}$ )	$z_{\text{R,eff}}$ (mm)	$M^2$
Nd:YAG	horizontal ( $x$ )	$25 \pm 2$	$1.7 \pm 0.2$	$2.2 \pm 0.4$
	vertical ( $y$ )	$27 \pm 2$	$1.7 \pm 0.2$	$2.5 \pm 0.4$
Dye	horizontal ( $x$ )	$22 \pm 3$	$1.3 \pm 0.2$	$2.0 \pm 0.6$
	vertical ( $y$ )	$51 \pm 2$	$3.3 \pm 0.2$	$4.1 \pm 0.4$

(see table 6.1). Additionally, from the waist radii of the dye laser, it can be seen that its beam profile is elliptical. This is a result of the design of the dye cell in the dye laser.

Five sets of electrodes with different widths  $W$  are used. Each of the used widths is greater than the Rayleigh lengths of the lasers. The gap between the electrodes is 3 mm and the corners of the electrodes are rounded and have a radius of 0.5 mm to reduce field amplification. The results of the measurements are shown in figure 7.10. Since the electric field of the parallel plate electrodes is directed along the  $x$ -axis, the horizontal properties of the laser beams are used in the calculation of the IR intensity. Moreover, the electric fields for the calculations are obtained from an electrostatic model of the electrodes in COMSOL. The results of the calculations for a wavevector mismatch of  $\Delta k_{\text{IR}} = -0.2 \text{ cm}^{-1}$  are shown in figure 7.11. For the largest two electrodes, 35 mm and 45 mm, the same qualitative behaviour can be observed in both the measurements and the calculations. There is a local minimum IR intensity value in the centre ( $z = 0$ ) that is approximately the same for these two electrode widths. When the electrode is displaced from the centre, the IR intensity first increases and then decreases. This behaviour is a combined result of the wavevector mismatch and the phase shifts of the incident beams. To illustrate, the Gouy phases of the incident waves result in a phase shift in the IR polarisation of (7.25) along the  $z$ -axis of

$$\Phi_2(z) - \Phi_1(z) = \arctan\left(\frac{z}{z_{\text{R}2}}\right) - \arctan\left(\frac{z}{z_{\text{R}1}}\right). \quad (7.41)$$

Unless the two incident waves have the same Rayleigh length, this causes a phase shift in the region close to the focus.

For the two shortest electrodes, 10 mm and 15 mm, the measurements in figure 7.10 demonstrate that there is also a minimum at the centre position  $\Delta z = 0$ . However, this behaviour is not predicted by the Gaussian beam solution in figure 7.11. To see whether this could be due to an underestimation of the wavevector mismatch, the calculations are repeated with a larger wavevector mismatch of  $-0.4 \text{ cm}^{-1}$ . The results are shown in figure 7.12. Although the behaviour changes, there is still no local minimum in the curves for the shortest electrode width. Moreover, the curve for  $W = 45 \text{ mm}$  now becomes lower than the curve for  $W = 35 \text{ mm}$ , which is not the case in the measurements. This leads to the conclusion that the behaviour observed in the measurements cannot only be attributed to a larger wavevector mismatch. Furthermore, an additional calculation, where the entire electric field distribution was



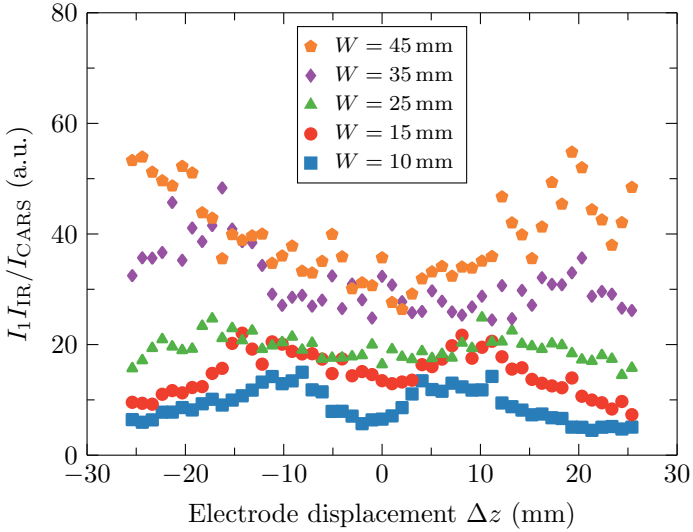


**Figure 7.10:** Measured intensity ratios as a function of the electrode displacement for several electrode widths.

accounted for, was performed to rule out that this is caused by field amplification at the edges of the electrodes.

This leads us to believe that higher order modes that are present in the laser beams might cause the observed behaviour for  $W = 10$  mm and  $W = 15$  mm. In fact, beam propagation factors of  $M^2 = 2.2 \pm 0.4$  and  $M^2 = 2.0 \pm 0.6$  were found for the pump laser and the Stokes laser in the horizontal direction respectively (see table 7.1). Fundamental Gaussian beams are characterised by  $M^2 = 1$ , and  $M^2 > 1$  indicates that higher order modes are present [171]. While the radius of curvature remains the same for higher order modes, they exhibit larger Gouy phase shifts. For example, the Gouy phase of the Hermite-Gaussian  $\text{TEM}_{mn}$  modes is given by [172]

$$\Phi_{mn}(z) = (m + n + 1) \arctan\left(\frac{z}{z_R}\right), \quad (7.42)$$

where  $m$  and  $n$  are the transverse mode numbers. Similarly, the Gouy phase for the Laguerre-Gaussian  $\text{TEM}_{pl}$  modes is given by [172]

$$\Phi_{pl}(z) = (2p + l + 1) \arctan\left(\frac{z}{z_R}\right), \quad (7.43)$$

where  $p$  and  $l$  are the radial and angular mode numbers.

If these results are indeed caused by the Gouy phases of higher order modes, such effects will be even more pronounced in the case of SHG-based four-wave mixing. The reason for this is that the combined Gouy phase  $\Phi_{\text{tot}}$  of the incident waves in the SH

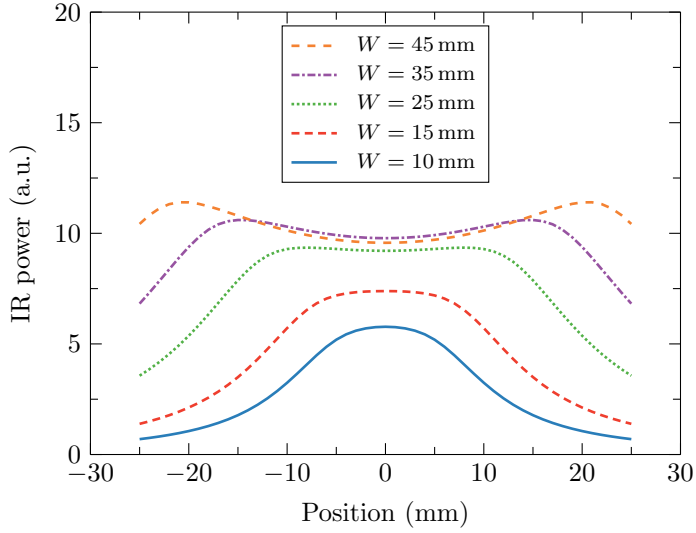


**Figure 7.11:** Calculated IR intensities as a function of the electrode displacement for a wavevector mismatch of  $\Delta k_{\text{IR}} = -0.2 \text{ cm}^{-1}$  and several electrode widths.

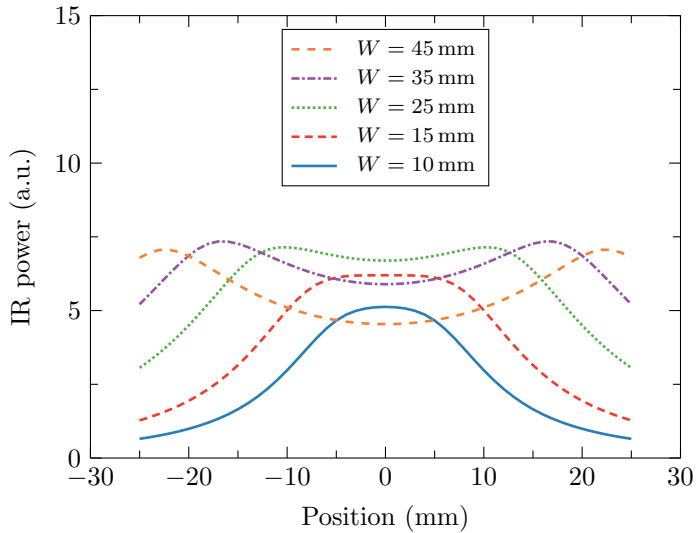


**Figure 7.12:** Calculated IR intensities as a function of the electrode displacement for a wavevector mismatch of  $\Delta k_{\text{IR}} = -0.4 \text{ cm}^{-1}$  and several electrode widths.

polarisation of (7.9) is given by

$$\Phi_{\text{tot}} = -2\Phi_1(z) = -2 \arctan\left(\frac{z}{z_{R1}}\right). \quad (7.44)$$

Whereas the Gouy phases of the incident waves in CRS-based four-wave mixing can (partly) cancel, this is not the case in SHG-based four-wave mixing.

## 7.6 Conclusions and outlook

In this work, a theoretical description of electric field four-wave mixing using Gaussian beams is given. The focus is on the CRS-based four-wave mixing method, but the developed theory can easily be adapted to the SHG-based four-wave mixing method. With this, the validity of the plane-wave approximation that is used in the analysis of electric field four-wave mixing experiments can be assessed, and the corresponding errors can be quantified. It is found that the IR intensity generated in the CRS-based four-wave mixing method calculated using the plane-wave approximation is accurate to within 10% when the typical spatial dimension of the electric field is smaller than 10% of the Rayleigh length of the lasers. Significant errors are introduced in the measured electric field values when the calibration measurement is performed using an electric field that has a spatial dimension of the order of the Rayleigh length and is larger than the electric field to be measured. For the measurements presented in chapter 6, it was determined that this led to a factor 2 error in the electric field values. Nevertheless, Gaussian beams are still an approximation to the real beams, and in reality higher order modes may be present. By translating two parallel plane electrodes along the laser beams, the behaviour predicted of the Gaussian beam solution is tested. Some behaviour that could not be explained by Gaussian beams was observed and is possibly related to higher order modes. Further investigation is required to confirm this.

## **Chapter 8**

---

# **General conclusions and recommendations**

In this work, multiple aspects of the physics of pulsed plasma jets have been investigated using various experimental techniques. The results of the performed research are presented in this thesis and have led to a greater understanding of the properties and physical mechanisms of guided streamer discharges produced in pulsed plasma jets. The most important conclusions are reviewed here.

### Reproducibility of pulsed plasma jets

One of the most notable properties of pulsed plasma jets is the fact that, under the right conditions, they produce highly reproducible guided streamers. The reproducibility of guided streamers in pulsed plasma jets in pure N<sub>2</sub>, He and Ar feed gas flowing into ambient air has been quantified using intensified charge-coupled device (ICCD) imaging and time-resolved emission measurements.

- Pulsed plasma jets in N<sub>2</sub> feed gas flowing into ambient air consist of guided streamer discharges with a radius of  $140 \pm 10 \mu\text{m}$  that travel along the centre of the jet. The spatial reproducibility of the discharge path is  $13 \mu\text{m}$ , and a temporal reproducibility of the inception of down to 500 ps can be achieved. It is proposed that the stable core of the flow, where the streamer propagates, plays a significant role in spatial reproducibility.
- Pulsed plasma jets in He feed gas flowing into ambient air consist of guided streamer discharges that propagate along the gas mixing layer, resulting in an annular discharge structure close to the nozzle. Because the discharge travels along the gas mixing layer, its position is prone to instabilities, which limits the spatial reproducibility. A temporal reproducibility of the inception of down to 500 ps can be achieved, similar to the case of N<sub>2</sub>.
- Pulsed plasma jets in Ar feed gas flowing into ambient air consist of either guided streamer discharges that propagate on the centre of the jet until they branch to the gas mixing layer at lower applied voltages or streamer discharges that immediately branch to the gas mixing layer at higher applied voltages. The branching discharges in the gas mixing layer exhibit meandering patterns and are not reproducible. A temporal reproducibility of the inception of down to 2 ns can be achieved. Despite the fact that the branching streamer discharges observed in Ar feed gas are not reproducible, they are still guided streamers in the sense that they are confined by the gas flow.

### Physical mechanisms of the memory effect

The reproducibility of pulsed plasma jets is generally ascribed to a memory effect: the required seed electrons for the next discharge are provided by remnants of the previous discharges. The development of the memory effect during the first discharges has been observed using ICCD imaging and time-resolved emission measurements for N<sub>2</sub> and He feed gas, and the involved mechanisms have been identified. Additionally, the role of charged species in the discharge remnants has been examined by manipulating the memory effect with an external electric field between consecutive discharges. The following conclusions can be drawn:

- 
- The first discharge may occur at any time during the voltage pulse. This very likely happens because the first discharge requires a background electron at the right location and time since there is no memory effect yet to provide seed electrons. This is the case for both  $N_2$  and He feed gas.
  - Starting from the second discharge, the moment of inception is sub-nanosecond reproducible. This shows that the first discharge provides sufficient remnants to mediate the temporal memory effect. This is the case for both  $N_2$  and He feed gas. It should be noted, however, that longer development times have been reported in the literature for He feed gas in a plasma source with a different design [59]. Therefore, the development of temporal reproducibility may depend on the specific plasma source.
  - For pulsed plasma jets in  $N_2$  feed gas, the spatial reproducibility and guiding mechanism are provided by a spatial memory effect, which develops in approximately ten discharges. In the first ten discharges, the guided streamer in  $N_2$  feed gas grows in length. Using a fluid dynamics model, it is demonstrated that the length of the first discharges is related to the distance that discharge remnants have been transported in the gas flow since the first discharge.
  - For pulsed plasma jets in He feed gas, the spatial guiding mechanism is provided by the He gas and the resulting gas mixing layer. All guided streamers, including the first ones, propagate along the gas mixing layer. Only the length of the first discharge may differ and depends on the moment in the voltage pulse at which the first discharge occurs. If the first discharge occurs early in the voltage pulse, the trajectory and length of the first discharge are the same as for subsequent discharges, showing that there is no spatial memory effect related to discharge remnants in this case.
  - Charged species play an important role in the spatial memory effect of guided streamers in  $N_2$ . This is demonstrated by the fact that trajectories of guided streamer discharges in  $N_2$  can be displaced from their usual position along the centre of the jet by manipulating the memory effect with an external electric field between successive discharges. The displacement is found to be related in direction and magnitude to positive ions. This result is surprising, as it was expected that the discharge would follow the electrons instead. The mechanism behind this is not yet understood.

To gain further insight in the guiding mechanism of guided streamers in  $N_2$ , it is recommended to develop a drift-diffusion type plasma model that includes both the discharge and the interaction between discharge remnants and an external electric field. Such a model can reveal why the discharges seemingly follow the positive ions and what the source of seed electrons is in this case.

### **Electron density between successive discharges in $N_2$**

The decay of the electron density between successive discharges in a pulsed plasma jet in  $N_2$  feed gas has been investigated using microwave cavity resonance spectroscopy (MCRS). The method and analysis were adapted to be able to apply this diagnostic to

a pulsed plasma jet at atmospheric pressure. The results were compared to a global model. The most important findings are listed.

- The achieved detection limit of MCRS for a pulsed plasma jet in  $N_2$  is of the order of  $10^{16} \text{ m}^{-3}$ . Measurements up to about  $60 \mu\text{s}$  after a discharge can be performed before the noise threshold is reached. This limit is approximately one order of magnitude too high to measure the entire decay between two successive discharges.
- The absolute accuracy of the measured electron density is limited to the order of magnitude. Assumptions on the spatial distribution of the electron density, which are required in the analysis of the measurements, determine this limit. Despite the large uncertainty in the absolute values, the measured electron densities are in the same range as those predicted by the global model.
- There is a good qualitative agreement in the decay rate between the measurements and the model. Although the error in absolute electron density is high, it is systematic. Therefore, the decay rate can still be measured.
- The minimum required seed electron density for repeatable guided streamers in a pulsed plasma jet in  $N_2$  feed gas is of the order of  $10^{15} \text{ m}^{-3}$ . The minimum repetition frequency at which reproducible guided streamers are generated is 2 kHz. From the global model, it is inferred that the electron density decreases to  $10^{15} \text{ m}^{-3}$  in the time between discharges at this frequency. This value is of the same order of magnitude as the minimum required seed electron density reported for He feed gas [9, 31].

While the presented results have demonstrated that MCRS could provide a useful electron density diagnostic for pulsed plasma jets in  $N_2$ , the accuracy in absolute electron densities has to be increased for future measurements. It is recommended to use a cavity with optical access to the side of the discharge. This would aid in determining the initial plasma volume and electron density distribution. Additionally, it is recommended to design the setup such that more than one mode is available for measurement. It has recently been demonstrated that multi-mode MCRS can be used to reconstruct electron density distributions [92], which would avoid the need for assumptions of the electron density distribution.

### **Electric field of guided streamer discharges in $N_2$**

The electric field of guided streamer discharges in a pulsed plasma jet in  $N_2$  feed gas has been investigated using polarisation-resolved electric field four-wave mixing. The method has been extended with an Abel-inversion method to obtain radially resolved field profiles, and an ex-situ calibration procedure with electrodes different from the discharge geometry has been demonstrated. The results were compared to a streamer model adapted to the experimental conditions. Additionally, a theoretical calculation of the four-wave mixing process with Gaussian beams instead of plane-waves has been performed to assess the validity of the plane-wave approximation, which is usually used in the analysis.

- 
- Due to the high streamer propagation velocity of the order of  $10^5$  m/s, (sub)-ns temporal resolution is required to measure the electric fields accurately. Since the experiments were performed with approximately 5 ns pulsed lasers, the measured electric fields are convolved with the laser pulse duration, which led to underestimated peak electric field values.
  - A radial profile has been obtained for the axial component of the electric field in front of the guided streamer with a peak value of about 12–18 kV/mm, depending on fit parameters, and a full width at half maximum of 750–900  $\mu\text{m}$ . While the limited temporal resolution of the system led to an underestimation of the true peak value, the found value is in the expected range for streamer discharges in  $\text{N}_2$  and  $\text{N}_2/\text{O}_2$  mixtures reported in the literature [156–158].
  - For comparison to the experiment, the electric field obtained from the streamer model was convolved with profiles of the laser beams. The streamer model predicted peak electric field values about a factor 2 lower than those measured in the experiment, as well as a faster radial decay. Although, these differences are reasonable considering the used approximations and the experimental uncertainties, one potential source for the error has been identified as the plane-wave approximation in the calibration measurement.
  - Temporal profiles were obtained for fixed points in space as the bullet propagates. Here it is found that the radial component of the electric field only reaches values above the measurement threshold after the front of the discharge has passed the measurement position. Qualitatively similar features were observed in the model.
  - Ex-situ calibration with electrodes different from the discharge geometry can be performed, but the validity of the plane-wave approximation should always be carefully considered. If the typical dimensions of the calibration field and the electric field to be measured are different, and especially if one of them is of the order of the Rayleigh length of the lasers or larger, large errors can be introduced in the measured field values. The theoretical analysis using Gaussian beams instead of plane-waves has shown the calibration factor was overestimated by a factor 2 in our measurements because of this.

To improve the electric field four-wave mixing measurements, most importantly the temporal resolution needs to be improved. It is therefore recommended to use a picosecond laser system instead of a nanosecond laser system in future measurements. Furthermore, it is recommended to design the laser setup and calibration field such that the typical dimension of the calibration field, as well as the electric field to be measured, are both much smaller than the Rayleigh length of the lasers. This way, significant errors due to deviations from the plane-wave approximation are avoided.





---

## Bibliography

- [1] Fridman A *Plasma Chemistry* 2008 (Cambridge: Cambridge University Press) ISBN 9780511546075
- [2] Lieberman M A and Lichtenberg A J *Principles of Plasma Discharges and Materials Processing* 2005 (Hoboken, New Jersey: Wiley) ISBN 9780471720010
- [3] von Keudell A and Schulz-von der Gathen V “Foundations of low-temperature plasma physics an introduction” 2017 *Plasma Sources Sci. Technol.* **26**, 113001
- [4] Raizer Y P *Gas Discharge Physics* 1991 (Berlin, Heidelberg: Springer Berlin Heidelberg) ISBN 9783642647604
- [5] Teschke M, Kedzierski J, Finantu-Dinu E, Korzec D and Engemann J “High-speed photographs of a dielectric barrier atmospheric pressure plasma jet” 2005 *IEEE Trans. Plasma Sci.* **33**, 310–311
- [6] Lu X and Laroussi M “Dynamics of an atmospheric pressure plasma plume generated by submicrosecond voltage pulses” 2006 *J. Appl. Phys.* **100**, 063302
- [7] Hofmann S, Sobota A and Bruggeman P “Transitions Between and Control of Guided and Branching Streamers in DC Nanosecond Pulsed Excited Plasma Jets” 2012 *IEEE Trans. Plasma Sci.* **40**, 2888–2899
- [8] Lu X, Naidis G V, Laroussi M and Ostrikov K “Guided ionization waves: Theory and experiments” 2014 *Phys. Rep.* **540**, 123–166
- [9] Lu X and Ostrikov K K “Guided ionization waves: The physics of repeatability” 2018 *Appl. Phys. Rev.* **5**, 031102
- [10] Lu X, Laroussi M and Puech V “On atmospheric-pressure non-equilibrium plasma jets and plasma bullets” 2012 *Plasma Sources Sci. Technol.* **21**, 034005
- [11] Bárdos L and Baránková H “Cold atmospheric plasma: Sources, processes, and applications” 2010 *Thin Solid Films* **518**, 6705–6713

- [12] Foest R, Kindel E, Lange H, Ohl A, Stieber M and Weltmann K D “RF Capillary Jet - A Tool for Localized Surface Treatment” 2007 *Contrib. to Plasma Phys.* **47**, 119–128
- [13] West A, van der Schans M, Xu C, Cooke M and Wagenaars E “Fast, downstream removal of photoresist using reactive oxygen species from the effluent of an atmospheric pressure plasma jet” 2016 *Plasma Sources Sci. Technol.* **25**, 02LT01
- [14] Fridman G, Friedman G, Gutsol A, Shekhter A B, Vasilets V N and Fridman A “Applied Plasma Medicine” 2008 *Plasma Process. Polym.* **5**, 503–533
- [15] Kong M G, Kroesen G, Morfill G, Nosenko T, Shimizu T, van Dijk J and Zimmermann J L “Plasma medicine: an introductory review” 2009 *New J. Phys.* **11**, 115012
- [16] von Woedtke T, Reuter S, Masur K and Weltmann K D “Plasmas for medicine” 2013 *Phys. Rep.* **530**, 291–320
- [17] Laroussi M “Nonthermal decontamination of biological media by atmospheric-pressure plasmas: review, analysis, and prospects” 2002 *IEEE Trans. Plasma Sci.* **30**, 1409–1415
- [18] Boekema B K H L, Vlig M, Guijt D, Hijnen K, Hofmann S, Smits P, Sobota A, van Veldhuizen E M, Bruggeman P and Middelkoop E “A new flexible DBD device for treating infected wounds: in vitro and ex vivo evaluation and comparison with a RF argon plasma jet” 2016 *J. Phys. D. Appl. Phys.* **49**, 044001
- [19] Miller V, Lin A and Fridman A “Why Target Immune Cells for Plasma Treatment of Cancer” 2016 *Plasma Chem. Plasma Process.* **36**, 259–268
- [20] Adamovich I, Baalrud S D, Bogaerts A, Bruggeman P J, Cappelli M, Colombo V, Czarnetzki U, Ebert U, Eden J G, Favia P *et al.* “The 2017 Plasma Roadmap: Low temperature plasma science and technology” 2017 *J. Phys. D. Appl. Phys.* **50**, 323001
- [21] Feng Z, Luo Y and Han Y “Design of LED freeform optical system for road lighting with high luminance/illuminance ratio” 2010 *Opt. Express* **18**, 22020
- [22] Wang K, Wu D, Chen F, Liu Z, Luo X and Liu S “Angular color uniformity enhancement of white light-emitting diodes integrated with freeform lenses” 2010 *Opt. Lett.* **35**, 1860
- [23] Fang F, Zhang X, Weckenmann A, Zhang G and Evans C “Manufacturing and measurement of freeform optics” 2013 *CIRP Ann.* **62**, 823–846
- [24] Winter J, Brandenburg R and Weltmann K D “Atmospheric pressure plasma jets: an overview of devices and new directions” 2015 *Plasma Sources Sci. Technol.* **24**, 064001
- [25] Hübner S, Hofmann S, van Veldhuizen E M and Bruggeman P J “Electron densities and energies of a guided argon streamer in argon and air environments” 2013 *Plasma Sources Sci. Technol.* **22**, 065011

- 
- [26] Linde Gas *Product Data Sheets* [https://www.linde-gas.nl/en/products\\_and\\_supply/product\\_data\\_sheets/index.html](https://www.linde-gas.nl/en/products_and_supply/product_data_sheets/index.html) Accessed: 19 May 2018
- [27] Naidis G V “Modelling of plasma bullet propagation along a helium jet in ambient air” 2011 *J. Phys. D. Appl. Phys.* **44**, 215203
- [28] Mericam-Bourdet N, Laroussi M, Begum A and Karakas E “Experimental investigations of plasma bullets” 2009 *J. Phys. D. Appl. Phys.* **42**, 055207
- [29] Karakas E, Koklu M and Laroussi M “Correlation between helium mole fraction and plasma bullet propagation in low temperature plasma jets” 2010 *J. Phys. D. Appl. Phys.* **43**, 155202
- [30] Xiong R, Xiong Q, Nikiforov A Y, Vanraes P and Leys C “Influence of helium mole fraction distribution on the properties of cold atmospheric pressure helium plasma jets” 2012 *J. Appl. Phys.* **112**, 033305
- [31] Nie L, Chang L, Xian Y and Lu X “The effect of seed electrons on the repeatability of atmospheric pressure plasma plume propagation: I. Experiment” 2016 *Phys. Plasmas* **23**, 093518
- [32] Pope S B *Turbulent Flows* 2000 (Cambridge: Cambridge University Press) ISBN 9780511840531
- [33] Takamura S, Saito S, Kushida G, Kando M and Ohno N “Fluid Mechanical Characteristics of Microwave Discharge Jet Plasmas at Atmospheric Gas Pressure” 2010 *IEEJ Trans. Fundam. Mater.* **130**, 493–500
- [34] van Gessel B, Brandenburg R and Bruggeman P “Electron properties and air mixing in radio frequency driven argon plasma jets at atmospheric pressure” 2013 *Appl. Phys. Lett.* **103**, 064103
- [35] Zhang S, Sobota A, van Veldhuizen E M and Bruggeman P J “Gas flow characteristics of a time modulated APPJ: the effect of gas heating on flow dynamics” 2015 *J. Phys. D. Appl. Phys.* **48**, 015203
- [36] Menter F R “Two-equation eddy-viscosity turbulence models for engineering applications” 1994 *AIAA J.* **32**, 1598–1605
- [37] Trelles J P “Advances and challenges in computational fluid dynamics of atmospheric pressure plasmas” 2018 *Plasma Sources Sci. Technol.* **27**, 093001
- [38] Wilkes J O *Fluid Mechanics for Chemical Engineers* 3rd ed 2017 (Boston, Massachusetts: Prentice Hall) ISBN 9780134712826
- [39] Papadopoulos P K, Vafeas P, Svarnas P, Gazeli K, Hatzikonstantinou P M, Gkelios A and Clément F “Interpretation of the gas flow field modification induced by guided streamer (‘plasma bullet’) propagation” 2014 *J. Phys. D. Appl. Phys.* **47**, 425203
- [40] Robert E, Sarron V, Darny T, Riès D, Dozias S, Fontane J, Joly L and Pouvesle J M “Rare gas flow structuration in plasma jet experiments” 2014 *Plasma Sources Sci. Technol.* **23**, 012003

- [41] Pei X, Ghasemi M, Xu H, Hasnain Q, Wu S, Tu Y and Lu X “Dynamics of the gas flow turbulent front in atmospheric pressure plasma jets” 2016 *Plasma Sources Sci. Technol.* **25**, 035013
- [42] Xian Y B, Hasnain Qaisrani M, Yue Y F and Lu X P “Discharge effects on gas flow dynamics in a plasma jet” 2016 *Phys. Plasmas* **23**, 103509
- [43] Lietz A M, Johnsen E and Kushner M J “Plasma-induced flow instabilities in atmospheric pressure plasma jets” 2017 *Appl. Phys. Lett.* **111**, 114101
- [44] Darny T, Pouvesle J M, Fontane J, Joly L, Dozias S and Robert E “Plasma action on helium flow in cold atmospheric pressure plasma jet experiments” 2017 *Plasma Sources Sci. Technol.* **26**, 105001
- [45] Park S, Cvelbar U, Choe W and Moon S Y “The creation of electric wind due to the electrohydrodynamic force” 2018 *Nat. Commun.* **9**, 371
- [46] Sretenović G B, Iskrenović P S, Krstić I B, Kovačević V V, Obradović B M and Kuraica M M “Quantitative analysis of plasma action on gas flow in a He plasma jet” 2018 *Plasma Sources Sci. Technol.* **27**, 07LT01
- [47] Šimek M, Babický V, Člupek M and Šunka P “Observation of the N<sub>2</sub> Herman infrared system in pulsed positive streamer induced emission at atmospheric pressure” 2001 *J. Phys. D. Appl. Phys.* **34**, 3185–3190
- [48] Šimek M, Člupek M, Babický V and Šunka P “Production of reactive species by atmospheric pressure streamers in N<sub>2</sub>-O<sub>2</sub> mixtures” 2006 *Pure Appl. Chem.* **78**, 1213–1225
- [49] Šimek M, Prukner V and Schmidt J “Optical and electrical characteristics of a single surface DBD micro-discharge produced in atmospheric-pressure nitrogen and synthetic air” 2011 *Plasma Sources Sci. Technol.* **20**, 025009
- [50] Bruggeman P J, Sadeghi N, Schram D C and Linss V “Gas temperature determination from rotational lines in non-equilibrium plasmas: a review” 2014 *Plasma Sources Sci. Technol.* **23**, 023001
- [51] Liu D X, Bruggeman P, Iza F, Rong M Z and Kong M G “Global model of low-temperature atmospheric-pressure He + H<sub>2</sub>O plasmas” 2010 *Plasma Sources Sci. Technol.* **19**, 025018
- [52] Liu J J and Kong M G “Sub-60 °C atmospheric helium-water plasma jets: modes, electron heating and downstream reaction chemistry” 2011 *J. Phys. D. Appl. Phys.* **44**, 345203
- [53] Xiong Q, Nikiforov A Y, Lu X P and Leys C “A Branching Streamer Propagation Argon Plasma Plume” 2011 *IEEE Trans. Plasma Sci.* **39**, 2094–2095
- [54] Reuter S, Schmidt-Bleker A, Iseni S, Winter J and Weltmann K D “On the Bullet-Streamer Dualism” 2014 *IEEE Trans. Plasma Sci.* **42**, 2428–2429
- [55] Wu S, Wang Z, Huang Q, Tan X, Lu X and Ostrikov K “Atmospheric-pressure plasma jets: Effect of gas flow, active species, and snake-like bullet propagation” 2013 *Phys. Plasmas* **20**, 023503

- 
- [56] Pearse R W B and Gaydon A G *The Identification of Molecular Spectra* 1965 (London: Chapman & Hall) ISBN 9780412014604
- [57] NIST *Atomic Spectra Database (version 5.5.6)* <https://physics.nist.gov/asd> Accessed: 19 May 2018
- [58] Directed Energy Inc *DEI PVX-4110 datasheet* <https://directedenergy.com/product/pvx-4110/> Accessed: 13 August 2018
- [59] Wu S and Lu X “The role of residual charges in the repeatability of the dynamics of atmospheric pressure room temperature plasma plume” 2014 *Phys. Plasmas* **21**, 123509
- [60] Kossyi I A, Kostinsky A Y, Matveyev A A and Silakov V P “Kinetic scheme of the non-equilibrium discharge in nitrogen-oxygen mixtures” 1992 *Plasma Sources Sci. Technol.* **1**, 207–220
- [61] Wu S, Lu X and Pan Y “Effects of seed electrons on the plasma bullet propagation” 2013 *Curr. Appl. Phys.* **13**, S1–S5
- [62] Lu X, Jiang Z, Xiong Q, Tang Z and Pan Y “A single electrode room-temperature plasma jet device for biomedical applications” 2008 *Appl. Phys. Lett.* **92**, 151504
- [63] Slikboer E, Guaitella O and Sobota A “Time-resolved electric field measurements during and after the initialization of a kHz plasma jet from streamers to guided streamers” 2016 *Plasma Sources Sci. Technol.* **25**, 03LT04
- [64] Nijdam S, Takahashi E, Teunissen J and Ebert U “Streamer discharges can move perpendicularly to the electric field” 2014 *New J. Phys.* **16**, 103038
- [65] Nijdam S, Teunissen J, Takahashi E and Ebert U “The role of free electrons in the guiding of positive streamers” 2016 *Plasma Sources Sci. Technol.* **25**, 044001
- [66] Walsh J L, Olszewski P and Bradley J W “The manipulation of atmospheric pressure dielectric barrier plasma jets” 2012 *Plasma Sources Sci. Technol.* **21**, 034007
- [67] Shashurin A, Shneider M N and Keidar M “Measurements of streamer head potential and conductivity of streamer column in cold nonequilibrium atmospheric plasmas” 2012 *Plasma Sources Sci. Technol.* **21**, 034006
- [68] Naidis G V and Walsh J L “The effects of an external electric field on the dynamics of cold plasma jets: experimental and computational studies” 2013 *J. Phys. D: Appl. Phys.* **46**, 095203
- [69] Lin L and Keidar M “Cold atmospheric plasma jet in an axial DC electric field” 2016 *Phys. Plasmas* **23**, 083529
- [70] Zhu P, Meng Z, Hu H and Ouyang J “Effect of external electric and magnetic field on propagation of atmospheric pressure plasma jet” 2017 *Phys. Plasmas* **24**, 103512
- [71] *COMSOL 5.3a Material Library*
- [72] McKnight L G, McAfee K B and Sipler D P “Low-field drift velocities and reactions of nitrogen ions in nitrogen” 1967 *Phys. Rev.* **164**, 62–70

- [73] *Phelps database* [www.lxcat.net](http://www.lxcat.net) Accessed: 02 October 2018
- [74] *BOLSIG+ solver ver. 03/2016* [www.lxcat.net](http://www.lxcat.net)
- [75] Nikiforov A Y, Leys C, Gonzalez M A and Walsh J L “Electron density measurement in atmospheric pressure plasma jets: Stark broadening of hydrogenated and non-hydrogenated lines” 2015 *Plasma Sources Sci. Technol.* **24**, 034001
- [76] van Gessel A F H, Carbone E A D, Bruggeman P J and van der Mullen J J A M “Laser scattering on an atmospheric pressure plasma jet: disentangling Rayleigh, Raman and Thomson scattering” 2012 *Plasma Sources Sci. Technol.* **21**, 015003
- [77] Hübner S, Sousa J S, van der Mullen J and Graham W G “Thomson scattering on non-thermal atmospheric pressure plasma jets” 2015 *Plasma Sources Sci. Technol.* **24**, 054005
- [78] Hübner S, Sousa J S, Puech V, Kroesen G M W and Sadeghi N “Electron properties in an atmospheric helium plasma jet determined by Thomson scattering” 2014 *J. Phys. D. Appl. Phys.* **47**, 432001
- [79] Klarenaar B L M, Guaitella O, Engeln R and Sobota A “How dielectric, metallic and liquid targets influence the evolution of electron properties in a pulsed He jet measured by Thomson and Raman scattering” 2018 *Plasma Sources Sci. Technol.* **27**, 085004
- [80] Lu X P and Laroussi M “Electron density and temperature measurement of an atmospheric pressure plasma by millimeter wave interferometer” 2008 *Appl. Phys. Lett.* **92**, 051501
- [81] Ito Y, Sakai O and Tachibana K “Measurement of electron density in a microdischarge-integrated device operated in nitrogen at atmospheric pressure using a millimetre-wave transmission method” 2010 *Plasma Sources Sci. Technol.* **19**, 025006
- [82] Wang X, Stockett P, Jagannath R, Bane S and Shashurin A “Time-resolved measurements of electron density in nanosecond pulsed plasmas using microwave scattering” 2018 *Plasma Sources Sci. Technol.* **27**, 07LT02
- [83] Haverlag M, Kroesen G M W, Bisschops T H J and de Hoog F J “Measurement of electron densities by a microwave cavity method in 13.56-MHz RF plasmas of Ar, CF<sub>4</sub>, C<sub>2</sub>F<sub>6</sub>, and CHF<sub>3</sub>” 1991 *Plasma Chem. Plasma Process.* **11**, 357–370
- [84] Stoffels E, Stoffels W W, Vender D, Kando M, Kroesen G M W and de Hoog F J “Negative ions in a radio-frequency oxygen plasma” 1995 *Phys. Rev. E* **51**, 2425–2435
- [85] Beckers J, Stoffels W W and Kroesen G M W “Temperature dependence of nucleation and growth of nanoparticles in low pressure Ar/CH<sub>4</sub> RF discharges” 2009 *J. Phys. D. Appl. Phys.* **42**
- [86] Van De Wetering F M J H, Beckers J and Kroesen G M W “Anion dynamics in the first 10 milliseconds of an argon-acetylene radio-frequency plasma” 2012 *J. Phys. D. Appl. Phys.* **45**

- 
- [87] van de Wetering F M J H, Brooimans R J C, Nijdam S, Beckers J and Kroesen G M W “Fast and interrupted expansion in cyclic void growth in dusty plasma” 2015 *J. Phys. D. Appl. Phys.* **48**, 035204
- [88] Franek J B, Nogami S H, Demidov V I, Koepke M E and Barnat E V “Correlating metastable-atom density, reduced electric field, and electron energy distribution in the post-transient stage of a 1-Torr argon discharge” 2015 *Plasma Sources Sci. Technol.* **24**, 034009
- [89] Beckers J, van der Horst R M, Osorio E A, Kroesen G M W and Banine V Y “Thermalization of electrons in decaying extreme ultraviolet photons induced low pressure argon plasma” 2016 *Plasma Sources Sci. Technol.* **25**, 035010
- [90] van der Horst R M, Beckers J, Osorio E A, Astakhov D I, Goedheer W J, Lee C J, Ivanov V V, Krivtsum V M, Koshelev K N, Lopaev D V *et al.* “Exploring the electron density in plasma induced by EUV radiation: I. Experimental study in hydrogen” 2016 *J. Phys. D. Appl. Phys.* **49**, 145203
- [91] van der Horst R M, Osorio E A, Banine V Y and Beckers J “The influence of the EUV spectrum on plasma induced by EUV radiation in argon and hydrogen gas” 2016 *Plasma Sources Sci. Technol.* **25**, 015012
- [92] Beckers J, van de Wetering F M J H, Platier B, van Ninhuijs M, Brussaard S, Banine V Y and Luiten O J “Mapping electron dynamics in highly transient EUV photon-induced plasmas: a novel diagnostic approach using multi-mode microwave cavity resonance spectroscopy” 2019 *J. Phys. D. Appl. Phys.* **52**, 034004
- [93] Jackson J D *Classical Electrodynamics* 3rd ed 1999 (New York: John Wiley & Sons) ISBN 9780471309321
- [94] Slater J C “Microwave Electronics” 1946 *Rev. Mod. Phys.* **18**, 441–512
- [95] Biondi M A “Measurement of the Electron Density in Ionized Gases by Microwave Techniques” 1951 *Rev. Sci. Instrum.* **22**, 500–502
- [96] Harrington R F *Time-Harmonic Electromagnetic Fields* 2001 (New York: Wiley-IEEE Press) ISBN 9780471208068
- [97] Franek J B, Nogami S H, Demidov V I, Koepke M E and Barnat E V “Reply to comment on ‘Correlating metastable-atom density, reduced electric field, and electron energy distribution in the post-transient stage of a 1 Torr argon discharge’ 2015 *Plasma Sources Sci. Technol.* 24 034009” 2016 *Plasma Sources Sci. Technol.* **25**, 038002
- [98] *Phelps database*, [www.lxcat.net](http://www.lxcat.net), retrieved on September 5, 2018
- [99] Lister G G, Li Y and Godyak V A “Electrical conductivity in highfrequency plasmas” 1996 *J. Appl. Phys.* **79**, 8993–8997
- [100] McColl W, Brooks C and Brake M L “Electron density and collision frequency of microwave-resonant-cavity-produced discharges” 1993 *J. Appl. Phys.* **74**, 3724–3735



- [101] Buchsbaum S J and Brown S C “Microwave Measurements of High Electron Densities” 1957 *Phys. Rev.* **106**, 196–199
- [102] van Dijk J, Peerenboom K, Jimenez M, Mihailova D and van der Mullen J “The plasma modelling toolkit Plasimo” 2009 *J. Phys. D. Appl. Phys.* **42**, 194012
- [103] *SIGLO database*, [www.lxcat.net](http://www.lxcat.net), retrieved on March 20, 2018
- [104] Hagelaar G J M and Pitchford L C “Solving the Boltzmann equation to obtain electron transport coefficients and rate coefficients for fluid models” 2005 *Plasma Sources Sci. Technol.* **14**, 722–733
- [105] Capitelli M, Ferreira C M, Gordiets B F and Osipov A I *Plasma Kinetics in Atmospheric Gases* 2000 (Berlin, Heidelberg: Springer Berlin Heidelberg) ISBN 9783642086830
- [106] Brandenburg R “Dielectric barrier discharges: progress on plasma sources and on the understanding of regimes and single filaments” 2017 *Plasma Sources Sci. Technol.* **26**, 053001
- [107] Lacoste D A, Bourdon A, Kuribara K, Urabe K, Stauss S and Terashima K “Pure airplasma bullets propagating inside microcapillaries and in ambient air” 2014 *Plasma Sources Sci. Technol.* **23**, 062006
- [108] Wujec T, Janus H W and Jelenski W “Spectroscopic measurements of electric field distributions in dielectric barrier discharges in hydrogen” 2003 *J. Phys. D. Appl. Phys.* **36**, 868–877
- [109] Wang Q, Koleva I, Donnelly V M and Economou D J “Spatially resolved diagnostics of an atmospheric pressure direct current helium microplasma” 2005 *J. Phys. D. Appl. Phys.* **38**, 1690–1697
- [110] Obradovic B M, Ivkovic S S and Kuraica M M “Spectroscopic measurement of electric field in dielectric barrier discharge in helium” 2008 *Appl. Phys. Lett.* **92**, 191501
- [111] Ivković S S, Obradović B M and Kuraica M M “Electric field measurement in a DBD in helium and heliumhydrogen mixture” 2012 *J. Phys. D. Appl. Phys.* **45**, 275204
- [112] Olszewski P, Wagenaars E, McKay K, Bradley J W and Walsh J L “Measurement and control of the streamer head electric field in an atmospheric-pressure dielectric barrier plasma jet” 2014 *Plasma Sources Sci. Technol.* **23**, 015010
- [113] Sretenović G B, Krstić I B, Kovačević V V, Obradović B M and Kuraica M M “Spatio-temporally resolved electric field measurements in helium plasma jet” 2014 *J. Phys. D. Appl. Phys.* **47**, 102001
- [114] Sobota A, Guaitella O, Sretenović G B, Krstić I B, Kovačević V V, Obrusník A, Nguyen Y N, Zajíčková L, Obradović B M and Kuraica M M “Electric field measurements in a kHz-driven He jet—the influence of the gas flow speed” 2016 *Plasma Sources Sci. Technol.* **25**, 065026
- [115] Ivković S S, Sretenović G B, Obradović B M, Cvetanović N and Kuraica M M “On the use of the intensity ratio of He lines for electric field measurements in

- atmospheric pressure dielectric barrier discharge” 2014 *J. Phys. D. Appl. Phys.* **47**, 055204
- [116] Kozlov K V, Wagner H E, Brandenburg R and Michel P “Spatio-temporally resolved spectroscopic diagnostics of the barrier discharge in air at atmospheric pressure” 2001 *J. Phys. D. Appl. Phys.* **34**, 3164–3176
- [117] Kozlov K V and Wagner H E “Progress in Spectroscopic Diagnostics of Barrier Discharges” 2007 *Contrib. to Plasma Phys.* **47**, 26–33
- [118] Robert E, Darny T, Dozias S, Iseni S and Pouvesle J M “New insights on the propagation of pulsed atmospheric plasma streams: From single jet to multi jet arrays” 2015 *Phys. Plasmas* **22**, 122007
- [119] Bourdon A, Darny T, Pechereau F, Pouvesle J M, Viegas P, Iséni S and Robert E “Numerical and experimental study of the dynamics of a  $\mu\text{s}$  helium plasma gun discharge with various amounts of  $\text{N}_2$  admixture” 2016 *Plasma Sources Sci. Technol.* **25**, 035002
- [120] Darny T, Pouvesle J M, Puech V, Douat C, Dozias S and Robert E “Analysis of conductive target influence in plasma jet experiments through helium metastable and electric field measurements” 2017 *Plasma Sources Sci. Technol.* **26**, 045008
- [121] Sobota A, Guaitella O and Garcia-Caurel E “Experimentally obtained values of electric field of an atmospheric pressure plasma jet impinging on a dielectric surface” 2013 *J. Phys. D. Appl. Phys.* **46**, 372001
- [122] Wild R, Gerling T, Bussiahn R, Weltmann K D and Stollenwerk L “Phase-resolved measurement of electric charge deposited by an atmospheric pressure plasma jet on a dielectric surface” 2014 *J. Phys. D. Appl. Phys.* **47**, 042001
- [123] Slikboer E, Garcia-Caurel E, Guaitella O and Sobota A “Charge transfer to a dielectric target by guided ionization waves using electric field measurements” 2017 *Plasma Sources Sci. Technol.* **26**, 035002
- [124] Gavrilenko V P, Kupryanova E B, Okolokulak V N, Ochkin V N, Savinov S Y, Tskhai S N and Yarashev A N “Generation of coherent IR light on a dipole-forbidden molecular transition with biharmonic pumping in a static electric field” 1992 *JETP Lett.* **56**, 1–4
- [125] Evsin O A, Kupryanova E B, Ochkin V N, Savinov S Y and Tskhai S N “Determination of the intensities of electric fields in gases and plasmas by the CARS method” 1995 *Quantum Electron.* **25**, 278–282
- [126] Akimov D A, Zheltikov A M, Koroteev N I and Naumov A N “Coherent Raman scattering in molecular hydrogen in a dc electric field” 1999 *Jetp Lett.* **70**, 375–379
- [127] Tskhai S N, Akimov D A, Mitko S V, Ochkin V N, Serdyuchenko A Y, Sidorov-Biryukov D A, Sinyaev D V and Zheltikov A M “Time-resolved polarization-sensitive measurements of the electric field in a sliding discharge by means of dc field-induced coherent Raman scattering” 2001 *J. Raman Spectrosc.* **32**, 177–181

- [128] Ito T, Kobayashi K, Czarnetzki U and Hamaguchi S “Rapid formation of electric field profiles in repetitively pulsed high-voltage high-pressure nanosecond discharges” 2010 *J. Phys. D. Appl. Phys.* **43**, 062001
- [129] Müller S, Luggenhölscher D and Czarnetzki U “Ignition of a nanosecond-pulsed near atmospheric pressure discharge in a narrow gap” 2011 *J. Phys. D. Appl. Phys.* **44**, 165202
- [130] Yatom S, Tskhai S and Krasik Y E “Electric Field in a Plasma Channel in a High-Pressure Nanosecond Discharge in Hydrogen: A Coherent Anti-Stokes Raman Scattering Study” 2013 *Phys. Rev. Lett.* **111**, 255001
- [131] Goldberg B M, Böhm P S, Czarnetzki U, Adamovich I V and Lempert W R “Electric field vector measurements in a surface ionization wave discharge” 2015 *Plasma Sources Sci. Technol.* **24**, 055017
- [132] Goldberg B M, Shkurenkov I, O’Byrne S, Adamovich I V and Lempert W R “Electric field measurements in a dielectric barrier nanosecond pulse discharge with sub-nanosecond time resolution” 2015 *Plasma Sources Sci. Technol.* **24**, 035010
- [133] Böhm P, Kettlitz M, Brandenburg R, Höft H and Czarnetzki U “Determination of the electric field strength of filamentary DBDs by CARS based fourwave mixing” 2016 *Plasma Sources Sci. Technol.* **25**, 054002
- [134] Goldberg B M, Shkurenkov I, Adamovich I V and Lempert W R “Electric field in an AC dielectric barrier discharge overlapped with a nanosecond pulse discharge” 2016 *Plasma Sources Sci. Technol.* **25**, 045008
- [135] Ito T, Kobayashi K, Müller S, Luggenhölscher D, Czarnetzki U and Hamaguchi S “Electric field measurement in an atmospheric or higher pressure gas by coherent Raman scattering of nitrogen” 2009 *J. Phys. D. Appl. Phys.* **42**, 092003
- [136] Lempert W R, Kearney S P and Barnat E V “Diagnostic study of four-wave-mixing-based electric-field measurements in high-pressure nitrogen plasmas” 2011 *Appl. Opt.* **50**, 5688
- [137] Ito T, Kanazawa T and Hamaguchi S “Rapid breakdown mechanisms of open air nanosecond dielectric barrier discharges” 2011 *Phys. Rev. Lett.* **107**, 1–4
- [138] Simeni Simeni M, Goldberg B M, Zhang C, Frederickson K, Lempert W R and Adamovich I V “Electric field measurements in a nanosecond pulse discharge in atmospheric air” 2017 *J. Phys. D. Appl. Phys.* **50**, 184002
- [139] Simeni M S, Goldberg B, Gulko I, Frederickson K and Adamovich I V “Sub-nanosecond resolution electric field measurements during ns pulse breakdown in ambient air” 2018 *J. Phys. D. Appl. Phys.* **51**, 01LT01
- [140] Simeni M S, Baratte E, Zhang C, Frederickson K and Adamovich I V “Electric field measurements in nanosecond pulse discharges in air over liquid water surface” 2018 *Plasma Sources Sci. Technol.* **27**, 015011
- [141] Dogariu A, Goldberg B M, O’Byrne S and Miles R B “Species-Independent Femtosecond Localized Electric Field Measurement” 2017 *Phys. Rev. Appl.* **7**, 024024

- [142] Goldberg B M, Chng T L, Dogariu A and Miles R B “Electric field measurements in a near atmospheric pressure nanosecond pulse discharge with picosecond electric field induced second harmonic generation” 2018 *Appl. Phys. Lett.* **112**, 064102
- [143] Ochkin V N *Spectroscopy of Low Temperature Plasma* 2009 (Weinheim, Germany: Wiley-VCH Verlag GmbH & Co. KGaA) ISBN 9783527627509
- [144] Lempert W R and Adamovich I V “Coherent anti-Stokes Raman scattering and spontaneous Raman scattering diagnostics of nonequilibrium plasmas and flows” 2014 *J. Phys. D. Appl. Phys.* **47**, 433001
- [145] Boyd R W *Nonlinear optics* 3rd ed 2008 (New York: Academic Press) ISBN 9780123694706
- [146] Gavrilenko V P, Ochkin V N and Tskhai S N 2002 “Progress in plasma spectroscopic diagnostics based on Stark effect in atoms and molecules” *Proc. SPIE - Int. Soc. Opt. Eng.* vol 4460 p 207
- [147] Griem H R *Principles of Plasma Spectroscopy* 1997 Cambridge Monographs on Plasma Physics (Cambridge: Cambridge University Press) ISBN 9780511524578
- [148] Pretzler G “A New Method for Numerical Abel-Inversion” 1991 *Zeitschrift für Naturforsch. A* **46a**, 639–641
- [149] Dribinski V, Ossadtchi A, Mandelshtam V A and Reisler H “Reconstruction of Abel-transformable images: The Gaussian basis-set expansion Abel transform method” 2002 *Rev. Sci. Instrum.* **73**, 2634
- [150] Luque A and Ebert U “Density models for streamer discharges: Beyond cylindrical symmetry and homogeneous media” 2012 *J. Comput. Phys.* **231**, 904–918
- [151] *Phelps database*, [www.lxcat.net](http://www.lxcat.net), retrieved on April 3 2017 [www.lxcat.net](http://www.lxcat.net)
- [152] Teunissen J and Ebert U “Afivo: A framework for quadtree/octree AMR with shared-memory parallelization and geometric multigrid methods” 2018 *Comput. Phys. Commun.* **233**, 156–166
- [153] Nijdam S, Takahashi E, Markosyan A H and Ebert U “Investigation of positive streamers by double-pulse experiments, effects of repetition rate and gas mixture” 2014 *Plasma Sources Sci. Technol.* **23**, 025008
- [154] Pancheshnyi S, Starikovskaia S and Starikovskii A “Collisional deactivation of  $N_2(C, v=0, 1, 2, 3)$  states by  $N_2$ ,  $O_2$ ,  $H_2$  and  $H_2O$  molecules” 2000 *Chem. Phys.* **262**, 349–357
- [155] Shcherbakov Y V and Sigmond R S “Subnanosecond spectral diagnostics of streamer discharges: I. Basic experimental results” 2007 *J. Phys. D. Appl. Phys.* **40**, 460–473
- [156] Naidis G V “Positive and negative streamers in air: Velocity-diameter relation” 2009 *Phys. Rev. E* **79**, 057401
- [157] Wormeester G, Pancheshnyi S, Luque A, Nijdam S and Ebert U “Probing photoionization: simulations of positive streamers in varying  $N_2:O_2$ -mixtures” 2010 *J. Phys. D. Appl. Phys.* **43**, 505201

- [158] Bonaventura Z, Bourdon A, Celestin S and Pasko V P “Electric field determination in streamer discharges in air at atmospheric pressure” 2011 *Plasma Sources Sci. Technol.* **20**, 035012
- [159] Boeuf J P, Yang L L and Pitchford L C “Dynamics of a guided streamer (‘plasma bullet’) in a helium jet in air at atmospheric pressure” 2013 *J. Phys. D. Appl. Phys.* **46**, 015201
- [160] Breden D, Miki K and Raja L L “Self-consistent two-dimensional modeling of cold atmospheric-pressure plasma jets/bullets” 2012 *Plasma Sources Sci. Technol.* **21**, 034011
- [161] Sretenović G B, Krstić I B, Kovačević V V, Obradović B M and Kuraica M M “The isolated head model of the plasma bullet/streamer propagation: electric field-velocity relation” 2014 *J. Phys. D. Appl. Phys.* **47**, 355201
- [162] Bruggeman P and Brandenburg R “Atmospheric pressure discharge filaments and microplasmas: physics, chemistry and diagnostics” 2013 *J. Phys. D. Appl. Phys.* **46**, 464001
- [163] Patnaik A K, Adamovich I, Gord J R and Roy S “Recent advances in ultrafast-laser-based spectroscopy and imaging for reacting plasmas and flames” 2017 *Plasma Sources Sci. Technol.* **26**, 103001
- [164] van der Schans M, Böhm P, Teunissen J, Nijdam S, IJzerman W and Czarnetzki U “Electric field measurements on plasma bullets in N<sub>2</sub> using four-wave mixing” 2017 *Plasma Sources Sci. Technol.* **26**, 115006
- [165] New G *Introduction to Nonlinear Optics* 2011 (Cambridge: Cambridge University Press) ISBN 9780511975851
- [166] Polyanskiy M N *Refractive index database* <https://refractiveindex.info> Accessed: 01 October 2018
- [167] Bjorklund G “Effects of focusing on third-order nonlinear processes in isotropic media” 1975 *IEEE J. Quantum Electron.* **11**, 287–296
- [168] Moosmüller H, Anderson S B and She C Y “Generation of four-wave mixing and stimulated Raman signals in focused Gaussian beams” 1989 *Phys. Rev. A* **40**, 6977–6982
- [169] Poularikas A *The Transforms and Applications Handbook* 2nd ed 2000 (Boca Raton: CRC Press) ISBN 9781420036756
- [170] Siegman A *Lasers* 1986 (Mill Valley, California: University Science Books) ISBN 9780935702118
- [171] Siegman A E 1998 “How to (Maybe) Measure Laser Beam Quality” *DPSS (Diode Pumped Solid State) Lasers Appl. Issues* vol 17 (Washington, D.C.: OSA) p MQ1
- [172] Kogelnik H and Li T “Laser Beams and Resonators” 1966 *Appl. Opt.* **5**, 1550

---

# List of publications

## Peer-reviewed journal articles

- **Electric field measurements on plasma bullets in N<sub>2</sub> using four-wave mixing**  
M. van der Schans, P. Böhm, J. Teunissen, S. Nijdam, W.L. IJzerman and U. Czarnetzki  
*Plasma Sources Science and Technology* **26** 115006 (2017)  
doi: <https://doi.org/10.1088/1361-6595/aa9146>
- **Dielectric barrier discharge in air with a controllable spatial distribution—a tomographic investigation**  
M. van der Schans, A. Sobota and G.M.W. Kroesen  
*Journal of Physics D: Applied Physics* **49** 195204 (2016)  
doi: <https://doi.org/10.1088/0022-3727/49/19/195204>
- **Fast, downstream removal of photoresist using reactive oxygen species from the effluent of an atmospheric pressure plasma jet**  
A. West, M. van der Schans, C. Xu, M. Cooke and E. Wagenaars  
*Plasma Sources Science and Technology* **25** 02LT01 (2016)  
doi: <https://doi.org/10.1088/0963-0252/25/2/02LT01>

## Conference contributions

### *Oral presentations*

- 16<sup>th</sup> International Symposium on High Pressure Low Temperature Plasma Chemistry (Hakone XVI), Beijing, China (2018)
- 30<sup>th</sup> Symposium on Plasma Physics and Radiation Technology, Lunteren, The Netherlands (2018)
- 69<sup>th</sup> Annual Gaseous Electronics Conference, Bochum, Germany (2016)

- 43<sup>rd</sup> IEEE International Conference on Plasma Science, Banff, Alberta, Canada (2016)
- 27<sup>th</sup> Symposium on Plasma Physics and Radiation Technology, Lunteren, The Netherlands (2015)
- 17<sup>th</sup> Workshop on the Exploration of Low Temperature Plasma Physics, Kerkrade, The Netherlands (2014)

*Poster presentations*

- Physics@Veldhoven, Veldhoven, The Netherlands (2018)
- 20<sup>th</sup> Workshop on the Exploration of Low Temperature Plasma Physics, Kerkrade, The Netherlands (2017)
- 33<sup>rd</sup> International Conference on Phenomena in Ionized Gases, Lisbon, Portugal (2017)
- 29<sup>th</sup> Symposium on Plasma Physics and Radiation Technology, Lunteren, The Netherlands (2017)
- 19<sup>th</sup> Workshop on the Exploration of Low Temperature Plasma Physics, Kerkrade, The Netherlands (2016)
- 28<sup>th</sup> Symposium on Plasma Physics and Radiation Technology, Lunteren, The Netherlands (2016)
- 18<sup>th</sup> Workshop on the Exploration of Low Temperature Plasma Physics, Kerkrade, The Netherlands (2015)
- 26<sup>th</sup> Symposium on Plasma Physics and Radiation Technology, Lunteren, The Netherlands (2014)

---

## Contributions of the author

This thesis presents the original work of the author. Nevertheless, parts of the presented research are the result of a joint effort. The contributions of others are outlined here.

- The microwave cavity resonance spectroscopy experiments and analysis, as presented in **chapter 5**, are attributed in equal parts to ir. B. Platier and the author. The global model presented in this chapter was developed and tested in collaboration with ir. P. M. J. Koelman. The description of the research is the author's effort.
- The electric field four-wave mixing experiments presented in **chapter 6** were performed together with dr. P. S. Böhm at the Ruhr-University Bochum in the group of Professor U. Czarnetzki. The streamer simulation that is presented in this chapter and the description thereof were provided by dr. H. J. Teunissen. Besides the simulation section, the description of the research in this chapter is the author's effort.





---

## Acknowledgements / Dankwoord

De vier jaar van mijn promotieproject zijn voorbij gevlogen. Het lijkt nog maar kort geleden dat ik de keuze maakte om nog een paar jaartjes door te gaan in de academische wereld. Nu alles bijna is afgerond kan ik zeggen dat ik daar zeker geen spijt van heb. Dit is voor een groot deel te danken aan een grote groep mensen. Jullie hulp, steun en interesse is enorm belangrijk geweest voor mij de afgelopen jaren en hiervoor wil ik jullie nu bedanken.

Als eerste bedank ik mijn promotor en copromotor, Wilbert IJzerman en Sander Nijdam, voor de fijne samenwerking in de afgelopen vier jaar. Jullie hebben mij veel vrijheid gegeven in mijn project en daar ben ik jullie erg dankbaar voor. Wilbert, met soms onverwachte maar altijd relevante opmerkingen en ideeën tijdens onze meetings heb je me laten zien dat het perspectief van iemand buiten een specifiek vakgebied ontzettend nuttig is. Sander, bedankt voor alle discussies, adviezen en je praktische blik op de uitdagingen die we gaandeweg zijn tegengekomen. Ook mijn tweede promotor, Gerrit Kroesen, wil ik graag bedanken. Jij hebt me vijf jaar geleden enthousiast weten te maken voor een afstudeerproject in de EPG groep, wat er uiteindelijk toe heeft geleid dat ik nog wel een aantal jaren wilde blijven voor een promotieonderzoek.

I would also like to thank the other members of the committee, Igor Adamovich, Ronny Brandenburg, Uwe Czarnetzki and Richard Engeln. Thank you for your willingness to read and assess my thesis and to serve on the doctorate committee.

Tijdens mijn promotieproject heb ik de gelegenheid gehad om samen te werken met collega's zowel binnen als buiten de groep. De MCRS-metingen en het model van hoofdstuk 5 zijn het resultaat van een samenwerking binnen de groep met Bart, Peter, Ferdi, Jan en Job. Ondanks dat we normaalgesproken niet dezelfde plasma's onderzoeken hebben we hier toch een mooi raakvlak weten te vinden. Zoals wel vaker was het allemaal wat complexer dan dat we in eerste instantie dachten. Jullie wil ik dan ook bedanken voor jullie inzet in deze samenwerking en de mooie resultaten die dat uiteindelijk opgeleverd heeft.

The four-wave mixing measurements and streamer model in chapter 6 are the result of a collaboration with Patrick Böhm and Uwe Czarnetzki from the Ruhr-Universität

Bochum and Jannis Teunissen from CWI. I would like to thank Professor Czarnetzki for welcoming me in his group in Bochum. The possibility of testing the four-wave mixing method on plasma bullets very early on in my PhD project was extremely helpful, and I'm happy that the final results are an important part of my thesis. Of course I could not have done these measurements without Patrick. I enjoyed working together with you in the lab, and your experience and knowledge of the setup definitely helped a lot in designing our own in Eindhoven. Jannis, thank you for adapting the streamer model to our experiments and for the useful discussions on the results. I'm still impressed how you managed to provide new model data nearly instantly whenever we asked for it.

Ook heb ik het genoeg gehad om een zestal bachelor eindprojecten te mogen begeleiden. Rick, Mark, Laurens, Joran, Stef en Sybren, jullie projecten hebben tot mooie resultaten geleid die direct en indirect bijgedragen hebben aan dit proefschrift. Bedankt voor jullie enthousiasme en inzet! Op de valreep heb ik ook nog een masterstudent kunnen begeleiden bij het begin van haar afstudeerproject. Anne, ik was blij om te horen dat je opzoek was naar een uitdagend project met lasers en dat je wel aan de slag wilde met de elektrische veldmetingen. Daarnaast ging je ook de uitdaging aan om typefouten in de vergelijkingen van hoofdstuk 7 te vinden, en niet zonder resultaat. Bedankt daarvoor!

Verder wil ik natuurlijk iedereen van de EPG groep bedanken. Jullie hebben gezorgd voor een goede sfeer en dat het nooit saai is tijdens lunch- en koffiepauzes, conferenties, de jaarlijkse kerstactiviteit in april of mei en de nodige barbecues. Geen van de experimenten beschreven in dit proefschrift zouden mogelijk zijn geweest zonder de bekwame EPG technici Ab en Pieter en hoofd laboratorium Eddie, bedankt voor al jullie hulp! Anita, jij zorgt ervoor dat alles altijd perfect geregeld is, bedankt daarvoor! Uiteraard verdienen mijn kantoorgenoten Bart, Tijn en Bart en kantoorbuurman Peter het om hier ook nog even bij naam genoemd te worden. Met jullie heb ik de afgelopen vier jaar de (soms kleine) overwinningen en de (soms grote) frustraties die bij wetenschappelijk onderzoek horen kunnen delen. En nog een extra bedankje voor Bart voor het proeflezen van mijn complete proefschrift.

Tijdens een promotieonderzoek is het is ook belangrijk om soms even niet met wetenschap bezig te zijn. Hiervoor wil ik mijn vrienden en familie bedanken. Sam, Lisa, Sjoerd, Diana, Rombout, Louise, Jeroen en Janine, bedankt voor alle gezellige avonden, weekenden en trips de afgelopen (en komende) jaren! Mijn ouders en zus wil ik bedanken voor meer dingen dan die ik hier kan opnoemen. Jullie staan altijd voor me klaar en hebben ervoor gezorgd dat ik dit heb kunnen bereiken.

Last but not most certainly not least, I want to thank Susana. It was not always easy, living in different countries and finishing a PhD project around the same time, but you were always there for me and always found a way to cheer me up. Thank you for your support, for believing in me, and also for your useful suggestions to improve my thesis. With both our PhD projects now finished, I'm excited to find out what the future holds for us!

---

# Curriculum Vitae

## **Marc van der Schans**

Born on 24 January 1989 in Waalwijk, The Netherlands

- 2001–2007**      Pre-university education (VWO)  
Dr. Mollercollege, Waalwijk
- 2007–2012**      Bachelor's degree (BSc) in Applied Physics  
Minor in Entrepreneurship & Innovation  
Eindhoven University of Technology
- 2012–2013**      Certificate programme in Technology Management  
Eindhoven University of Technology
- 2012–2014**      Master's degree (MSc) in Applied Physics  
Specialisation in Plasma Physics and Radiation Technology  
Eindhoven University of Technology
- Summer 2013**      Research Internship at the York Plasma Institute  
University of York, United Kingdom
- 2014–present**      PhD candidate  
Elementary Processes in Gas discharges group  
Department of Applied Physics  
Eindhoven University of Technology